GUEST DYNAMICS IN METHANE HYDRATES AND HYDROGEN HYDRATES UNDER HIGH PRESSURE

THÈSE N^{O} 8920 (2018)

PRÉSENTÉE LE 9 NOVEMBRE 2018
À LA FACULTÉ DES SCIENCES DE BASE
LABORATOIRE DE SCIENCES DE LA TERRE ET DES PLANÈTES
PROGRAMME DOCTORAL EN PHYSIQUE

ÉCOLE POLYTECHNIQUE FÉDÉRALE DE LAUSANNE

POUR L'OBTENTION DU GRADE DE DOCTEUR ÈS SCIENCES

PAR

Umbertoluca RANIERI

acceptée sur proposition du jury:

Prof. V. Savona, président du jury
Prof. Ph. Gillet, Prof. L. E. Bove Kado, directeurs de thèse
Dr A. Desmedt, rapporteur
Dr L. Ulivi, rapporteur
Prof. H. M. Rønnow, rapporteur

ÉCOLE POLYTECHNIQUE
FÉDÉRALE DE LAUSANNE

Suisse
2018

Preamble

This thesis was part of the PhD programme of the Ecole Polytechnique Fédérale de Lausanne (EPFL) in Switzerland, jointly with the Institut Laue-Langevin (ILL) in Grenoble, France, co-founded by the two institutes. The work was supervised by Prof. Livia E. Bove Kado and Prof. Philippe Gillet at the EPFL, and by Dr Michael Marek Koza at the ILL.

Acknowledgements

First and foremost, I would like to thank my supervisors Livia E. Bove, Philippe Gillet, and Michael Marek Koza for proposing to me this subject and for giving me all the means and support necessary. A special thanks to Livia and Marek for their constant availability and their countless hints and explanations.

The results of this thesis would not have been achieved without the contribution of many scientists. Werner F. Kuhs, Richard Gaal, Stefan Klotz, Andrzej Falenty, Sofiane Schaack, Fabio Finocchi, Philippe Depondt, Jacques Ollivier, and Dirk Wallacher directly contributed to the work presented here and helped me a lot in many ways. Werner, Richard, and Stefan in particular really acted as additional thesis advisors throughout these years.

I also would like to express my gratitude to Thomas C. Hansen, Paola Giura, Frederico Alabarse, Annalisa Polidori, Luigi Paolasini, Federico A. Gorelli, Mario Santoro, Christophe Bellin, Ferdinando Formisano, Bernhard Frick, and Mohamed Mezouar for their contribution to the work we performed during the last four years which is not part of this thesis. I am indebted to Robert Pick for his valuable help and advice, and to José Teixeira, Daniele Antonangeli, Simon Huppert, Sandra Ninet, Frédéric Datchi, and Marco Saitta for the useful discussions they initiated.

My thanks also go to Claude Payre, James Maurice, Jérôme Halbwachs, Richard Ammer, Alessio Laloni, and Eddy Lelievre-Berna for technical assistance during the experiments at ILL, and in particular to Claude and James for their patience.

I would like to acknowledge Arnaud Desmedt, Henrik Rønnow, Vincenzo Savona, and Lorenzo Ulivi for accepting to be members of the jury of my doctoral exam.

I want to thank my dear lab mates at the Earth and Planetary Science Laboratory at EPFL (Farhang Nabiei, Hélène Piet, Charles Pépin, Susannah Dorfman, Harold Clenet, Elodie Amiguet, and James Badro) and all the wonderful people I met at ILL (I cannot mention them all) for the many lunches and discussions, and the fun we had together.

Many thanks to Caroline Antonioli and Anh Eymann at EPFL, and to Laurence Tellier at ILL who were always very efficient and helpful in administrative support. Thanks to

Hannu Mutka and Henry Fischer for being excellent heads of the graduate school at ILL, and to David Hess for his help in the chemistry laboratory at ILL.

Grenoble, 1 July 2018 U. R.

Abstract

Hydrates of gas are non-stoichiometric inclusion compounds constituted of water and gas. Therein, the water molecules are hydrogen-bonded and form three-dimensional crystalline networks incorporating different kinds of polar or nonpolar 'guest' gas molecules. Those networks are clathrate structures at relatively low pressures and non-clathrate, filled ice structures at very high pressures (in the GPa range and above). Gas hydrates spontaneously form whenever water and a hydrate-forming gas are in contact at high pressure and/or low temperature.

In those systems the guest molecules may perform many different dynamical processes: rotation, diffusive or quantized confined motion, cage-to-cage hopping, and translational diffusion at the structure interface. The guest dynamics is the key for stabilizing those structures and therefore to understand the process of clathrates formation as well as gas exchange processes within the structures. Investigating the guest dynamics is thus a very interesting topic from a fundamental point of view (e.g. to understand water–gas interaction) and highly relevant to the technological issues involving gas hydrates (e.g. energy recovery, flow assurance, gas transportation and storage).

This thesis focuses on the dynamics of the guest molecules in the hydrates of methane and hydrogen under high pressure, over a wide range up to 150 GPa. Pressure is a key parameter in the study of gas hydrates as it induces substantial variations in the water–gas distances as well as complete structural rearrangements. Furthermore, gas hydrates could be major constituents of the interiors of icy bodies of the Universe and therefore their high-pressure properties are of interest to planetary modeling.

We use inelastic and quasielastic neutron scattering, and Raman spectroscopy measurements on laboratory-produced methane hydrate and hydrogen hydrate samples. Interpretation of the Raman data is supported by molecular dynamics simulations. Complementary neutron and synchrotron x-ray diffraction measurements are used to monitor the system structure and structural changes. Different types of high-pressure cells are employed to span such a wide pressure range with different experimental techniques, namely a gas pressure cell, a Paris-Edinburgh cell, and a diamond anvil cell.

Three main topics are treated. In the first part, we measure the classical translational diffusion of methane molecules at the interface of two clathrate structures by quasielastic neutron scattering at 0.8 GPa. We find a remarkably fast diffusion, faster than that expected in pure methane at comparable pressure and temperature.

In the second part, we study the vibrational dynamics, orientational ordering, and distortion of methane molecules embedded in methane hydrate at extremely high pressures by simulations up to 45 GPa and Raman spectroscopy up to 150 GPa. We observe complete locking-in of the rotations at about 20 GPa, and no hints of decomposition up to the highest investigated pressure.

Finally, we investigate the quantum roto-translational dynamics of hydrogen molecules nanoconfined in two different hydrate structures by inelastic neutron scattering at pressures up to 1.4 GPa and temperatures below 50 K. Among other things, we report the first experimental observation of quantized translational dynamics for H_2 and D_2 in the large cage of clathrate structure II.

Key words: gas hydrates, clathrates, high pressure, dynamical properties, neutron spectroscopy, Raman spectroscopy, gas pressure cell, Paris-Edinburgh cell, diamond anvil cell, molecular dynamics simulations

Résumé

Les hydrates de gaz sont des complexes d'inclusion non-stœchiométriques constitués d'eau et de gaz. Les molécules d'eau sont liées par liaison hydrogène et forment des réseaux cristallins tridimensionnels incorporant plusieurs types de molécules de gaz polaires ou apolaires, dites 'invitées'. Ces réseaux sont des structures de type clathrate à des pressions relativement basses et des structures différentes, de type glace rempli à très haute pression (dans le domaine du GPa et au-delà). Les hydrates de gaz se forment spontanément quand l'eau et un gaz adéquat se trouvent en contact à haute pression et/ou basse température.

Dans ces systèmes les molécules invitées peuvent accomplir de nombreux processus dynamiques : rotation, diffusion confinée classique ou quantique, saut entre cages et translation à l'interface des structures. La dynamique des molécules invitées est l'élément clé pour stabiliser ces structures et par conséquent dans la compréhension à la fois du processus de formation des clathrates et des processus d'échange de gaz dans ces structures. Etudier la dynamique des molécules invitées est donc un sujet très intéressant d'un point de vue fondamental (par exemple pour comprendre l'interaction entre eau et gaz) et particulièrement important dans le contexte des implications technologiques des hydrates de gaz (par exemple la récupération d'énergie, l'assurance d'écoulement, le transport et le stockage de gaz).

Cette thèse se concentre sur la dynamique des molécules invitées dans les hydrates de méthane et d'hydrogène sous haute pression, dans un vaste intervalle allant jusqu'à 150 GPa. La pression est un paramètre clé dans l'étude des hydrates de gaz étant donné qu'elle peut induire des variations importantes des distances entre eau et gaz ainsi que des changements de structure. Par ailleurs, les hydrates de méthane sont suspectés d'exister en grosses quantités à l'intérieur de corps glacés de l'Univers et de ce fait leurs propriétés à haute pression sont intéressantes pour la modélisation des planètes.

Nous utilisons des mesures de diffusion inélastique et quasiélastique de neutrons, et de spectroscopie Raman sur des échantillons d'hydrate de méthane et d'hydrogène préparés en laboratoire. Dans l'interprétation des données Raman nous nous appuyons sur des simulations de dynamique moléculaire. Des mesures complémentaires de diffraction de neutrons et de rayons X sont utilisées pour surveiller la structure du système et ses changements. Des cellules haute pression différentes sont utilisées pour couvrir ce vaste intervalle de pression avec plusieurs techniques expérimentales, notamment une cellule haute pression à gaz, une cellule Paris-Edinburgh et une cellule à enclumes de diamant.

Trois sujets principaux sont traités. Dans la première partie, nous mesurons la diffusion translationnelle classique des molécules de méthane à l'interface de deux structures de type clathrate par diffusion quasiélastique de neutrons à 0.8 GPa. Nous trouvons une diffusion remarquablement rapide, plus rapide que celle attendue pour du méthane pur à pression et température comparables.

Dans la deuxième partie, nous étudions la dynamique vibrationnelle, l'ordonnement des rotations et la distorsion des molécules de méthane intégrées dans l'hydrate de méthane à des pressions extrêmement élevées par simulations jusqu'à 45 GPa et spectroscopie Raman jusqu'à 150 GPa. Nous observons un verrouillage complet des rotations vers 20 GPa et pas de signes de décomposition jusqu'à la pression maximale de notre étude.

Enfin, nous examinons la dynamique roto-translationnelle quantique des molécules d'hydrogène nanoconfinées dans deux structures d'hydrate différentes par diffusion inélastique de neutrons à des pressions jusqu'à 1.4 GPa et des températures en dessous de 50 K. Nous présentons, entre autres, la première observation de dynamique translationnelle quantique pour les molécules de H_2 et D_2 dans les grandes cages de la structure clathrate de type II.

Mots clefs : hydrates de gaz, clathrates, haute pression, proprietés dynamiques, spectroscopie de neutrons, spectroscopie Raman, cellule haute pression à gaz, cellule Paris-Edinburgh, cellule à enclumes de diamant, simulations de dynamique moléculaire

Contents

Preamble **v**

Acknowledgements **vii**

Abstract (English/Français) **ix**

1 Introduction **1**

2 Sample preparation **7**

2.1 Sample preparation procedure . . . 7

2.1.1 Methane hydrate preparation . . . 9

2.1.2 Hydrogen hydrate preparation . . . 9

3 Sample environments **11**

3.1 Gas pressure cells . . . 11

3.2 Paris-Edinburgh cells . . . 13

3.3 Diamond anvil cells . . . 15

4 Experimental techniques **17**

4.1 Neutron spectroscopy . . . 17

4.1.1 Theory of neutron scattering . . . 17

4.1.2 Neutron spectrometers (the spectrometers IN5 and IN6 at the ILL) 21

4.2 Raman spectroscopy . . . 24

4.2.1 Theory of Raman scattering . . . 24

4.2.2 Raman spectrometers . . . 25

5 Guest dynamics in methane hydrates under high pressure **27**

5.1 Motivations . . . 27

5.2 Guest dynamics in methane clathrate hydrates . . . 29

5.2.1 Introduction . . . 29

5.2.2 Article: “Fast methane diffusion at the interface of two clathrate structures” . . . 33

5.2.3 Next future steps . . . 51

5.3 Guest dynamics in methane-filled ice . . . 52

5.3.1 Introduction . . . 52
5.3.2 Article: "Orientational ordering, locking-in and distortion of CH_4 molecules in methane hydrate III under high pressure" . . . 57
5.3.3 Next future steps . . . 88
5.3.4 High-pressure Raman study of methane hydrate up to 150 GPa . . 89

6 Guest dynamics in hydrogen hydrates under high pressure 95
6.1 Motivations . . . 95
6.2 Guest dynamics in hydrogen hydrates . . . 97
6.2.1 Introduction . . . 97
6.2.2 Article: "Quantum dynamics of H_2 and D_2 confined in hydrate structures as a function of pressure and temperature" . . . 103
6.2.3 Next future steps . . . 152

7 Conclusion 153

Bibliography 167

1 Introduction

Methane hydrates and hydrogen hydrates belong to the general class of inclusion compounds called gas hydrates, which are solids made of water and small-sized, generally nonpolar molecules [1]. Those molecules, such as CH_4 and H_2 or CO_2 or N_2, typically have sizes from 4 to 9 Å and mostly exist in gaseous form at ambient conditions. At the molecular scale, gas hydrates consist of a three-dimensional crystalline network of hydrogen-bonded water molecules incorporating a smaller number of 'guest' molecules. Hydrates spontaneously form whenever water and a hydrate-forming gas are in contact at high pressure and/or low temperature. They exist in nature in the deep oceans and permafrost regions as well as in extraterrestrial environments, and can be also produced in laboratory.

At normal pressures, the crystal units of all gas hydrates are made of polyhedral 'cages' of different shapes and sizes encapsulating the gas molecules, i.e. hydrate structures are clathrate structures. Thus the name 'ice clathrate' is often used interchangeably with the designation 'gas hydrate'. However, at very high pressure (in the GPa range and above) non-clathrate structures are formed instead, as discussed below and later in this dissertation. Most hydrate-forming gases are nonpolar and hydrophobic; however, SO_2 and H_2S are polar and do form hydrates. In general, it is *not* an oversimplification to state that any molecule small enough to fit into a clathrate cage and that does not form strong hydrogen bonds with water is a good candidate for forming an hydrate. Gas clathrate hydrates have been known for approximately two centuries and during this time more than 130 guest species have been recognized to form hydrates [1].

Clathrate hydrate structures are topological duals of Frank-Kasper crystals, which are common in metal alloys [2]. Even though other structures are occasionally observed, the vast majority of the gas clathrate hydrates form one of the following three structures: the primitive cubic structure I (sI), the face-centered cubic structure II (sII), or the hexagonal structure H (sH). Those structures differ by the types and number of polyhedral cages forming their unit cells, as shown in Figure 1.1. Cages have a number of faces ranging

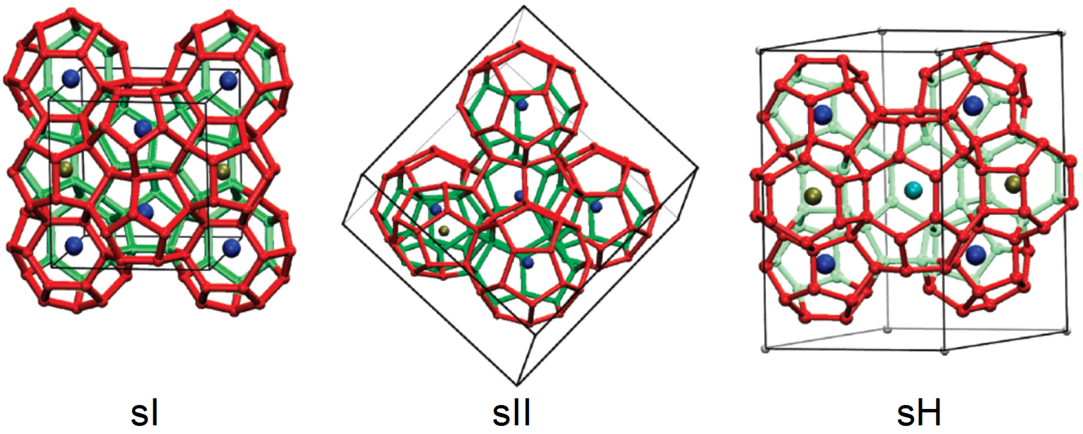

Figure 1.1: Crystal unit cells of clathrate sI, sII and sH, reproduced from ref [3]. Only a selected number of cages are represented. The vertices of the polyhedra correspond to oxygen atoms and the edges correspond to hydrogen bonds. For simplicity, spheres located at the center of the cages represent the guest molecules.

from 12 to 20 and average radii ranging from 3.9 to 5.8 Å. In all three structures, one guest molecule typically occupies each cage at normal pressures. More structural details will be given later in this dissertation.

Clathrate hydrates typically have water-to-gas molar ratios of about 6 to 1 and, being constituted for 85% of hydrogen-bonded water molecules, naturally share most of their properties with ice Ih. Yield strength, thermal expansivity and thermal conductivity are well-known exceptions. Nevertheless, the amount of gas contained in clathrate hydrates can be regarded as being remarkable when compared to the typical solubilities of (nonpolar) gases in water and therefore gas hydrates can be seen as exotic states of the water–gas systems. As an example, solubility of CH_4 in water at ambient conditions is only $2.48 \cdot 10^{-5}$ mole fraction [1], which corresponds to a molar ratio of about 40000 to 1. Furthermore, clathrate hydrates are very dense in guest molecules also in comparison to the pure gas phases–for example, one volume of methane clathrate hydrate may contain the same amount of gas as 180 volumes of pure methane at standard conditions or as one volume of pure methane at 18 MPa and 273 K [4].

Compared to other inclusion compounds, gas hydrates are peculiar in at least two respects. First, they are both crystalline and non-stoichiometric–a minority of the cages can be empty. Second, their stability relies on the combination of two different types of molecular bonding–the water molecules form hydrogen bonds between them while Van der Waals interactions exist between water and the guests and between the guests. It must be noted that the completely emptied clathrate hydrate structure is only metastable at atmospheric pressure and low temperatures but is a stable form of ice at negative pressures [5]. The interaction between water and gas molecules plays an important role in the properties of gas hydrates (in addition to their stability) and it is safe to assert that its understanding drives most of the fundamental research that is performed nowadays on gas hydrates.

Because of their importance in the economy, ecology, and gas industry, hydrates of methane are probably the most extensively studied among all gas hydrates. The existence of large quantities of methane clathrate hydrate-containing sediments on ocean floors is likely to be exploited in the future as a source of energy but is also seen as a serious environmental concern since large-scale dissociation of clathrates in those sediments would release large amounts of greenhouse gas into the atmosphere. Also, methane hydrates occasionally form in offshore gas and oil pipelines, which creates serious safety and economic problems to the gas and petroleum industry in case of complete blockage. Finally, methane hydrates are envisaged to be used for a more economic transportation and storage of gas. All these important societal challenges justify the huge efforts that are currently being made by researches to reach a better understanding of the formation and dissociation processes in gas hydrates, also at the molecular scale. Other phenomena such as structural coexistence and gas exchange also attracted considerable attention.

Hydrogen hydrates are also of great interest for their potential technological applications, being considered as a promising candidate material for hydrogen storage. From a fundamental point of view, hydrogen hydrates are model systems for studying the effect of confinement on the quantum dynamics of a light molecule and offer the possibility to investigate different confinement sizes and topologies. Hydrogen clathrate hydrate is peculiar compared to other clathrate hydrates as more than one guest molecule can be accommodated within the large cages even at ambient pressure [6, 7].

At high pressures of about 0.5–2.0 GPa, gas hydrates can undergo structural transitions to other clathrate structures but also to so-called ‘filled ice’ structures, whose water networks are not organized in cages and resemble those of some known phases of ice [1, 9]. For example, at normal pressures methane hydrate preferentially crystallizes into clathrate sI and metastably forms clathrate sII, then with increasing pressure it transforms to a phase similar to clathrate sH at around 1.0 GPa, and finally to an orthorhombic filled ice structure (‘methane hydrate-III’ or ‘MH-III’) closely related to ice Ih at around 2.0 GPa. Hydrogen hydrate forms clathrate sII below 0.4 GPa [6, 7], then it transforms to the so-called structure ‘C0’ at 0.4 GPa [10, 11], to a rhombohedral filled ice structure related to ice II at ∼0.7 GPa [12] and finally to a cubic filled ice structure related to ice Ic above ∼2.5 GPa [12]. Interestingly, structure C0 is not a clathrate structure and is unrelated to any known phase of ice. Figure 1.2 illustrates the structural changes of methane and hydrogen hydrates, and of some other gas hydrates; a detailed description can be found in refs [1, 9].

Experiments investigating molecular-level properties of gas hydrates under high pressure are then motivated by the study of water–gas interactions in a variety of water network

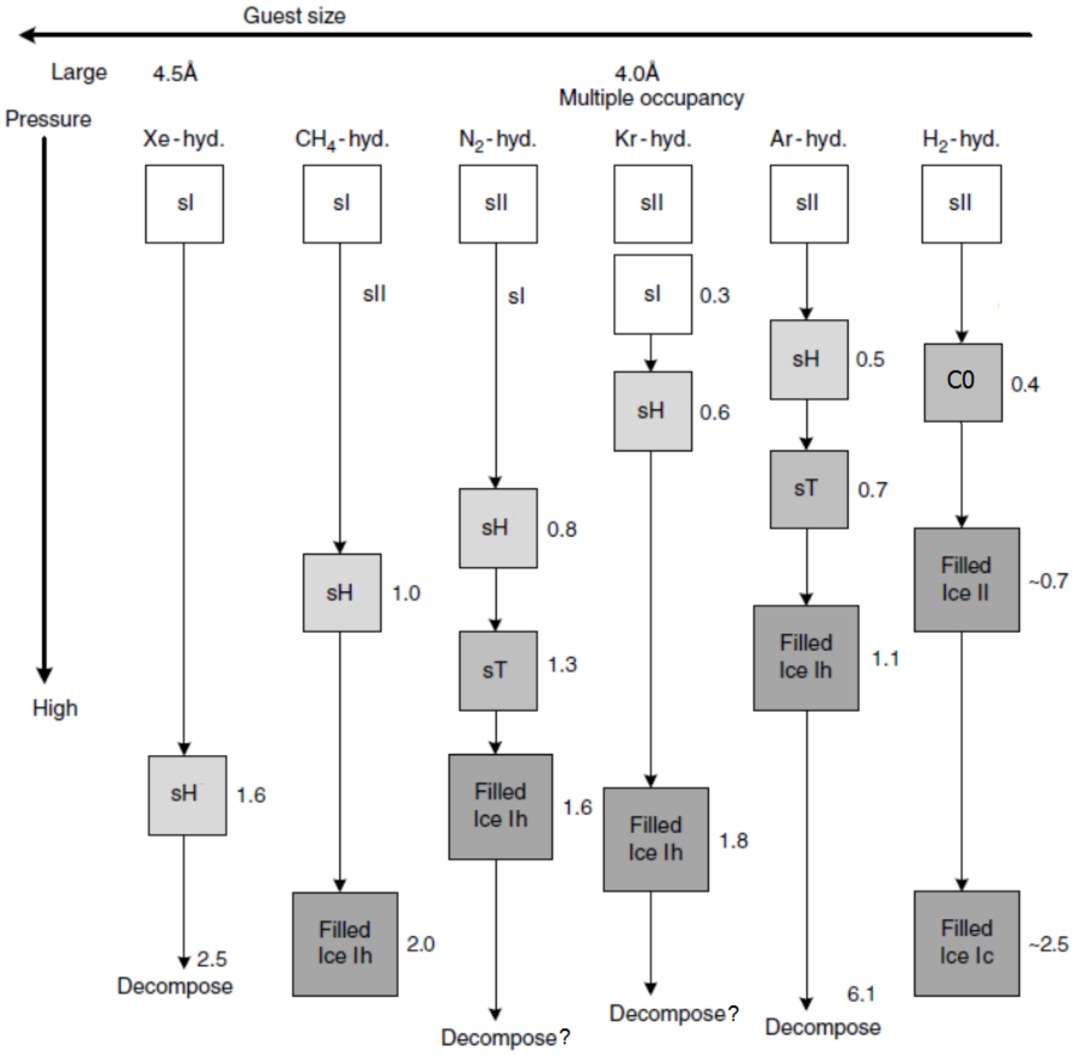
Guest size
Large
4.5Å
4.0Å
Multiple occupancy
Pressure
High
Xe-hyd.
CH$_4$-hyd.
N$_2$-hyd.
Kr-hyd.
Ar-hyd.
H$_2$-hyd.
sI
sII
sH
Filled Ice Ih
Filled Ice II
Filled Ice Ic
sT
C0
0.3
0.4
0.5
0.6
0.7
~0.7
0.8
1.0
1.1
1.3
1.6
1.8
2.0
2.5
~2.5
6.1
Decompose
Decompose?

Figure 1.2: Structural changes of some gas hydrates at high pressure and room temperature or close to room temperature, adapted from ref [1] and initially reported in ref [8]. Numbers adjacent to square boxes indicate transition pressures in GPa.

]

topologies. Furthermore, CH_4 and H_2 hydrates were found to be stable up to extremely high pressures of at least 86 and 77 GPa, respectively [13, 14]. At those pressures water-gas distances are much shorter than what can be found at normal pressures and thus methane and hydrogen hydrates provide experimental access to a completely unexplored regime of the water–gas interactions. Finally, gas hydrates are believed to exist under high pressure in the interiors of different icy bodies of the Universe and therefore their high-pressure properties are of interest to planetary scientists [15].

Over the last fifteen years several works have been performed on high-pressure gas hydrates but most of them focused on structural properties. At present very little is know about the dynamics of the guest molecules in high-pressure gas hydrates. In this thesis we use neutron spectroscopy and Raman spectroscopy measurements on laboratory-produced methane hydrate and hydrogen hydrate samples to investigate the guest dynamics in these compounds. Neutron spectroscopy provides information on diffusive motions of the guest molecule as a whole; such as classical or quantum translations and rotations. Raman spectroscopy provide information about the (intra-molecular) vibrational modes of the guests molecules, such as bending or stretching modes. Raman data were interpreted with assistance from ab-initio molecular dynamics simulations. Experiments were performed at pressures ranging from fractions of GPa to 150 GPa using different types of high-pressure devices. Pressure was used in some cases to produce high-pressure phases of the sample and in other cases as an external parameter to follow the pressure dependence of the sample properties within the same phase.

In particular, the results reported in this thesis are concerned with three main topics:

- Classical translational dynamics of methane molecules at the interface of two clathrate structures by quasielastic neutron scattering at 0.8 GPa and temperatures between 212 and 282 K (section 5.2).
- Vibrational and orientational dynamics of methane molecules embedded in the high-pressure filled ice structure of methane hydrate by Raman spectroscopy and ab-initio molecular dynamics simulations at pressures up to 45 GPa and room temperature. Extremely high pressure behavior of methane hydrate by Raman spectroscopy up to 150 GPa and room temperature (section 5.3).
- Quantum rotational and translational dynamics of hydrogen molecules confined in hydrate structures by inelastic neutron scattering at pressures below 1.4 GPa and temperatures below 50 K (section 6.2).

The dissertation is organized as follows: chapter 2 describes the sample preparation, chapter 3 describes the experimental high-pressure setups and chapter 4 describes the basic theoretical and instrumental background related to the experimental techniques. Chapters 5 and 6 are dedicated to the results and their discussion. Chapter 7 concludes the dissertation.

2 Sample preparation

This chapter describes the preparation of methane hydrate and hydrogen hydrate samples.

2.1 Sample preparation procedure

Laboratory production of gas hydrate samples relies on the spontaneous reaction between water and a hydrate-forming gas at high gas pressure and/or low temperature. As a large specific surface area is needed to speed up the formation reaction, gas hydrates are commonly prepared by exposing water ice powders to high-pressure gas following a prescription generalized in the 1990s [16, 17, 18]. Preparation from liquid water is also possible.

Polycrystalline methane hydrate and hydrogen hydrate samples were prepared during this thesis from ice powders and high-pressure methane or hydrogen. Both types of preparation were performed by following a similar procedure; however the pressures and timescales involved greatly differed. Clathrate sI methane hydrate forms at pressures in the MPa range on a timescale of hours whereas clathrate sII hydrogen hydrate forms above ∼0.1 GPa on a timescale of minutes. Figures 2.1 and 2.2 report the predicted dissociation curve of methane hydrate up to 80 MPa from ref [1] and the measured dissociation curve of hydrogen hydrate up to 0.35 GPa from ref [19].

The main steps of the preparation procedure are:

1. The precursor ice sample is prepared. This is powder ice Ih made of spherical particles with typical diameter of several tens of micrometers which is produced by a shock-freezing method through spraying liquid water into liquid nitrogen as described in ref [20]. The spraying is done in a sealed glovebox under dry nitrogen atmosphere to avoid contamination with atmospheric water.
2. The starting ice is placed into cylindrical aluminum vials of 6 or 8 mm in diameter

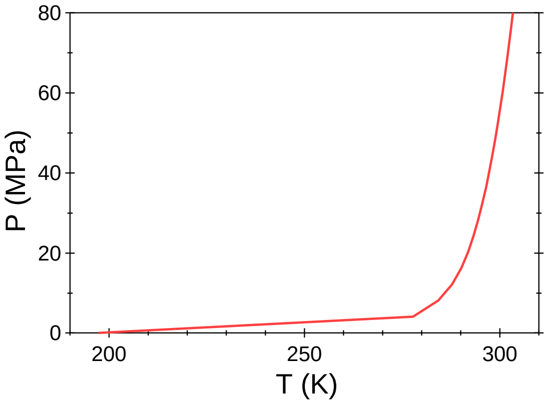

Figure 2.1: Dissociation curve of methane hydrate as given by the CSM-Gem software by E. D. Sloan and C. A. Koh [1]. Clathrate sI is stable at high pressure and low temperature.

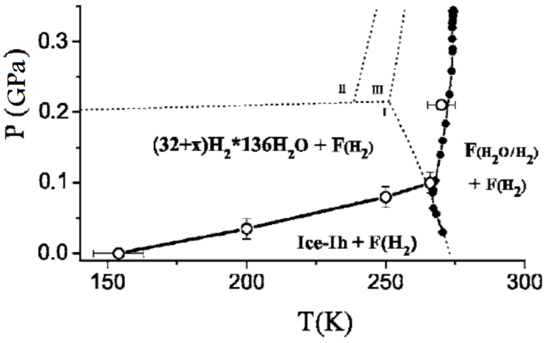

Figure 2.2: Pressure-temperature phase diagram of the H_2–H_2O system in excess of hydrogen (heavy lines and symbols), adapted from ref [19]. The phase diagram of H_2O is also plotted (dotted lines and Roman numerals for the stable ice phases). $F(H_2)$ and $F(H_2O/H_2)$ correspond to the fluid/liquid phases of H_2 and H_2 dissolved in water, $(32+x)H_2*136H_2O$ corresponds to clathrate sII.

for hydrogen hydrate production or larger polytetrafluoroethylene-polymer jars for methane hydrate production. The sample holder is then inserted into a pre-cooled pressure cell. The cell is immediately after immersed into a cold bath at the intended formation temperature and equilibrated for about 10 min.

3. The formation reaction takes place at the pressure and temperature conditions which are given in the next two subsections.

4. At the end of the formation process, the cell is cooled down in liquid nitrogen for 30–40 s. Then pressure is released and the cell is opened to recover the sample.

The preparation procedure described above provides methane hydrate and hydrogen hydrate samples containing a negligible amount of unreacted ice. However, during step 4 of the preparation, when pressure is released and the sample is recovered, special attention should be paid to avoid partial decomposition of the sample. This means that the transfer process is to be accomplished with particular care to avoid sample heating.

The prepared methane hydrate and hydrogen hydrate samples were stored in a liquid nitrogen dewar; their quality was checked by x-ray or neutron diffraction prior to the spectroscopy experiments. The quenched hydrate samples are metastable at ambient pressure: methane hydrate survives to approximately 190–200 K [1] and hydrogen hydrate survives to approximately 145–160 K [6, 7].

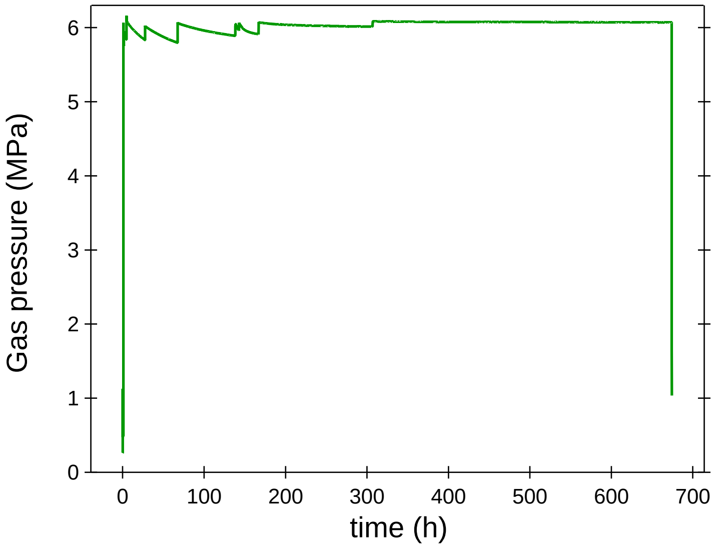

Figure 2.3: Measured gas pressure as a function of time during a methane hydrate production at University of Göttingen, as an example.

2.1.1 Methane hydrate preparation

The methane hydrate samples employed for this thesis have been prepared at the Department of Crystallography of the University of Göttingen (Germany) in collaboration with Andrzej Falenty and Werner F. Kuhs. We prepared clathrate sI CH_4–D_2O hydrate samples using 99.9% deuterated D_2O purchased from Sigma-Aldrich. During each preparation the formation reaction lasted 3–4 weeks and throughout this time the gas pressure was adjusted to be as constant as possible at about 6 MPa. Temperature was kept below the melting point during the first week, then it was increased in order to enhance molecular mobility and kept slightly above the melting during the rest of the formation reaction. Figure 2.3 reports the measured evolution of the gas pressure throughout a preparation run, as an example. Average methane occupation of samples prepared following this procedure is high and reproducible; it was found to be 0.86 molecules for the small cage and 0.99 molecules for the large cage by synchrotron x-ray diffraction [21]. Finally, samples prepared following this procedure have no detectable grain texture or crystallographic orientation and the average size of the crystallites is typically 2–4 µm [22].

2.1.2 Hydrogen hydrate preparation

The laboratory production of clathrate sII hydrogen hydrate poses some technical challenges due to the very high hydrogen pressure required. It has been first accomplished by Mao et al. [6] in 2002 and, since then, by a few other groups worldwide.

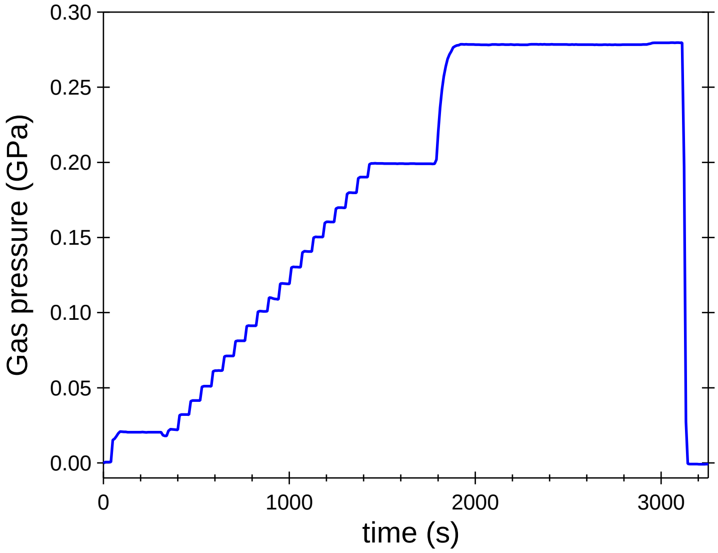

Figure 2.4: Measured gas pressure as a function of time during a hydrogen hydrate production at Helmholtz-Zentrum Berlin, as an example.

The hydrogen hydrate samples employed for this thesis have been prepared at the German neutron facility Helmholtz-Zentrum Berlin in collaboration with Dirk Wallacher (Helmholtz-Zentrum Berlin), Andrzej Falenty, and Werner F. Kuhs. We prepared clathrate sII H_2–D_2O and D_2–D_2O hydrate samples using 99.9% deuterated D_2O purchased from Sigma-Aldrich. During each preparation the formation reaction lasted about 50 min. The temperature was kept at the constant value of 244 K while the gas pressure was progressively increased to 0.28 GPa as shown in Figure 2.4. It was found by neutron diffraction measurements performed before this thesis and during this thesis that the typical average hydrogen occupation of our samples is about 0.85–1.0 molecules for the small cage and 1.5–1.8 molecules for the large cage depending on the specific sample. Clearly, guest occupation in the hydrogen clathrate hydrate samples was less reproducible compared to the methane clathrate hydrate samples.

3 Sample environments

This chapter briefly describes the pressure cells employed in the high-pressure measurements reported in this thesis. To prevent destabilization of the methane hydrate or hydrogen hydrate sample, the sample loadings into the high-pressure cells had to be performed at low temperature. This introduced a supplementary technical challenge which was overcome as explained in the following.

3.1 Gas pressure cells

Gas pressure cells are high-pressure devices employed to compress samples of the order of 1–10 cm^3 in volume to the pressure range up to 1.0 GPa (and generally up to 0.5 GPa). In those cells the pressure is increased hydrostatically, by injecting a high-pressure gas into the sample chamber. Gas pressure is controlled by a gas compressor and can be measured easily by a standard manometer or an electronic pressure gauge. Since the gas is kept permanently connected to the compressor during the measurement, the pressure can be changed in situ at any moment. In most experiments the gas is helium.

Most gas pressure cells have a cylindrical shape, but in general the geometry of the cell may differ depending on the particular application. Usually the cell can be screwed to a cryostat stick and fits into a standard helium cryostat allowing for measurements to be routinely carried out at temperatures as low as 1.5 K. For the main body of the cell, high-strength Al-alloys, Ti-Zr and Cu-Be alloys are the most commonly used materials in neutron scattering experiments. For inelastic neutron scattering, Al-alloys are certainly the most common choices.

The gas pressure cell employed in this thesis for inelastic and quasielastic neutron scattering measurements below 0.5 GPa (see section 6.2) is made of 7049A-T6 aluminum alloy and belongs to the ILL. As can be seen in Figure 3.1, it consists of a cylindrical body with an inner diameter of 6 mm and an outer diameter of 15 mm. The cell has two open ends. The capillary is connected to the top end of the cell; the sample is loaded

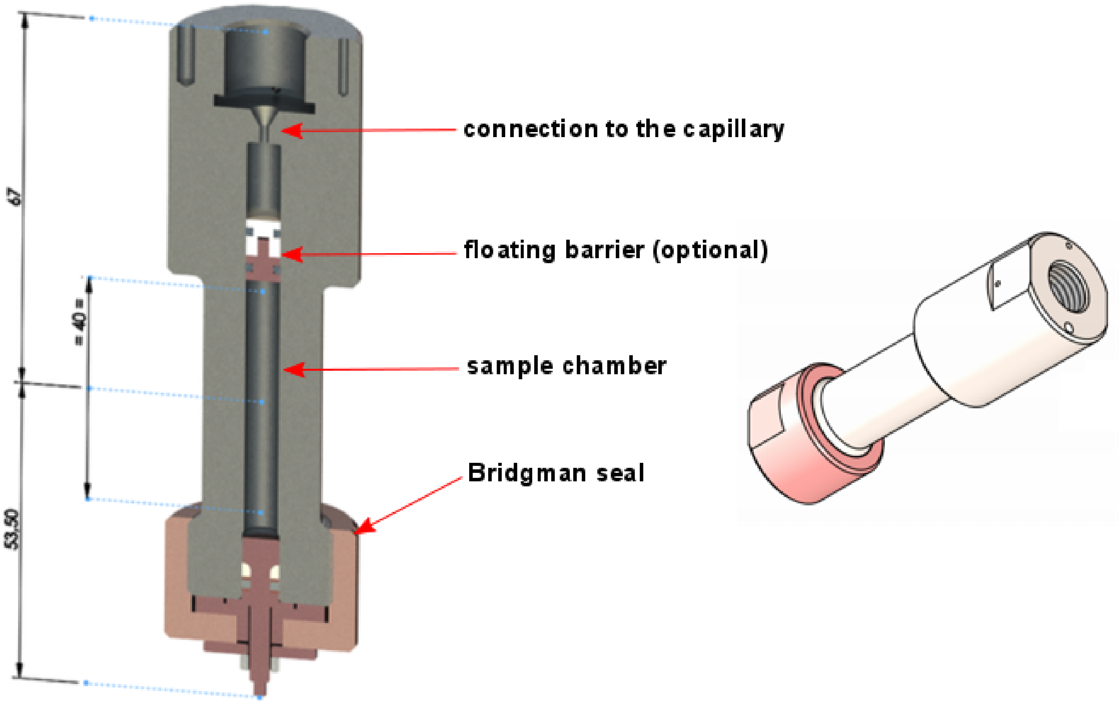
67
=40=
53,50
connection to the capillary
floating barrier (optional)
sample chamber
Bridgman seal

Figure 3.1: Cross-section and 3D drawing of the aluminum alloy gas/liquid pressure cell. Source: https://www.ill.eu/fr/users/support-labs-infrastructure/sample-environment/equipment/high-pressures/liquid-pressure-cells/17pl50al6, accessed on 15.05.2018.

from the bottom and the cell is closed by a mushroom plug with Bridgman seal. This cell can be also used for liquid samples and liquid pressure transmitting media with a floating barrier which separates the compression liquid from the sample. More details can be found in ref [23]. With this type of cell sample loading can be performed at low temperature in a liquid nitrogen bath with no major difficulties.

3.2 Paris-Edinburgh cells

Paris-Edinburgh cells or *Paris-Edinburgh presses* are compact hydraulic pressure cells which can sustain loads up to 50–500 tonnes and use an opposed anvils geometry to compress samples of typically 10–100 mm^3 in volume into the multi-GPa pressure range (generally up to 20 GPa or so) [24]. They have been first developed in the early 1990s by the groups of Jean-Michel Besson (Pierre et Marie Curie University in Paris, France) and Richard Nelmes (University of Edinburgh, UK). In those cells a hydraulic fluid pushes on a piston, which transmits the pressure to a backing disc and eventually to the anvils. The hydraulic fluid is generally a hydraulic oil at room and high temperature, and helium in low-temperature experiments.

Paris-Edinburgh cells have been initially designed for neutron diffraction but can be used for other neutron scattering techniques such as inelastic and quasielastic neutron scattering. They also found applications beyond neutron scattering. Depending on the particular application, anvils and gaskets of different kinds can be used. This choice typically translates into different pressure efficiencies, which is given by the slope of the relation between sample pressure and load on the anvils. In the normal mode of operation anvils are directly mounted into the Paris-Edinburgh press.

In the inelastic and quasielastic neutron scattering experiments between 0.4 and 1.4 GPa reported in this thesis (sections 5.2 and 6.2) we used a VX5-type Paris-Edinburgh cell in combination with a loading clamp. As shown in the drawing of Figure 3.2, such clamps include pistons, backing discs and anvils.

By applying a load of typically 5–15 tonnes to the upper clamp piston and by then tightening the locking ring, a loading clamp can be used to apply pressure on the sample before the experiment starts. Once loaded, the clamp is inserted into the Paris-Edinburgh cell for the experiment. We used recently developed anvils with non-toroidal profile made of zirconia-toughened alumina ceramics [25]. This material is highly transparent to neutrons. We used a type-25 copper-beryllium encapsulating gasket of 0.8 mm in thickness. Loading clamps are small and light devices which can be handled in a liquid nitrogen bath. Sample loading was performed at low temperature according to the following procedure:

1. Using a small dedicated press operating in a liquid nitrogen bath, the sample is compacted to a spherical pellet (of approximately 40 mm^3 in volume) of the same exact shape of the pressure chamber. This is a key step as incomplete filling of the pressure chamber is known to deteriorate the pressure efficiency. The dedicated press was designed and developed in our laboratory at the EPFL.

2. The pellet is loaded into the pre-cooled encapsulating gasket and the sample-gasket assembly is placed in an aluminum ring between pre-cooled anvils. No pressure

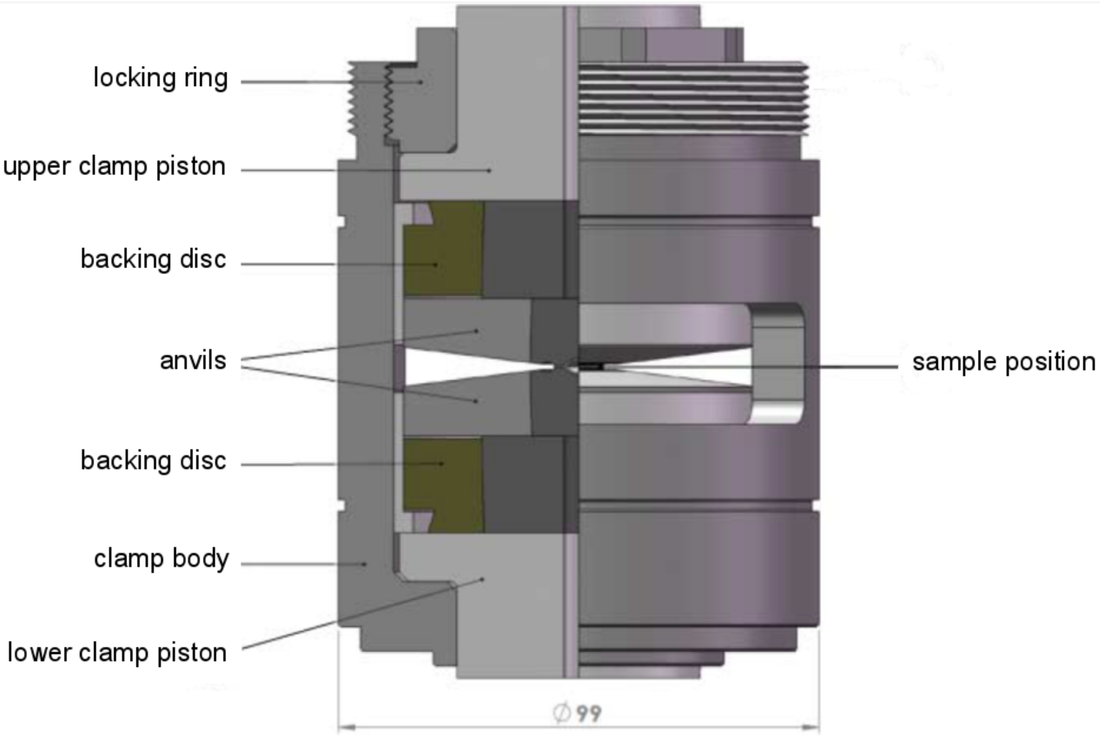
locking ring
upper clamp piston
backing disc
anvils
sample position
backing disc
clamp body
lower clamp piston
∅99

Figure 3.2: Loading clamp for Paris-Edinburgh presses with cross-section on the left half to illustrate interior, adapted from ref [27]. The clamp we used is a scaled-down version with 80 mm diameter.

transmitting medium is used.

3. While keeping the assembled loading clamp in liquid nitrogen, a load of 5–15 tonnes is applied using a hydraulic ram and locked. Such a load is high enough to seal the gasket and to increase the sample pressure to approximately 0.5–1.5 GPa.
4. The clamp is warmed up from liquid nitrogen temperature to room temperature out of the beam and finally inserted into the Paris-Edinburgh cell. Methane hydrate is stable at room temperature above 60 MPa [1] and hydrogen hydrate is stable at room temperature above 0.7 GPa [26].

Paris-Edinburgh cells are relatively big devices and do not fit into standard cryostats; dedicated cryostats can be used for low-temperature studies.

3.3 Diamond anvil cells

Diamond anvil cells are miniature hand-held devices employed to reach pressures up to 300–400 GPa. Similarly to Paris-Edinburgh cells, diamond anvil cells use opposed anvils geometry but forces involved are three orders of magnitude lower (typically 0.1 tonnes) and samples are five orders of magnitude smaller (typically 10^{-4}–10^{-3} mm^3). The force is generated either by screws or from the inflation of a membrane. Anvil diamonds are single-crystalline and of gem-quality. Depending of the target pressure range, their flat tips (culets) range from 700 to 20 µm in size. A pre-indented foil (gasket) is used to encapsulate the sample.

In the Raman spectroscopy experiments on methane hydrate up to 150 GPa reported in this thesis (section 5.3) we used a symmetric Mao–Bell-type diamond anvil cell [28] and generated the force using screws. A photograph of two cells of this type (one open and one closed) is reported in Figure 3.3. The full length of the cell in the pressurization direction is 35.9 mm; its diameter is 47.63 mm. For our experiments below 45 GPa ultralow-fluorescence type IIs synthetic diamonds with culet sizes of 300 µm were employed. The gasket was made of rhenium; a cylindrical sample chamber of $\sim$130 µm in diameter and $\sim$45 µm in thickness was drilled in its center using a laser drilling system. For the Raman spectroscopy experiment up to 150 GPa we used ultralow-fluorescence type IIs synthetic diamonds with an inner culet of 100 µm and an outer culet of 300 µm. The laser-drilled sample chamber was $\sim$40 µm in diameter and $\sim$25 µm in thickness.

Sample loading was performed in a liquid nitrogen bath in a portable glovebox under nitrogen atmosphere. A small ruby ball was generally trapped in the sample chamber during the sample loading in order to serve as a pressure gauge. Because of the low scattering cross sections of D_2O and CH_4 at high pressure, it is of vital importance to limit the amount of impurities trapped in the sample chamber during the loading. Hence, it is recommended that the sample loading is performed as fast as possible and that all components that will be in contact with liquid nitrogen are free of dust and frost. We also found preferable to use a cell for which the piston slides smoothly inside the cylinder. During some loadings a small amount of nitrogen was intentionally trapped in the sample chamber and behaved as pressure transmitting medium. In other runs no nitrogen was trapped; in this case it is recommended to use a well-compacted powder sample and to fill the sample chamber as much as possible. Our experience is that the unavoidable pressure gradient was largely dominated in our experiments by other factors (mainly the gradient of the force applied itself and the compactness of the powder sample) rather than the presence of a pressure transmitting medium.

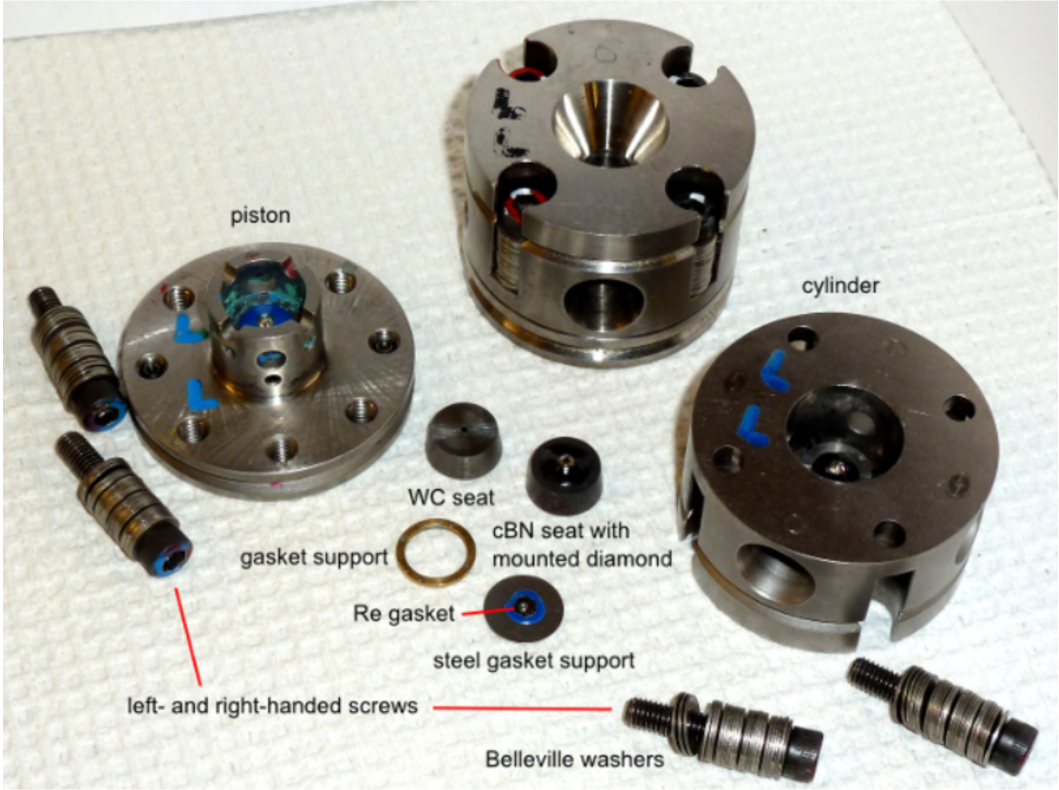
piston
cylinder
WC seat
cBN seat with
mounted diamond
gasket support
Re gasket
steel gasket support
left- and right-handed screws
Belleville washers

Figure 3.3: Photograph of two symmetric Mao–Bell-type diamond anvil cells belonging to our laboratory at the EPFL. Source: https://epsl.epfl.ch/page-78191.html, accessed on 15.05.2018.

4 Experimental techniques

Two spectroscopic experimental techniques are employed in this thesis to get insight into the dynamical behavior of methane and hydrogen in methane hydrates and hydrogen hydrates, respectively. They are briefly introduced in the following.

4.1 Neutron spectroscopy

Neutron spectroscopy employs inelastic and quasielastic neutron scattering to study atomic and molecular motion as well as magnetic and crystal field excitations of condensed matter.

4.1.1 Theory of neutron scattering

This subsection will summarize some of the main results of the non-relativistic theory of neutron scattering [29, 30]. Magnetic scattering and polarization are not relevant for this thesis and will not be treated here. Let us define m, $|\vec{k_i}\rangle$ and $|\vec{k_f}\rangle$ the mass and the initial and final states of the neutron, and $|\lambda_i\rangle$ and $|\lambda_f\rangle$ the initial and final states of the scattering system (the sample). We also define E_i and E_f the initial and final energies of the neutron, and E_{λ_i} and E_{λ_f} the initial and final energies of the scattering system. The partial (or double) differential cross section $\mathrm{d}^2\sigma/\mathrm{d}\Omega\mathrm{d}E_f$ characterizes the scattering process. It gives the probability that a normalized incident neutron flux of wavevector $\vec{k_i}$ is scattered into a solid angle element $\mathrm{d}\Omega$ perpendicular to the direction of the final neutron wavevector $\vec{k_f}$ with energies comprised between E_f and $E_f + \mathrm{d}E_f$. Within perturbation theory, it is possible to derive the following expression for $\mathrm{d}^2\sigma/\mathrm{d}\Omega\mathrm{d}E_f$:

$$\frac{\mathrm{d}^2\sigma_{\vec{k_i}\to\vec{k_f}}}{\mathrm{d}\Omega\mathrm{d}E_f} = \frac{k_f}{k_i}\frac{(2\pi)^4 m^2}{\hbar^4}\sum_{\lambda_i,\lambda_f} p(\lambda_i)|\langle\lambda_f,\vec{k_f}|V|\lambda_i,\vec{k_i}\rangle|^2\delta(E_{\lambda_i} - E_{\lambda_f} + E_i - E_f). \quad (4.1)$$

The previous expression is called the *master equation* of scattering and its derivation makes use of the fact that the scattering process can be treated within the (first) Born approximation. We are dealing here with the conditional scattering cross section of the probe changing its state from $|\vec{k_i}\rangle$ to $|\vec{k_f}\rangle$, while all the initial and final quantum states of the scattering system are included in the sum of equation (4.1). $p(\lambda_i)$ is the statistical weight of the initial state of the scattering system and $|\langle\lambda_f, \vec{k_f}|V|\lambda_i, \vec{k_i}\rangle|$ is the matrix element of the interaction potential V. The square of the matrix element gives the probability of the transition from the state $|\lambda_i, \vec{k_i}\rangle$ to the state $|\lambda_f, \vec{k_f}\rangle$ and the Dirac delta function represents conservation of energy.

By making use of the fact that i) the interaction potential is a sum of contributions of the interaction potentials of the individual scatterers and that ii) those individual interaction potentials are short-ranged enough to be represented by a Dirac delta function, it can be shown that equation (4.1) can be written as:

$$\frac{\mathrm{d}^2\sigma_{\vec{k_i}\to\vec{k_f}}}{\mathrm{d}\Omega\mathrm{d}E_f} = \frac{k_f}{k_i}\frac{1}{2\pi\hbar}\sum_{\lambda_i} p(\lambda_i) \sum_{j,j'=1}^{N} b_j b_{j'}^{*} \int_{-\infty}^{\infty} \mathrm{d}t \langle\lambda_i|\mathrm{e}^{-\mathrm{i}\vec{Q}\cdot\vec{R}_{j'}(0)}\mathrm{e}^{\mathrm{i}\vec{Q}\cdot\vec{R}_j(t)}|\lambda_i\rangle \mathrm{e}^{-\mathrm{i}\omega t}, \tag{4.2}$$

where $\vec{Q}$ is the wavevector transfer and is defined as $(\vec{k_i} - \vec{k_f})$, $\hbar\omega$ is the energy transfer and is defined as $(E_i - E_f)$, and $\vec{R}_j(t)$ is the coordinate of the jth nucleus at time t. The *scattering length* b_j of the jth nucleus, which is in general a complex number, is a measure of the strength of the neutron-nucleus interaction and depends on the isotope *and* on the spin state of the system formed by the neutron and the nucleus. The second sum in (4.2) is over all the pairs (j, j') formed by the N scatterers in the sample.

The next step consists in distinguishing between *coherent* scattering and *incoherent* scattering. The coherent scattering is the scattering the same system would give if all the scattering lengths were equal to their mean value. The incoherent scattering arises from the deviations of the scattering lengths of the actual system from their mean value. Assuming that the scattering system contains a large number of scatterers and that every possible nuclear isotope or spin orientation exists with its correct statistical weight (i.e. the distribution of nuclear isotopes and spin orientations in the sample is random), equation (4.2) can be reformulated as follows:

$$\begin{aligned}
\frac{\mathrm{d}^2\sigma}{\mathrm{d}\Omega\mathrm{d}E_f} &= \left(\frac{\mathrm{d}^2\sigma}{\mathrm{d}\Omega\mathrm{d}E_f}\right)_{coh} + \left(\frac{\mathrm{d}^2\sigma}{\mathrm{d}\Omega\mathrm{d}E_f}\right)_{inc}, \\
\left(\frac{\mathrm{d}^2\sigma}{\mathrm{d}\Omega\mathrm{d}E_f}\right)_{coh} &= \frac{k_f}{k_i}\frac{1}{2\pi\hbar}\sum_{\lambda_i} p(\lambda_i) \sum_{j,j'=1}^{N} \overline{b_j b_{j'}^{*}} \int_{-\infty}^{\infty} \mathrm{d}t \langle\lambda_i|\mathrm{e}^{-\mathrm{i}\vec{Q}\cdot\vec{R}_{j'}(0)}\mathrm{e}^{\mathrm{i}\vec{Q}\cdot\vec{R}_j(t)}|\lambda_i\rangle \mathrm{e}^{-\mathrm{i}\omega t}, \\
\left(\frac{\mathrm{d}^2\sigma}{\mathrm{d}\Omega\mathrm{d}E_f}\right)_{inc} &= \frac{k_f}{k_i}\frac{1}{2\pi\hbar}\sum_{\lambda_i} p(\lambda_i) \sum_{j=1}^{N} \left(\overline{b_j^2} - (\overline{b_j})^2\right) \int_{-\infty}^{\infty} \mathrm{d}t \langle\lambda_i|\mathrm{e}^{-\mathrm{i}\vec{Q}\cdot\vec{R}_j(0)}\mathrm{e}^{\mathrm{i}\vec{Q}\cdot\vec{R}_j(t)}|\lambda_i\rangle \mathrm{e}^{-\mathrm{i}\omega t},
\end{aligned} \tag{4.3}$$

with the definitions $\overline{b_j} = \sum_i p_j^i \cdot b_j^i$ and $\overline{b_j^2} = \sum_i p_j^i \cdot (b_j^i)^2$, p_j^i being the probability that the scattering length of the element at position $\vec{R}_j$ has the value b_j^i.

Finally, if the scattering system is monoatomic, it is common practice to define the coherent and incoherent scattering cross sections

$$\sigma_{coh} = 4\pi(\bar{b})^2 \qquad \text{and} \qquad \sigma_{inc} = 4\pi\left[\overline{b^2} - (\bar{b})^2\right] \tag{4.4}$$

and the coherent and incoherent *scattering functions*

$$\begin{aligned} S_{coh}(\vec{Q},\omega) &= \frac{1}{2\pi\hbar}\sum_{\lambda_i} p(\lambda_i)\sum_{j,j'=1}^{N}\int_{-\infty}^{\infty}\mathrm{d}t\langle\lambda_i|\mathrm{e}^{-\mathrm{i}\vec{Q}\cdot\vec{R}_{j'}(0)}\mathrm{e}^{\mathrm{i}\vec{Q}\cdot\vec{R}_j(t)}|\lambda_i\rangle\mathrm{e}^{-\mathrm{i}\omega t} \qquad \text{and} \\ S_{inc}(\vec{Q},\omega) &= \frac{1}{2\pi\hbar}\sum_{\lambda_i} p(\lambda_i)\sum_{j=1}^{N}\int_{-\infty}^{\infty}\mathrm{d}t\langle\lambda_i|\mathrm{e}^{-\mathrm{i}\vec{Q}\cdot\vec{R}_j(0)}\mathrm{e}^{\mathrm{i}\vec{Q}\cdot\vec{R}_j(t)}|\lambda_i\rangle\mathrm{e}^{-\mathrm{i}\omega t} \end{aligned} \tag{4.5}$$

so that the differential cross section takes the following simple form:

$$\frac{\mathrm{d}^2\sigma}{\mathrm{d}\Omega\mathrm{d}E_f} = \frac{k_f}{k_i}\left(\frac{\sigma_{coh}}{4\pi}S_{coh}(\vec{Q},\omega) + \frac{\sigma_{inc}}{4\pi}S_{inc}(\vec{Q},\omega)\right). \tag{4.6}$$

The expression in (4.6) is very convenient because σ_{coh} and σ_{inc} reflect the interaction between the neutron and the sample while $S_{coh}(\vec{Q},\omega)$ and $S_{inc}(\vec{Q},\omega)$ reflect the physics of the sample exclusively. From equation (4.5), it can be seen that $S_{coh}(\vec{Q},\omega)$ depends on the correlation between the positions of the same nucleus at different times and of different nuclei at different times, and that $S_{inc}(\vec{Q},\omega)$ depends on the correlation between the positions of the same nucleus at different times. $S_{coh}(\vec{Q},\omega)$ is the double space-time Fourier transform of the pair correlation function, which describes the probability of observing any nucleus at distance r and after a time t in relation to the position of a given nucleus at $t = 0$. $S_{inc}(\vec{Q},\omega)$ is the double space-time Fourier transform of the self correlation function, which gives the probability of finding exactly the same nucleus at distance r and after time t.

Experimentally obtained values for σ_{coh} and σ_{inc} (or alternatively b_{coh} and b_{inc}, with $\sigma_{coh} = 4\pi b_{coh}^2$ and $\sigma_{inc} = 4\pi b_{inc}^2$) for all common isotopes are given in literature [31]. Graphical comparison between σ_{coh} and σ_{inc} for some elements and isotopes is reported in Figure 4.1. For most isotopes $\sigma_{coh} >> \sigma_{inc}$. However, for hydrogen σ_{inc} is exceptionally large and much bigger than σ_{coh}. It is also much bigger than the coherent and incoherent scattering cross sections of all other elements and isotopes, including deuterium. Thus incoherent neutron scattering is a powerful tool to investigate the dynamics of hydrogenated molecules and by substituting the protons by deuterons it is possible to change the neutron scattering signal of a sample considerably. The total neutron scattering cross section is defined as $b_{coh} + b_{inc}$.

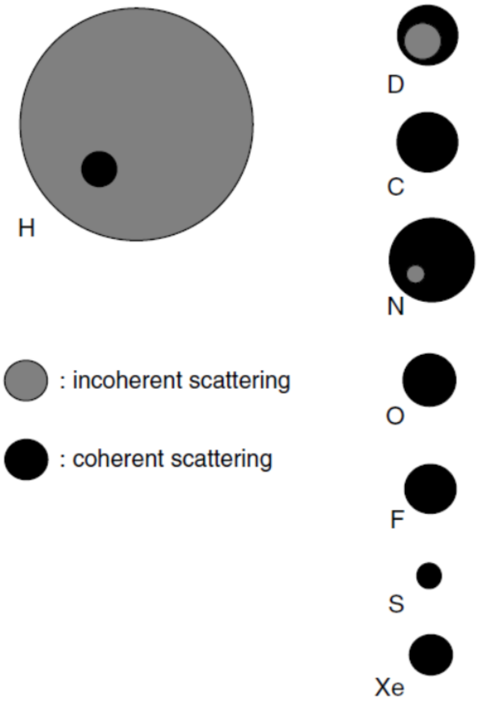

Figure 4.1: Neutron scattering cross sections for some elements and isotopes, reproduced from ref [32]. The larger the area of the circle, the larger the cross section.

4.1.2 Neutron spectrometers (the spectrometers IN5 and IN6 at the ILL)

In this subsection we shall give a brief description of *direct-geometry time-of-flight* neutron spectrometers [33] and of the spectrometers IN5 and IN6 of the ILL in particular [34]. In direct-geometry spectrometers neutrons are monochromized prior to the scattering event either by reflection from a monochromator crystal or by a multichopper system and, also before the scattering event, the neutron beam is pulsed by a chopper. The monochromatic pulsed neutron beam impinges on the sample and is scattered under all possible scattering angles. Finally, scattered neutrons are recorded on a bank of detectors surrounding the sample, generally on the surface of a cylinder. The final neutron wavelength is determined from the time-of-flight of the neutrons using simple kinematic equations for the neutron as a particle.

IN5 and IN6 are direct-geometry time-of-flight spectrometers for *cold* neutrons of the ILL. Cold neutrons are defined as having energies between 0.12 meV and 12 meV or, alternatively, wavelengths between 26.1 and 2.6 Å ($\lambda[\text{Å}] = 9.045/\sqrt{E[meV]}$). Both IN5 and IN6 are used to study dynamical processes with energies in the meV range as a function of wavevector transfer $\vec{Q}$. Experiments on powder samples are rather concerned with the modulus Q of the wavevector transfer. Because of energy and momentum conservation, only a restricted region in the $(Q, \hbar\omega)$ space can be accessed. The accessible region depends on the choice of the incident neutron energy and on the placement of the detectors; using more energetic neutrons and increasing the scattering angular range covered by the detectors will give access to a wider region. To illustrate this, two examples of such regions are plotted in Figure 4.2.

IN5 is located at the end of the cold neutron guide H16 and is a multichopper instrument. Its scheme is reported in Figure 4.3. Choppers are used to i) pulse the incident neutron beam, ii) remove harmonics, iii) suppress some of the produced pulses to prevent frame overlap, and iv) select the incident neutron wavelength within the range 1.8–20 Å. The multichopper system of IN5 provides an energy resolution function which remains nearly Gaussian down to 1/10000 of its height. The width of the elastic energy resolution is about 1% of the incident neutron energy. The detector bank is located 4.0 m from the sample and is 3.0 m high, with a total detection surface of 30 m^2. It is constituted by 362 ^{3}He detector tubes, which cover a range of scattering angles from -11.5 to 135° and are position sensitive in the vertical direction. The accessible Q range at zero energy transfer is 0.04–2.36 Å^{-1} for an incident neutron wavelength of 5.0 Å.

IN6 is a time-focusing spectrometer located on the cold guide H15. Its scheme is reported in Figure 4.4. Three composite pyrolytic graphite monochromators extract three neutron beams from the guide. The three beams are focused onto the sample. Each monochromator delivers a beam of slightly distinct energy and, thus, of distinct velocity. A beryllium filter is used to remove the second-order reflection from the monochromators.

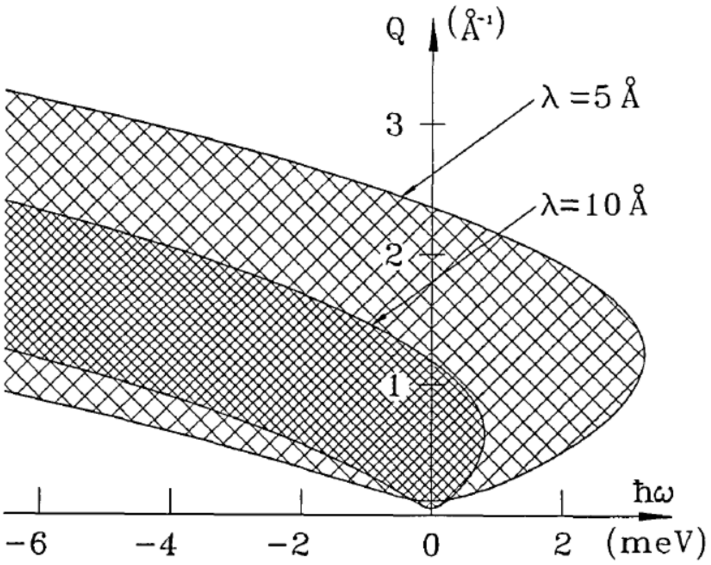

Figure 4.2: Plots of the accessible region in the $(Q, \hbar\omega)$ space for a spectrometer having detectors placed at scattering angles between 5° and 140° and using neutrons of wavelength 5 or 10 Å, reproduced from ref [35]. There is no (theoretical) limit to the energy transfer in neutron energy gain.

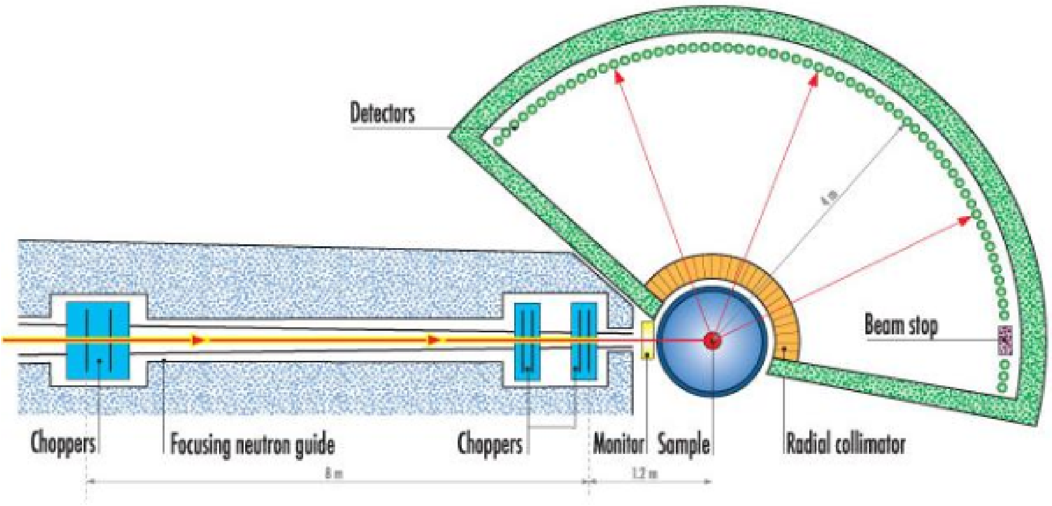
Detectors
4 m
Beam stop
Choppers
Focusing neutron guide
Choppers
Monitor
Sample
Radial collimator
8 m
1.2 m

Figure 4.3: Schematic representation of the IN5 spectrometer at the ILL. Source: https://www.ill.eu/users/instruments/instruments-list/in5/description/instrument-layout, accessed on 10.06.2018.

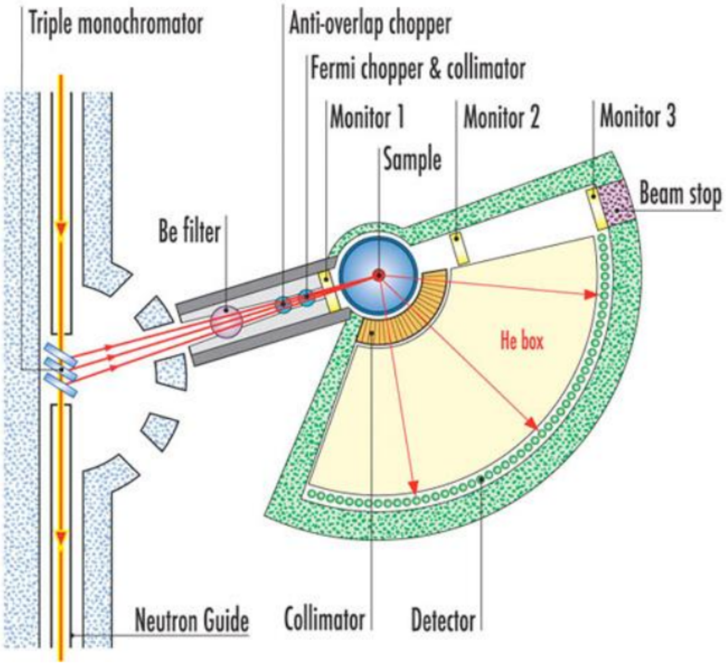
Triple monochromator
Anti-overlap chopper
Fermi chopper & collimator
Monitor 1
Monitor 2
Monitor 3
Sample
Beam stop
Be filter
He box
Neutron Guide
Collimator
Detector

Figure 4.4: Schematic representation of the IN6 spectrometer at the ILL. Source: https://www.ill.eu/users/instruments/instruments-list/in6-sharp/description/instrument-layout, accessed on 10.06.2018.

Then a Fermi chopper, which is a fast rotating slit collimator, pulses the beam and also compensates for the velocity difference in the three incident beams (by allowing the slower neutrons to pass earlier than the fast ones). This is the principle of the so-called time-focusing technique; its merit is to increase the intensity by a factor of three compared to the setup with only one monochromator. The incident neutron wavelength is in the range 4.1–5.9 Å. The elastic energy resolution has a width ranging between 0.05 to 0.17 meV depending on the chosen incident wavelength. It is mainly Gaussian but contains a small (∼5%) Lorentzian component. A suppressor chopper placed before the Fermi chopper and rotating in phase with the latter at a lower speed can be used to prevent frame overlap. 337 ^{3}He detector tubes are located 2.48 m from the sample within an angular range from 10 to 115° and cover a sensitive area of 4 m^2. They are arranged in three rows, with 107 tubes in the top row, 123 in the middle row and 107 in the bottom row. The accessible Q range at zero energy transfer is 0.3–2.05 Å^{-1} for an incident wavelength of 5.1 Å.

4.2 Raman spectroscopy

Raman scattering is an inelastic light scattering phenomenon which is typically employed to probe the vibrational modes of a material in the range of optical frequencies (1–100 THz). Usually, Raman spectra are plotted as a function of wavenumber in reciprocal centimeters (1 meV $\simeq$ 8.065 cm^{-1} $\simeq$ 0.2418 THz)

4.2.1 Theory of Raman scattering

When matter (gas, liquid, or solid) is illuminated with a monochromatic light beam, most of the radiation is scattered elastically and a small component is scattered inelastically. In the classical theory [36], the emission of a scattered radiation is explained by the periodic variations of the induced dipole moment as an effect of molecular vibrations. An electromagnetic wave illuminating a molecule induces an electric dipole moment $\vec{P}$ given by, at first order:

$$\vec{P} = \alpha \vec{E}, \tag{4.7}$$

where α is the polarizability and $\vec{E}$ is the electric field strength of the electromagnetic wave:

$$\vec{E} = \vec{E_0} \cos(2\pi\nu_0 t). \tag{4.8}$$

If the molecule is vibrating with frequency ν_m, the nuclear displacement due to the vibration can be expressed as:

$$q = q_0 \cos(2\pi\nu_m t), \tag{4.9}$$

where q_0 is the vibrational amplitude. For a small amplitude of variation, the polarizability can be written as a Taylor expansion, namely:

$$\alpha = \alpha_0 + \left(\frac{\partial\alpha}{\partial q}\right)_0 q, \tag{4.10}$$

where α_0 is the polarizability at equilibrium position. Combining (4.7), (4.8), (4.9) and (4.10), we obtain

$$\begin{aligned} \vec{P} =& \alpha_0 \vec{E} + \left(\frac{\partial\alpha}{\partial q}\right)_0 q_0 \cos(2\pi\nu_m t) \vec{E_0} \cos(2\pi\nu_0 t) \\ =& \alpha_0 \vec{E} + \frac{1}{2}\left(\frac{\partial\alpha}{\partial q}\right)_0 q_0 \vec{E_0} \cos\left[2\pi(\nu_0 - \nu_m)t\right] + \frac{1}{2}\left(\frac{\partial\alpha}{\partial q}\right)_0 q_0 \vec{E_0} \cos\left[2\pi(\nu_0 + \nu_m)t\right]. \end{aligned} \tag{4.11}$$

According to the classical theory, the first term in the right-hand side of equation (4.11) corresponds to the elastic part of the scattered radiation, while the second term corresponds to the Raman scattering of frequency $\nu_0 - \nu_m$ (Stokes scattering) and the third term corresponds to the Raman scattering of frequency $\nu_0 + \nu_m$ (anti-Stokes scattering). Equation (4.11) also indicates that the vibration is 'Raman active' if $\left(\frac{\partial \alpha}{\partial q}\right)_0$ is different from zero. In other words, the Raman effect can only exist if there is a change in polarizability for the considered vibration. Experimentally, Stokes and anti-Stokes Raman scattering are observed in the spectrum by the appearance of pairs of spectral lines, at symmetrical frequencies either side of the elastic line.

In the quantum-mechanical treatment of Raman scattering, an incident photon can induce the creation or the annihilation of a phonon during the scattering process. Momentum is conserved in the scattering process and therefore the modulus Q of the wavevector of phonons studied by (one-phonon) Raman scattering must be of the order of the moduli of the wavevectors of the incident and scattered photons. With an exciting light in the visible spectrum and a sample with refractive index of about 3, Q must be of the order of 10^6 cm^{-1}. This value is about 1/100 of the typical size of the first Brillouin zone, meaning that Raman spectroscopy probes zone-center phonons only.

4.2.2 Raman spectrometers

Raman spectrometers generally measure Raman Stokes scattering only and consist of four major components: i) an excitation source, which is generally a continuous-wave visible laser, ii) a sample illumination and collection system, iii) a wavelength selector and iv) a detector, which is generally a CCD detector. The sample illumination and collection system and the wavelength selector may differ considerably between different spectrometers.

For our high-pressure Raman spectroscopy measurements in diamond anvil cell, we used a commercial Horiba Jobin-Yvon LabRam HR800 spectrometer equipped with a Cobolt Samba 532 nm DPSS green laser as excitation source. The sample illumination and collection system is based on a 180° back-scattering geometry, in which the incident laser beam is focused on the sample through an objective lens and the scattered light is collected and sent to the wavelength selector by the same optical system. This means that the incident and scattered beams both pass through one diamond anvil. This geometry is schematically shown in Figure 4.5. Objective lenses with a long working distance are necessary, as the distance between the sample and the top of the cell is approximately 15 mm. Objectives with a 50 times magnification offering a working distance of 20.5 mm (and a depth of focus of 1.6 µm) are commercially available. We used a Mitutoyo SL50X objective (numerical aperture of 0.42). Measurements are complicated by the geometric and chromatic aberrations induced by the presence of a diamond of 2–3 mm in thickness in the optical path. One direct consequence is that the depth selectivity turns out to be comparable in size to the thickness of the sample (10–20 µm) in experiments reaching pressures of the order of 100 GPa.

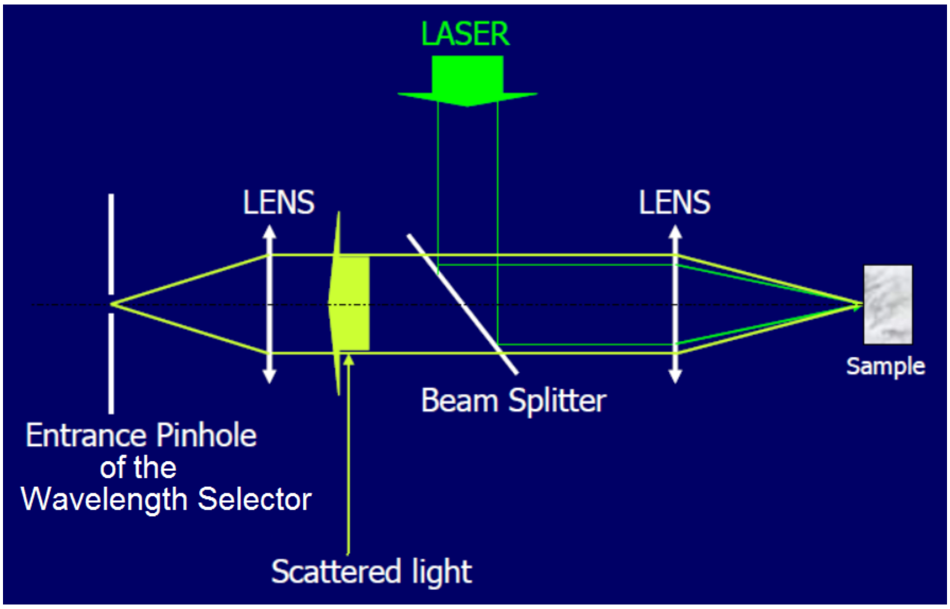

Figure 4.5: Schematic representation of the back-scattering setup of our Raman spectrometer.

In our spectrometer a reflection diffraction grating is used to separate the wavelengths present in the scattered light. The groove frequency of the grating partially determines the spectral resolution that can be achieved by the spectrometer and also determines the wavelength range that can be measured in a single acquisition. Two switchable gratings can be used, and are made of 1800 and 600 grooves per mm. The first grating provides a better spectral resolution (0.5 cm^{-1} half-width-half-maximum) and a shorter wavelength range; the second grating provides a worse resolution (1.5 cm^{-1} half-width-half-maximum) and a larger wavelength range. Finally, a liquid nitrogen-cooled CCD detector (1024×256 px) is used to measure the relative amounts of radiation at each wavelength.

Before each measurement, the wavenumber accuracy of the spectrometer was systematically calibrated using strong emission lines of Ne. The intensity scale was linearized using the transfer function derived from measuring a calibrated broadband source.

5 Guest dynamics in methane hydrates under high pressure

5.1 Motivations

The investigation, both experimental and computational, of molecular-level processes in gas clathrate hydrates is a very active research field in chemical physics. In particular, hydrates of methane attracted wide attention over the past decade in the light of their role in a broad range of technological issues (e.g. energy recovery, flow assurance, gas transportation and storage) and were the subject of a large number of publications, most of which focused on structural properties.

Despite its wide importance, very little is known about the guest dynamics in methane hydrates at present. Undoubtedly, diffusion of the guest molecules plays a paramount role during out-of-equilibrium phenomena such as formation or decomposition of a clathrate structure, structural coexistence and gas exchange; and the kinetics of some stages of these key phenomena is limited by gas diffusion rates. Detailed information on the guest diffusion during these processes is thus of interest for a broad research community. Furthermore, in the high-pressure non-clathrate structure of methane hydrate (MH-III), where water–methane distances are much shorter than in clathrate structures, the vibrational and orientational dynamics of the trapped guest molecules may reveal important insights into the repulsive region of the water–guest interaction potential.

This chapter will focus on the dynamics of methane molecules in methane hydrates and will be divided into two main topics: i) diffusive dynamics of methane molecules at grain boundaries during coexistence of two clathrate structures and ii) vibrational and orientational dynamics of methane molecules embedded in the high-pressure structure MH-III. As will be explained further below, methane hydrate is an excellent choice for both investigations as it shows i) persistent coexistence of stable structure I and metastable structure II at pressures of a fraction of GPa and ii) an extremely wide range of stability extending up to 150 GPa at least. The main results and their discussion are reported in the form of published articles; they are preceded by an introductory subsection giving the general context and followed by a subsection presenting open questions and indications of possible future studies. In the last subsection of the chapter we present results on methane hydrate under extremely high pressures by Raman spectroscopy up to 150 GPa and their preliminary discussion.

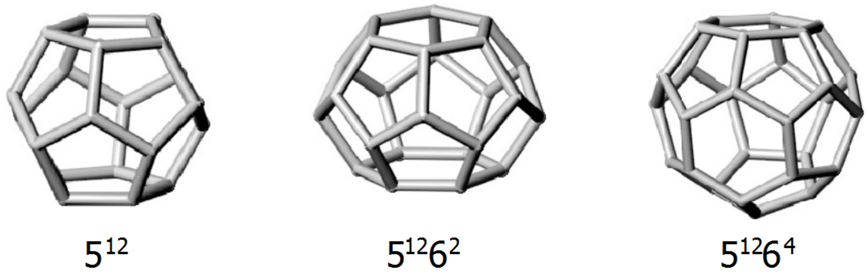

Figure 5.1: The three polyhedral cages found in the type I and type II clathrate structures, reproduced from ref [1].

5.2 Guest dynamics in methane clathrate hydrates

5.2.1 Introduction

Structural metastabilities and structural transitions are ubiquitous in clathrate hydrate science. Indeed, metastable structures are commonly observed to appear during nucleation of hydrates, often coexisting with the stable phase and sometimes surviving for timescales as long as days or weeks [37, 38, 39, 40, 41, 42, 43, 44]. Also, small changes in the thermodynamic conditions of formation may translate into a different structure formed, in a way that is often poorly understood and sometimes counter-intuitive [45, 46, 47].

The majority of the gas clathrate hydrates adopt either clathrate crystal structure I or clathrate crystal structure II. Those structures are build from the combination of small and large cages. Figure 5.1 represents the three types of cavities forming structure I and structure II (ordered by increasing cavity size), namely the pentagonal dodecahedron (noted 5^{12}), the tetrakaidecahedron formed by 12 pentagons and two hexagons ($5^{12}6^{2}$) and the hexakaidecahedron formed by 12 pentagons and four hexagons ($5^{12}6^{4}$). Their average cavity radius is 3.91–3.95, 4.33 and 4.73 Å. The pentagonal dodecahedron is slightly smaller in sII compared to sI.

Table 5.1 reports the main characteristics of the clathrate structures I and II. Both structures have a cubic crystal system and large unit cell dimensions ($\sim$12 Å for sI and $\sim$17.3 Å for sII). The unit cell of sI contains two small 5^{12} water cages and six large $5^{12}6^{2}$ cages. The unit cell of sII contains 16 small 5^{12} water cages and eight large $5^{12}6^{4}$ cages (Table 5.1). Of course cavity radii and unit cell dimensions will vary with temperature, pressure, and guest composition.

There is yet a third clathrate structure that is worth mentioning here. Structure H has the space group P6/mmm and consists of small 5^{12}, medium $4^{3}5^{6}6^{3}$ and very large $5^{12}6^{8}$ cages. The guest molecules occupying the large icosahedral ($5^{12}6^{8}$) cages have diameters between 7.5 and 8.6 Å, such as adamantane and methylcyclohexane [48]. Clathrate sH

Table 5.1: Structural details for clathrate crystal structures I and II (values after ref [1]).

	Clathrate structure I		Clathrate structure II	
Crystal system	Cubic		Cubic	
Space group	Pm$\bar{3}$n (No. 223)		Fd$\bar{3}$m (No. 227)	
Approx. lattice parameter (Å)	12		17.3	
No. of water molecules per unit cell	46		136	
Cavities	Small	Large	Small	Large
Geometry	5^{12}	$5^{12}6^{2}$	5^{12}	$5^{12}6^{4}$
No. of cavities per unit cell	2	6	16	8
Average cavity radius (Å)	3.95	4.33	3.91	4.73

is not stable with empty small and medium cages and therefore normally requires the enclosure of both small and large guest molecules.

As a general rule, guest molecules with a van der Waals diameter comprised between 4.3 and 6.0 Å (e.g. methane and carbon dioxide) prefer to form structure I while guest molecules with diameters above 6.0 Å (e.g. propane and isobutene) or below 4.3 Å (e.g. H_2, N_2, and O_2) prefer to form structure II. Very large guests stabilize sII by occupying the large $5^{12}6^{4}$ cages exclusively while very small molecules also stabilize sII because sII has a higher proportion of small cages than sI and because the large $5^{12}6^{4}$ cages can accommodate multiple small molecules [1].

In practice, despite those general rules many medium-sized guests can stabilize both structure I and structure II and the formed structure (or structures) depend on the conditions of formation, and results from a non-trivial interplay between thermodynamics and kinetic factors. For example, CO and N_2 clathrate hydrates have been observed to initially crystallize into sI and then gradually transform into sII over days or weeks [37, 38, 39]. CO_2 is a sI-former; however, transient formation of a type II-like structure was observed in the initial stages of its formation [40]. Hydrates of cyclopropane forms either clathrate structure I or II depending on temperature [45] and hydrate of trimethylene oxide forms either structure I or II depending on the water-to-gas molar ratio in the sample [47].

The scenario is even more complicated when considering binary hydrates. For example, simple CH_4 clathrate normally forms sI but adding only 1% of C_3H_8 induces transformation into sII, as reported in ref [1] (page 77). While simple CH_4 and simple C_2H_6 clathrate hydrates both form sI, the binary CH_4–C_2H_6 hydrate may form sII for certain gas compositions [46, 49].

In our experiments we focused on the metastability of sII in simple methane clathrate hydrate. Similarly to the case of carbon dioxide, cages characteristic of sII have been transiently detected in the initial stages of the formation of CH_4 hydrates, both in experiments [41, 42] and simulations [43, 44]. This suggests that sII is kinetically favored while the sI phase is thermodynamically stable and seems to be related to the observation that small cages are easier to form in the initial stages of clathrate formation, as evidenced in two NMR works [50, 51]. Somehow surprisingly, in methane hydrates at room temperature and pressures up to 0.6 GPa, sII has been reported to persistently coexist with sI [52, 53, 54].

Because of the relevance of structural metastabilities in clathrate hydrate science, it is of great interest to investigate the diffusion of methane molecules during coexistence between clathrate sI and sII. We addressed this investigation by means of quasielastic neutron scattering (QENS) experiments [33]. QENS is a well-suited technique for studying dynamics of hydrogenated molecules because of the very large incoherent neutron scattering cross section of the proton but requires relatively long acquisition times ranging from minutes to hours. Therefore our measurements were performed at 0.8 GPa in order to exploit the exceptional persistence of sII in methane hydrates under high pressure. No information on the guest diffusion at the interface of clathrate structures in general is available in literature.

The issue of guest *inter-cage* (cage-to-cage) diffusion through bulk methane clathrate sI hydrate has been first addressed in an indirect way in ref [20] using neutron diffraction data and later in ref [55] using molecular dynamics simulations; both works found very small translational diffusion coefficients of the order of 10^{-11}–10^{-12} cm^2 s^{-1} at 250 K. Recently, a molecular dynamics simulation study [56] focused on the methane diffusion at grain boundary-like structures of defective clathrates and reported diffusion coefficients in the nanosecond time scale, namely 3–4 orders of magnitude faster compared to the diffusion in the bulk. Those values remain much smaller (by four orders of magnitude) than the diffusion coefficient of free methane [57], though. Similarly, a simulation study [58] found a remarkable enhancement of the inter-cage diffusion coefficient of carbon dioxide in bulk clathrate sI by two and four orders of magnitude after introducing few water vacancy defects and a 3% change in cage occupancy, respectively. Here we show that the (extra-cage) diffusion coefficient of methane at the interface of clathrate sI and sII at 0.8 GPa is in the picosecond time scale, namely 7–8 orders of magnitude higher than those reported in literature for inter-cage diffusion through bulk clathrate sI and even a factor of 2–3 faster than that expected for bulk free methane at the same pressure.

QENS probes diffusive motion by looking at the quasielastic neutron scattering associated with dynamical processes occurring with a distribution of energies. By definition the QENS signal is always centered in zero energy transfer, as shown schematically in the spectrum of Figure 5.2. The momentum transfer dependence of the quasielastic signal provides information about the type of motion, which can be rotation, simple translation, jump translation, confined translation, etc... . Depending on the used instrument, QENS probes a typical range of timescales (for example 1–10 picoseconds on the instruments

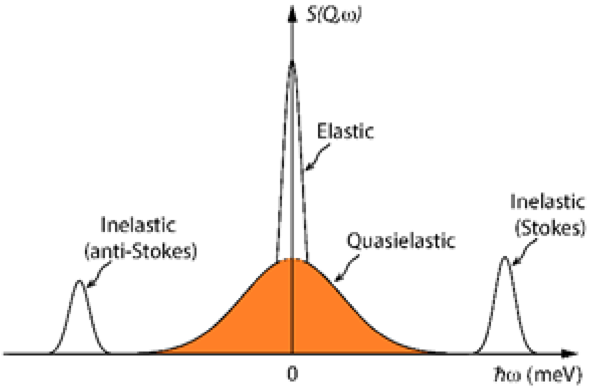

Figure 5.2: Schematic example of a neutron scattering spectrum including elastic line, quasielastic signal, inelastic Stokes and anti-Stokes peaks.

IN5 and IN6 at the ILL); the lower limit of which is set by the energy resolution, the upper limit by the accessible energy transfer range. Sample dynamics which is slower than the probed timescales will simply contribute to the elastic line and sample dynamics which is faster than the probed timescales will essentially give rise to a flat background.

Our experiments were performed at the neutron spectrometer IN6 at the ILL. A Paris-Edinburgh cell was employed to generate high pressure. Methane hydrate samples were prepared following the procedure described in chapter 2 and their quality was checked by x-ray diffraction. To highlight the signal from the CH_4 molecules, samples were prepared from deuterated water. All starting samples were in the form of clathrate structure I and were loaded at liquid nitrogen temperature into the loading clamp of the Paris-Edinburgh cell as explained in section 3.2. The samples were compressed at cold to pressures of 0.4–1.0 GPa and the loaded clamps were finally warmed up to room temperature out of the beam. Three different loadings were performed and different behaviors were observed depending on the reached pressure: after being warmed up to room temperature the sample compressed to (0.4±0.1) GPa was still in pure structure I, the sample compressed to (0.8±0.1) GPa was found to contain a mixture of sI and sII, and the sample compressed to (1.0±0.1) GPa was found to contain a mixture of sI and sH.

Spectra of the clathrate sI sample show no quasielastic signal, as expected (inter-cage methane diffusion is so slow that the corresponding quasielastic signal cannot be observed) and spectra of clathrate sI–sH sample show an extremely weak quasielastic signal. Spectra of the clathrate sI–sII sample show a clear quasielastic signal, whose analysis indicates that the observed methane diffusion process is a random-jump translational diffusion taking place at grain boundaries. From the intensity of the quasielastic signal we evaluated that the observed diffusion process involves about one third of the methane molecules in the sample. The rotational contribution of methane molecules is expected to be very fast

[59] and to give rise to a flat background in our spectra.

High-pressure QENS measurements of the sample showing coexistence of sI and sII were performed at different temperatures between 212 and 282 K at the constant pressure of 0.8 GPa. The measurements of this sample took about 21 hours and during this time no destabilization of the clathrate structures was observed in the IN6 diffraction pattern of the sample. No significant change in the intensity of the quasielastic signal was observed neither.

These results have been published in October 2017 in the journal *Nature Communications* in an article entitled "Fast methane diffusion at the interface of two clathrate structures" and authored by Umbertoluca Ranieri, Michael Marek Koza, Werner F. Kuhs, Stefan Klotz, Andrzej Falenty, Philippe Gillet, and Livia E. Bove. The article is attached in the following pages and followed by its Supporting Information file. The DOI is 10.1038/s41467-017-01167-2. Author contributions are given at the end of the article.

Finally, it should be mentioned that quasielastic neutron scattering experiments under pressures in the GPa range are not routine work. First experiments of this type have been performed on liquid water by our group short before the beginning of this thesis project and reported in 2013 in refs [60, 61] and during this thesis project as reported in 2016 in ref [62].

5.2.2 Article: "Fast methane diffusion at the interface of two clathrate structures"

nature COMMUNICATIONS

ARTICLE

DOI: 10.1038/s41467-017-01167-2 OPEN

Fast methane diffusion at the interface of two clathrate structures

Umbertoluca Ranieri[1,2], Michael Marek Koza[2], Werner F. Kuhs[3], Stefan Klotz[4], Andrzej Falenty[3],
Philippe Gillet[1] & Livia E. Bove[1,4]

Methane hydrates naturally form on Earth and in the interiors of some icy bodies of the Universe, and are also expected to play a paramount role in future energy and environmental technologies. Here we report experimental observation of an extremely fast methane diffusion at the interface of the two most common clathrate hydrate structures, namely clathrate structures I and II. Methane translational diffusion—measured by quasielastic neutron scattering at 0.8 GPa—is faster than that expected in pure supercritical methane at comparable pressure and temperature. This phenomenon could be an effect of strong confinement or of methane aggregation in the form of micro-nanobubbles at the interface of the two structures. Our results could have implications for understanding the replacement kinetics during sI–sII conversion in gas exchange experiments and for establishing the methane mobility in methane hydrates embedded in the cryosphere of large icy bodies in the Universe.

---

[1] EPSL, ICMP, École polytechnique fédérale de Lausanne (EPFL), Station 3, CH-1015 Lausanne, Switzerland. [2] Institut Laue-Langevin, 71 avenue des Martyrs, CS 20156, 38042 Grenoble cedex 9, France. [3] GZG Abt. Kristallographie, Universität Göttingen, Goldschmidtstrasse 1, 37077 Göttingen, Germany. [4] Institut de Minéralogie, de Physique des Matériaux et de Cosmochimie, Université Pierre et Marie Curie Paris 06, CNRS Unité Mixte de Recherche 7590, Sorbonne Universités, F-75252 Paris, France. Correspondence and requests for materials should be addressed to U.R. (email: ranieriu@ill.fr)
or to L.E.B. (email: livia.bove@impmc.upmc.fr)

Gas clathrate hydrates are a general class of compounds composed of water (hosts) molecules and gas (guests) atoms or molecules[1]. Among them, clathrate hydrates of methane are probably the most extensively studied. The natural occurrence of methane hydrate-containing sediments in permafrost areas and ocean shelves, the risk due to their formation in oil and gas pipelines, as well as their potential application as gas transportation media in soft conditions (i.e., close to atmospheric pressure and room temperature) explain the wide interest shown for these materials[1, 2]. Exchanging the guests in natural gas hydrate deposits with CO_2 has been suggested as a two-in-one approach of energy recovery and concomitant CO_2 mitigation[3]. As they are believed to be the dominant methane-bearing phase in the nebula from which the outer planets and satellites are formed, the properties of methane hydrates are also crucial to models of bodies in the outer solar system[4]. From a physical–chemical point of view, methane hydrates represent prototypical examples of hydrates of hydrophobic guests: the combination of low temperature, high pressure, a weak gas–water interaction between the guest molecules and the host lattice, and the relatively strong hydrogen bonds between host molecules allow for the formation of open crystalline water networks encaging CH_4 molecules. The topology of the water cages and the number of gas molecules trapped in these cages critically depend on the specific thermodynamic conditions of formation of the clathrate hydrate and on its formation kinetics[1, 5].

The most common structures formed by clathrate hydrates at relatively moderate pressures are the clathrate structures I and II (noted sI and sII). The unit cell of clathrate sI (space group $Pm\bar{3}n$) contains two small dodecahedral (5^{12}) water cages and six bigger tetrakaidecahedral ($5^{12}6^2$) cages. The unit cell of sII (space group $Fd\bar{3}m$) contains 16 5^{12} cages and eight large hexadecahedral ($5^{12}6^4$) cages[1] (Fig. 1). It is well accepted that methane hydrates preferentially crystallise into sI[1]. However, cages characteristic of sII have been transiently detected in the initial stages of the formation of methane hydrates in both experiments[6, 7] and simulations[8–12]. This is not surprising since (i) the difference in free energy between sI and sII is small[13] and (ii) appearance of metastable polymorphs or transient non-equilibrium states is commonly observed during nucleation of hydrates[5, 13–16]. It is noteworthy that sI and sII are topologically incompatible without the intercalation of pentakaidecahedral ($5^{12}6^3$) cages;[8] the interplay between kinetic factors and thermodynamic stability during sI–sII cross-nucleation has been discussed in details[17]. In methane hydrates at room temperature and pressures up to 0.6 GPa, sII has been reported to persistently coexist with sI[18–20]. Therefore, the resulting coexistence of structures in high-pressure samples can be seen as a frozen form on laboratory timescales of the metastable sI–sII polymorphs usually encountered during nucleation of methane hydrates.

Low-temperature translational and rotational excitations, as well as cage-to-cage hopping of CH_4 molecules trapped in clathrate sI were previously investigated at ambient and low pressures[21–24]. However, no information is available on the extra-cage diffusivity of the guest molecules in methane hydrates; this information could be highly relevant for the modelling of the subcrustal layers of methane clathrates embedded in the cryosphere of icy planets and large icy satellites[25, 26]. Recently, a study based on molecular dynamics simulations reported diffusion coefficient values in the nanosecond time scale for methane diffusion at grain boundary-like structures of defective clathrates[27].

In this work, we probe the microscopic diffusion of methane in a methane hydrate (CH_4–D_2O) sample exhibiting coexistence of clathrate sI and sII by quasielastic neutron scattering (QENS) measurements. Coexistence of structures is promoted by applying high pressure. QENS is a well-suited technique to study dynamics on the picosecond time and Å length scales[28]. Spectra of the sI–sII clathrate show a clear quasielastic signal whose analysis reveals a very fast extra-cage translational diffusion of methane molecules on the picosecond time scale. For comparison, we also measure methane hydrates in pure sI clathrate, in pure hexagonal clathrate structure H (space group P6/mmm)[26] and during transformation from sI to structure H (noted sH); the spectra of sI and sH do not exhibit any visible quasielastic signal, and the spectra of sI–sH show a very weak signal, orders of magnitude smaller than the signal from sI–sII.

Results

QENS experiments and elastic scattering. The experiments were performed at the time-of-flight spectrometer IN6 at the Institut Laue-Langevin in Grenoble (France) using a Paris-Edinburgh

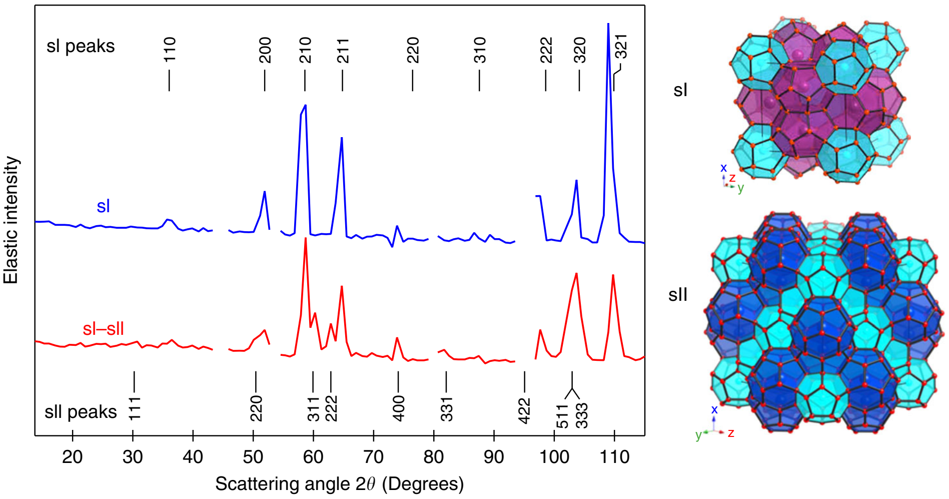

Fig. 1 Neutron diffraction patterns. Powder diffraction patterns of methane hydrate in pure sI clathrate at 0.4 GPa and 290 K and in the sI–sII clathrate at 0.8 GPa and 282 K. Breaks correspond to noisy detectors and to the strong Bragg peak of alumina from the anvils at 95°. The positions of the Bragg peaks for sI (cell parameter 11.7 Å) and for sII (cell parameter 17.0 Å) are reported. On the right, we present views of the unit cells of sI and sII (5^{12} cages in cyan, $5^{12}6^2$ cages in purple, $5^{12}6^4$ cages in blue)

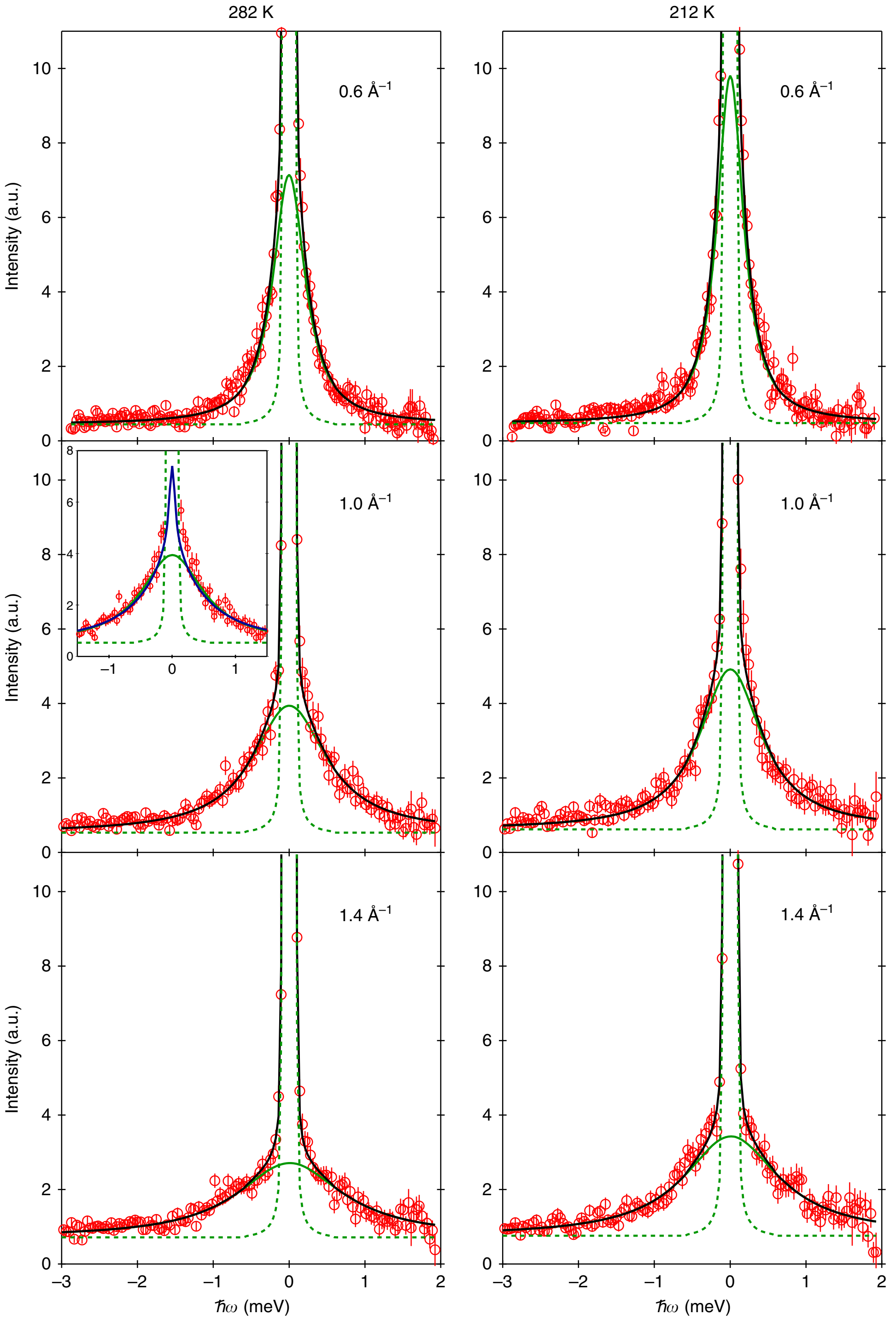

Fig. 2 Examples of measured QENS spectra. QENS spectra of methane hydrate in the sI–sII clathrate at 0.8 GPa and selected temperature T and momentum transfer Q values. Experimental data (empty circles) are compared to their best fits (black lines). Error bars were calculated by the square root of absolute neutron count combined with the law of propagation of errors. Quasielastic Lorentzian (solid green lines) and elastic (dashed green lines) components are also shown (upshifted by the value of the flat background for clarity). In the inset, a Lorentzian fit is compared to the 2D diffusion fit (blue line) of the same spectrum

press and recently developed ceramics anvils[29]. The wavelength of the incoming neutrons was 5.12 Å, resulting in an instrumental resolution of 0.08 meV. This corresponds to an observation time of ~8 ps. The sample exhibiting coexistence of clathrate sI and sII was prepared according to the following procedure: we compressed methane hydrate (originally in sI) to 0.8 GPa at liquid nitrogen temperature and then warmed it up to 282 K. The neutron powder diffraction pattern of the sample at 0.8 GPa and 282 K is presented in red in Fig. 1. It indicates that the sample contained about half as much sII than sI, on the basis of peak heights. The pattern was obtained directly on IN6 by comparing the intensities of the elastic peaks, at each scattering angle, with those measured on a vanadium standard which gives isotropic elastic scattering. All the Bragg peaks of the sample can be indexed within the space groups of sI and sII. Figure 1 also depicts the diffraction pattern of pure sI clathrate. The diffraction patterns of pure sH clathrate and of the sample transforming from sI to sH are presented in Supplementary Fig. 1. We recorded QENS spectra of the sI–sII clathrate at the constant temperature T of 282 K and pressure of 0.8 GPa during 6 h. The amount of sII was constant during this time. Then we continuously decreased the temperature to 200 K over 15 h to characterize the T dependence of the probed diffusion at 0.8 GPa. Spectra measured between 282 and 200 K were merged into three groups of 5 h of acquisition time each, corresponding to the following average temperature values: 267, 238 and 212 K. Upon cooling down, the relative amount of sI and sII remained approximately constant. The diffraction patterns recorded at 267, 238 and 212 K are reported in Supplementary Fig. 2. More details about the experiments are given in the Methods section.

Fitting of the QENS spectra. Figure 2 depicts typical QENS spectra of the methane hydrate sample exhibiting coexistence of clathrate sI and sII at 0.8 GPa. Examples of spectra of methane hydrate in pure sI clathrate, in pure sH clathrate and in the sI–sH clathrate are shown in Supplementary Fig. 3. Spectra in Fig. 2 show a clear quasielastic signal, i.e., a broadening of the elastic line produced by interactions of the neutrons with diffusing atoms of the sample. Since the incoherent cross-section of hydrogen is almost two orders of magnitude larger than that of other atoms, the measured signal is essentially due to the dynamics of protons in the guest molecules[30, 31]. We first applied the most common model used to fit quasielastic data, i.e., a Lorentzian function (whose half-width-half-maximum is noted Γ). A delta function was used to fit the elastic line of the spectra, which is due to the contribution of the water network and of the slowly-diffusing or non-diffusing methane molecules trapped in the clathrate structures. Total best fits to the experimental data are presented in Fig. 2 and can be seen to accurately describe the spectra. Based on the integrated areas of the quasielastic and elastic lines (after subtraction of the empty cell measurement), we roughly estimate that about one third of the methane molecules in the sample contribute to the fitted quasielastic signal, at each investigated T. More details on this estimation are given in Supplementary Note 1. Since cage occupancies in the newly formed sII clathrate might be lower compared to the starting sI clathrate hydrate, part of the methane molecules in the starting sI clathrate could indeed have been released from the starting sI hydrate into the grain boundary network during transformation from sI to sII and would be available to perform extra-cage translational diffusion. However, a minimum level of occupancies is required to ensure stability of sII and one can estimate that no more than 10% of the methane in the sample could have been released without destabilization of the water matrix. The existence of a fraction of fast diffusing methane molecules as high as one third strongly suggests that an appreciable fraction of water molecules in the sample are in a disordered state. Such disordered regions would form at the front line of the transformation between clathrate sI and sII, and their sizes are most likely far below the typical size of the crystallites (that is a few micrometres[32]). This point is further discussed in Supplementary Note 2. Moreover, the absence of a prominent quasielastic signal in the spectra of the sI–sH methane clathrate hydrate highlights the very particular nature of the interfaces between coexisting sI and sII, compared to the temperature-induced or pressure-induced structural transition taking place at high driving forces between two stable forms of methane hydrates such as sI and sH. The micro-structural properties of sI and sII coexisting assemblies certainly deserve to be further investigated.

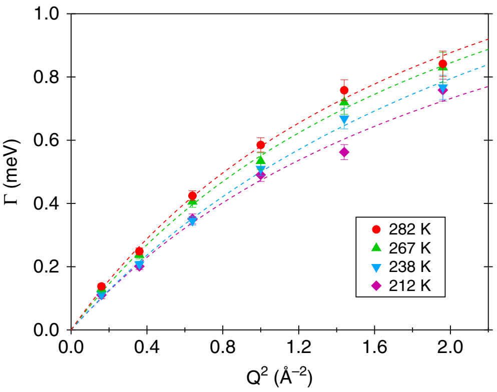

Fig. 3 Momentum transfer Q dependence of the QENS signal. Half-width-half-maximum Γ of the Lorentzian quasielastic component of the fits (Fig. 2) as a function of Q^2 at 0.8 GPa and the investigated temperatures. Error bars correspond to one standard deviation. The best fits to the data according to Eq. (1) are shown as dashed lines

Momentum transfer Q dependence of the QENS signal. Figure 3 depicts the parameter Γ as a function of Q^2. The Q dependence of Γ provides information about the characteristic time and nature of the probed motion. The monotonic increase of Γ rules out that the measured quasielastic signal is due to a localised (rotational) dynamics of methane, which would be indicated by a Q-independent Γ. Instead, it clearly highlights that a translational diffusion process is at the origin of the signal[28]. It must be also noted that the rotational quasielastic contribution of methane molecules trapped in clathrate sI is very large (half width above 5 meV) at 150 K[22] and thus only contributes to the background of the spectra here. Similar rotational behaviour can be reasonably expected for CH_4 molecules in a clathrate sII, as no indication of inequivalent environments for the guest molecule emerged from the low-temperature rotational spectra of sI methane clathrate[23] (although methane occupies the two types of cages of sI). As can be seen in Fig. 3, Γ extrapolates to 0 for $Q \to 0$. Hence, the measured quasielastic signal is not associated with an intra-cage diffusive motion of CH_4 molecules, since for a particle restricted to move in a confined geometry Γ shows[30, 31] a plateau at small Q. For example, for a particle moving within a sphere of radius R, Γ shows[33] a plateau for $Q < \pi/R$. The Q dependence of Γ is best approximated within the random jump diffusion model of Singwi and Sjolander by:

$$\Gamma(Q) = \frac{\hbar D Q^2}{1 + D Q^2 \tau}, \qquad (1)$$

with D representing the isotropic translational diffusion coefficient and τ the mean residence time between jumps[28]. The corresponding formula for a continuous free translational diffusion process would be $\Gamma(Q) = \hbar D Q^2$. Fits of $\Gamma(Q^2)$ according to Eq. (1) are presented in Fig. 3; the values obtained for D and τ are reported in green in Fig. 4. The translational diffusion coefficient turns out to be of the order of $10^{-4}\,\mathrm{cm^2\,s^{-1}}$ and its temperature dependence is rather weak (25% over the investigated T range). An Arrhenius fit of D provides an activation energy of $0.48 \pm 0.11\,\mathrm{kcal\,mol^{-1}}$. This value is small compared to the activation energies reported in literature for the cage-to-cage hopping of CH_4 in sI clathrates (for example, $12.4\,\mathrm{kcal\,mol^{-1}}$ in ref. [21]) and points at van der Waals interactions as main rate-limiting interactions for the observed methane diffusion. The parameter τ is a fraction of picosecond and does not show any temperature dependence within the error bars over the investigated T range.

2D diffusion model. The choice of a Lorentzian fit function for the quasielastic signal implicitly assumes that the probed motion is three-dimensional (3D)[28]. An other possibility is that the

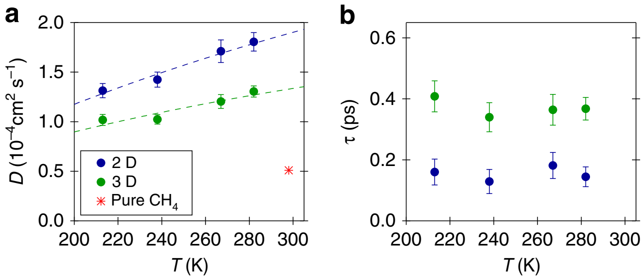

Fig. 4 Translational diffusion coefficient D and mean residence time τ. Temperature dependencies of D (**a**) and τ (**b**) for methane hydrate in the sI–sII clathrate at 0.8 GPa, as obtained in the 3D and 2D diffusion models employed in this work. Error bars correspond to one standard deviation. Arrhenius fits of D are shown as dashed lines. Estimated value for D in pure methane from literature[40, 41] is also reported. Legend of **a** also applies to **b**

methane diffuses essentially bi-dimensionally on the length scale probed by the instrument, if the grain boundary network or the intercalated disordered regions between crystals of sI and sII are sufficiently thin. In such a case the fit function for the quasielastic signal is no longer Lorentzian and has a logarithmic singularity at $\omega = 0$[34] (see Supplementary Note 3 for its expression). Nevertheless, the singularity is suppressed by the convolution with the instrumental resolution and the convoluted fit function differs from the convoluted Lorentzian only near $\omega = 0$ where it is more peaked[35]. The inset of Fig. 2 depicts an example of fit using this 2D diffusion fit function and compares it to the Lorentzian fit of the same QENS spectrum. The two fits are actually indistinguishable outside the instrumental resolution-dominated region close to $\omega = 0$ and this is true for all other measured spectra. Therefore it is not possible to unequivocally establish if bulk or planar diffusion is taking place. The values for the translational diffusion coefficient and the mean residence time obtained in the 2D diffusion model are reported in blue in Fig. 4. The activation energy (0.57 ± 0.12 kcal mol^{-1}) is comparable to that obtained in the 3D diffusion model. More details about the data analysis are given in the Methods section.

Discussion

The methane diffusion probed in the present study is much faster than that reported in the literature for the cage-to-cage hopping of CH$_4$ molecules through clathrate sI. Cage-to-cage hopping is a rare event that requires distortion of the host network[36] and the associated diffusion coefficient is of the order of 10^{-11} to 10^{-12} cm^2 s^{-1} at 250 K, as revealed by experimental[21] and computational[24] studies. Similar conclusions have been reported for the cage-to-cage hopping of other guest molecules[37, 38], including molecules forming clathrate sII[37]. It is also interesting to compare the present results to the translational diffusion coefficients of CH$_4$ in bulk water–methane mixtures and bulk pure methane. At 0.02 GPa and 273 K, the diffusion coefficient of methane in water was found to be 0.16×10^{-4} cm^2 s^{-1}, i.e., an order of magnitude smaller than those measured here[39]. This value was obtained for the moderate methane-saturated concentration that is possible at low pressures[39]. In pure methane the experimental diffusion coefficient is 2.08×10^{-4} cm^2 s^{-1} at 0.164 GPa and 298 K[40]. Its temperature dependence is rather strong, with an activation energy of ~1.0 kcal mol^{-1} between 223 and 323 K at 0.15 GPa. The diffusion coefficient at 0.8 GPa can be estimated based on the assumption that its product with the shear viscosity is constant along isotherms (Stokes–Einstein relation). The pressure dependence of the viscosity in methane at 298 K is known[41] and one gets a value of 0.5×10^{-4} cm^2 s^{-1} at 0.8 GPa and 298 K. This value is reported in Fig. 4 and is a factor of 2–3 smaller than our results extrapolated at the same T. Based on the same assumption, it is possible to estimate that pure methane at about 0.2–0.3 GPa should show a diffusion coefficient comparable to that measured here.

To summarise, we observed a remarkably fast mobility of methane molecules at the interface of two clathrate structures (I and II) and measured the associated translational diffusion coefficient D at 0.8 GPa and temperatures between 212 and 282 K. The obtained coefficients are 7–8 orders of magnitude higher than those reported in literature for cage-to-cage hopping of methane through clathrate sI at low pressure, one order of magnitude higher than that of methane dissolved in water at low pressure and a factor of 2–3 higher than that expected for pure bulk supercritical methane at comparable pressure and temperature. The activation energy (of about 0.5 kcal mol^{-1}) is a factor of two smaller than that of pure methane at 0.15 GPa and more than one order of magnitude smaller than that of the hydrogen bond in the water network and of the cage-to-cage hopping process as reported in literature[21]. This fast mobility involves a sizable fraction of the methane in the sample (approximately one third, as rough estimation), does not induce destabilization of the clathrate structures and is probably observable for times much longer than the duration of our experiment (~21 h).

We infer that the rapidity of the methane diffusion probed here could be an effect of confinement in the extensive grain boundary network[32] or intercalated disordered regions between crystals of clathrate sI and sII. Similar behaviour was already reported in literature. For example, the diffusivity of CH$_4$ is only 4×10^{-11} cm^2 s^{-1} in zeolite 4A[42], ~10^{-4} cm^2 s^{-1} in silicalite[43] and is predicted to be of the same order of magnitude as that of the gas phase (10^{-1} cm^2 s^{-1}) in infinitely long single-walled carbon nanotubes[44]. Alternatively, the observed fast diffusion could also well be explained by the spontaneous formation of micro-scale to nano-scale gas bubbles from a supersaturated water–methane mixture. Micro-nanobubbles formation was suggested to occur after decomposition of hydrates in different works[45–47]. The diffusion properties of methane inside these bubbles can be considerably different from the bulk fluid and a first study of CH$_4$-mobility in nanobubbles suggested indeed an enhanced diffusion[48]. Further investigation including large-scale molecular dynamics simulations of the guest diffusivity at the structures interface are needed to shed light on these points.

In the context of energy recovery from natural gas hydrate deposits with CO$_2$ injections, gas replacement rates are key parameters to assess its technological viability. Earlier experimental evidences underlined greatly enhanced replacement rates during sI–sII conversion[49, 50] in comparison to the case of isostructural sI–sI replacement[51]. If extended to moderate pressures, our results might provide an explanation for that. Likewise, our results should be taken into account in the modelling of methane clathrates layers existing at depth in the interiors of large icy bodies in both solar and extra-solar systems[25, 26], for which the steady-states depend on the diffusion timescales as compared to the formation and dissociation rates. As an example, the observed fast mobility of methane could be relevant to understand the phenomenon of methane release into the atmosphere of Titan, which is likely to originate from methane clathrates embedded in its crust and mantle[25, 26].

Methods

Sample production. The procedure followed to prepare the CH$_4$–D$_2$O methane hydrate sample was described in refs. [21, 52]. It basically consists in keeping D$_2$O ice under an atmosphere of 6 MPa of CH$_4$ gas at a temperature close to the melting during 4 weeks. The starting deuterated ice was a powder of ice Ih of spherical shape (typical diameter of several tens of micrometres[21]) previously produced by a shock-freezing method through spraying liquid D$_2$O (99.9% deuterated) into liquid nitrogen. The spraying was done in a glove box under dry nitrogen atmosphere to avoid contamination with atmospheric water. The quality of the prepared methane hydrate sample was checked by X-ray diffraction. We found that the sample was in clathrate sI with a negligible amount of water ice impurity (below 2%). The size of the crystallites is typically a few micrometres[32]. Typical methane occupation is 86% for the small cages and 99% for the large cages[52].

Experimental details. The QENS experiments were carried out using the VX5 Paris-Edinburgh press. The procedure of loading the methane hydrate sample in the clamp module[53] of the press was done under liquid nitrogen. The sample was first compacted to a spherical pellet (of ~40 mm^3) using a dedicated press operating under liquid nitrogen. The pellet was subsequently loaded into a precooled type-25 copper-beryllium encapsulating gasket and the sample-gasket assembly was placed in an aluminium ring between precooled ceramics anvils. We used recently developed zirconia-toughened alumina ceramics anvils which are highly transparent to neutrons. Their performances are described in ref. [29].

To prepare the sample exhibiting coexistence of clathrate sI and sII, the gasket was sealed by applying a load of 100 kN on the anvils under liquid nitrogen. This corresponds to a pressure of about (0.8 ± 0.1) GPa in the sample, on the basis of our calibration of the used anvils. The assembled clamp was then warmed up from liquid nitrogen temperature to room temperature out of the beam before insertion (~12 h later) in the Paris-Edinburgh press. During the experiment, temperature was decreased by cooling down the whole Paris-Edinburgh press in a liquid nitrogen cryostat. It is known that the cooling of samples in such a pressure cell is approximately isochoric and this leads to a small pressure drop (typically below 5% for a change in temperature between 282 and 200 K). The measured Bragg peaks did not shift with temperature within the angular resolution of the instrument.

During a different sample loading, the gasket was sealed by applying a smaller load (50 kN), corresponding to a sample pressure of 0.4 GPa. After being warmed up to 290 K, this sample was still in pure structure I (see Fig. 1 for the diffraction pattern). We compressed this sample isothermally at 290 K and observed transformation to clathrate sH, in agreement with previous studies[20, 26].

During another sample loading, the gasket was sealed by applying a higher load (120 kN), corresponding to a sample pressure of 1.0 GPa. After being warmed up to 295 K, this sample was found to contain a mixture of structure I and structure H. The relative amount of structure H was found to slowly increase over time and the transformation was completed within ~12 h.

The instrumental energy resolution was estimated by measuring a sphere of vanadium of the same size as the sample, which was loaded into the gasket and the Paris-Edinburgh press in the same set-up as the sample at ambient pressure and ambient temperature.

Data analysis details. The scattering angles 2θ covered by the detectors of IN6 are in the range 10°–115°. Spectra measured by several detectors were grouped together into constant-Q spectra with 0.2 Å^{-1} steps, from 0.4 to 1.8 Å^{-1}. For the data analysis, we did not consider the two highest Q values (1.6 and 1.8 Å^{-1}) for which competition of the quasielastic signal with the flat background gives rise to large uncertainties for the free-fitting parameters. Six free-fitting parameters were used in the data fitting with the 3D diffusion model: intensities and half-width-half-maximum of the Lorentzian and delta functions, flat background and zero-shift of the energy-transfer axis. Six free-fitting parameters were used as well in the data fitting with the 2D diffusion model, $D_{2D}(Q)$ substituting the half-width-half-maximum of the Lorentzian. Stokes/anti-Stokes detailed balance and convolution with the instrumental energy resolution function were taken into account. Multiple scattering contribution to the spectra was neglected as the estimated sample transmission is about 89% of the incident beam.

Data availability. Raw data were generated at the Institut Laue-Langevin large-scale facility. Derived data supporting the findings of this study are available from the corresponding authors upon request.

Received: 10 May 2017 Accepted: 23 August 2017
Published online: 20 October 2017

References

1. Sloan, E. D. & Koh, C. A. *Clathrate Hydrates of Natural Gases* 3rd edn (CRC Press: Boca Raton, Florida, 2008).
2. Koh, C. A., Sum, A. K. & Sloan, E. D. Gas hydrates: Unlocking the energy from icy cages. *J. Appl. Phys.* **106**, 061101 (2009).
3. Brewer, P. G., Friederich, G., Peltzer, E. T. & Orr, F. M. Jr. Direct experiments on the ocean disposal of fossil fuel CO_2. *Science* **284**, 943–945 (1999).
4. Luspay-Kuti, A. et al. The presence of clathrates in comet 67P/Churyumov-Gerasimenko. *Sci. Adv.* **2**, e1501781 (2016).
5. Staykova, D. K., Kuhs, W. F., Salamatin, A. N. & Hansen, T. Formation of porous gas hydrates from ice powders: Diffraction experiments and multistage model. *J. Phys. Chem. B* **107**, 10299–10311 (2003).
6. Schicks, J. M. & Ripmeester, J. A. The coexistence of two different methane hydrate phases under moderate pressure and temperature conditions: Kinetic versus thermodynamic products. *Angew. Chem. Int. Ed.* **43**, 3310–3313 (2004).
7. Schicks, J. M. & Luzi-Helbing, M. Kinetic and thermodynamic aspects of clathrate hydrate nucleation and growth. *J. Chem. Eng. Data* **60**, 269–277 (2015).
8. Vatamanu, J. & Kusalik, P. G. Unusual crystalline and polycrystalline structures in methane hydrates. *J. Am. Chem. Soc.* **128**, 15588–15589 (2006).
9. Walsh, M. R., Koh, C. A., Sloan, E. D., Sum, A. K. & Wu, D. T. Microsecond simulations of spontaneous methane hydrate nucleation and growth. *Science* **326**, 1095–1098 (2009).
10. Jiménez-Ángeles, F. & Firoozabadi, A. Nucleation of methane hydrates at moderate subcooling by molecular dynamics simulations. *J. Phys. Chem. C* **118**, 11310–11318 (2014).
11. Małolepsza, E. & Keyes, T. Pathways through equilibrated states with coexisting phases for gas hydrate formation. *J. Phys. Chem. B* **119**, 15857–15865 (2015).
12. Lauricella, M. et al. Clathrate structure-type recognition: Application to hydrate nucleation and crystallisation. *J. Chem. Phys.* **142**, 244503 (2015).
13. Jacobson, L. C. & Molinero, V. Can amorphous nuclei grow crystalline clathrates? The size and crystallinity of critical clathrate nuclei. *J. Am. Chem. Soc.* **133**, 6458–6463 (2011).
14. Moudrakovski, I. L., Sanchez, A. A., Ratcliffe, C. I. & Ripmeester, J. A. Nucleation and growth of hydrates on ice surfaces: New insights from ^{129}Xe NMR experiments with hyperpolarized xenon. *J. Phys. Chem. B* **105**, 12338–12347 (2001).
15. Míguez, J. M. et al. Molecular dynamics simulation of CO_2 hydrates: Prediction of three phase coexistence line. *J. Chem. Phys.* **142**, 124505 (2015).
16. Sarupria, S. & Debenedetti, P. G. Homogeneous nucleation of methane hydrate in microsecond molecular dynamics simulations. *J. Phys. Chem. Lett.* **3**, 2942–2947 (2012).
17. Nguyen, A. H. & Molinero, V. Cross-nucleation between clathrate hydrate polymorphs: Assessing the role of stability, growth rate, and structure matching. *J. Chem. Phys.* **140**, 084506 (2014).
18. Choukroun, M., Morizet, Y. & Grasset, O. Raman study of methane clathrate hydrates under pressure: New evidence for the metastability of structure II. *J. Raman Spectrosc.* **38**, 440–451 (2007).
19. Chou, I.-M. et al. Transformations in methane hydrates. *Proc. Natl Acad. Sci. USA* **97**, 13484–13487 (2000).
20. Shu, J. et al. Structural stability of methane hydrate at high pressures. *Geosci. Front.* **2**, 93–100 (2011).
21. Kuhs, W. F., Staykova, D. K. & Salamatin, A. N. Formation of methane hydrate from polydisperse ice powders. *J. Phys. Chem. B* **110**, 13283–13295 (2006).
22. Baumert, J. et al. Lattice dynamics of methane and xenon hydrate: Observation of symmetry-avoided crossing by experiment and theory. *Phys. Rev. B* **68**, 174301 (2003).
23. Tse, J. S., Ratcliffe, C. I., Powell, B. M., Sears, V. F. & Handa, Y. P. Rotational and translational motions of trapped methane. Incoherent inelastic neutron scattering of methane hydrate. *J. Phys. Chem. A* **101**, 4491–4495 (1997).
24. Peters, B., Zimmermann, N. E. R., Beckham, G. T., Tester, J. W. & Trout, B. L. Path sampling calculation of methane diffusivity in natural gas hydrates from a water-vacancy assisted mechanism. *J. Am. Chem. Soc.* **130**, 17342–17350 (2008).
25. Choukroun, M., Grasset, O., Tobie, G. & Sotin, C. Stability of methane clathrate hydrates under pressure: Influence on outgassing processes of methane on Titan. *Icarus* **205**, 581–593 (2010).
26. Loveday, J. S. et al. Stable methane hydrate above 2 GPa and the source of Titan's atmospheric methane. *Nature* **410**, 661–663 (2001).
27. Lo, H., Lee, M.-T. & Lin, S.-T. Water vacancy driven diffusion in clathrate hydrates: Molecular dynamics simulation study. *J. Phys. Chem. C* **121**, 8280–8289 (2017).
28. Bée, M. *Quasielastic Neutron Scattering* (Adam Hilger: Bristol, 1988).
29. Komatsu, K. et al. Performance of ceramic anvils for high pressure neutron scattering. *High Press Res.* **34**, 494–499 (2014).
30. Desmedt, A., Soetens, J. C., Prager, M., Russina, M. & Ollivier, J. Dynamics of methyl iodide clathrate hydrate, investigated by MD simulations and QENS experiments. *J. Phys. Chem. C* **115**, 12689–12701 (2011).
31. Pefoute, E., Kemner, E., Soetens, J. C., Russina, M. & Desmedt, A. Diffusive motions of molecular hydrogen confined in THF clathrate hydrate. *J. Phys. Chem. C* **116**, 16823–16829 (2012).
32. Chaouachi, M., Neher, S. H., Falenty, A. & Kuhs, W. F. Time resolved coarsening of clathrate crystals: The case of gas hydrates. *Cryst. Growth Des.* **17**, 2458–2472 (2017).
33. Volino, F. & Dianoux, A. J. Neutron incoherent scattering law for diffusion in a potential of spherical symmetry: General formalism and application to diffusion inside a sphere. *Mol. Phys.* **41**, 271–279 (1980).
34. Dianoux, A. J., Volino, F. & Hervet, H. Incoherent scattering law for neutron quasi-elastic scattering in liquid crystals. *Mol. Phys.* **30**, 1181–1194 (1975).

35. Lechner, R. E. Effects of low-dimensionality in solid-state protonic conductors. *Solid State Ion.* **77**, 280–286 (1995).
36. Vidal-Vidal, Á., Pérez-Rodríguez, M. & Piñeiro, M. M. Direct transition mechanism for molecular diffusion in gas hydrates. *RSC Adv.* **6**, 1966–1972 (2016).
37. Burnham, C. J. & English, N. J. Free-energy calculations of the intercage hopping barriers of hydrogen molecules in clathrate hydrates. *J. Phys. Chem. C* **120**, 16561–16567 (2016).
38. Liang, S., Liang, D., Wu, N., Yi, L. & Hu, G. Molecular mechanisms of gas diffusion in CO_2 hydrates. *J. Phys. Chem. C* **120**, 16298–16304 (2016).
39. Guo, H., Chen, Y., Lu, W., Li, L. & Wang, M. In situ Raman spectroscopic study of diffusion coefficients of methane in liquid water under high pressure and wide temperatures. *Fluid Phase Equilib.* **360**, 274–278 (2013).
40. Harris, K. R. & Trappeniers, N. J. The density dependence of the self-diffusion coefficient of liquid methane. *Physica* **104A**, 262–280 (1980).
41. Van der Gulik, P. S., Mostert, R. & Van den Berg, H. R. The viscosity of methane at 25 °C up to 10 kbar. *Physica. A* **151**, 153–166 (1988).
42. Kärger, J. & Ruthven, D. M. *Diffusion in Zeolites and other Microporous Solids* (John Wiley and Sons: New York, 1992).
43. Skoulidas, A. I. & Sholl, D. S. Transport diffusivities of CH_4, CF_4, He, Ne, Ar, Xe, and SF_6 in silicalite from atomistic simulations. *J. Phys. Chem. B* **106**, 5058–5067 (2002).
44. Skoulidas, A. I., Ackerman, D. M., Johnson, J. K. & Sholl, D. S. Rapid transport of gases in carbon nanotubes. *Phys. Rev. Lett.* **89**, 185901 (2002).
45. Bagherzadeh, S. A., Alavi, S., Ripmeester, J. & Englezos, P. Formation of methane nano-bubbles during hydrate decomposition and their effect on hydrate growth. *J. Chem. Phys.* **142**, 214701 (2015).
46. Uchida, T., Yamazaki, K. & Gohara, K. Generation of micro- and nano-bubbles in water by dissociation of gas hydrates. *Korean J. Chem. Eng.* **33**, 1749–1755 (2016).
47. Yang, L., Falenty, A., Chaouachi, M., Haberthür, D. & Kuhs, W. F. Synchrotron X-ray computed microtomography study on gas hydrate decomposition in a sedimentary matrix. *Geochem. Geophys. Geosyst.* **17**, 3717–3732 (2016).
48. Uddin, M. & Coombe, D. Kinetics of CH_4 and CO_2 hydrate dissociation and gas bubble evolution via MD simulation. *J. Phys. Chem. A* **118**, 1971–1988 (2014).
49. Halpern, Y., Thieu, V., Henning, R. W., Wang, X. & Schultz, A. J. Time-resolved in situ neutron diffraction studies of gas hydrate: Transformation of structure II (sII) to structure I (sI). *J. Am. Chem. Soc.* **123**, 12826–12831 (2001).
50. Murshed, M. M., Schmidt, B. C. & Kuhs, W. F. Kinetics of methane-ethane gas replacement in clathrate-hydrates studied by time-resolved neutron diffraction and Raman spectroscopy. *J. Phys. Chem. A* **114**, 247–255 (2010).
51. Falenty, A., Qin, J., Salamatin, A. N., Yang, L. & Kuhs, W. F. Fluid composition and kinetics of the in situ replacement in CH_4-CO_2 hydrate system. *J. Phys. Chem. C* **120**, 27159–27172 (2016).
52. Hansen, T. C., Falenty, A. & Kuhs, W. F. Lattice constants and expansivities of gas hydrates from 10 K up to the stability limit. *J. Chem. Phys.* **144**, 054301 (2016).
53. Klotz, S., Philippe, J., Bull, C. L., Loveday, J. S. & Nelmes, R. J. A 3 kbar hydrogen-compatible gas loader for Paris–Edinburgh presses. *High Press Res.* **33**, 214–220 (2013).

Acknowledgements

This work was supported by the Swiss National Science Foundation through FNS Grant 200021–149847, and by the French state funds managed by ANR within the Blanc International programme PACS (reference ANR-13-IS04-0006-01) and the Investissements d'Avenir programme (reference ANR-11-IDEX-0004-02) and more specifically within the framework of the Cluster of Excellence MATériaux Interfaces Surfaces Environnement (MATISSE) led by Sorbonne Universités. We acknowledge the Institut Laue-Langevin for provision of beam time through LTP 6-6, and Claude Payre and James Maurice for technical assistance during the experiments. We thank José Teixeira (LLB) and Robert Pick (IMPMC) for a critical reading of the manuscript.

Author contributions

U.R., W.F.K. and A.F. prepared the sample. U.R., M.M.K., W.F.K., S.K. and L.E.B. performed the experiments. U.R., M.M.K. and L.E.B. analysed the data. All authors discussed the results and contributed to writing the manuscript.

Additional information

Supplementary Information accompanies this paper at doi:10.1038/s41467-017-01167-2.

Competing interests: The authors declare no competing financial interests.

Reprints and permission information is available online at http://npg.nature.com/reprintsandpermissions/

Publisher's note: Springer Nature remains neutral with regard to jurisdictional claims in published maps and institutional affiliations.

Open Access This article is licensed under a Creative Commons Attribution 4.0 International License, which permits use, sharing, adaptation, distribution and reproduction in any medium or format, as long as you give appropriate credit to the original author(s) and the source, provide a link to the Creative Commons license, and indicate if changes were made. The images or other third party material in this article are included in the article's Creative Commons license, unless indicated otherwise in a credit line to the material. If material is not included in the article's Creative Commons license and your intended use is not permitted by statutory regulation or exceeds the permitted use, you will need to obtain permission directly from the copyright holder. To view a copy of this license, visit http://creativecommons.org/licenses/by/4.0/.

© The Author(s) 2017

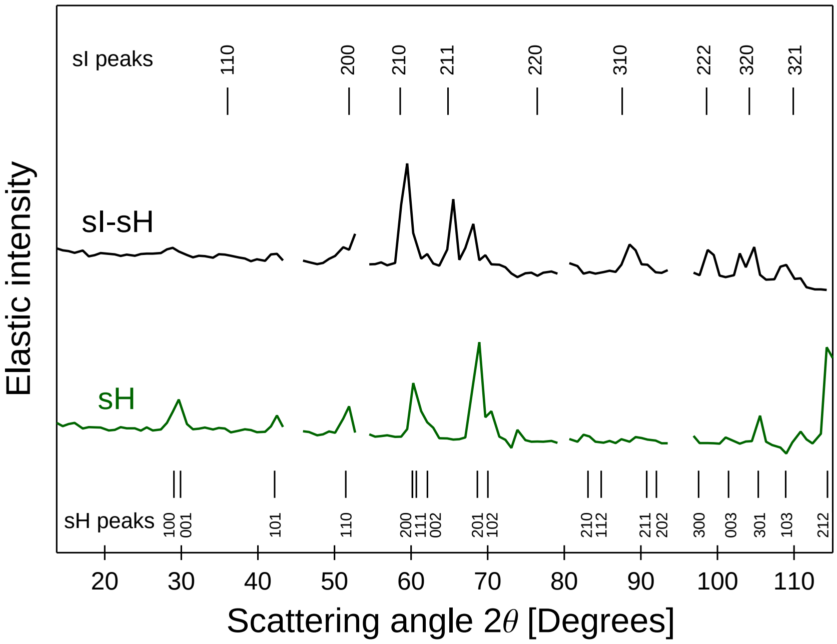

Supplementary Figure 1. Powder diffraction patterns of methane hydrate in pure clathrate sH at 1.4 GPa and 290 K and in the clathrate sI–sH at 1.0 GPa and 295 K. Breaks correspond to noisy detectors and to the strong Bragg peak of alumina in the anvils at 95°. The positions of the Bragg peaks for sI (cell parameter of 11.7 Å) and for sH (cell parameters of 11.7911 and 9.921 Å) are reported.

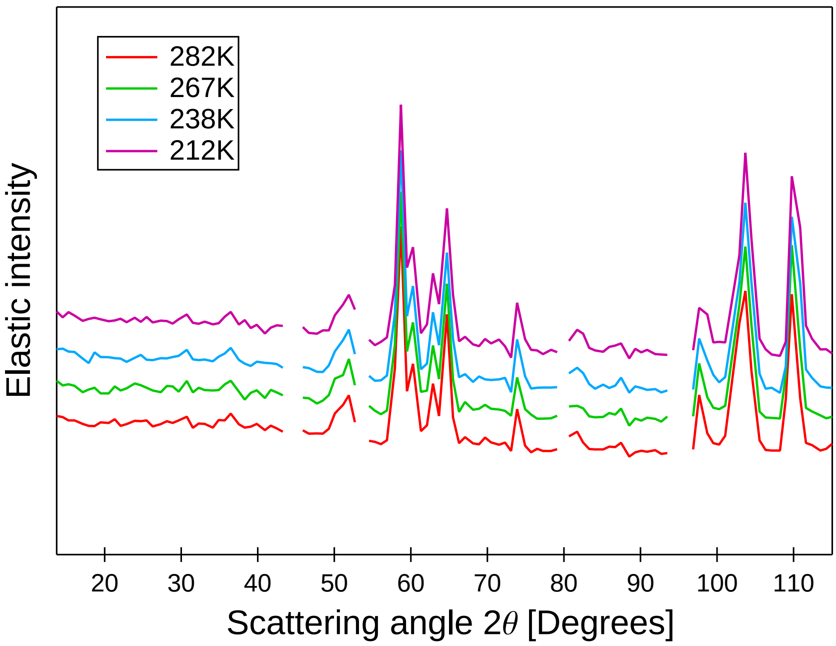

Supplementary Figure 2. Powder diffraction patterns of methane hydrate in the clathrate sI–sII at 0.8 GPa and the investigated temperatures. Breaks correspond to noisy detectors and to the strong Bragg peak of alumina in the anvils at 95°. The pattern at 282 K is also presented in Fig.1 of the main text.

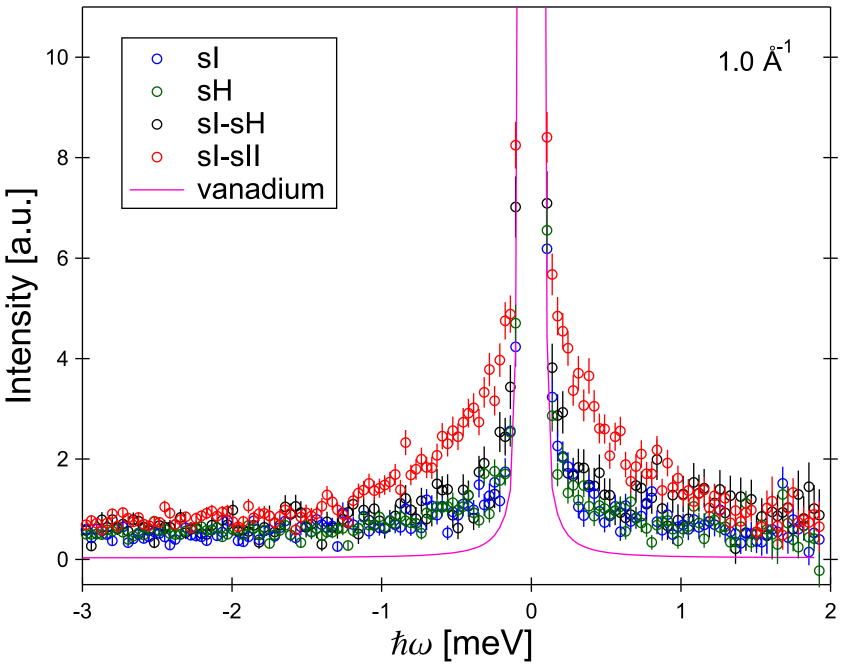

Supplementary Figure 3. Examples of QENS spectra of methane hydrate at 1.0 Å^{-1} in pure structure I (at 0.4 GPa and 290 K), in pure structure H (1.4 GPa and 290 K), in the clathrate sI–sH (1.0 GPa and 295 K) and in the clathrate sI–sII (0.8 GPa and 282 K). Error bars were calculated by the square root of absolute neutron count combined with the law of propagation of errors. The instrumental resolution function is also shown.

Supplementary Note 1: Estimating the Population of Diffusing Extra-Cage Methane

We roughly estimated the population of methane molecules that is contributing to the quasielastic signal, based on the integrated areas of the quasielastic and elastic lines of the spectra. At 282 K, the ratio between the areas of the quasielastic and elastic components at 0.8 and 1.0 $Å^{-1}$, where no Bragg peaks are expected, is 0.4 with the 3D diffusion model and 0.45 with the 2D diffusion model. The relative temperature changes of those ratios are less than 10%.

The assumptions we used for this estimation are: i) the contribution from diffusing methane is completely comprised in the quasielastic component of the spectra, ii) the contribution from methane trapped in the clathrate is completely comprised in the elastic component of the spectra, iii) the contribution from methane is weighted by the total scattering cross section of CH_4, iv) the contribution from water is completely comprised in the elastic component of the spectra, v) the contribution from water is weighted by the total scattering cross section of D_2O and vi) there are 6 water molecules per methane molecule in the sample. Assumption iii does not consider that the rotational contribution to the spectra is in fact comprised in the flat background for methane of both populations; nevertheless, the rotational contribution is almost an order of magnitude less intense than the translational contribution at 0.8-1.0 $Å^{-1}$.

If we assume that for a cystalline matrix the D_2O coherent cross section does not contribute to the elastic component of the spectra, the result of the estimation is lowered by 15%. In the scenario of a partial decomposition of the water clathrate structure, the result of the estimation is lowered by 25% at most.

Supplementary Note 2: Estimating the Origin of the Diffusing Extra-Cage Methane

Let us first assume that no sI methane hydrate decomposes. In the starting sI clathrate hydrate cage occupancies are typically 86% for the small cages and 99% for the large cages. If similar occupancies are maintained in the sI hydrate and also characterise the sII hydrate of the sI-sII clathrate sample, then almost no methane can be released during transformation from sI to sII. However, if occupancies in sI are maintained but the cages of the sII hydrate contain a lower amount of methane, a significant fraction of methane could be released during the transformation. For example, one can calculate that approximately 10% of the methane in the sample is released if cage occupancies in sII are as low as 65% for the small cages and 85% for the large cages (based on the estimated composition of the sI-sII sample in terms of sI and sII, that is 2/3 and 1/3 respectively).

On the other hand, part of the diffusing extra-cage methane must originate from partial decomposition of the clathrate structure. Though the starting sI methane clathrate hydrate sample is in a stable and equilibrated phase, where all water molecules are part of the crystalline structure and all methane molecules are trapped in the cages of the structure, the compressed sample shows coexistence of stable structure I and metastable structure II and such coexistence in near equilibrium is likely characterised by a continuous dynamical rearrangement of water and methane molecules at phase boundaries. During the sI and sII coexistence, the two structures have been suggested to develop intercalated micrometer-sized thin layers[1] and disordered regions where methane is able to diffuse would form in between them. It must be noted that the liquid-like contribution of such disordered regions to the diffraction patterns would be hardly detectable compared to a bulk amorphous or liquid. The previous estimation of a fraction of one third for the diffusing extra-cage methane suggests that a fraction of approximately 20-25% of the water molecules in the sample could belong to these disordered regions between clathrate sI and sII.

Supplementary Note 3: 2D Diffusion Model

For a particle restricted to move along a single plane, the scattering law is a Lorentzian whose half-width-half-maximum is $D_{2D}(Q)(Q\sin\theta)^2$, where $D_{2D}(Q)$ is the Q-dependent 2D translational diffusion coefficient and θ is the angle between the vector $\overrightarrow{Q}$ and the normal to the plane[2,3]. Then, for a polycrystalline sample where a large number of planes are oriented randomly the experimentally observed scattering law $< S_{2D}(Q,\omega) >_{orient.}$ is the isotropic orientational average:

$$< S_{2D}(Q,\omega) >_{orient.} = \frac{1}{2}\int_0^{\pi} \frac{1}{\pi}\frac{D_{2D}(Q)(Q\sin\theta)^2}{[D_{2D}(Q)(Q\sin\theta)^2]^2+\omega^2}\sin\theta \mathrm{d}\theta. \tag{1}$$

The integral can be calculated analytically and gives the following expression[2,3]:

$$< S_{2D}(Q,\omega) >_{orient.} = \frac{1}{8\pi k^3 D_{2D}(Q)Q^2}\times\left[\frac{1+k^2}{\cos\alpha/2}\ln\frac{1+2k\cos\alpha/2+k^2}{1-2k\cos\alpha/2+k^2}+\frac{2(1-k^2)}{\sin\alpha/2}\mathrm{arctg}\frac{2k\sin\alpha/2}{k^2-1}\right], \tag{2}$$

where

$$\begin{aligned} k &= \left[1+\left(\frac{\omega}{D_{2D}(Q)Q^2}\right)^2\right]^{1/4}, \\ \cos\alpha &= \left[1+\left(\frac{\omega}{D_{2D}(Q)Q^2}\right)^2\right]^{-1/2}, \\ \sin\alpha/2 &= \left[\frac{1-\cos\alpha}{2}\right]^{1/2}, \\ \cos\alpha/2 &= \left[\frac{1+\cos\alpha}{2}\right]^{1/2}. \end{aligned}$$

In our 2D diffusion data analysis, the expression for $< S_{2D}(Q,\omega) >_{orient.}$ given in equation (2) substituted the simple Lorentzian scattering law used in the 3D diffusion data analysis. Supplementary Fig. 4 depicts $\hbar D_{2D}(Q)Q^2$ as a function of Q^2 and is the 2D-analogous of Fig. 3 of the main text. By analogy with the Singwi–Sjolander random jump diffusion model applied to normal 3D liquids, the coefficient $D_{2D}(Q)$ was fitted by $D_{2D}(Q) = D_{2D}/(1 + D_{2D}Q^2\tau_{2D})$, with D_{2D} the 2D translational diffusion coefficient and τ_{2D} the mean time between jumps[2].

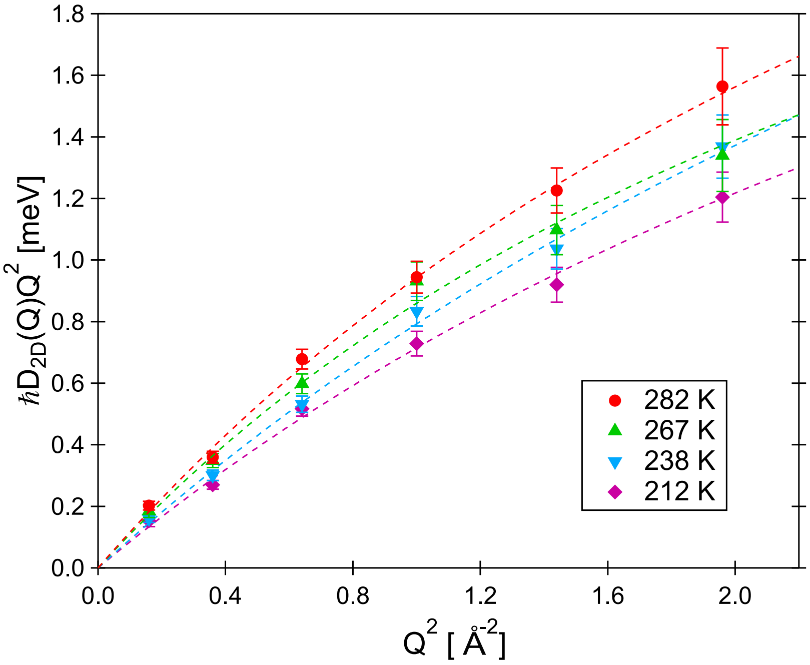

Supplementary Figure 4. $\hbar D_{2D}(Q)Q^2$ as a function of Q^2 at 0.8 GPa and the investigated temperatures as obtained from the 2D diffusion fits. Error bars correspond to one standard deviation. The best fits to the data according to a Singwi–Sjolander random jump diffusion model $[D_{2D}(Q) = D_{2D}/(1 + D_{2D}Q^2\tau_{2D})]$ are shown as dashed lines. The values obtained for D_{2D} and τ_{2D} are reported in Fig. 4 of the main text.

Supplementary References

1. Schicks, J. M. & Ripmeester, J. A. The coexistence of two different methane hydrate phases under moderate pressure and temperature conditions: Kinetic versus thermodynamic products. *Angew. Chem., Int. Ed.* **43**, 3310–3313 (2004).

2. Dianoux, A. J., Volino, F. & Hervet, H. Incoherent scattering law for neutron quasi-elastic scattering in liquid crystals. *Mol. Phys.* **30**, 1181–1194 (1975).

3. Lechner, R. E. Effects of low-dimensionality in solid-state protonic conductors. *Solid State Ionics* **77**, 280–286 (1995).

5.2.3 Next future steps

We have reported the first observation of fast translational diffusion of methane molecules at the interface of the clathrate structures I and II. The precise microscopic origin of this phenomenon is not clear. We could imagine that the observed fast mobility is an effect of confinement or of gas bubbles formation at the interface of the two structures. To shed light on this point, it could be useful to repeat the QENS measurements on a CD_4–H_2O methane hydrate sample to check the existence of water molecules diffusion on the picosecond timescale. It could be also useful to perform the QENS measurement of a melted CH_4–D_2O methane hydrate sample at 0.8 GPa and a temperature just above the melting ($\sim$325 K from ref [63]). This would provide the methane diffusion coefficient in the resulting supersaturated liquid water–methane mixture, as methane cannot escape from the sample chamber of the Paris-Edinburgh press.

Large-scale molecular dynamics simulations could also help elucidating our unexpected results. In the last few years there have been a growing interest for the investigation of inter-cage diffusion of different guest molecules through bulk clathrate hydrates by simulations [56, 58, 64, 65, 66, 67, 68, 69, 70] and we hope that our study will motivate the development of simulations accessing the guest diffusivity at the structures interface. Those simulations should be performed on a large length scale including thousands of molecules, so possibly using a coarse-graining approach [71].

Future studies might also try to generalize the observation reported here for methane hydrate at 0.8 GPa and 212–282 K to wider ranges of pressure and temperature. Similarly, it could be possible to generalize the present observation to the hydrates of other guest molecules; good candidates should i) have hydrogenated guests molecules and ii) show persistent coexistence of two structures. Concerning the issue of CH_4–CO_2 replacement in natural gas hydrates for CH_4 recovery and CO_2 sequestration, it might be that our observation of a fast methane diffusion can be extended to sI–sII samples during CH_4–CO_2 gas exchange but this needs to be checked by future targeted QENS studies in the relevant pressure and temperature ranges.

5.3 Guest dynamics in methane-filled ice

5.3.1 Introduction

Gas clathrate hydrates have been extensively studied for decades in the relatively low-pressure regime (below 0.5 GPa) and broad information was obtained on the interaction between water and the gas molecules, which is undoubtedly one of the key factors that determines the properties of those systems. Even though a full understanding of the water–gas interaction in clathrate hydrates is still missing, it is clear that the interaction between water and guest molecules, which are Van der Waals interactions, are noticeable but weak in comparison to the interactions between the hydrogen-bonded water molecules. In other words, the guest molecules are encaged by the host structure with no strong chemical bonding between hosts and guests molecules. It follows that the guest molecules are relatively free to rotate and to translate within their cages. The extent of these motions depend on the size of the guest, on the size of the cage, on the details of the interaction between the two, and on the number of guests per cage.

A completely different scenario is expected in gas hydrates having high-pressure filled ice structures. In those structures the hydrogen-bonded water networks are based on distortions of the networks of known phases of ice and the voids are filled with guests molecules. The $O\cdots C$ distances are much shorter than in the clathrate structures. The high-pressure structure formed by methane, krypton, argon, and nitrogen hydrates has been first observed for methane hydrate in the pioneering works by Loveday et al. [72, 73] and is generally referred to as structure MH-III.

MH-III is a body-centered orthorhombic structure with space group Imcm (a variation of the space group Imma, No. 74) and unit cell dimensions of about a=4.7 Å, b=8.1 Å, and c=7.8 Å at 3 GPa. There are eight water molecules and four methane molecules in the unit cell, implying a theoretical water-to-methane molar ratio of 2 to 1. The hydrogen-bonded (most likely proton-disordered) water network of MH-III is related to ice Ih and has six-membered rings of water molecules that are aligned to form hexagonal channels running along the c axis, as can be seen in Figure 5.3. Methane molecules are located along the channels at approximately midway between two adjacent six-membered rings, but slightly offset from the centers of the channels in a zigzag arrangement along the c axis.

Differences between MH-III and ice Ih are easy to spot, nevertheless. Ice Ih has six-membered water rings forming channels along all three directions; those rings are puckered and the O atoms of each ring *alternatively* bond in opposite directions to the upper and bottom adjacent rings along the same channel (Figure 5.3). MH-III presents six-membered water rings along the c axis only; rings are almost flat but inclined with respect to the axis c. The O atoms of each six-membered ring of MH-III do not bond alternatively to the upper and bottom adjacent rings but three consecutive O atoms bond

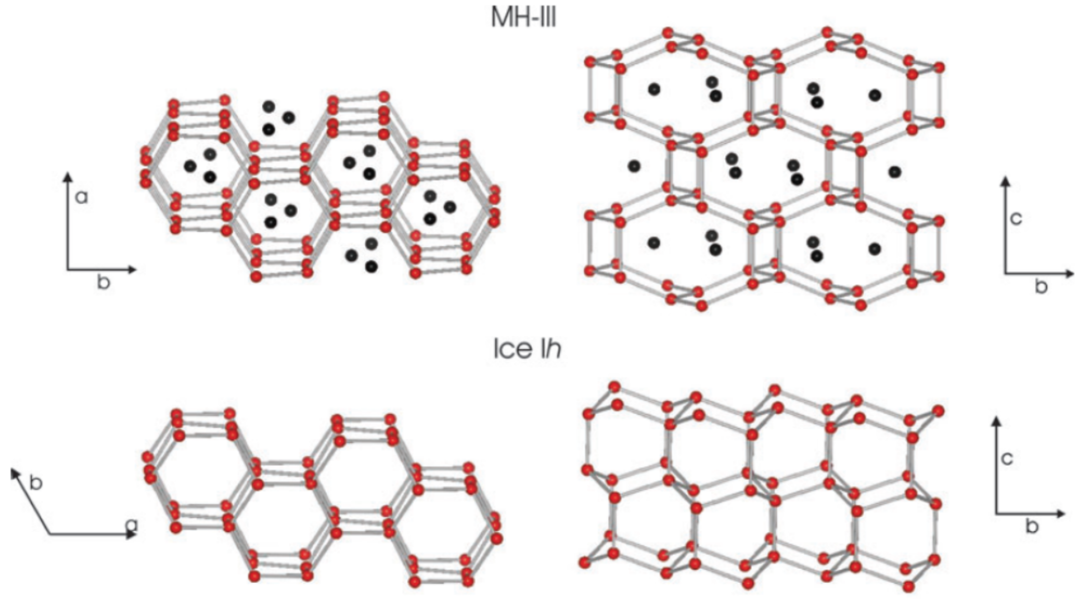

Figure 5.3: The structures of methane-filled ice Ih (MH-III) and ice Ih in two different crystallographic planes, reproduced from ref [9]. The oxygen atoms are shown as red balls and the carbon atoms as black balls. For clarity the hydrogen atoms have been omitted and oxygen atoms connected along hydrogen bonds.

to the upper adjacent ring and the three other ones bond to the bottom adjacent ring (Figure 5.3). This distortion compared to ice Ih creates enough space to accommodate the methane molecules within the structure. It follows that in the bc plane MH-III presents two types of alternating channels running along the axis a, namely channels made of large eight-membered water rings which are filled with two non-aligned methane molecules and empty channels made of small four-membered rings.

In MH-III at 3 GPa the shortest O$\cdots$C distances are ∼3.3 Å, while these are ∼3.8 Å in clathrate structure I. The shortest C$\cdots$C distances are ∼3.8 Å, close to the value found in solid methane (phase I) at the same pressure. The hydrogen bond lengths are only 1% longer than in ice Ih but O–O–O angles are very distorted and range between 90° and 120° [73].

Loveday et al. [73] reported stability of MH-III up to 9 GPa. They also noticed that the density of MH-III is close to the mean density of a mixture of ice VII and methane I in 2 to 1 proportions and suggested that MH-III might be stable over a wide pressure range up to several tens of GPa. This prediction was confirmed by Hirai et al. [8], who reported synchrotron x-ray diffraction data in which no decomposition into free methane and ice was observed up to the highest investigated pressure of 40 GPa. Later, in a series of Raman spectroscopy and x-ray diffraction experiments reaching a maximum pressure of 86 GPa [13, 74, 75, 76, 77], the group of Hirai suggested the existence of a transition to a different structure occurring at around 40 GPa. The high-pressure structure, which would survive up to 86 GPa at least, could not be solved [13, 74, 75, 76, 77]. Therefore, high-pressure methane hydrate offers the fascinating possibility to explore the water–methane interaction over a wide range of intermolecular distances.

One way to follow the water–methane interaction is to study the dynamics of the methane molecules with increasing pressure. At 3 GPa methane molecules are expected to be orientationally disordered [73] but there is no doubt that the methane orientational disorder must disappear as soon as pressure approaches 20–30 GPa and inter-molecular distances decrease. The shortest $O\cdots C$ distances are expected to change from 3.3 Å at 3 GPa to less than 3.0 Å at 40–50 GPa [9], based on the experimental lattice parameters reported in refs [8, 76] and assuming little change in the fractional coordinates. Orientational ordering of the methane molecules must eventually result into complete locking-in of the rotations and this could possibly happen along with formation of hydrogen bonds between water and methane.

Some information exists in the literature concerning the effect of pressure on the guest dynamics in MH-III but a unified picture is still missing. Hirai et al. [75, 76] observed a splitting of the methane stretching modes above 15–20 GPa by Raman spectroscopy and a change in the compressibility of the c axis by x-ray diffraction at 20–25 GPa and interpreted both changes as evidence of orientational ordering of the methane molecules in the structure. Klug et al. [78] observed a splitting of the antisymmetric stretching mode above 19 GPa by infrared spectroscopy and interpreted it as evidence of distortion of the methane molecules and consequent lift of degeneracy of the mode.

In the next subsection (5.3.2) we address the following open questions regarding MH-III at very high pressure by using Raman spectroscopy experiments and ab-initio molecular dynamics simulations in the pressure range up to 45 GPa:

- Is the orientational ordering of methane molecules a gradual or an abrupt transition? At which pressure(s) does it happen?
- What are the preferred orientations for the methane molecules in MH-III after locking-in of the rotations? Are there hydrogen bonds between water and methane?
- What is the nature of the vibrational modes of both water and methane in MH-III at 40 GPa? Is there mode coupling?

The behavior of methane hydrate between 45 and 150 GPa will be addressed in subsection 5.3.4.

Raman spectroscopy provide information about internal (intra-molecular) vibrational modes, such as stretching or bending or rocking modes, as well as about external (inter-molecular) modes. The methane molecule has four fundamental vibrational modes, all of which are Raman active: symmetric stretching (symmetry A1), rocking (symmetry E), antisymmetric stretching, and bending (both symmetry F2). In general the stretching modes of methane is very sensitive to the surrounding molecular environment. For example the frequency of the symmetric stretching mode of methane molecules in the small cages of clathrate sI is smaller than that of methane in the vapor phase but larger than that of methane molecules in the large cages of sI [79]; this somehow counter-intuitive observation is to be explained by attractive water–methane interaction in clathrate structures. The water molecule has three fundamental vibrational modes, all of which are Raman active: symmetric stretching and bending (both symmetry A1), and antisymmetric stretching (symmetry B2).

Raman spectroscopy experiments on CH_4–D_2O methane hydrate up to 45 GPa have been performed in our laboratory at the EPFL. The starting sample was in the form of clathrate sI and had been prepared as explained in chapter 2. Starting clathrate sI sample was loaded into a diamond anvil cell in a liquid nitrogen bath as explained in section 3.3 and compressed to the GPa pressure range at cold. The closed cell was then warmed up from liquid nitrogen temperature to room temperature and all measurements were carried out at room temperature. Data from two different loadings will be presented in the following subsection. For both of them it was possible to load a well-compacted powder of methane hydrate filling almost completely the sample chamber so that the amount of nitrogen was minimized and the sample signal was maximized. Sample of the first loading was compressed to 12 GPa at cold and then measured by Raman spectroscopy at pressures between 12 and 45 GPa. Sample of the second loading was compressed to 3 GPa at cold, measured by Raman spectroscopy between 3 and 22 GPa and then by x-ray diffraction between 22 and 48 GPa at the beamline ID27 at the ESRF in Grenoble (France). Figure 5.4 reports a photo of the sample chamber after the first loading.

Figure 5.5 reports a typical raw (non background-subtracted) Raman spectrum of the sample measured at high pressure in diamond anvil cell. Different modes can be easily distinguished: the lattice mode at 400 cm^{-1}, the CH_4 rocking mode at 1570 cm^{-1}, the OD stretching modes at 2100 and 2240 cm^{-1}, and the CH stretching modes at 3070 and 3200 cm^{-1}. With increasing pressure the lattice mode, the CH_4 rocking mode and CH stretching modes shift to higher frequencies while the OD stretching modes shift to smaller frequencies. It must be noted that, since the MH-III structure is richer in methane than clathrate sI, the high-pressure sample contained excess D_2O which is in the form of ice VII in the pressure range investigated and contributed substantially to the measured lattice and OD stretching modes. The water-to-methane molar ratio is about 6 to 1 in the starting clathrate sI sample and presumably 2 to 1 in MH-III, therefore approximately two thirds of the water molecules in the high-pressure sample are expected to be in the form of ice VII. Diamond first-order signal at 1350 cm^{-1} and second-order at 2400–2700 cm^{-1}, and the vibron peak of nitrogen at 2365 cm^{-1} are also visible in the spectrum of Figure 5.5.

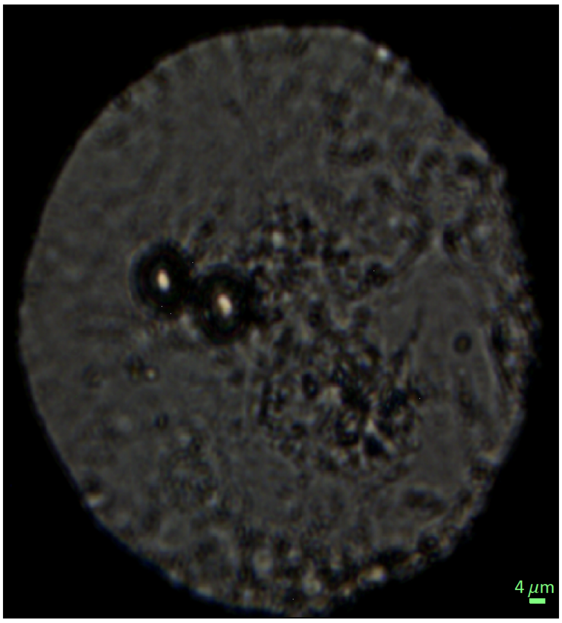

Figure 5.4: Photo of the sample chamber (~130 µm in diameter) at 12 GPa. The two dark circles of about ~15 µm in diameter are two ruby balls.

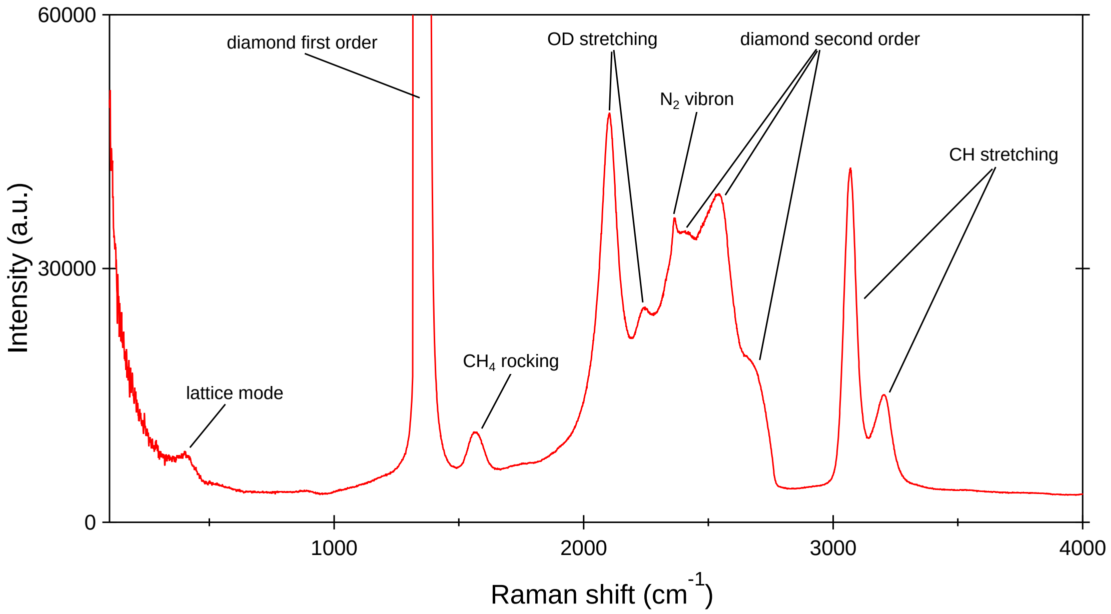

Figure 5.5: Raw experimental Raman spectrum of methane hydrate (and excess ice) at room temperature and 20.9 GPa.

Frame-hydrogenated methane hydrate (CH_4–H_2O) samples were also measured but for these samples formation of structure MH-III was found to be challenging, in agreement with previous observations [72, 80], and corresponding results will not be presented in the following.

Ab initio density functional theory molecular dynamics simulations have been performed on both CH_4–D_2O and CH_4–H_2O in the range between 2 and 45 GPa. They provide vibrational spectra by Fourier transform of the velocity autocorrelation functions and can also give important information about the orientational configuration of the methane molecules and about possible mode coupling which are not accessible by Raman spectroscopy. Nuclear quantum effects were included using the quantum thermal bath (QTB) [81] and the path integral+generalized Langevin equation (PI+GLE) [82] methods. The QTB method is less expensive than PI+GLE and typically provides qualitatively correct results for the vibrational spectra. The PI+GLE method provides correct quantum distributions (in the limit of a infinite number of beads) but is more expensive.

QTB simulations were performed for a large number of pressure points between 3 and 45 GPa and PI+GLE simulations were performed at five pressure points only (2.4, 6.9, 16.4, 25.3, and 36.4 GPa). QTB simulations were found to correctly reproduce the experimental lattice parameters reported in refs [8, 76] and our experimental Raman frequencies for the methane stretching mode and, to some extent, the methane rocking mode. They provide details of the coupling between methane and water modes. On the other hand PI+GLE trajectories can be employed to extract statistical distributions for the methane orientational configuration and for the geometry of the methane molecule.

Our results on Raman spectroscopy and molecular dynamics simulations of methane hydrate up to 45 GPa have been published in May 2018 in the journal *Journal of Physical Chemistry C* in an article entitled “Orientational ordering, locking-in and distortion of CH_4 molecules in methane hydrate III under high pressure” and authored by Sofiane Schaack, Umbertoluca Ranieri, Philippe Depondt, Richard Gaal, Werner F. Kuhs, Andrzej Falenty, Philippe Gillet, Fabio Finocchi, and Livia E. Bove. The article is attached in the following pages and followed by its Supporting Information file. The article publisher’s version is reprinted with permission from J. Phys. Chem. C 122. Copyright 2018 American Chemical Society. The DOI is 10.1021/acs.jpcc.8b02783. Author contributions are as follows: U.R., W.F.K., and A.F. prepared the sample. U.R., R.G., and L.E.B. performed the experiments. S.S., P.D., and F.F. performed the simulations. All authors discussed the results. S.S., F.F., and L.E.B. wrote the manuscript with input from all the other authors.

5.3.2 Article: “Orientational ordering, locking-in and distortion of CH_4 molecules in methane hydrate III under high pressure”

THE JOURNAL OF
PHYSICAL CHEMISTRY C

Article

Cite This: J. Phys. Chem. C 2018, 122, 11159−11166

pubs.acs.org/JPCC

Orientational Ordering, Locking-in, and Distortion of CH_4 Molecules in Methane Hydrate III under High Pressure

Sofiane Schaack,[†] Umbertoluca Ranieri,[‡,§] Philippe Depondt,[†] Richard Gaal,[§] Werner F. Kuhs,[‖] Andrzej Falenty,[‖] Philippe Gillet,[§] Fabio Finocchi,[*,†] and Livia E. Bove[*,§,⊥]

[†] Sorbonne Université, CNRS UMR 7588, Institut des Nanosciences de Paris (INSP), 75005 Paris, France

[‡] Institut Laue-Langevin, 71, avenue des Martyrs, CS 20156, 38042 Grenoble Cedex 9, France

[§] EPSL, ICMP, École polytechnique fédérale de Lausanne (EPFL), Station 3, CH-1015 Lausanne, Switzerland

[‖] GZG Abt. Kristallographie, Universität Göttingen, Goldschmidtstrasse 1, 37077 Göttingen, Germany

[⊥] Sorbonne Université, CNRS UMR 7590, Institut de minéralogie, de physique des matériaux et de cosmochimie (IMPMC), 75005 Paris, France

Supporting Information

ABSTRACT: We investigate the effects of high pressure on the reorientational and vibrational dynamics of methane molecules embedded in methane hydrate III—the stable form of methane for pressures above 2 GPa at room temperature—by combining high-pressure Raman spectroscopy with ab initio simulations including nuclear quantum effects. We observe a clear evolution of the system from a gas-filled ice structure, where methane molecules occupy the channels of the ice skeleton and rotate almost freely, to a $CH_4{:}D_2O$ compound where methane rotations are hindered, and methane and water dynamics are tightly coupled. The gradual orientational ordering of the guest molecules results in a complete locking-in at approximately 20 GPa. This happens along with a progressive distortion of the guest molecules. Finally, as pressure increases beyond 20 GPa, the system enters a strong mode coupling regime where methane guests and water hosts dynamics are intimately paired.

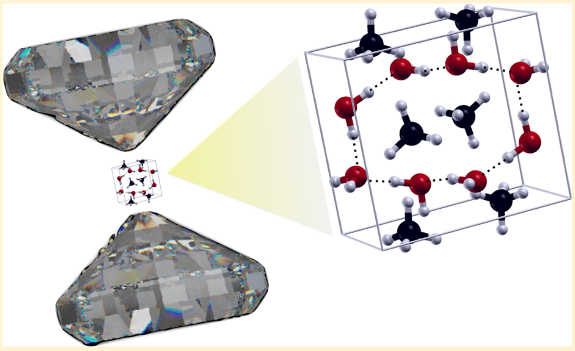

INTRODUCTION

Ice clathrates are inclusion compounds wherein small nonpolar gas (guest) molecules are enclosed inside polyhedral cavities, or cages, formed by hydrogen-bonded water (host) molecules.[1,2] The interaction between the guest molecule and the ice skeleton is mostly repulsive, which makes clathrate hydrates interesting prototypes for the study of hydrophobic interactions that are encountered in the more complex living matter.[3] Clathrate hydrates can be stabilized by rather modest pressure, typically in the megapascal range, depending on the specific guest gas molecule, and once formed they keep the guest molecules efficiently trapped at low temperature. For this reason, they are envisaged as potentially attractive hosting environments for physical hydrogen storage[4,5] or for CO_2 sequestrations.[6] Among the different clathrate hydrates, methane hydrate is the most widespread naturally occurring gas hydrate as it is present in large quantities in subsurface deposits, both in oceanic shelf sediments and in permafrost regions.[7] Methane hydrates are also suspected to exist at depth in many water-rich objects populating the outer solar system.[8] Therefore, several experimental studies in the last years focused on the high-pressure behavior of methane hydrates.[8−24]

As pressure increases beyond the kilobar range, typically above 1−2 GPa, most ice clathrates undergo profound structural changes: the cages shrink and reorganize into structures bearing some resemblance to ice phases, known as filled ices,[9] where the guest molecules occupy interstices in the ice lattices.[10] In filled ices, three different structures have been observed so far, and more recently, a new "chiral hydrate" was established.[25,26]

Many entangled phenomena are expected to occur in the system as pressure rises, such as the change in nature of the guest−host interaction, the likely coupling of guest and host dynamics, and possibly orientational ordering of the guests and structure rearrangements. At moderate pressures, a coupling between the localized rattling modes of the guests and the host lattice phonons has been recognized as an essential ingredient for stabilizing the clathrate structure.[27,28] As the pressure rises, the guest molecules are expected to deviate strongly from free rotors because of the increasing interaction with the water frame toward a frozen crystalline structure at very high

Received: March 22, 2018
Revised: April 26, 2018
Published: April 26, 2018

ACS Publications © 2018 American Chemical Society

DOI: 10.1021/acs.jpcc.8b02783
J. Phys. Chem. C 2018, 122, 11159−11166

pressure. However, the evolution of the hydrate between these two regimes is rarely investigated. A microscopic description of the behavior of the gas molecules enclosed under tight confinement within the water frame is still lacking, and the nature of the guest–host interaction in this regime remains elusive.

In this paper, we focus on the methane hydrate III (MH-III) phase, which is the stable phase of methane hydrates above 2 GPa at room temperature and shares its filled ice structure with krypton, argon, and nitrogen hydrates.[8,10] The structure of MH-III is related to ice Ih, especially in the a–b plane, where it shows characteristic tilted sixfold water rings. The channel-like voids along the c axis are filled with methane molecules, with their centers arranged in a zig-zag fashion along the c axis. At variance with ice Ih, MH-III has also four- and eightfold water rings. The coexistence of distinct ice rings within the same structure gives MH-III a marked crystalline anisotropy, which is particularly evident at high pressures (see Supporting Information Figure S7).

High-pressure methane hydrate has been widely investigated by different techniques, including Raman spectroscopy,[16−21,29] X-ray diffraction,[9,11−16,21] and neutron diffraction.[8,9,30] The preparation of hydrates with 90–95% of the maximum theoretical occupation of the guest sites is quite challenging, and the risk of structural destabilization under compression increases drastically if the filling ratio of the starting clathrate is not high enough. MH-III was found to be stable up to 86 GPa at least,[15] though a possible transition to an unresolved high-pressure structure was reported to occur at around 40 GPa.[14,15,19,21] A splitting of the symmetric (ν_1) and antisymmetric (ν_3) CH stretching mode peaks above 15–20 GPa has also been observed, which some authors attributed to the CH_4 orientational ordering[14,19,21] and others ascribed to the distortion of the methane molecules at high pressure.[22] Finally, the appearance of a possible Fermi resonance between the overtone of the D_2O bending mode and the OD stretching mode was observed[22] at 15 GPa, while symmetrization of the hydrogen bond network was predicted to occur above 60 GPa from ab initio molecular simulations.[22,23] However, a clear interpretation of the previous observations and a unified picture of the interplay of those different phenomena are still lacking.

In the following, we investigate the pressure effects on the reorientational and vibrational motion of the methane molecules embedded in MH-III, as well as the modification of the host–guest coupling, by combining high-resolution Raman spectroscopy under high pressure with ab initio density functional theory molecular dynamics (DFT-MD) simulations,[31] including nuclear quantum effects through the quantum thermal bath (QTB)[32−35] and path integral-generalized Langevin equation (PI + GLE)[36] methods at the 2/1 theoretical ratio of water/methane. Through the analysis of MD trajectories, we anticipate that two pressure domains can be identified: for $P < 20$ GPa, the methane molecules become orientationally ordered as the pressure increases, whereas the guest molecules undergo angular distortions; beyond a pressure threshold of about 20 GPa, methane and water vibrational modes are strongly coupled.

■ METHODS

Sample Preparation. Starting sI methane clathrate hydrate samples of this study were prepared using a finely ground D_2O ice impregnated with methane gas at 60 bar, following the method described in ref 37. Synthesized samples were kept at liquid nitrogen temperature and extensively characterized by X-ray and neutron diffraction. The diamond anvil cells (DACs) were cooled to liquid nitrogen temperature and loaded cold with sI methane clathrate hydrate under nitrogen atmosphere in a portable glovebox, to avoid contamination by atmospheric water. A small ruby ball was also trapped to serve as a pressure gauge. Pressure was applied on the cold sample to achieve high enough pressure to stabilize the sample even at room temperature. After the initial pressurization, the samples were warmed up and all measurements were carried out at 300 K. Pressure was varied between 10 and 45 GPa. The absence of hysteresis effects was verified by sweeping the pressure up and down. Compression/decompression rates were typically 2 GPa/h. The starting sI CH_4:D_2O clathrate hydrate sample was also characterized by infrared and Raman scattering and shown to have a 86% methane filling ratio in the small cages and 99% in the big cages. Under slow compression (2 GPa/h ca.), the clathrate transformed with loss of water to the hexagonal clathrate sH at ~1 GPa and then to the MH-III structure at around 2 GPa with further loss of water. Finally, we investigated the pressure dependence of the CH stretching mode and of the CH_4 rocking mode between 3 and 22 GPa during a dedicated Raman experiment. No ruby was used during this loading; pressure was evaluated with a precision of 0.5 GPa based on the measured shift of the diamond Raman signal measured in the center of the culet, compared to earlier runs when both diamond Raman and ruby fluorescence were measured.

High-Pressure Raman Scattering. The pressure dependence of the Raman spectra of CH_4:D_2O was measured with a HR-800 spectrometer using a Cobolt Samba 532 nm laser for excitation and a 600 L/mm grating. The spectrometer is coupled to a microscope, and a Mitutoyo SL50X objective allowed direct measurements inside the DAC. The resolution of the instrument under these conditions is about 0.5 cm^{-1}, as determined from measuring the emission lines of a He–Ne gas lamp. Pressure was generated in a symmetric Mao-type DAC using 300 micron culet type IIs diamonds for minimal fluorescence and monitored by ruby fluorescence using the pressure scale from refs 38 and 39. As the sample signal overlaps with the second-order Raman signal of the diamond, we systematically measured the Raman spectra on the gasket close to the sample chamber and used it as a background, together with a quadratic function to approximate fluorescence from the lower diamond, invisible in the gasket measurements. Details of the procedure are given in the Supporting Information of our earlier paper.[40]

Simulations. MD simulations at room temperature of both CH_4:$(D_2O)_2$ and CH_4:$(H_2O)_2$ methane hydrates were carried out using the QTB method[32,35] (details in Supporting Information) and the PI + GLE method,[36] to include nuclear quantum effects that are especially important on light nuclei such as H and D. Although a semi-classical approximation, the QTB is quite efficient in computing vibrational spectra,[35,41] while PI + GLE yields exact distributions in the limit of an infinite number of beads. The samples for the QTB simulations consist of 16 methane molecules and 32 water molecules in a 2 × 1 × 2 orthorhombic supercell, with an initial MH-III structure taken from ref 10. A sample of four methane molecules and eight water molecules with eight beads was used for the PI + GLE simulations. Oxygen and carbon atoms were initially set at their crystallographic positions, while hydrogen (deuterium) atoms were let to relax during short simulations

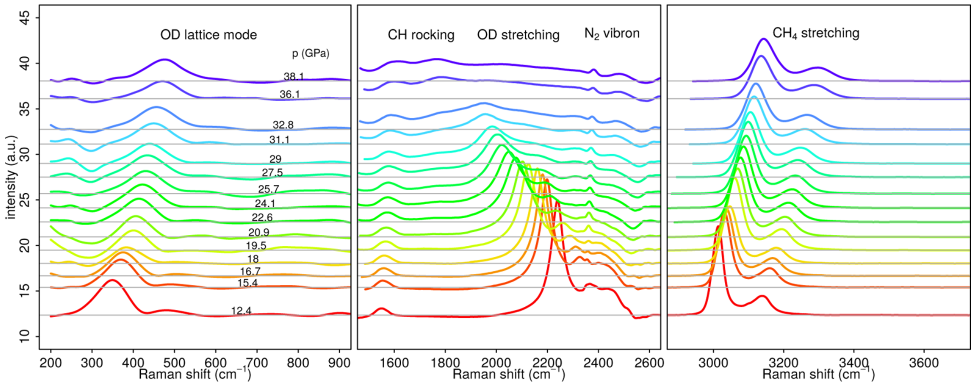

Figure 1. Experimental Raman spectra of the sample at pressures between 12 and 45 GPa. Left: lattice mode; center: CH_4 rocking and OD stretching modes; right: CH stretching modes.

with large friction coefficients γ to explore different configurations and start with variable orientations for the CH_4 molecules. The electronic structure and atomic forces were described within the generalized gradient approximation (GGA)[42] to the DFT. van der Waals (vdW) interactions were added by following the semi-empirical D2 scheme by Grimme;[43] after extensive tests, a better agreement with experimental lattice constants and compressibility could be obtained within GGA + D2 than in the GGA; vibrational spectra are not affected by the introduction of the vdW correction. All calculations were carried out by using the Quantum ESPRESSO package[31] in combination with a QTB implementation[33] or the i-PI package[44] for PI + GLE. Ultrasoft pseudopotentials were used to describe the interaction between the ionic cores and the valence electrons: a plane-wave expansion cutoff of E_{cut} = 40 Ry ensured convergence of total energy, pressure, and atomic forces. A 2 × 1 × 2 k-point grid sampling was used. Simulations were run at constant volume, with lattice parameters chosen to obtain isotropic stress tensors within the statistical error, in the range 3–45 GPa. The typical duration time of the simulations was 30 ps. The reader can refer to the Supporting Information for technical details.

■ RESULTS AND DISCUSSION

Pressure Dependence of the Raman Spectra. Raman spectra of a CH_4:D_2O clathrate were measured at room temperature, while the stability of the MH-III structure up to 45 GPa was checked by X-ray diffraction (Supporting Information Figure S1).

In Figure 1, we show the pressure dependence of the background-subtracted Raman spectra over three significant frequency ranges (the full measured spectrum before background subtraction is reported in Supporting Information Figure S2). Several bands related to MH-III disperse with pressure, which we identify as follows: the lattice vibration of the water frame (350–450 cm^{-1}), the rocking of the CH_4 molecules (1550–1600 cm^{-1}), the OD stretching mode of the water frame (1600 and 2400 cm^{-1}), and the symmetric and antisymmetric CH stretching modes (3000 and 3300 cm^{-1}). As the sample contained excess ice, we checked how the OD lattice and stretching modes are measured on the sample compared to those of pure ice (Supporting Information Figure S3).

Figure 2 shows the experimental Raman shifts as the pressure is increased along with the vibrational frequencies provided by our QTB-MD simulations, for the methane stretching and rocking modes and the D_2O lattice mode. Despite the discrepancy of about 35 cm^{-1} between the observed and calculated CH_4 rocking mode, the methane rocking mode frequency at 25 GPa is located at a value that is quite similar to the calculated one reported in ref 22 and remains within expected DFT precision. One can notice that an extrapolation from our values to ambient pressure gives values, which are

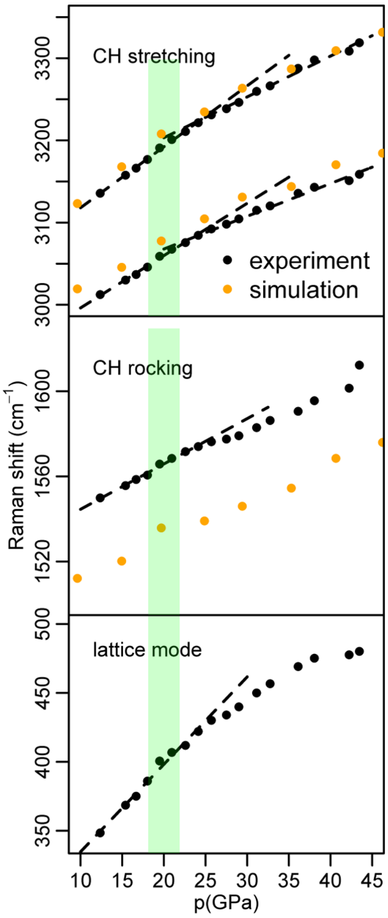

Figure 2. Lattice mode, CH_4 stretching mode frequencies as a function of pressure. Dashed lines are linear fit of the experimental data points below 25 GPa. A deviation from the linear trend is evident for all data points above 25 GPa.

DOI: 10.1021/acs.jpcc.8b02783
J. Phys. Chem. C 2018, 122, 11159–11166

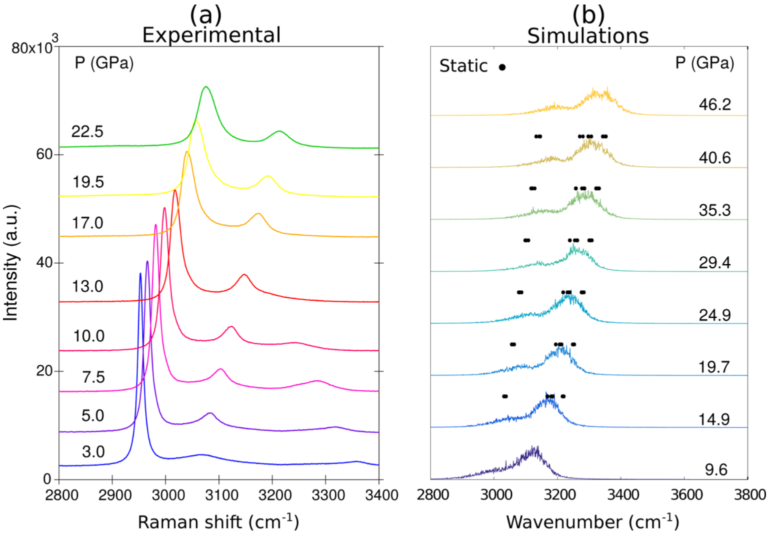

Figure 3. (a) Experimental high-resolution Raman spectra of the CH stretching mode of the sample at different pressures. There was no indication of splitting of peaks as claimed to be observed at approximately 15 GPa in refs.[14,19,21] (b) Spectra computed from the velocity correlation functions from the simulation trajectories (color lines) and relevant eigenfrequencies from a dynamical matrix analysis (dots).

reasonably close to the calculated rocking mode frequency (~1450−1465 cm^{-1}) in ref 45. The high quality of the collected Raman data in the full pressure range allows to keep the error bars on the Raman shift smaller than the plotted dots. Details of the fitting procedure are reported in the Supporting Information. The absence of new peaks in our Raman spectra indicates that methane hydrate neither destabilized nor underwent main structural rearrangements, as also observed by X-ray diffraction (Supporting Information Figure S1). More importantly, our results reveal that the observed vibrational modes follow the same evolution upon compression; in particular, all frequency dependencies on pressure deviate from a simple linear behavior at $P \approx 20$ GPa. This behavior concerns the modes of both the CH_4 molecules and the D_2O network. The observed changes in the slope of the pressure dependence in both water frame and guest modes around 20 GPa consistently indicate an enhanced coupling of the guest and host dynamics, which has been conjectured but never detailed so far. The calculated spectra quantitatively reproduce all the main features and the trends that we observed in the measured ones.

In particular, the symmetric (ν_1) and antisymmetric (ν_3) CH stretching modes of the methane molecules in MH-III have often been discussed: three works[14,19,21] reported a splitting correlated with the appearance of a new MH-III phase with orientationally ordered methane molecules. Other authors interpreted that the splitting is due to a CH_4 molecule distortion and to the consequent lift of degeneracy of the methane stretching mode as observed by infrared vibrational spectroscopy.[22] The onset of this splitting and its nature are controversial, as it could also be due to a partial destabilization of the MH-III structure under compression and to the consequent appearance of solid methane or of a new hydrate phase promoted by the laser heating.

While our low-pressure data are in excellent agreement with previous authors,[14,19,21] we observed a different behavior above 15−20 GPa. Specifically, both peaks progressively broaden with pressure (see Figure 1, right panel); however, we detected no splitting of either the ν_1 or ν_3 modes in the range 15−20 GPa or beyond; details of this frequency range are plotted in Figure 3 and compared with our simulation data. Indeed, the methane stretching mode frequencies as a function of pressure both within the harmonic approximation at $T = 0$ K and from our MD trajectories at ambient temperature were computed. The methane stretching mode frequencies computed on the optimized configurations (Figure 3b) present a lift of degeneracy around 15 GPa for the asymmetric ν_3 mode and around 25 GPa for the symmetric ν_1 mode. However, when at ambient temperature, the dynamics of the molecules is properly taken into account, and the clear-cut splitting (approximately 80 cm^{-1} in the above-mentioned references) rather broadens (approximately 60 cm^{-1}). Within the pressure range of our simulations, we found no evidence of the CH bond length asymmetry beyond the statistical noise.

As far as the data of refs[14,19,21] are concerned, the additional stretching band indeed matches the frequency of the CH stretching mode in pure methane.[46,47] We could imagine that in the experiments of refs,[14,19,21] a partial decomposition of the MH-III structure could have been caused by a low amount of methane in the sample and/or a too fast compression. It has been shown that under fast compression, methane clathrate hydrate transforms into ice VII and solid methane at 2.3 GPa, whereas under slow compression, it transforms into MH-III.[10−12]

Orientational Ordering. The rotation of the enclosed molecules has often been discussed in filled ices. For comparison, the CH_4 molecules enclosed in metal−organic framework (MOF)[48] undergo rotational motion; however, methane−methane and methane frame distances are larger than those in MH-III examined here.

Thus, to understand the transition for the methane rotational motion from relatively free to tightly locked to the cage, we studied the orientation, distortion, and vibrational mode coupling of CH_4 in deuterated MH-III (specifically CH_4:$(D_2O)_2$), at room temperature and for pressures between 3 and 45 GPa by MD simulation. Technical details are available in the Supporting Information.

DOI: 10.1021/acs.jpcc.8b02783
J. Phys. Chem. C 2018, 122, 11159−11166

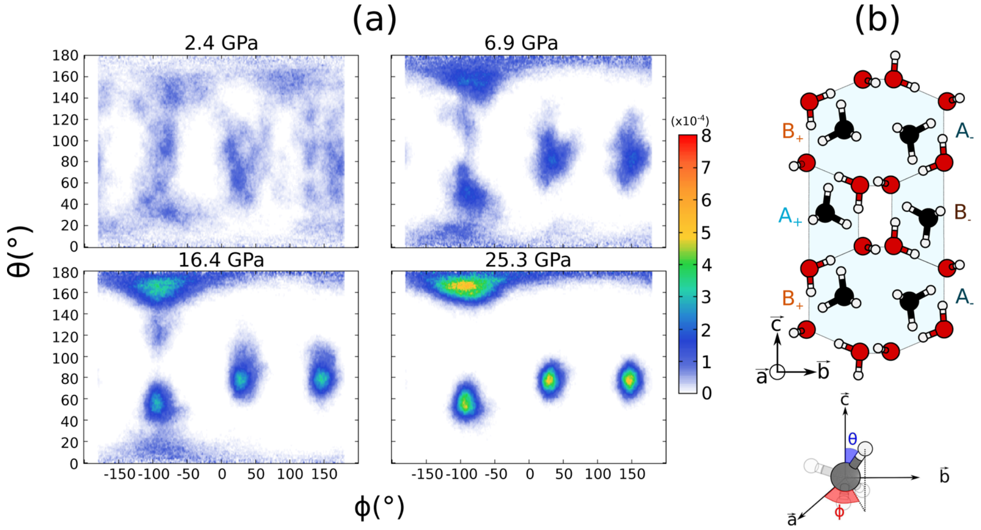

Figure 4. (a) Probability distributions of CH vector polar angles $P_{CH}(\theta, \phi)$ computed at 6.9, 16.4, 25.3, and 36.4 GPa via PI + GLE for a molecule in a B_- configuration. (b) Sketch of the most probable methane configurations $A_\pm$ and $B_\pm$.

The orientation of the methane molecules enclosed within the water frame was investigated by calculating the orientational probability density function (OPDF) $P_{CH}(\theta, \phi)$ of the CH bonds for different pressures: the OPDF for one molecule is shown in Figure 4a. For the sake of simplicity, the high-pressure case (P = 25.3 GPa) is considered first: four well-defined peaks corresponding to the four CH bonds are observed. This is a clear indication of an ordered situation. The guests are distributed among the four configurations $A_\pm$ and $B_\pm$ in the conventions of Figure 4b. The example in Figure 4a described above corresponds to a B_- configuration. Thus, the high-pressure structure, schematically represented in Figure 4b, yields A_+/B_- (or A_-/B_-) stacking along the b axis, while we observe A_+/B_+ (or A_-/B_-) stacking along c axis and finally A_+/A_- (or B_+/B_-) stacking along a. This picture is not altered as the pressure is increased up to 35 GPa.

In contrast, at low pressure, the picture is rapidly blurred as orientational disorder sets in: new, rather broad, peaks appear while the two peaks at ϕ = 30 and 150° broaden toward θ = 90°. At the two intermediate pressures, namely, 6.9 and 16.4 GPa, the distribution dependence on the angle ϕ remains essentially unaltered, while the θ dependence broadens significantly. We interpret this as a dynamical disorder between A_+ and A_- (and also between B_+ and B_-). Moreover, at the lowest pressure (P = 2.4 GPa), one also observes the onset of A/B dynamical disorder.

To summarize, as the pressure is increased from ~3 to 45 GPa, $P_{CH}(\theta, \phi)$ clearly exhibits an increasing anisotropy, which illustrates that the guest methane molecules undergo a definite pressure-induced orientational locking-in in two main steps: first, around 5 GPa, A/B motions disappear, and at approximately 20 GPa, +/− orientations lock-in. In close analogy with pure methane,[47] it has been conjectured[19,22] that methane orientational ordering in MH-III could occur at 20 GPa. We provide direct evidence for such an orientational ordering, which turns out not to be absolutely straightforward.

Methane Distortion. The evolution of the six $H\hat{C}H$ (α_n, n = 1,...,6) angles per methane molecule follows an interesting trend. At low pressure (3 GPa), all angle probability distributions $P(\alpha_n)$ are centered around the tetrahedral angle of 109.47°. Upon increasing the pressure, two of them shift progressively away from the tetrahedral angle (Figure 5). The agreement between static relaxation and PI + GLE simulations indicates that the dynamics, whether classical or quantum, plays a small role in this issue.

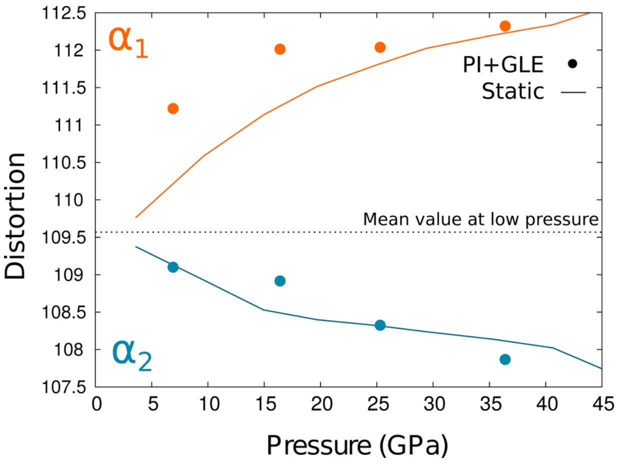

Figure 5. Mean angles $\langle\alpha_{1,2}\rangle$ in CH_4 as a function of pressure from static relaxed configurations and PI + GLE simulations.

We label α_1 the $H\hat{C}H$ angles that are close to parallel to the (a,b) plane and α_2 those angles that are in the (b,c) plane. Figure 5 shows that α_1 increases as the pressure is increased, where α_2 decreases from the ideal value, thus making the $H-H$ distance decrease along c. The latter effect is due to compression along the c axis, for which the lattice constant decreases rapidly (Supporting Information Figure S7). The former can be understood as the flattening out of the molecule as the nearest neighbors are the hydrogen atoms of the next methane molecule in the b direction.

Mode Mixing. The mode analysis within the harmonic approximation shows that at low pressure (P < 10 GPa), the eigenvectors of the CH_4 rocking modes are fully localized on the methane molecules. In contrast, as the pressure increases, they progressively mix with the atomic displacements of the water frame. To quantify the coupling between the water and the methane molecules, we projected the mode eigenvectors $\vec{e}^{(\nu)}$ at each pressure on atomic displacements that are centered either on the deuterated water frame or on the methane molecules

$$\vec{e}^{(\nu)} = \sum_{i\in \mathrm{D_2O}} b_i^{(\nu)}\vec{x}_i + \sum_{j\in \mathrm{CH_4}} c_j^{(\nu)}\vec{x}_j \tag{1}$$

where $b_i^{(\nu)}$ and $c_j^{(\nu)}$ are the coefficients of the respective expansions for the mode at frequency ν.

We then calculate a methane participation ratio $P_{\mathrm{CH_4}}(\nu)$ which describes the participation of the methane degrees of freedom (DoF) to the vibrational mode ν.

$$P_{\mathrm{CH_4}}(\nu) = \sum_{\mathrm{CH_4}}^{\mathrm{DoF}} \frac{c_j^{(\nu)^2}}{\vec{e}^{(\nu)}\cdot\vec{e}^{(\nu)}} \tag{2}$$

where the sum runs over all the CH_4 DoF. The same expression holds for $P_{\mathrm{D_2O}}(\nu)$ in which $c_j^{(\nu)}$ is replaced with $b_i^{(\nu)}$, which ensures that

$$P_{\mathrm{CH_4}}(\nu) = 1 - P_{\mathrm{D_2O}}(\nu) \tag{3}$$

In the case $P_{\mathrm{CH_4}}(\nu) = 1$, the mode ν is totally characterized by the methane DoF contribution, while if $P_{\mathrm{CH_4}}(\nu) = 0$, it is characterized by the water frame DoF only. Figure 6 shows the participation ratios ($P_{\mathrm{CH_4}}$,$P_{\mathrm{D_2O}}$) calculated for each methane bending and OD stretching modes as the pressure increases. Up to 20 GPa, $P_{\mathrm{CH_4}} \approx 1$ or 0, the investigated modes are totally described either by the methane or by the water DoF contribution. Starting at 20 GPa, some vibrational modes are described by a combination of the methane and water DoF contributions, leading to a contribution coefficient $0 < P_{\mathrm{CH_4}} < 1$. This behavior describes the pressure-induced mode coupling occurring in MH-III at 20 GPa as it is not possible to attribute these modes to a methane bending or an OD stretching vibrational mode but rather to a mixed one. Their characters therefore deeply change in this pressure range, which could be at the root of the chaotic behavior of the measured OD stretching modes (detailed in Supporting Information Figure S3). We note in passing that the resonance between the CH_4 rocking modes and the water OD stretching modes only occurs in the deuterated system CH_4:D_2O. In the protonated system (CH_4:H_2O), another type of resonance takes place between the host and guest vibrational modes. Indeed, the water OH stretching modes vibrate at higher frequencies, while the frequencies of the water and methane bending modes overlap even at low pressure.

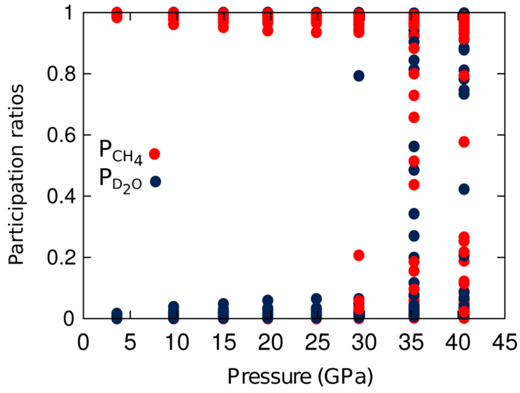

Figure 6. Mode participation ratios for methane (blue) and D_2O frame (red), computed according to eqs 1 and 2.

Over the pressure range considered here, methane−water frame distances along the trajectories remain longer than the typical ones for strong hydrogen bonds (Supporting Information Figure S8). Also, the orientation of two CH bonds that point toward hollow sites of the water frame rather than oxygen atoms is consistent with mostly repulsive interactions between CH_4 and the water frame. More details on the mode coupling in protonated CH_4−$(H_2O)_2$ hydrate can be found in Supporting Information (Figures S8 and S13).

We note that the methane rocking mode, herein measured for the first time to the best of our knowledge (Supporting Information Figure S6), becomes more defined and intense as the pressure increases. This is likely a consequence of the guest orientational ordering.

CONCLUSIONS

To conclude, our study shows that the evolution from an enclathrated almost free rotor to a strongly interacting CH_4:D_2O compound is rather complex and passes through several stages: first, the orientational ordering of the methane molecules in a A−B pairwise fashion in the channels along the c axis; second, the progressive locking-in of A_+/A_- and B_+/B_- methane rotations mainly due to steric hindrance and which is complete from 20 GPa onward, along with methane angular distortion; and third, a strong coupling between the guest and host modes, with deep consequences on the very distinction between the methane and the water DoF.

Therefore, the system undergoes a transformation from a pure hydrophobic hydrated nonstoichiometric material (still with noticeable vdW interactions) to a strongly interacting, probably a stoichiometric mixed molecular crystal. Analyzing in more detail the possibility of H-bonding between the water host and methane guest molecules, we find no hint of such an interaction even at the maximum pressure investigated here. In contrast with what was observed for methane molecules absorbed in hydroxyl-decorated MOF, where a clear $D_4C^{\mathrm{guest}}\cdots H{-}O^{\mathrm{host}}$ binding interaction is present,[48] in methane-filled ice the guest−host mode coupling is rather driven by repulsive interactions even under the tight confinement conditions reached at the high pressure.

ASSOCIATED CONTENT

Ⓢ Supporting Information

The Supporting Information is available free of charge on the ACS Publications website at DOI: 10.1021/acs.jpcc.8b02783.

> X-ray diffraction, Raman spectra, fitting procedure, CH_4 rocking mode, lattice parameters, change of compressibility, pair correlation functions, QTB description, and methane stretching mode splitting analysis (PDF)

AUTHOR INFORMATION

Corresponding Authors

*E-mail: fabio.finocchi@sorbonne-universite.fr (F.F.).
*E-mail: livia.bove@sorbonne-universite.fr. Phone: +33 (0) 144275116, +33 (0)144275219 (L.E.B.).

ORCID

Sofiane Schaack: 0000-0002-6526-9989
Umbertoluca Ranieri: 0000-0003-2026-6132
Andrzej Falenty: 0000-0001-5995-9900

Notes

The authors declare no competing financial interest.

■ ACKNOWLEDGMENTS

This work was granted access to the HPC resources of CINES under the allocation A0010906719 made by GENCI. The experimental work was supported by the Swiss National Science Fund under grant number 200021_149487. The authors acknowledge influential remarks by Simon Huppert and constructive criticism by our referees.

■ REFERENCES

(1) Jeffrey, G. A. Water structure in organic hydrates. *Acc. Chem. Res.* **1969**, *2*, 344−352.

(2) Sloan, E.; Koh, C. *Clathrate Hydrates of Natural Gases*, 3rd ed.; CRC press: Boca Raton, 2007.

(3) Hummer, G.; Garde, S.; Garcia, A. E.; Paulaitis, M. E.; Pratt, L. R. The pressure dependence of hydrophobic interactions is consistent with the observed pressure denaturation of proteins. *Proc. Natl. Acad. Sci. U. S. A.* **1998**, *95*, 1552−1555.

(4) Mao, W. L.; Mao, H.-k. Hydrogen storage in molecular compounds. *Proc. Natl. Acad. Sci. U. S. A.* **2004**, *101*, 708−710.

(5) Struzhkin, V. V.; Militzer, B.; Mao, W. L.; Mao, H.-k.; Hemley, R. J. Hydrogen storage in molecular clathrates. *Chem. Rev.* **2007**, *107*, 4133−4151.

(6) Brewer, P. G.; Friederich, G.; Peltzer, E. T.; Orr, F. M. Direct experiments on the ocean disposal of fossil fuel CO2. *Science* **1999**, *284*, 943−945.

(7) Demirbas, A. *Green Energy and Technology*; Springer: London, 2010.

(8) Loveday, J. S.; Nelmes, R. J. High-pressure neutron diffraction and models of Titan. *High Pressure Res.* **2003**, *23*, 41−47.

(9) Loveday, J. S.; Nelmes, R. J.; Guthrie, M.; Klug, D. D.; Tse, J. S. Transition from cage clathrate to filled ice: The structure of methane hydrate III. *Phys. Rev. Lett.* **2001**, *87*, 215501.

(10) Loveday, J. S.; Nelmes, R. J. High-pressure gas hydrates. *Phys. Chem. Chem. Phys.* **2008**, *10*, 937−950.

(11) Hirai, H.; Kondo, T.; Hasegawa, M.; Yagi, T.; Yamamoto, Y.; Komai, T.; Nagashima, K.; Sakashita, M.; Fujihisa, H.; Aoki, K. Methane hydrate behavior under high pressure. *J. Phys. Chem. B* **2000**, *104*, 1429−1433.

(12) Hirai, H.; Uchihara, Y.; Fujihisa, H.; Sakashita, M.; Katoh, E.; Aoki, K.; Nagashima, K.; Yamamoto, Y.; Yagi, T. High-pressure structures of methane hydrate observed up to 8 GPa at room temperature. *J. Chem. Phys.* **2001**, *115*, 7066−7070.

(13) Hirai, H.; Tanaka, T.; Kawamura, T.; Yamamoto, Y.; Yagi, T. Retention of filled ice structure of methane hydrate up to 42 GPa. *Phys. Rev. B: Condens. Matter Mater. Phys.* **2003**, *68*, 172102.

(14) Hirai, H.; Machida, S.-i.; Kawamura, T.; Yamamoto, Y.; Yagi, T. Stabilizing of methane hydrate and transition to a new high-pressure structure at 40 GPa. *Am. Mineral.* **2006**, *91*, 826−830.

(15) Machida, S.-i.; Hirai, H.; Kawamura, T.; Yamamoto, Y.; Yagi, T. A new high-pressure structure of methane hydrate surviving to 86GPa and its implications for the interiors of giant icy planets. *Phys. Earth Planet. Inter.* **2006**, *155*, 170−176.

(16) Chou, I.-M.; Sharma, A.; Burruss, R. C.; Shu, J.; Mao, H.-k.; Hemley, R. J.; Goncharov, A. F.; Stern, L. A.; Kirby, S. H. Transformations in methane hydrates. *Proc. Natl. Acad. Sci. U. S. A.* **2000**, *97*, 13484−13487.

(17) Kumazaki, T.; Kito, Y.; Sasaki, S.; Kume, T.; Shimizu, H. Single-crystal growth of the high-pressure phase II of methane hydrate and its Raman scattering study. *Chem. Phys. Lett.* **2004**, *388*, 18−22.

(18) Shimizu, H.; Kumazaki, T.; Kume, T.; Sasaki, S. In situ observations of high-pressure phase transformations in a synthetic methane hydrate. *J. Phys. Chem. B* **2002**, *106*, 30−33.

(19) Machida, S.-I.; Hirai, H.; Kawamura, T.; Yamamoto, Y.; Yagi, T. Raman spectra of methane hydrate up to 86 GPa. *Phys. Chem. Miner.* **2007**, *34*, 31−35.

(20) Choukroun, M.; Grasset, O.; Tobie, G.; Sotin, C. Stability of methane clathrate hydrates under pressure: Influence on outgassing processes of methane on Titan. *Icarus* **2010**, *205*, 581−593.

(21) Tanaka, T.; Hirai, H.; Matsuoka, T.; Ohishi, Y.; Yagi, T.; Ohtake, M.; Yamamoto, Y.; Nakano, S.; Irifune, T. Phase changes of filled ice Ih methane hydrate under low temperature and high pressure. *J. Chem. Phys.* **2013**, *139*, 104701.

(22) Klug, D. D.; Tse, J. S.; Liu, Z.; Hemley, R. J. Hydrogen-bond dynamics and Fermi resonance in high-pressure methane filled ice. *J. Chem. Phys.* **2006**, *125*, 154509.

(23) Iitaka, T.; Ebisuzaki, T. Methane hydrate under high pressure. *Phys. Rev. B: Condens. Matter Mater. Phys.* **2003**, *68*, 172105.

(24) Ranieri, U.; Koza, M. M.; Kuhs, W. F.; Klotz, S.; Falenty, A.; Gillet, P.; Bove, L. E. Fast methane diffusion at the interface of two clathrate structures. *Nat. Commun.* **2017**, *8*, 1076.

(25) Del Rosso, L.; Celli, M.; Ulivi, L. New porous water ice metastable at atmospheric pressure obtained by emptying a hydrogen-filled ice. *Nat. Commun.* **2016**, *7*, 13394.

(26) Amos, D. M.; Donnelly, M.-E.; Teeratchanan, P.; Bull, C. L.; Falenty, A.; Kuhs, W. F.; Hermann, A.; Loveday, J. S. A Chiral Gas−Hydrate Structure Common to the Carbon Dioxide−Water and Hydrogen−Water Systems. *J. Phys. Chem. Lett.* **2017**, *8*, 4295−4299.

(27) Baumert, J.; Gutt, C.; Shpakov, V. P.; Tse, J. S.; Krisch, M.; Müller, M.; Requardt, H.; Klug, D. D.; Janssen, S.; Press, W. Lattice dynamics of methane and xenon hydrate: Observation of symmetry-avoided crossing by experiment and theory. *Phys. Rev. B: Condens. Matter Mater. Phys.* **2003**, *68*, 174301.

(28) Schober, H.; Itoh, H.; Klapproth, A.; Chihaia, V.; Kuhs, W. F. Guest-host coupling and anharmonicity in clathrate hydrates. *Eur. Phys. J. E* **2003**, *12*, 41−49.

(29) Bezacier, L.; Le Menn, E.; Grasset, O.; Bollengier, O.; Oancea, A.; Mezouar, M.; Tobie, G. Experimental investigation of methane hydrates dissociation up to 5GPa: Implications for Titan's interior. *Phys. Earth Planet. Inter.* **2014**, *229*, 144−152.

(30) Loveday, J. S. *High-Pressure Crystallography*; Katrusiak, A., McMillan, P., Eds.; Springer: Netherlands, Dordrecht, 2004; pp 69−80.

(31) Giannozzi, P.; Baroni, S.; Bonini, N.; Calandra, M.; Car, R.; Cavazzoni, C.; Ceresoli, D.; Chiarotti, G. L.; Cococcioni, M.; Dabo, I.; et al. QUANTUM ESPRESSO: A modular and open-source software project for quantum simulations of materials. *J. Phys.: Condens. Matter* **2009**, *21*, 395502.

(32) Dammak, H.; Chalopin, Y.; Laroche, M.; Hayoun, M.; Greffet, J.-J. Quantum thermal bath for molecular dynamics simulation. *Phys. Rev. Lett.* **2009**, *103*, 190601.

(33) Bronstein, Y.; Depondt, P.; Finocchi, F.; Saitta, A. M. Quantum-driven phase transition in ice described via an efficient Langevin approach. *Phys. Rev. B: Condens. Matter Mater. Phys.* **2014**, *89*, 214101.

(34) Bronstein, Y.; Depondt, P.; Bove, L. E.; Gaal, R.; Saitta, A. M.; Finocchi, F. Quantum versus classical protons in pure and salty ice under pressure. *Phys. Rev. B: Condens. Matter Mater. Phys.* **2016**, *93*, 024104.

(35) Brieuc, F.; Bronstein, Y.; Dammak, H.; Depondt, P.; Finocchi, F.; Hayoun, M. Zero-point energy leakage in quantum thermal bath molecular dynamics simulations. *J. Chem. Theory Comput.* **2016**, *12*, 5688−5697.

(36) Ceriotti, M.; Manolopoulos, D. E.; Parrinello, M. Accelerating the convergence of path integral dynamics with a generalized Langevin equation. *J. Chem. Phys.* **2011**, *134*, 084104.

(37) Kuhs, W. F.; Staykova, D. K.; Salamatin, A. N. Formation of methane hydrate from polydisperse ice powders. *J. Phys. Chem. B* **2006**, *110*, 13283−13295.

(38) Datchi, F.; Dewaele, A.; Le Godec, Y.; Loubeyre, P. Equation of state of cubic boron nitride at high pressures and temperatures. *Phys. Rev. B: Condens. Matter Mater. Phys.* **2007**, *75*, 214104.

(39) Dewaele, A.; Torrent, M.; Loubeyre, P.; Mezouar, M. Compression curves of transition metals in the Mbar range: Experiments and projector augmented-wave calculations. *Phys. Rev. B: Condens. Matter Mater. Phys.* **2008**, *78*, 104102.

(40) Bove, L. E.; Gaal, R.; Raza, Z.; Ludl, A.-A.; Klotz, S.; Saitta, A. M.; Goncharov, A. F.; Gillet, P. Effect of salt on the H-bond symmetrization in ice. *Proc. Natl. Acad. Sci. U. S. A.* **2015**, *112*, 8216−8220.

(41) Calvo, F.; Van-Oanh, N.-T.; Parneix, P.; Falvo, C. Vibrational spectra of polyatomic molecules assisted by quantum thermal baths. *Phys. Chem. Chem. Phys.* **2012**, *14*, 10503−10506.

(42) Perdew, J. P.; Burke, K.; Ernzerhof, M. Generalized gradient approximation made simple. *Phys. Rev. Lett.* **1996**, *77*, 3865.

(43) Grimme, S. Semiempirical GGA-type density functional constructed with a long-range dispersion correction. *J. Comput. Chem.* **2006**, *27*, 1787−1799.

(44) Ceriotti, M.; More, J.; Manolopoulos, D. E. i-PI: A Python interface for ab initio path integral molecular dynamics simulations. *Comput. Phys. Commun.* **2014**, *185*, 1019.

(45) Hiratsuka, M.; Ohmura, R.; Sum, A. K.; Yasuoka, K. Vibrational modes of methane in the structure H clathrate hydrate from ab initio molecular dynamics simulation. *J. Chem. Phys.* **2012**, *137*, 144306.

(46) Chen, P.-N.; Zha, C.-S.; Chen, X.-J.; Shu, J.; Hemley, R. J.; Mao, H.-k. Raman study of phase transitions in compressed methane using moissanite anvil cells. *Phys. Rev. B: Condens. Matter Mater. Phys.* **2011**, *84*, 104110.

(47) Bini, R.; Pratesi, G. High-pressure infrared study of solid methane: Phase diagram up to 30 GPa. *Phys. Rev. B: Condens. Matter Mater. Phys.* **1997**, *55*, 14800.

(48) Savage, M.; Da Silva, I.; Johnson, M.; Carter, J. H.; Newby, R.; Suyetin, M.; Besley, E.; Manuel, P.; Rudić, S.; Fitch, A. N.; et al. Observation of binding and rotation of methane and hydrogen within a functional metal−organic framework. *J. Am. Chem. Soc.* **2016**, *138*, 9119−9127.

Supporting information for: Orientational Ordering, Locking-in, and Distortion of CH_4 molecules in Methane Hydrate III under High Pressure

Sofiane Schaack,† Umbertoluca Ranieri,‡,¶ Philippe Depondt,† Richard Gaal,¶ Werner F. Kuhs,§ Andrzej Falenty,§ Philippe Gillet,¶ Fabio Finocchi,*,† and Livia E. Bove*,‖,¶

†*Sorbonne Université, CNRS UMR 7588, Institut des Nanosciences de Paris ,INSP, 75005 Paris, France*

‡*Institut Laue-Langevin, 71, avenue des Martyrs, CS 20156, 38042 Grenoble, Cedex 9, France*

¶*EPSL, ICMP, École polytechnique fédérale de Lausanne (EPFL), Station 3, CH-1015 Lausanne, Switzerland*

§*GZG Abt. Kristallographie, Universität Göttingen, Goldschmidtstrasse 1, 37077, Göttingen, Germany*

‖*Sorbonne Université, CNRS UMR 7590, Institut de minéralogie, de physique des matériaux et de cosmochimie, IMPMC, 75005 Paris, France*

E-mail: fabio.finocchi@sorbonne-universite.fr; livia.bove@sorbonne-universite.fr

Phone: +33 (0)144275116; +33 (0)144275219

Experimental details

Synchrotron radiation X-ray diffraction in DAC

We have measured the structure of D_2O:CH_4 clathrate at ambient temperature between 20 and 42 GPa at the ID27 beamline at ESRF. The wavelength was 0.3738Å and the 2θ range from 0 to 20.3°, the beam size was $\approx$ 3 microns. CeO_2 was used to calibrate the instrument. Two-dimensional diffractograms were recorded and integrated using the Dioptas program.[S1]The diamond signal had been masked directly in the 2D diffractograms. The sample was loaded together with a small Au pressure calibrant[S2] at liquid nitrogen temperature in a diamond anvil cell, as described in the Methods section of the main text. The pressure was increased to approximately 3 GPa at the loading temperature, and then the DAC was warmed up. Prior to the structural measurement the sample was characterized by Raman spectroscopy from 3 to 22 GPa (part of these spectra are reported on Figures S5 and S6). The compression rate was typically 3 GPa/hour. The diffraction patterns as a function of pressure are reported in Figure S1. The brightest signal observed is from ice VII. Four peaks are clearly visible (10.05, 12.3, 14.25 and 17.45°) at the lower pressure and disperse following the expected equation of state of ice VII. The remaining four peaks can be assigned to the sample and are compatible with the structure reported in literature for MHIII (by Loveday et al.[S3]) and used in our simulations. We do not observe any sudden change of the parameters with pressure, suggesting that the sample is stable in the explored pressure range.

Raman scattering experiments in DAC

In Figure S2 we show a representative set of the Raman spectra of the sample that have been used in the analysis presented in the paper. In order of increasing frequency, the lattice mode, the CH rocking mode, the OD stretching mode and the CH stretching modes are clearly visible, together with parasitic signals of the N_2 vibron and the second order signal

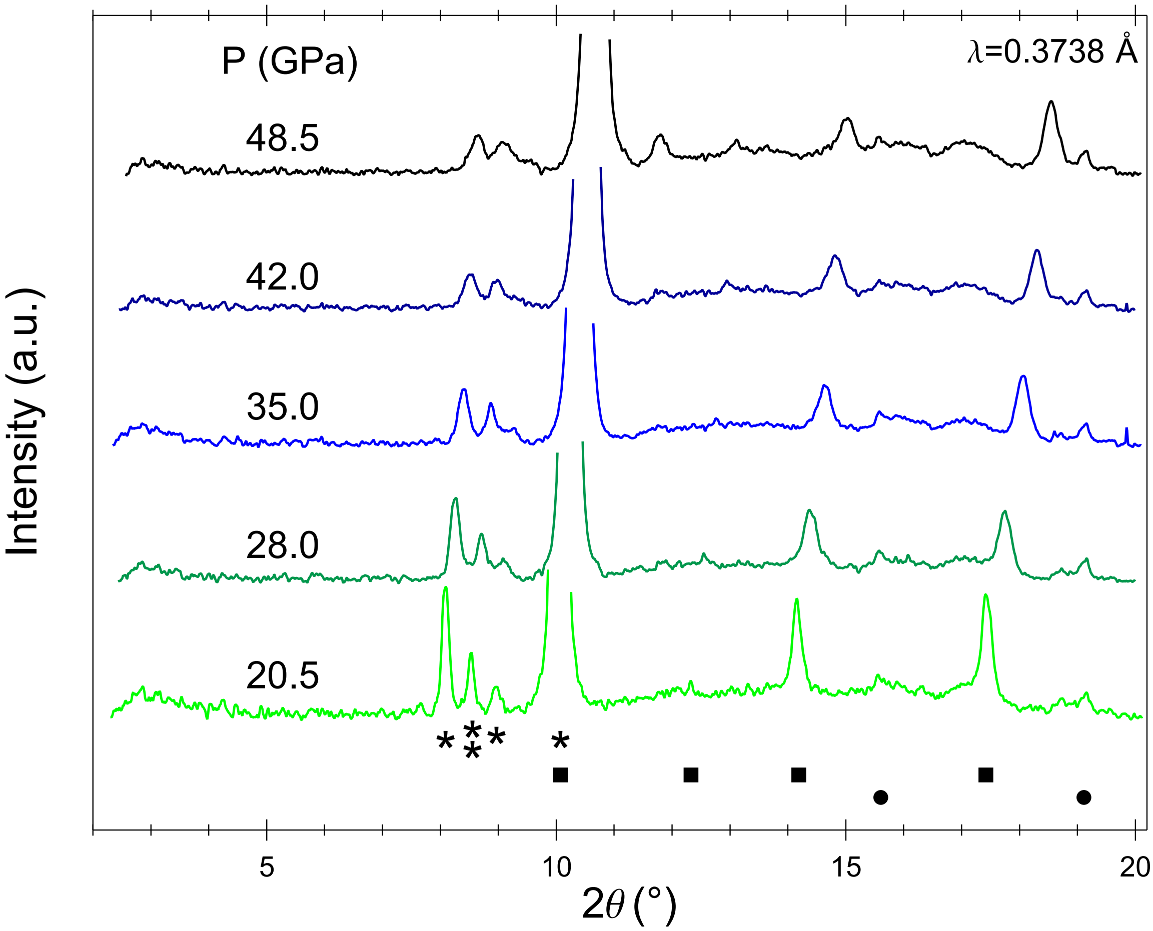

Figure S1: XRD patterns of the sample at 300 K and different pressures, after subtraction of a smooth polynomial background. Patterns were measured at ID27 (ESRF) in diamond anvil cell. Stars indicate observed reflections of MH-III (indexable as 112, 211, 202, 103 and 301 in the orthorhombic Imcm space group). Squares indicate the 110, 111, 200 and 211 reflections of ice VII. Points indicate two weak peaks whose positions do not change with pressure.

of diamond. The former is sufficiently narrow to be removed by assuming a single spectral line plus quadratic background in a narrow frequency range, while the later was removed with the help of background spectra measured on the gasket near the edge of the sample chamber. The method has been described in ref S4.

Figure S3 shows the pressure dependence of the OD stretching mode frequencies both in the sample and in pure D_2O ice VII. In the band of the sample associated with the OD

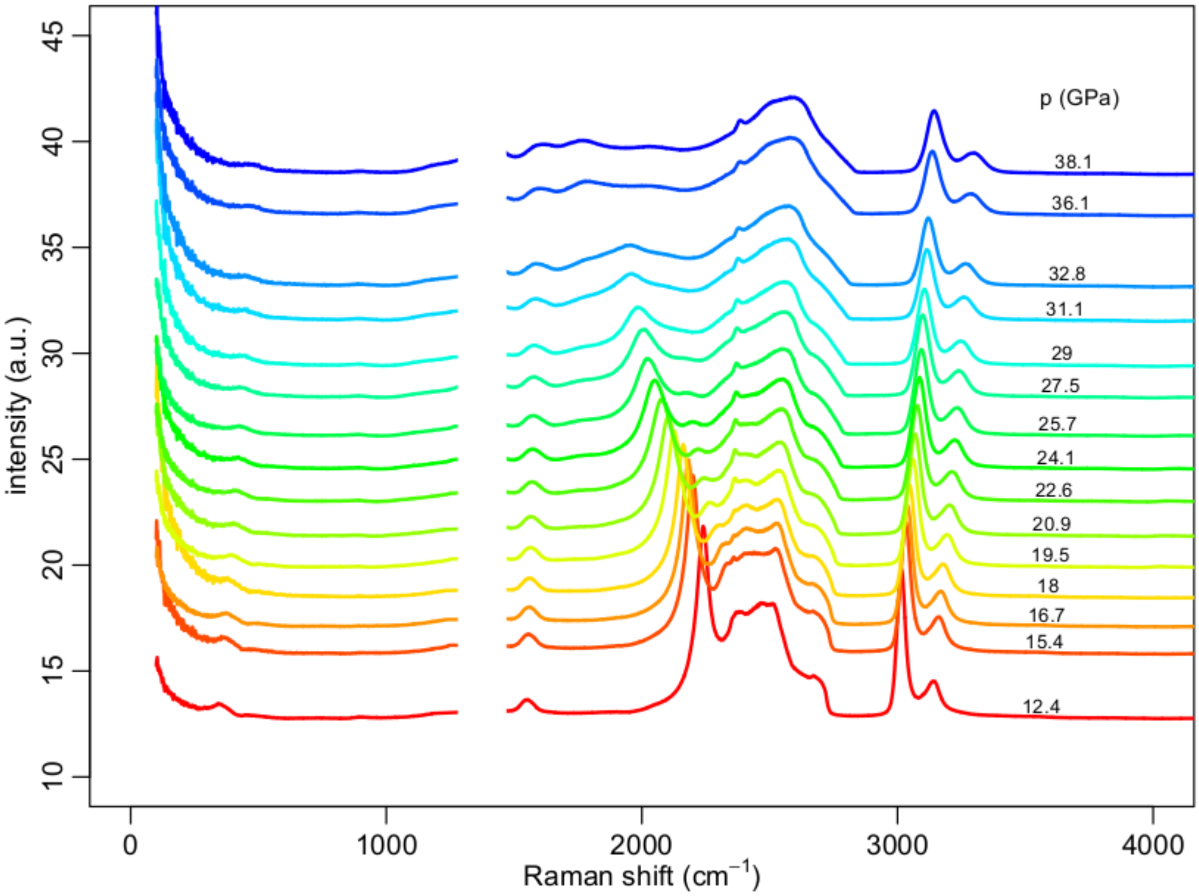

Figure S2: Raw experimental high-resolution Raman spectra of the sample collected along the 295 K isotherm between 12 GPa and 40 GPa.

stretching mode we could reasonably identify two components only, and consider the lowest frequency one the most reliable as the one with the largest amplitude. As can be seen in Figure S3 lowest-frequency OD stretching mode crosses the frequency of the CH_4 rocking mode at around 45 GPa. Although frequencies are roughly equal, in the hydrate they are very difficult identify as their amplitude drops and they become broader. We believe that this is due to the increasing coupling of the host stretching mode to the rocking mode of the guest in the structure. The naturally occurring OD stretching mode degeneracy favors this coupling.

In Figure S4 we show representative Raman spectra of the symmetric and asymmetric stretching modes of CH_4 in the methane hydrate. We have found that the signal in this

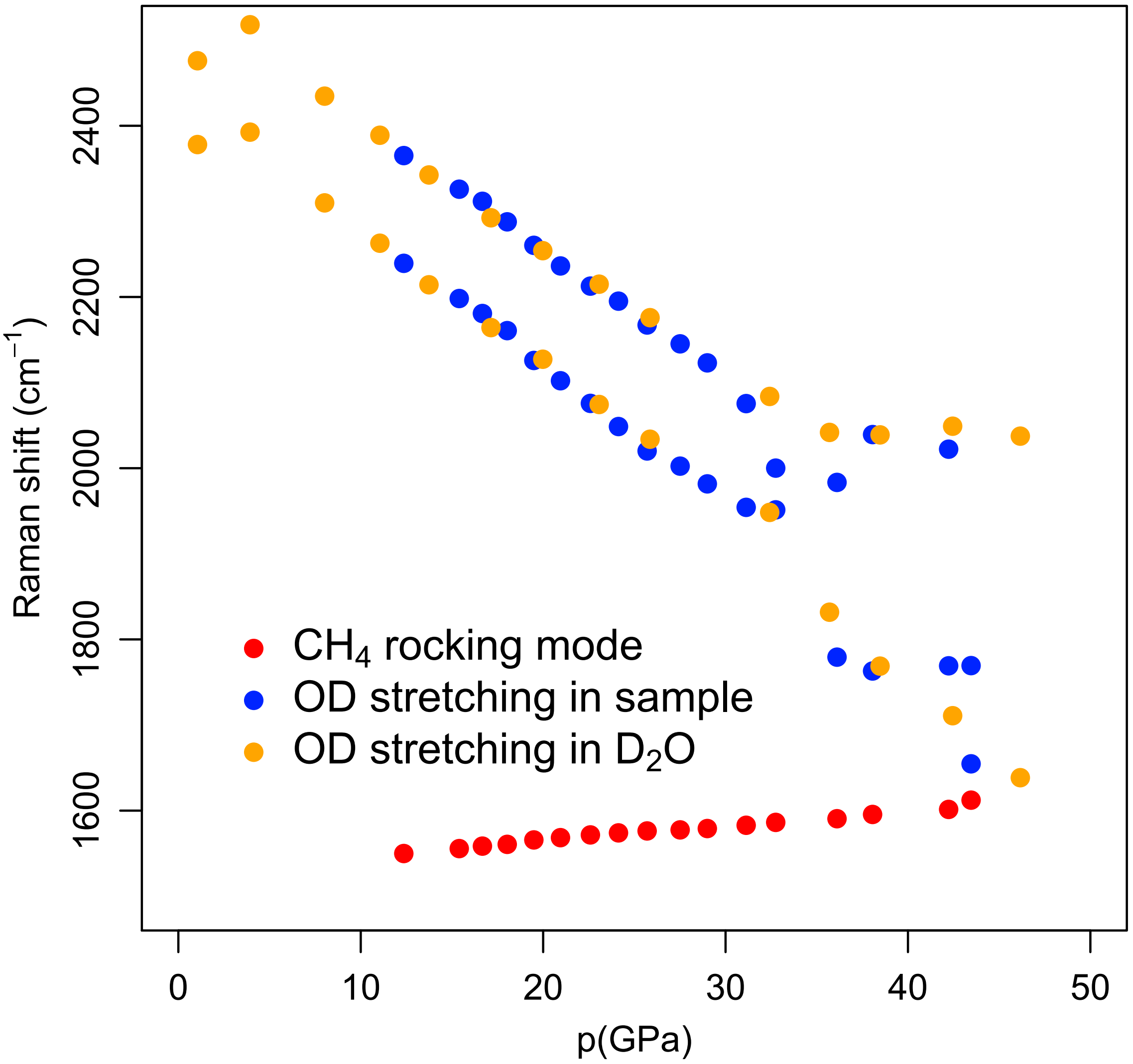

Figure S3: Pressure dependence of the Raman shift of the CH rocking mode (red), the OD stretching mode in the sample (blue) and the OD stretching mode in pure D_2O ”ice VII” (orange) as a function of pressure.

frequency range could be satisfactorily fitted with two asymmetric Pearson VII lineshapes of the form :

$$I(f) = A\left(1+\frac{(f-f_0)^2}{w^2m}\right)^{-m}$$

where A is the amplitude of the line, f_0 its position and w its width in all fitting of our Raman spectra. The parameter m interpolates between Lorentzian ($m = 1$) and Gaussian line shape ($m = \infty$). The asymmetry is introduced by letting the width vary according to a sigmoidal function : $w(f) = \frac{2w_0}{1+exp(a(f-f_0))}$ where w_0 is the width of the line and a the asymmetry parameter. The sign of a determines which way the line will be skewed : for $a = 0$ the function gives a symmetric line with width equal to w_0. We systematically tested whether the asymmetry is significant.

We have tried fitting the spectra using two asymmetric or three symmetric Pearson VII lines. The residuals in the two cases were similar, but since some fit parameters in the case of three symmetric lines varied in an uncontrolled fashion with pressure, we opted for the two line fits with asymmetric lineshapes which give results in agreement with literature data[S5,S6] in the low pressure range. The frequency determination is robust and the quality of the fit is high enough to assure an error bar lower than the point size.

Finally, we investigated the pressure dependence of the CH stretching mode and of the CH_4 rocking mode between 3 and 22 GPa during a dedicated Raman experiment. No ruby was used during this loading; pressure was evaluated with a precision of 0.5 GPa based on the measured shift of the diamond Raman signal measured in the center of the culet, and comparing this to earlier runs when both diamond Raman and ruby fluorescence were measured. Again no splitting of the stretching peaks is observed over the full investigated pressure range, as clearly shown by Figure S5. The rocking mode peak was fitted using a Gaussian distribution plus a linear background, as shown in Figure S6. Even though a quantitative calibration of the Raman intensity was not performed, it is clear that the area of the rocking mode peak rises considerably as pressure is increased between 3 and 15-20 GPa, a behavior that could be ascribed to the progressive locking-in of the CH_4 molecule rotational dynamics in the hydrate.

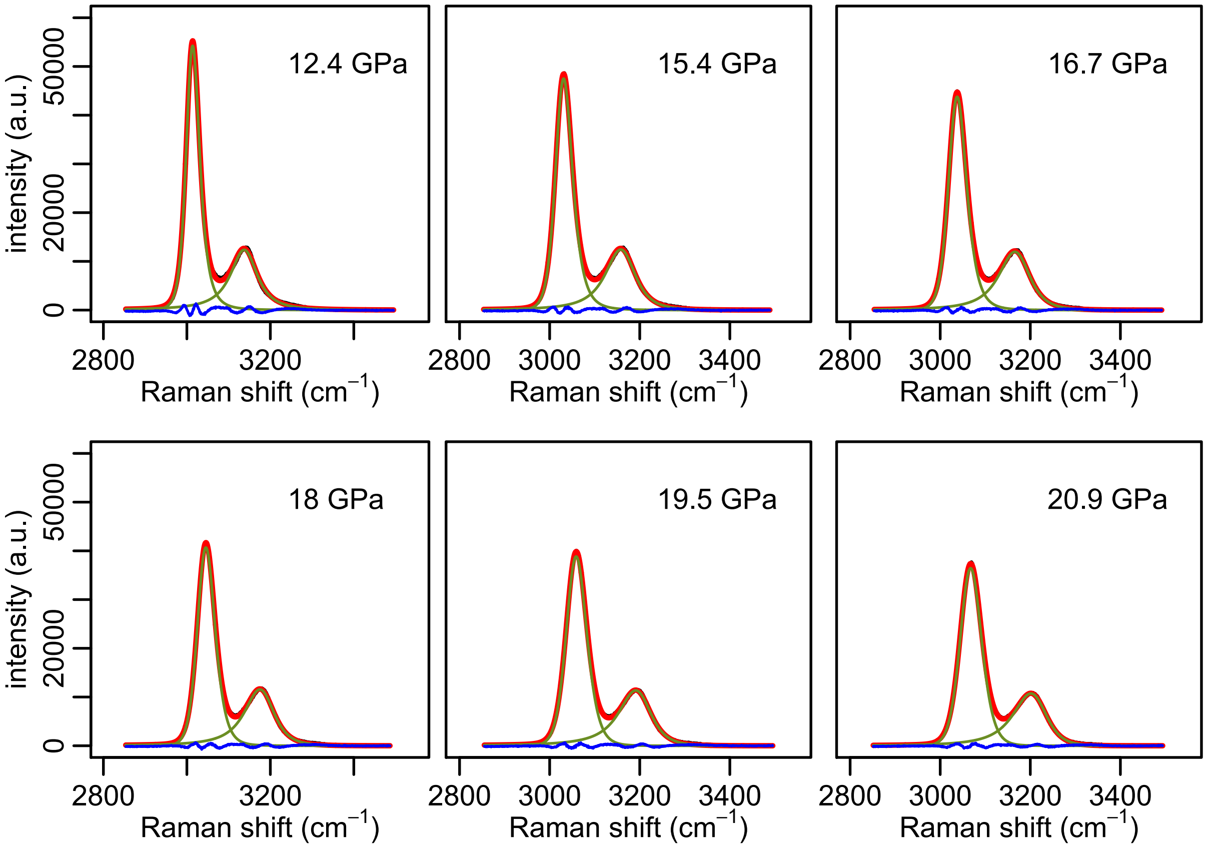

Figure S4: CH stretching modes measured in CH_4:D_2O at different pressures. Black dots are experimental data after a single quadratic background was subtracted, green lines are the two asymmetric Pearson VII lines fitted, red line is the sum of these two and blue is the residuum.

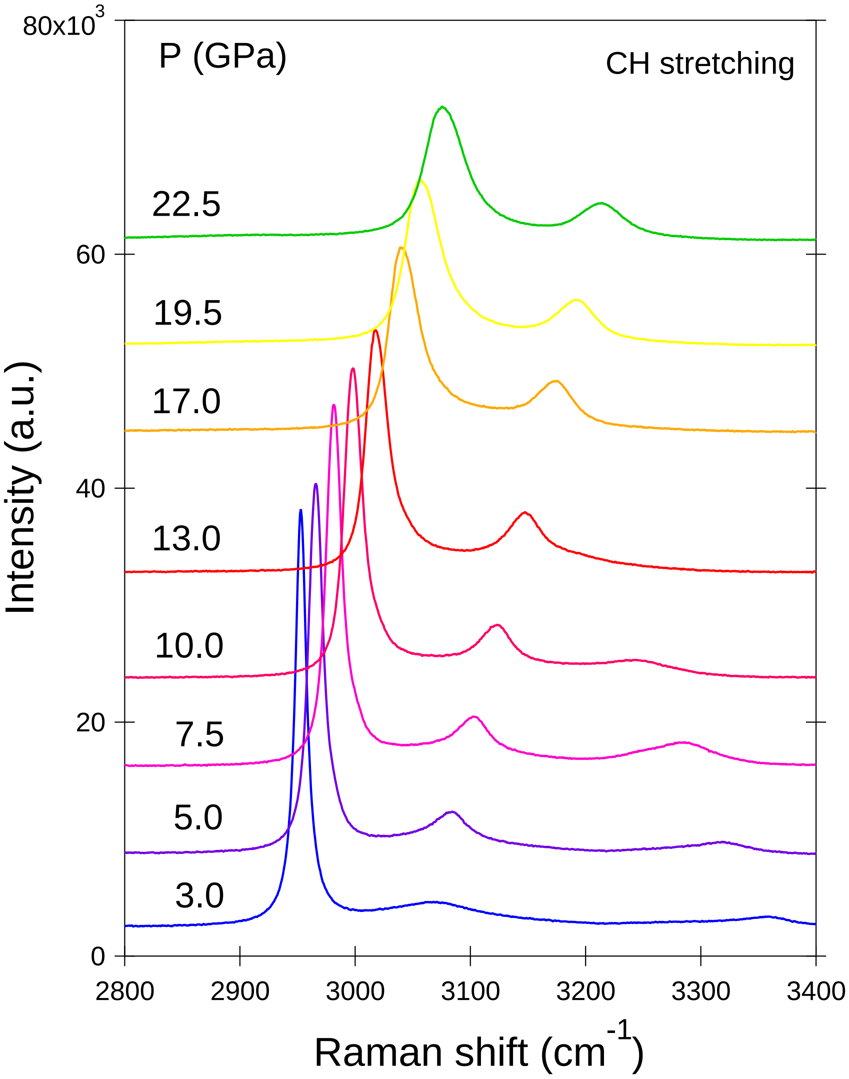

Figure S5: Experimental high-resolution Raman spectra of the CH stretching mode of the sample at different pressures. No indications of peaks splitting as claimed to be observed at approximately 15 GPa in refs S5–S7 is observed.

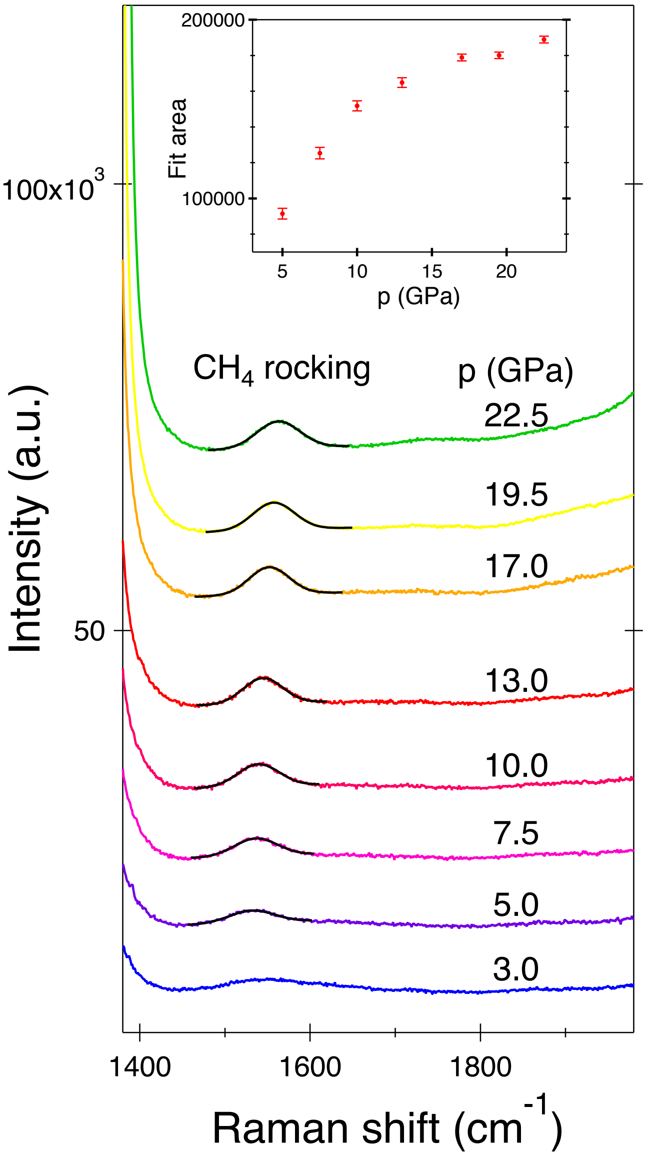

Figure S6: Experimental high-resolution Raman spectra of the CH_4 rocking mode of the sample at different pressures. A fit containing a Gaussian distribution and a linear background is also shown. In the inset we report the pressure dependence of the area of the Gaussian of the fit. The intensity increase at 1400 cm-1 corresponds to the diamond signal

Lattice parameter

Van der Waals interactions

Variable-cell static calculations (T=0K) of MH-III $(D_2O)_2{:}CH_4$ were done in order to obtain the lattice parameters of the system at a given pressure. To be the more accurate, these quantities were measured both with and without Van der Waals correction (Grimme D2) to the simulations and were compared with experimental values present in ref S7,S8. Figure S7a shows the lattice parameters as a function of pressure from molecular dynamics simulation of the system taking values from the static calculations. Resulting values are gathered in Table S1.

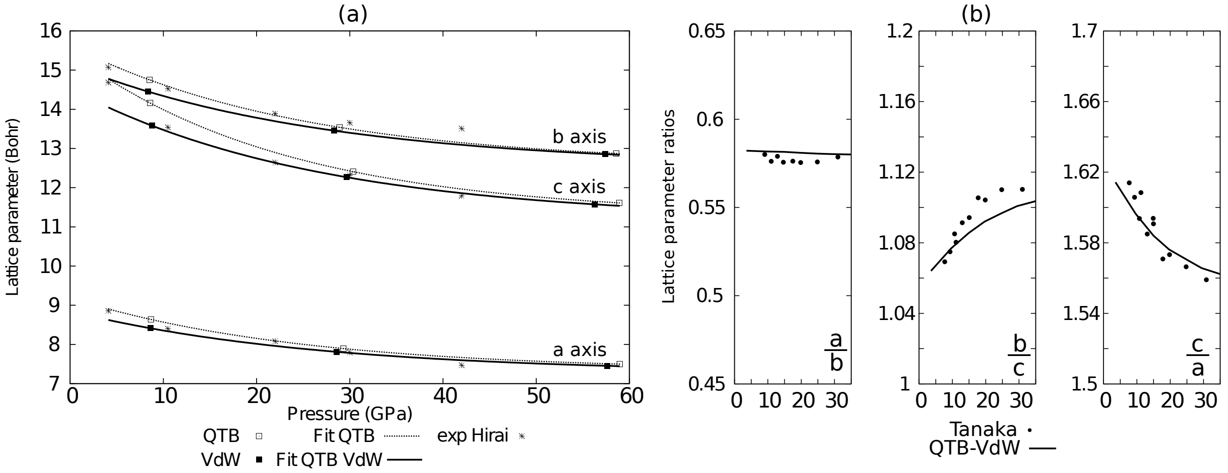

Figure S7: (a)Lattice parameter obtained by static relaxation calculations. Pressure values computed from dynamic calculations, taking into account the kinetic pressure. (b) Lattice parameter ratios (a/b, b/c, c/a) as a function of pressure. Dot : Experimental results from ref S7,S8, Dashed line QTB-VdW simulations.

The lattice parameters as well as the compressibility and equation of state of MH-III are better described with the Grimme's correction, in particular above 10 GPa. Thus, the Grimme D2 correction was used during the simulations.

Table S1: Lattice parameters a,b, and c as a function of pressure calculated by variable cell relaxation at T=0K. Pressure values correspond to the pressure obtained during MD simulations at T=300K, taking into account kinetic pressure.

Pressure	a(Å)	b(Å)	c(Å)
3.6	4.67654	7.93279	7.86146
9.6	4.45232	7.64756	7.18739
14.9	4.33522	7.45246	6.9209
19.7	4.25363	7.31492	6.73801
24.9	4.18821	7.20861	6.60127
29.4	4.13338	7.12008	6.51846
35.3	4.08664	7.04293	6.39818
40.7	4.04489	6.97387	6.31848
46.2	4.00616	6.91058	6.24858
51.9	3.97275	6.85189	6.18502
62.9	3.92046	6.76199	6.06495

Change of compressibility

Results reveal a strong compressibility anisotropy in MH-III, with the c lattice parameter being softer than a an b. Furthermore, the lattice parameters ratio evolutions with pressure (Figure S7b) show that the c axis presents a stronger change of compressibility than the two other axes with increasing pressure.

This change occurs around 20-25 GPa and has to be related with the observed guest-host interaction enhancement and mode coupling discussed in the main text. Moreover, this is a direct consequence of methane ordering in methane hydrate happening at the same pressure and giving rise to the observed A-B-A-B... stacking along b and c.

Methane - water distances

As shown in Figure S8 the H-O and D-C distances are longer than the typical H-bond length. This prevents the methane molecule from forming strong H-bonds with the ice frame.

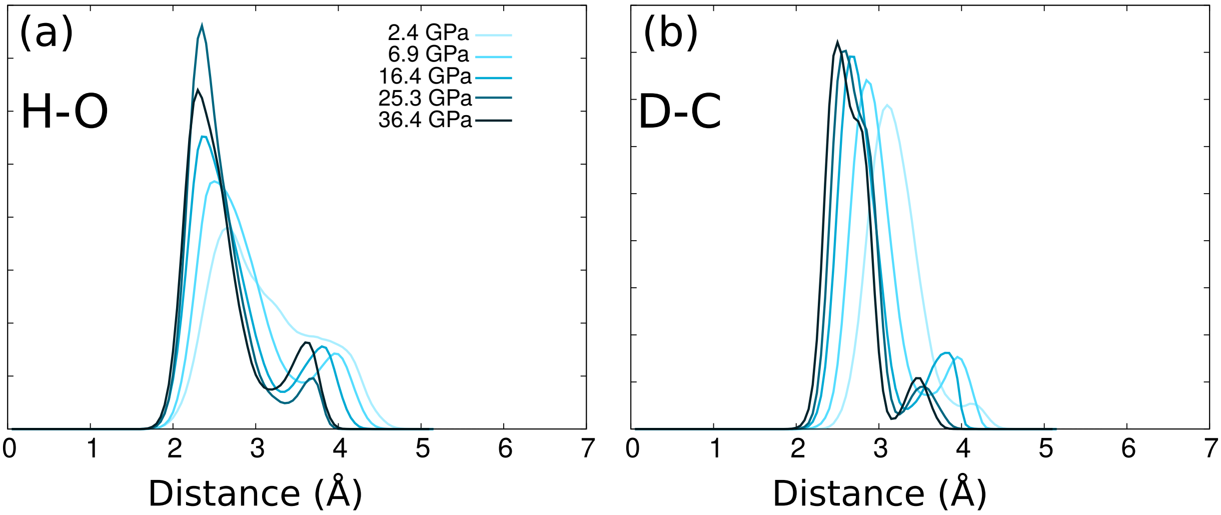

Figure S8: Simulated pair correlation function : (a)H-O and (b)D-C.

Methane - Methane distances

The evolution of the C-C distances with respect to the pressure (Figure S9) present a change of slope at ∼ 30 GPa. The related methane molecules which present the shortest C-C distance are arranged along the *c* axis. Therefore we can link this change of slope to the noticeable change of compressibility of MH-III along the same axis (Figure S7).

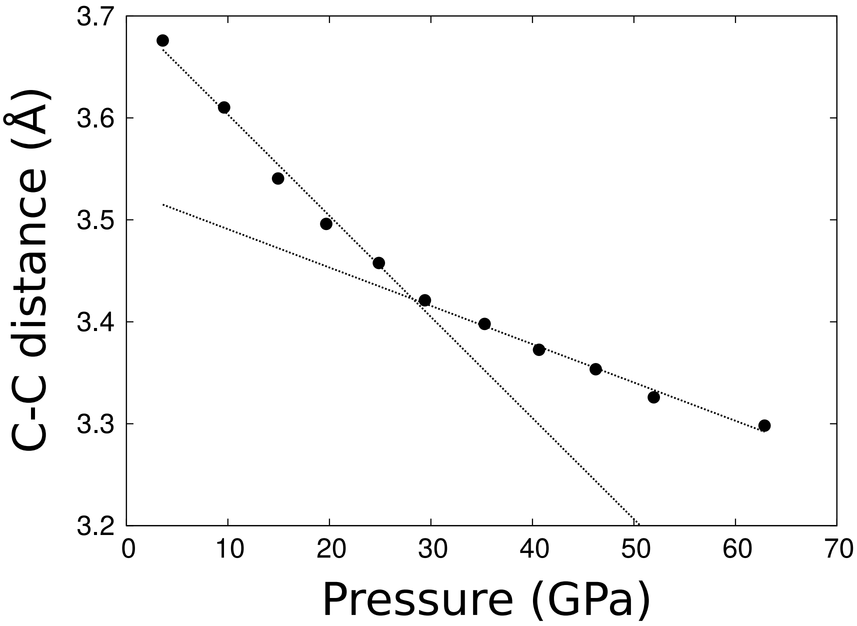

Figure S9: C-C (first neighbour) distance with respect to the pressure.

Simulation method

The quantum thermal bath

Hydrate systems are mainly composed of hydrogen atoms which are light particles with a non-negligible De Broglie thermal wavelength ($\lambda_{\mathbf{th}} \sim 1$Å). Thus, such systems can exhibit processes driven by nuclear quantum effects (NQE), following the example of the ice VII-X transition.[S9,S10] Therefore, in this study, nuclei were treated by the so-called Quantum Thermal Bath Molecular Dynamics[S11] (QTB-MD), which gives access to NQE such as zero-point energy and tunneling effects.

Based on the Langevin description of brownian motions, this semi-classical method couples a classical system with a quantum bath through the equation of motion:

$$m_i \frac{d^2 x_i}{dt^2} = f(x_i) - \gamma m_i \frac{dx_i}{dt} + R(t) \tag{1}$$

where m_i is the mass of particle x_i which is submitted to the inter-atomic forces $f(x_i)$ computed by density functional theory (DFT), γ the friction coefficient, $R(t)$ a stochastic force.

In QTB-MD the stochastic force R(t) is a colored noise, whose Fourier transform $\tilde{R}(\omega)$ is linked with the friction coefficient γ through the quantum fluctuation-dissipation theorem[S12] :

$$|\tilde{R}(\omega)|^2 = 2m_i\gamma\hbar\omega \left[\frac{1}{2} + \frac{1}{\exp(\frac{\hbar\omega}{K_bT} - 1)}\right] \tag{2}$$

with K_b the Boltzmann constant.

Owing to the zero point energy $\frac{\hbar\omega}{2}$ and the Bose-Einstein distribution $\frac{\hbar\omega}{exp(\frac{\hbar\omega}{K_bT}-1)}$ the bath insures the correct description of the energy distribution in case of a harmonic potential. For anharmonic systems, QTB-MD is an approximation which gives rise in particular to zero-point energy leakage (ZPEL),[S13] but has proven useful and reliable in several cases.[S10,S14,S15] Alternative methods such as RPMD[S16] or CMD[S17] are computationaly expensive while QTB-MD gives access to dynamical properties (time correlation function) with almost no additionnal cost to the DFT calculations.

PI+GLE

In addition to QTB, we performed PIMD simulations with a generalized Langevin equation thermostat (PI+GLE) described in ref. S18,S19 . Doing so, we have access to vibrational spectra through the velocity autocorrelation function (VACF) as given by the QTB, while quantum distributions are extracted from PIMD trajectories. Figure S10 presents the convergence of both the kinetic and potential energy of the system with respect to the number of beads.

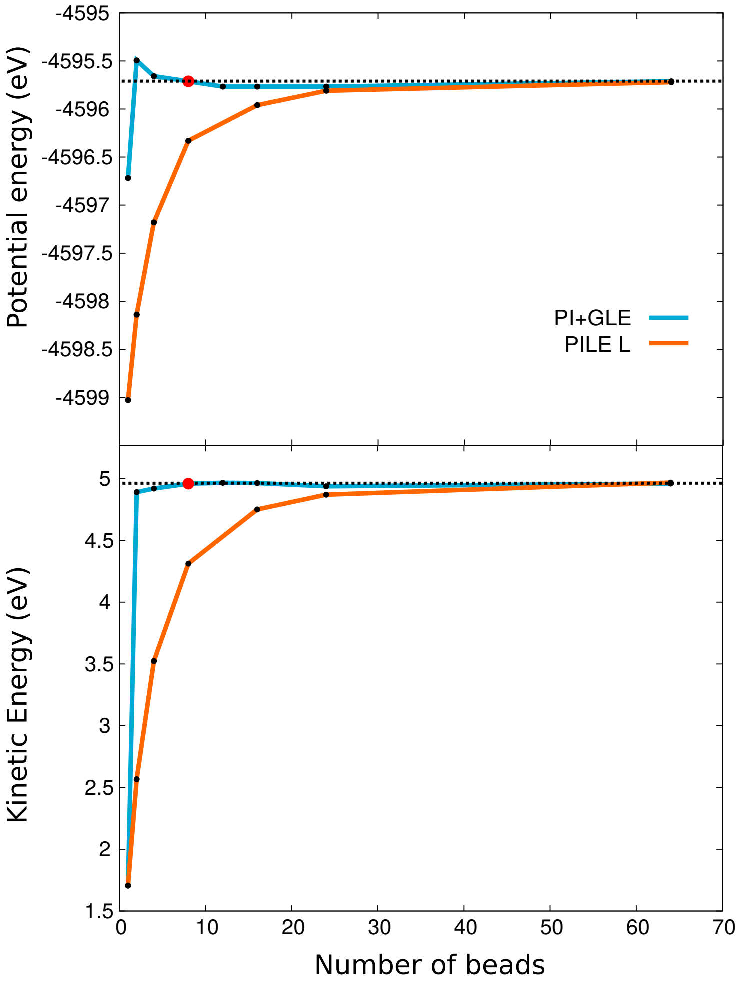

Figure S10: Potential and Kinetic energies convergence with the number of beads for the PI+GLE and PILE L thermostats.

Thanks to the GLE thermostat the simulations converged for eight beads where the classical Langevin PILE L[S19] converged for higher values. However, it was necessary to decrease the integration step for the PI+GLE to converge to the same energy values as PILE L. Thus, we used the GLE thermostat with eight beads and a timestep of $dt = 0.24189$ fs.

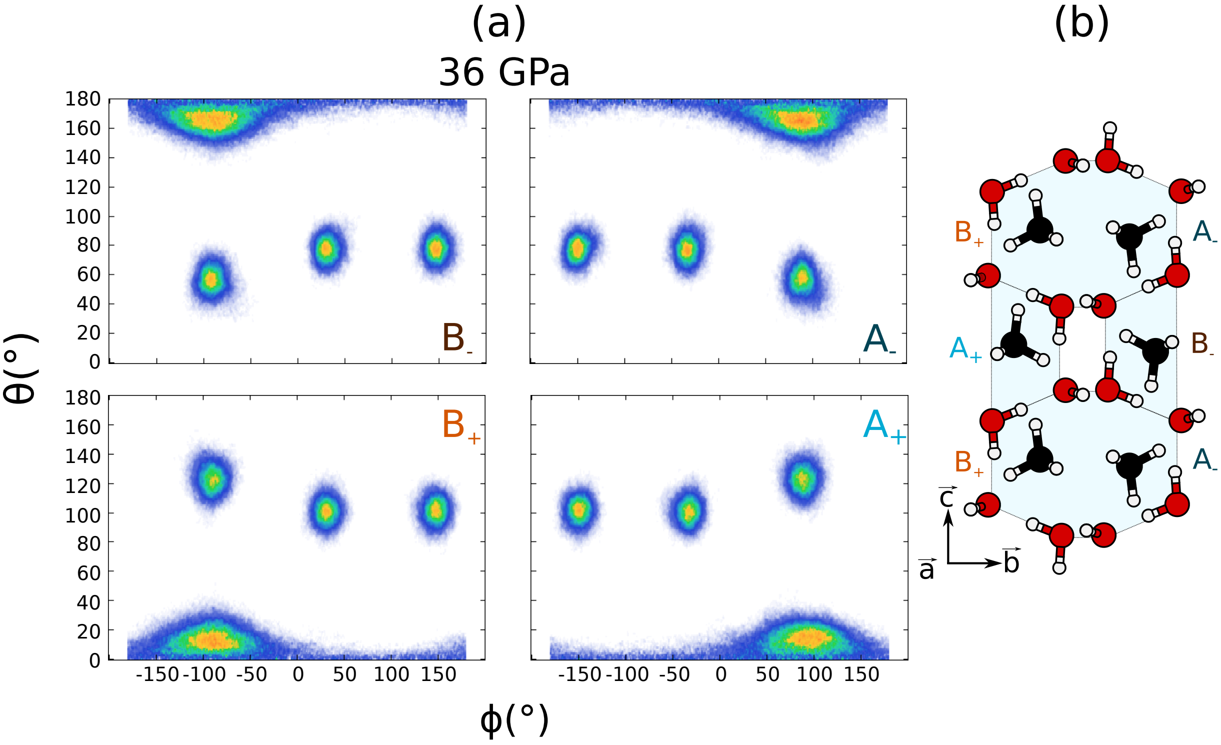

Figure S11: (a) Methane molecule configurations at 36 GPa. (b) Sketch of the corresponding configurations in the structure.

Methane rotation

Figure S11a presents four OPDF at 36 GPa corresponding to the four configurations methane molecule can adopt at high pressure and which have been sketched in Figure S11b . In order to better estimate the pressure dependence, the OPDF p(θ,ϕ) can be integrated either on ϕ or θ to yield marginal distributions P(θ) and P(ϕ), respectively. These are shown in Figure S12. P(θ) clearly evolves as a function of pressure up to P=25GPa and then remains stable, while P(ϕ) changes much less. This is consistent with a locking-in of the dynamical disorder for angle θ as described in the main text.

Methane distortion

While increasing the pressure, the methane molecules undergoe a distortion through a change of their tetrahedral angles. The distorted angles are those for which the H-C-H bisector

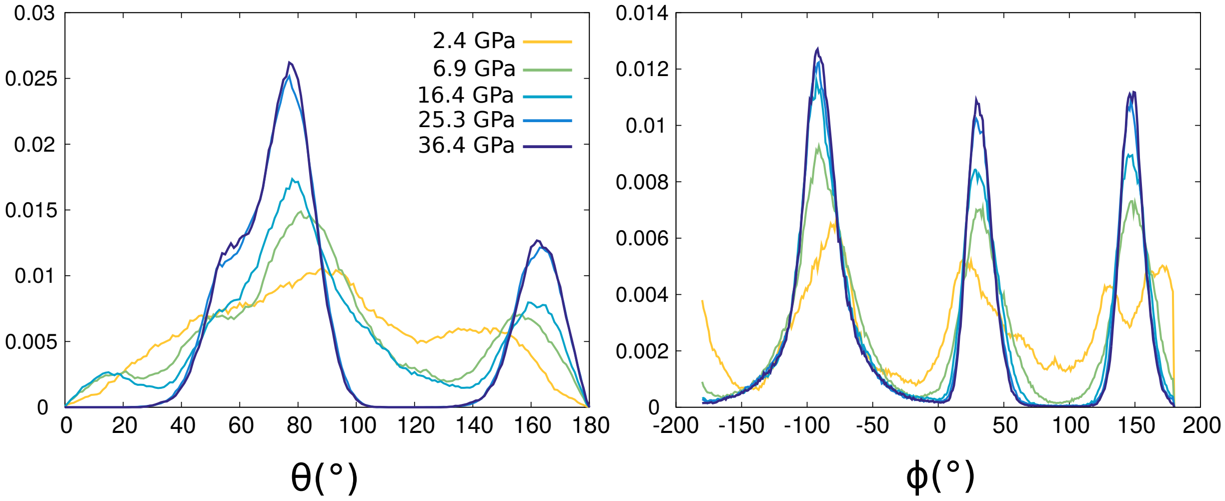

Figure S12: Methane orientational marginal probability distributions P(θ) (left) and P(ϕ) (right)

is parallel to the c axis. As the molecular dynamics present reorientational motion, we calculated the tetrahedral angles probability distribution functions in the molecular frame, as shown in Figure S13a.

CH stretching mode

Figure S13b presents the CH stretching vibrational modes spectra calculated by Fourier transform of the velocity autocorrelation function, and the frequencies calculated within the harmonic approximation at T=0K. The static calculations show a lift of degeneracy of ν_1 and ν_3 upon compression. While analysing the molecular dynamics (at T=300K), this lift of degeneracy is no more observed but a broadening of the peaks of the simulated spectra appears as pressure increases. Reorientational motion of the methane molecules along with interaction enhancement with the ice frame prevents the lift of degeneracy to be resolved within the statistical noise.

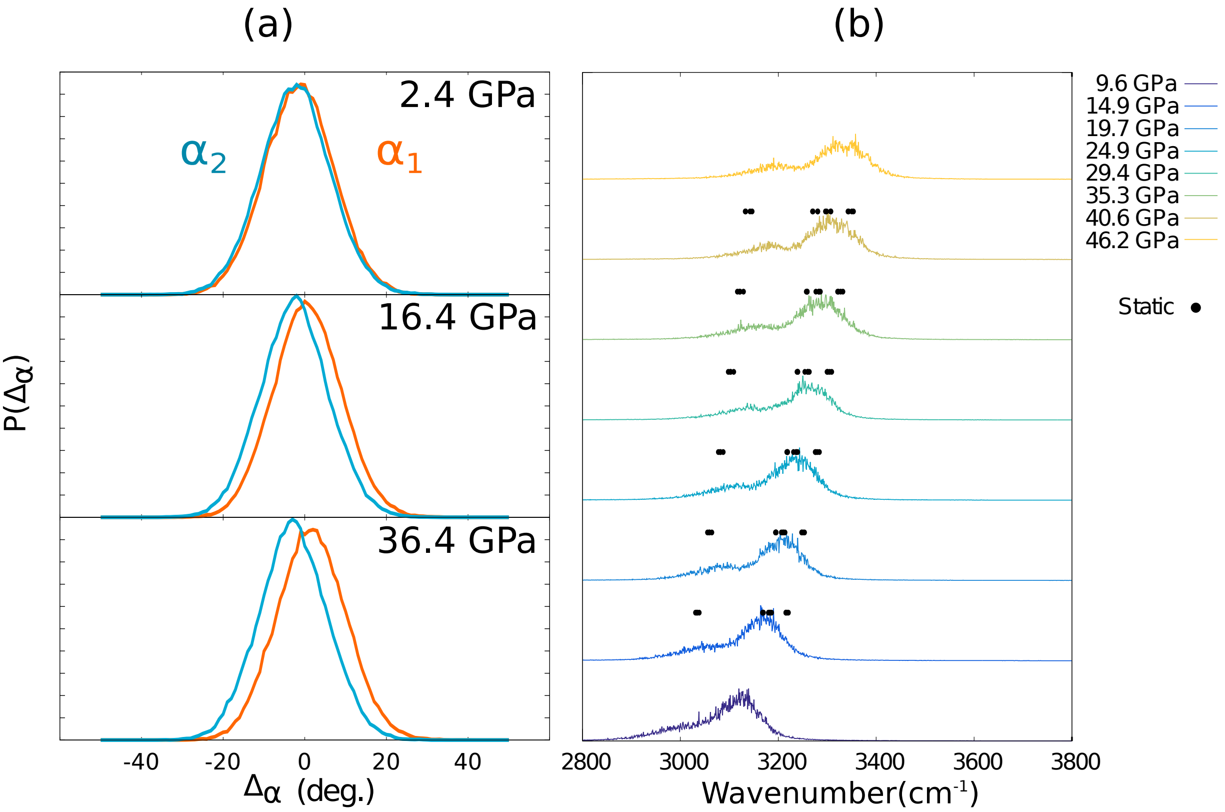

Figure S13: (a) Simulated probability distribution of the α tetrahedral angles of the methane molecules. (b) Lines : Fourier transform of the C-H autocorrelation function; Dots : Methane stretching modes obtained within the harmonic approximation.

Resonance

Figure S14 shows the vibrational spectra of both the deuterated and protonated frame MHIII obtained by Fourier transform of the velocities autocorrelation functions. In CH_4:D_2O, at low pressure the methane rocking mode is almost isolated. When increasing the pressure we can observe the flattening of the OD stretching modes due to the progressive H-bonds symmetrisation transition. Moreover, the OD stretching modes are downshifted. This gives rise to the progressive mode coupling and eventually the resonance between the CH_4 rocking and OD stretching modes, occuring at $\sim$ 20-25 GPa in CH_4:D_2O. In contrast, in the protonated frame MHIII (CH_4:H_2O), methane rocking and H_2O bending modes vibrate at the same frequency even at the lower pressure, while the OD stretching mode vibrate at much higher frequencies. Therefore, in the protonated system a coupling is already occuring at

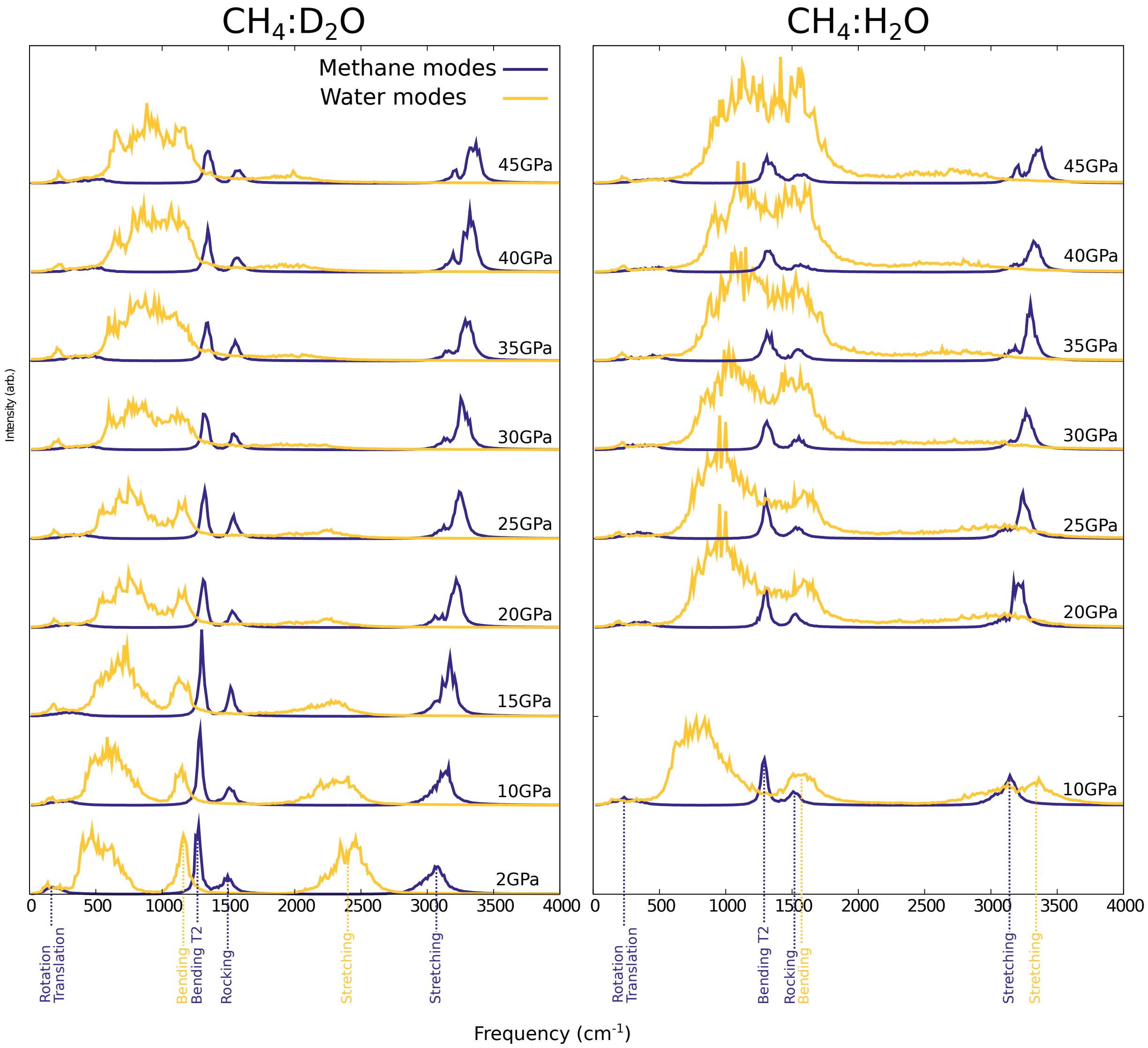

Figure S14: Methane and water frame vibrational spectra calculated with the Fourier transform of the velocities autocorrelation functions. left: deuterated system CH$_4$:D$_2$O; right: protonated system CH$_4$:H2O.

the formation of protonated MHIII between the H$_2$O bending methane rocking modes, while the OH stretching is not likely to intefere with the latter.

References

(S1) Prescher, C.; Prakapenka, V. B. DIOPTAS: a program for reduction of two-dimensional X-ray diffraction data and data exploration. *High Pres. Res.* **2015**, *35*, 223–230.

(S2) Fei, Y.; Ricolleau, A.; Frank, M.; Mibe, K.; Shen, G.; Prakapenka, V. Toward an internally consistent pressure scale. *PNAS* **2007**, *104*, 9182–9186.

(S3) Loveday, J.; Nelmes, R.; Guthrie, M.; Klug, D.; Tse, J. Transition from cage clathrate to filled ice: the structure of methane hydrate III. *Phys. Rev. Lett.* **2001**, *87*, 215501.

(S4) Bove, L. E.; Gaal, R.; Raza, Z.; Ludl, A.-A.; Klotz, S.; Saitta, A. M.; Goncharov, A. F.; Gillet, P. Effect of salt on the H-bond symmetrization in ice. *PNAS* **2015**, *112*, 8216–8220.

(S5) Hirai, H.; Machida, S.-i.; Kawamura, T.; Yamamoto, Y.; Yagi, T. Stabilizing of methane hydrate and transition to a new high-pressure structure at 40 GPa. *Am. Mineral.* **2006**, *91*, 826–830.

(S6) Machida, S.-I.; Hirai, H.; Kawamura, T.; Yamamoto, Y.; Yagi, T. Raman spectra of methane hydrate up to 86 GPa. *Phys. Chem. Miner.* **2007**, *34*, 31–35.

(S7) Tanaka, T.; Hirai, H.; Matsuoka, T.; Ohishi, Y.; Yagi, T.; Ohtake, M.; Yamamoto, Y.; Nakano, S.; Irifune, T. Phase changes of filled ice Ih methane hydrate under low temperature and high pressure. *J. Chem. Phys* **2013**, *139*, 104701.

(S8) Hirai, H.; Tanaka, T.; Kawamura, T.; Yamamoto, Y.; Yagi, T. Retention of filled ice structure of methane hydrate up to 42 GPa. *Phys. Rev. B* **2003**, *68*, 172102.

(S9) Benoit, M.; Marx, D.; Parrinello, M. Tunnelling and zero-point motion in high-pressure ice. *Nature* **1998**, *392*, 258–261.

(S10) Bronstein, Y.; Depondt, P.; Finocchi, F.; Saitta, A. M. Quantum-driven phase transition in ice described via an efficient Langevin approach. *Phys. Rev. B* **2014**, *89*, 214101.

(S11) Dammak, H.; Chalopin, Y.; Laroche, M.; Hayoun, M.; Greffet, J.-J. Quantum thermal bath for molecular dynamics simulation. *Phys. Rev. Lett.* **2009**, *103*, 190601.

(S12) Callen, T. A., H. B.;Welton Irreversibility and Generalized Noise. *Phys. Rev.* **1951**, *83*, 34–40.

(S13) Brieuc, F.; Bronstein, Y.; Dammak, H.; Depondt, P.; Finocchi, F.; Hayoun, M. Zero-point energy leakage in Quantum Thermal Bath molecular dynamics simulations. *J. Chem. Theory Comput.* **2016**, *12*, 5688–5697.

(S14) Bronstein, Y.; Depondt, P.; Bove, L. E.; Gaal, R.; Saitta, A. M.; Finocchi, F. Quantum versus classical protons in pure and salty ice under pressure. *Phys. Rev. B* **2016**, *93*, 024104.

(S15) Dammak, H.; Antoshchenkova, E.; Hayoun, M.; Finocchi, F. Isotope effects in lithium hydride and lithium deuteride crystals by molecular dynamics simulations. *J. Phys. Condens. Matter* **2012**, *24*, 435402.

(S16) Craig, D., I. R.;Manolopoulos Quantum statistics and classical mechanics: Real time correlation functions from ring polymer molecular dynamics. *J. Chem. Phys.* **2004**, *121*, 3368–3373.

(S17) Cao, G., J.;Voth The formulation of quantum statistical mechanics based on the Feynman path centroid density. IV. Algorithms for centroid molecular dynamics. *J. Chem. Phys.* **1994**, *101*, 6168–6183.

(S18) Ceriotti, M.; Manolopoulos, D. E. Efficient first-principles calculation of the quantum kinetic energy and momentum distribution of nuclei. *Phys. Rev. Lett.* **2012**, *109*, 100604.

(S19) Ceriotti, M.; Manolopoulos, D. E.; Parrinello, M. Accelerating the convergence of path integral dynamics with a generalized Langevin equation. *J. Chem. Phys.* **2011**, *134*, 084104.

5.3.3 Next future steps

We have reported a detailed description of the change in guest dynamics when structure MH-III is compressed from 2 to 45 GPa. At 2–3 GPa methane molecules rotate almost freely, in agreement with previous expectation [73], but four favored orientations are already noticeable in the simulations. Those four methane configurations, which are noted A_+, A_-, B_+, and B_- in the article, are shown again in Figure 5.6. Simulation results indicate that rotational motion changing A_+ or A_- into B_+ or B_- is hindered above 5 GPa but motion changing A_+ into A_- and B_+ into B_- is still possible. Above 20 GPa all types of rotational motion are hindered and methane molecules are arranged as $A_+/A_-/A_+$ along the axis a, as $A_+/B_-/A_+$ along the axis b, and as $A_+/B_+/A_+$ along c. Alternatively, they are arranged as $B_+/B_-/B_+$ along the axis a, as $A_-/B_+/A_-$ along the axis b, and as $A_-/B_-/A_-$ along c.

Confirming those results on the orientational ordering of methane molecules in MH-III by diffraction experiments is certainly not an easy task, since i) hydrogen has a very small x-ray scattering cross section and ii) the high-pressure setups employed in neutron scattering experiment cannot reach pressures above ~20 GPa. However, two new technologies have shown a promising potential for this scientific problem. A specially designed diamond anvil cell has been used to collect neutron diffraction patterns of ice up to 50 GPa [83] and a novel NMR resonator structure has been recently used to measure ^{1}H-NMR spectra of ice in diamond anvil cell up to 90 GPa [84].

All past experiments on MH-III methane hydrate were complicated by having clathrate sI methane hydrate as the starting material, so that the resulting high-pressure samples always contained excess ice. It is clear that finding a way to produce pure MH-III with no excess ice would be a remarkable step forward in the research field.

Finally, the work presented here could be extended to the other gas hydrates that are known to form filled ice structures, namely argon, nitrogen, krypton, hydrogen, carbon dioxide, neon, and helium. Of course, the hydrates having wide stability ranges extending above 10–20 GPa would be the best candidates for those investigations; also, polyatomic systems present more interesting dynamical behaviors. The hydrate of argon has been reported to decompose into free argon and ice at 6.1 GPa [85] and therefore would not be a good candidate. Hirai et al. [8] stated that the hydrates of nitrogen and krypton decompose at 3.8 and 5.5 GPa, respectively, but did not present either a reference or data to support this statement. Sasaki et al. [86, 87] measured both nitrogen and krypton hydrates by Raman spectroscopy up to 6.0 and 5.2 GPa, respectively, and did not observe decomposition into gas and water. In addition, Loveday and Nelmes [9] stated having unpublished data indicating stability of nitrogen hydrate up to at least 30 GPa.

Hydrogen hydrate is the only gas hydrate other than methane hydrate that has been investigated above 10 GPa in the past; it was found to be stable up to at least 77 GPa

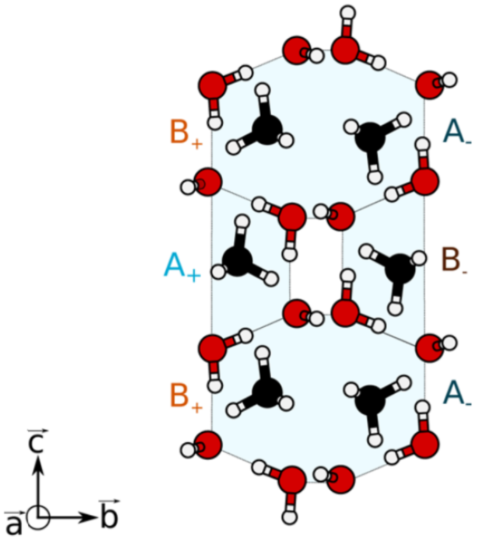

Figure 5.6: Sketch of structure MH-III with the four methane configurations A_+, A_-, B_+, and B_-. The oxygen, carbon, and hydrogen atoms are shown as red, black, and white balls.

[14]. By x-ray diffraction Hirai et al. [88] found a small tetragonal distortion of the cubic filled ice structure at about 20 GPa and suggested a possible link with orientational ordering of the H_2 molecules in the structure.

5.3.4 High-pressure Raman study of methane hydrate up to 150 GPa

In 2003 a study based on first-principles electronic structure calculations [89] suggested that the hydrogen bonds of the water molecules in structure MH-III should symmetrize at around 40 GPa. Compared to ice VII [90], MH-III would then show hydrogen-bond symmetrization at considerably smaller pressures. This is somehow reasonable as $O\cdots O$ distances are shorter in MH-III than in ice VII. On the other hand, molecular dynamics calculation results by Klug et al. [78] suggested that the hydrogen bonds in MH-III should symmetrize at 60 GPa, if structure MH-III is retained at such high pressures.

The group of Hirai [13, 74, 75, 76] observed disappearance of some diffraction peaks and appearance of new peaks at ∼40 GPa by synchrotron x-ray diffraction on CH_4–H_2O methane hydrate and concluded that MH-III transforms into a different structure above 40–50 GPa. The quality of the diffraction patterns did not permit solution of the new structure [13, 74, 75, 76]. The authors initially suggested that transition to the high-pressure phase might be related to the symmetrization of the hydrogen bonds in the water molecules [13, 74, 75]; however, more recently the same group investigated a CH_4–D_2O methane hydrate sample and concluded that the effect of isotopic exchange on the transition is *not* compatible with hydrogen-bond symmetrization [76].

In this subsection we present Raman spectroscopy data of methane hydrate up to 150 GPa which are matter of an article under preparation. This study is motivated by the following open questions regarding methane hydrate at extremely high pressures:

- Is there a change in the structure of methane hydrate above 40 GPa?
- Is there hydrogen-bond symmetrization of the water network of methane hydrate?
- What is the stability limit of methane hydrate under high pressure?

Measurements were carried out at room temperature and pressures between 4 and 150 GPa in our laboratory at the EPFL. We employed the same diamond anvil cell we used for the Raman experiments reported above in subsection 5.3.2 but diamond anvils having smaller culets (see section 3.3). Starting CH_4–D_2O clathrate sI sample was loaded into a diamond anvil cell in a liquid nitrogen bath and compressed to 4 GPa at cold; finally the cell was warmed up to room temperature. No ruby was used during this loading; pressure was evaluated with a precision of 0.5 GPa based on the shift of the diamond first-order Raman signal measured in the center of the culet and the pressure scale from ref [91].

The top panel of Figure 5.7 reports the Raman spectra of the sample measured at pressures between 36 and 150 GPa. With increasing pressure the two CH stretching modes at 3200–3500 cm^{-1} shift to higher frequencies and can be clearly seen up to the maximum investigated pressure of 150 GPa. The lattice mode at ∼500 cm^{-1} looses intensity upon compression and is barely distinguishable above 50–60 GPa. Similarly, the CH_4 rocking mode broadens considerably upon compression above 35 GPa and has no detectable intensity above 50–60 GPa. The two OD stretching modes loose intensity very sharply over the range between 35 and 45 GPa. Upon pressure increase to 100 GPa a new peak appears at ∼950 cm^{-1}. The peak clearly has two components (see the bottom panel of Figure 5.7) and is well fitted by two pseudo-Voigt functions. This excitation is very likely to correspond to the O–O vibrational mode of T_{2g} symmetry that is observed in ice after hydrogen-bond symmetrization has occurred and the symmetric phase of ice (noted ice X) has formed [90]. Nevertheless, in pure ice the T_{2g} O–O vibrational mode appears as a single peak.

The top panel of Figure 5.8 reports all measured Raman frequencies as a function of pressure between 12 and 150 GPa, including frequencies from our published data below 45 GPa. The pressure dependence of the frequency of the CH stretching modes is smooth over the pressure range between 20 and 150 GPa and can be nicely fitted by a polynomial function (see the bottom panel of Figure 5.8). At all pressures the CH stretching modes frequency is different from that of pure methane as reported in ref [92], indicating that methane hydrate did not decompose into free methane and ice up to the maximum pressure of 150 GPa. As can been seen in Figure 5.8, the frequencies of the OD

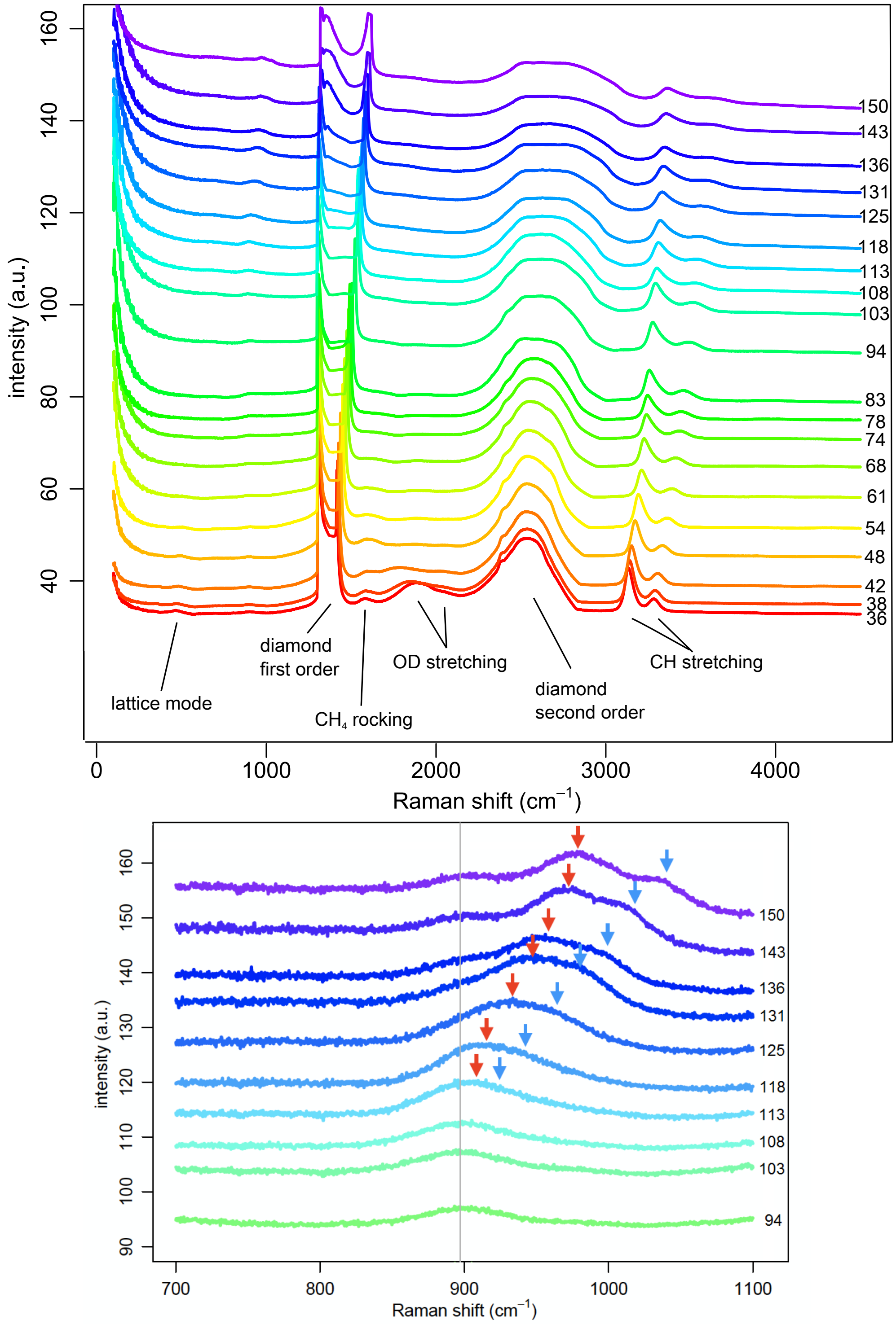

Figure 5.7: Top: Raw Raman spectra of CH_4–D_2O methane hydrate (and excess ice) at room temperature and the indicated pressures between 36 and 150 GPa. Bottom: the spectra from 94 to 150 GPa are plotted over a shorter Raman shift range. The vertical line indicates a weak instrumental peak.

stretching modes show a chaotic behavior in the range 35–45 GPa where they approach the frequency of the CH_4 rocking mode. In the same pressure range our simulations indicate a strong coupling between the two modes, as detailed above in the published article.

In Figure 5.9 we compare the frequency of two components of the 'T_{2g}' mode of the sample to the frequency of the same mode in pure D_2O. The frequency of both components measured in the sample increases with increasing pressure, with the component at lower frequency being essentially at the same frequency as the T_{2g} mode of pure D_2O. Since the sample contained excess ice, it is then reasonable to conclude that this component arises from excess ice in the sample. On the other hand, the higher-frequency component should be due to methane hydrate and could indicate hydrogen-bond symmetrization of a high-symmetry methane hydrate structure similar to that of ice X.

Finally, Figure 5.10 reports the frequency of the lattice mode of the sample below 55 GPa compared to that of pure D_2O, as well as their intensity (through the area of the circles). Intensities have been normalized to the OD stretching intensities. Figure 5.10 suggests that the lattice mode measured on the sample should be due to a composition of pure ice VII lattice mode and hydrate lattice mode and that the latter persists at slightly higher pressures.

To summarize, we were able to measure Raman spectra of a CH_4–D_2O methane hydrate sample up to 150 GPa using a diamond anvil cell. No decomposition into free methane and ice was observed. In the pressure range above 50–60 GPa only few excitations are visible in the spectra. The lattice mode frequency is almost flat as a function of pressure above ∼50 GPa but the intensity of the mode is very weak. The CH stretching modes remain clearly visible up to 150 GPa; their frequency increases smoothly with pressure. Above ∼100 GPa a double peak appears at about 950 cm^{-1}. This peak is likely to be at least partially due to excess ice in the sample. If the peak also arises from methane hydrate, it could be an analogue of the T_{2g} mode of ice X.

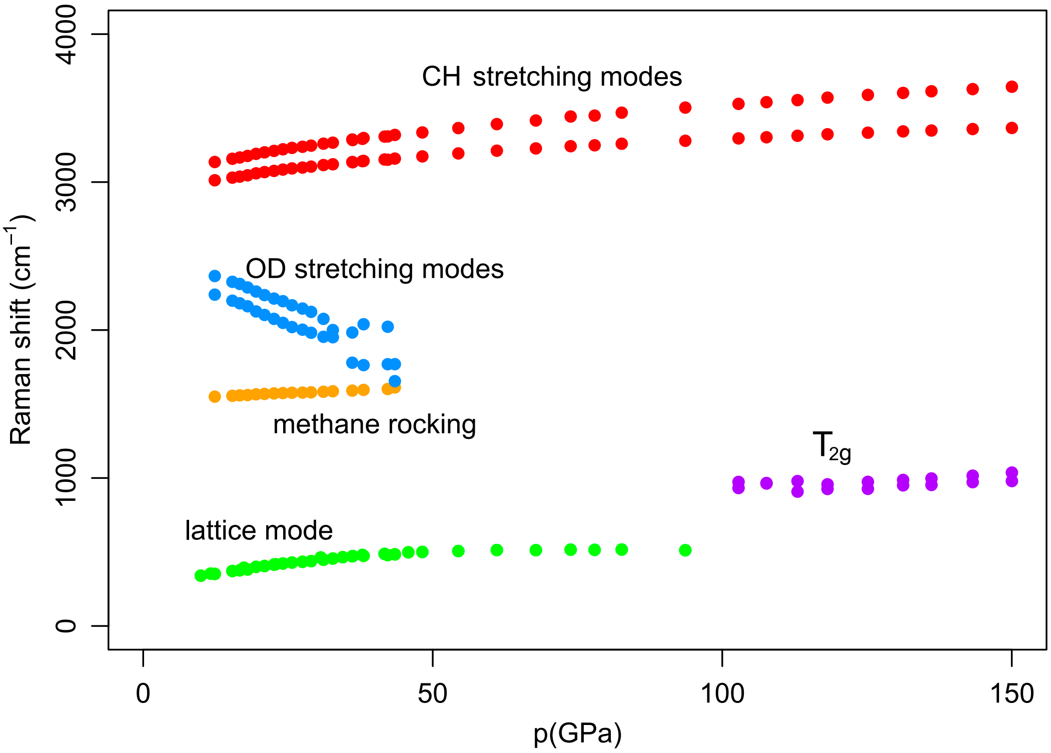

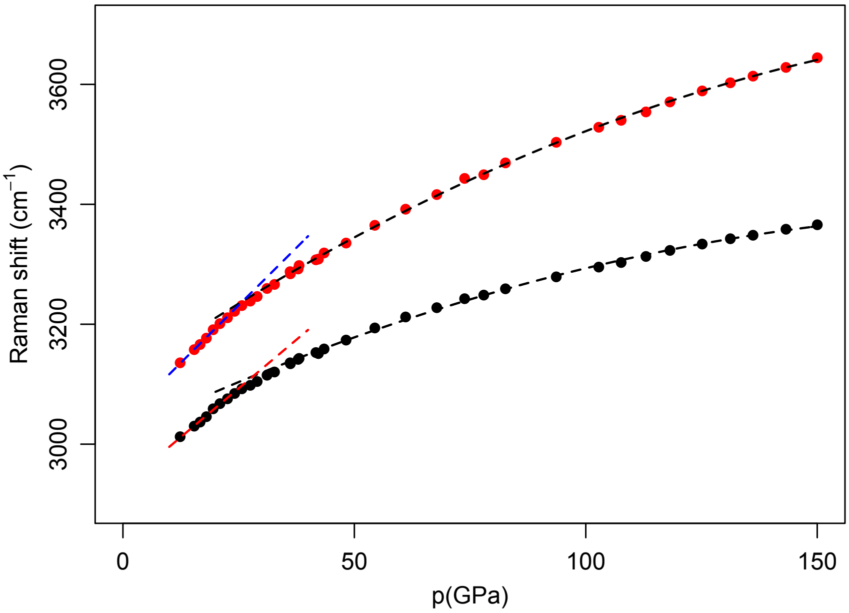

Figure 5.8: Top: Pressure dependence of the Raman frequencies of CH_4–D_2O methane hydrate (and excess ice) between 12 and 150 GPa. Reliability parameters from the fits are smaller than the plotted circles. Bottom: Zoom of the top panel for the frequencies of the CH stretching modes. A linear fit below 20 GPa and a smooth polynomial fit above 20 GPa are also shown.

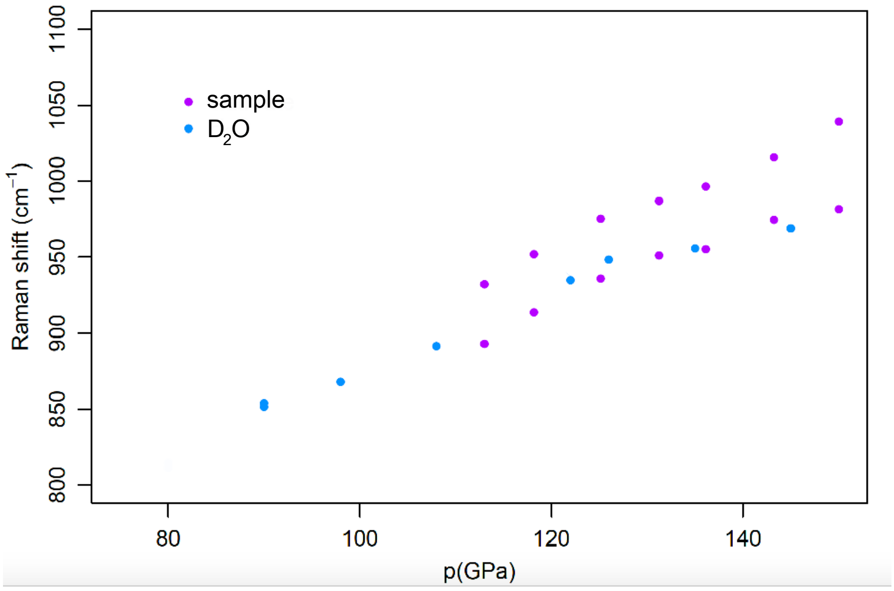

Figure 5.9: Pressure dependence of the Raman ‘T_{2g}’ mode frequency of CH_4–D_2O methane hydrate (and excess ice), compared to that of pure D_2O.

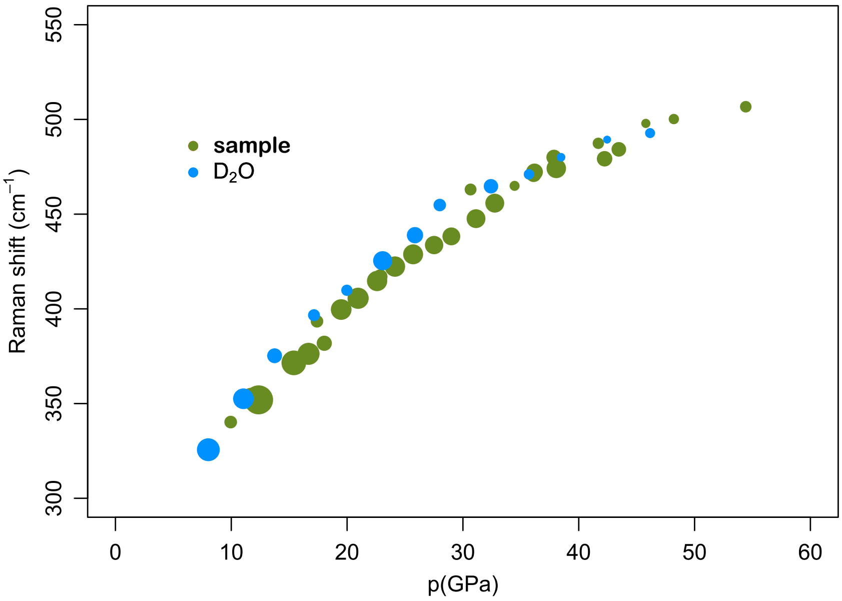

Figure 5.10: Pressure dependence of the Raman lattice mode frequency of CH_4–D_2O methane hydrate (and excess ice) below 55 GPa, compared to that of pure D_2O. The area of the circles is proportional to the peak intensity in the spectra.

6 Guest dynamics in hydrogen hydrates under high pressure

6.1 Motivations

Over the last fifteen years, hydrogen hydrates attracted vast attention because of their potential as environmentally friendly hydrogen-storage materials [3]. Clathrate structure II contains one hydrogen molecule per small cage and up to four hydrogen molecules per large cage [7], equivalent to ~3.8 wt % of molecular hydrogen. However, practical application for hydrogen storage is made unrealistic by the high pressure needed to form the compound (~0.1 GPa). Considerable research efforts are currently aimed at exploring possibilities for stabilizing sII or other clathrate structures at near-ambient pressure, including binary and ternary clathrate hydrates, and similar systems (e.g. semiclathrates) [3].

Hydrogen hydrates can be seen as nanoporous materials of remarkable simplicity, where i) only two types of molecules exist, namely water and molecular hydrogen, ii) water molecules are arranged in crystalline structures that are well known, and iii) hydrogen molecules, the simplest molecules, occupy well defined nanometric cages or cavities from which they cannot escape (at low temperature). For these reasons, the properties of hydrogen hydrates are of fundamental importance in chemical physics. It can be also mentioned that water and hydrogen are likely to be the two most common molecules in the Universe.

Since hydrogen molecules are light and because of the nanoscale size of their confinement, hydrogen molecules trapped in hydrate structures inherently constitute quantum-mechanical objects. The cage (for clathrate structures) or the cavity (for filled ice structures) produces a confining potential for the hydrogen molecule therein and the result is a good approximation of the problem of a particle in a potential well which is at the very heart of quantum mechanics.

This chapter will focus on the quantum roto-translational dynamics of hydrogen molecules confined in hydrogen hydrates having clathrate sII and the high-pressure filled ice II structure (noted C1) at low temperature.

6.2 Guest dynamics in hydrogen hydrates

6.2.1 Introduction

In quantum mechanics [93], the discrete rotational states of molecular hydrogen are specified by the rotational quantum number J=0,1,2,... . The component of angular momentum about the laboratory z axis is allowed to have the values $M_J\hbar$, with M_J=J, $J-1$,..., $-J$ and $\hbar$ the reduced Planck constant. The rotational energy is given by $BJ(J+1)$, where the rotational constant B is defined as $\hbar^2/2I$ and I is the moment of inertia. Since the energy is independent of M_J, each energy level is $(2J+1)$-fold degenerate. It follows that the first excited rotational state is at $2B$ and is triply degenerated, the second one is at $6B$ and is five-fold degenerated, etc... .

The rotational spectrum of hydrogen molecules is then made of discrete lines corresponding to all possible transitions $J \rightarrow J'$. The intensity of each line $J \rightarrow J'$ depends on the number of molecules in the sample having the initial value J. In general populations are expected to follow the Boltzmann distribution, so the number of molecules with energy $BJ(J+1)$ would be simply given by the product between the degeneracy of the level $(2J+1)$ and the exponential factor $\mathrm{e}^{-BJ(J+1)/k_BT}$, with k_B the Boltzmann constant. However, for H_2 and D_2 (or any homonuclear diatomic molecule) a complicating feature arises from the fact that the nuclear spin state restricts the permissible rotational states of the molecule.

Rotation of a homonuclear diatomic molecule interchanges two identical particles, which are fermions in H_2 and bosons in D_2. The Pauli principle requires the overall wavefunction ψ to change sign under permutation of two identical fermions and to remain unchanged under permutation of two identical bosons. If P is the label permutation operator, this condition can be written as $P\psi$=$-\psi$ for H_2 and $P\psi$=ψ for D_2. The overall wavefunction contains electronic, vibrational, rotational and nuclear wavefunctions and can be written as $\psi = \psi^{\mathrm{el}}\psi^{\mathrm{vib}}\psi^{\mathrm{rot}}\psi^{\mathrm{nuc}}$ within the Born-Oppenheimer approximation with obvious notations. Under nuclear exchange ψ^{el} and ψ^{vib} are unchanged and ψ^{rot} changes sign by $(-1)^J$. Therefore $P\psi = (-1)^J\psi^{\mathrm{el}}\psi^{\mathrm{vib}}\psi^{\mathrm{rot}}p_{\mathrm{nuc}}\psi^{\mathrm{nuc}}$, where p_{nuc} is the state permutation operator. On the other hand, the effect of p_{nuc} on ψ^{nuc} depends on the spin configuration of the molecule. For H_2, each proton has spin 1/2 and can be in one of the two spin states, noted ↑ and ↓. Hence there must be four states for the molecule and the nuclear wavefunction is either

$$ {}^3\psi^{\mathrm{nuc}} = \begin{cases} |\uparrow\uparrow\rangle \\ \frac{1}{\sqrt{2}}(|\uparrow\downarrow\rangle + |\downarrow\uparrow\rangle) \\ |\downarrow\downarrow\rangle \end{cases} \tag{6.1} $$

or

$$^{1}\psi^{\text{nuc}} = \frac{1}{\sqrt{2}}(|\uparrow\downarrow\rangle - |\downarrow\uparrow\rangle) \tag{6.2}$$

The wavefunction of the nuclear spin triplet $^{3}\psi^{\text{nuc}}$ is symmetric under nuclear exchange ($p_{\text{nuc}}{}^{3}\psi^{\text{nuc}} = {}^{3}\psi^{\text{nuc}}$) and the wavefunction of the nuclear spin singlet $^{1}\psi^{\text{nuc}}$ is antisymmetric under nuclear exchange ($p_{\text{nuc}}{}^{1}\psi^{\text{nuc}} = -{}^{1}\psi^{\text{nuc}}$). In summary, if the protons are described by the triplet state, $P\psi = (-1)^{J}\psi$ and J must be odd to conform to the Pauli principle. If the protons are described by the singlet state, $P\psi = (-1)^{J+1}\psi$ and J must be even.

The previous discussion leads to the important conclusion that H_2 molecules exist in two species: one which can only exist with odd rotational states J=1,3,... and is referred to as *ortho*-H_2, and the other which can only exist with even rotational states J=0,2,... and is referred to as *para*-H_2. The difference in energy between the ground state of *ortho*-H_2 (J=1) and that of *para*-H_2 (J=0) is ∼14 meV, much smaller than the thermal energy at room temperature ($KT \sim 26$ meV at 300 K). Thus at room temperature and at thermodynamic equilibrium *ortho*-H_2 is three times more abundant than *para*-H_2, since there are three *ortho* nuclear spin states but only one *para* state.

For D_2 molecules, each nucleus has spin 1 so there are 3 different spin states for each nucleus and nine for the molecule; one can check that six of them are symmetric and three are antisymmetric [94]. Because the overall wavefunction must remain unchanged under permutation of two identical bosons, D_2 molecules with symmetric spin states (noted *ortho*-D_2) exist with even rotational states J and D_2 molecules with antisymmetric spin states (noted *para*-D_2) exist with odd rotational states J. It follows that at room temperature the equilibrium concentrations of *ortho*-D_2 and *para*-D_2 are in the ratio 2 to 1.

The existence of two allotropic species for H_2 and D_2 has far-reaching implications on their quantum dynamics. Since *ortho*-*para* conversion can be only mediated by a magnetic interaction connecting space and spin, conversion times can be extremely long. In general the two species do *not* thermally equilibrate with each other; populations of the rotational energy levels do *not* follow the Boltzmann distribution, but populations of the levels of each of the two species do. This is not the case for the heteronuclear isotopologue HD.

In addition to the quantized rotational states, (center-of-mass) translational motion of molecular hydrogen confined in a nanocavity is also quantized as an effect of confinement. This can be understood by analogy with the problem of the localized motion of a quantum particle in a potential well.

Inelastic neutron scattering probes dynamical processes occurring with discrete energies and is the experimental technique of choice for studying the quantum dynamics of hydrogen molecules because of the very large incoherent neutron scattering cross section of the proton. Furthermore, inelastic neutron scattering from discrete molecular systems is not subject to selection rules and has the capability to access transitions involving a change in nuclear spin state, which are strictly forbidden in IR, Raman, and magnetic resonance spectroscopies.

Neglecting the coherent part of the scattering, on account of the overwhelming incoherent scattering cross section of the proton, the expression for the partial differential cross section simply contains a convolution product between vibrational, rotational, and translational contributions [95]. This is valid under the assumption that vibrational, rotational, and translational degrees of freedom are not coupled. In the low energy-transfer regime below 20–30 meV, vibrations contribute to the spectra through a Debye-Waller factor.

Here we are interested in the roto-translational quantum dynamics of molecular hydrogen confined in the cages of clathrate structure II and in the nanometric channels of structure C1. While no similar investigation exist in literature for structure C1, the quantum dynamics of molecular hydrogen in the cages of clathrate structure II has been previously studied theoretically by rigorous fully quantum simulations [96, 97, 98, 99, 100, 101, 102] and experimentally by inelastic neutron scattering [95, 103, 104, 105].

Those theoretical works calculate the fully coupled quantum 5D roto-translational energy levels and wave functions of a hydrogen molecule confined in a clathrate cage by diagonalizing a 5D Hamiltonian that includes explicitly the three translational and the two rotational degrees of freedom of the molecule. Only the interaction with the water molecules of the confining cage is usually considered, except for the work of ref [102]. The water cage and guest molecule are treated as rigid. The hydrogen-bonded water network of clathrate structure II is proton-disordered, and computations are typically performed for one proton configuration chosen at random among all the ones respecting the Bernal and Fowler rules [106].

Over the last decade, inelastic neutron scattering works [95, 103, 104, 105] have used binary clathrate sII hydrogen-tetrahydrofuran hydrate samples, where hydrogen molecules reside exclusively in the small cages of the structure, to access the intra-cage dynamics of hydrogen molecules confined in the small cage. The rotational energies are close to those of the isolated molecule, indicating that hydrogen molecules rotate relatively ‘unhindered’ in the small cages of sII [95, 103, 104, 105]. The translational motion is usually described in terms of a ‘rattling’ [95, 104, 105]. Degeneracy of both rotational and translational states is lifted due to the angular and radial anisotropy of the potential energy surface for the hydrogen molecule in the cage. Many rotational and translational energy levels and sub-levels have been established experimentally with good precision for both H_2 and HD [95, 103, 104, 105] and were found to be very well reproduced by the latest theoretical investigations [100, 101].

On the other hand, for hydrogen molecules confined in the large cages of clathrate sII, experiments are complicated by the fact that i) translational energy levels are closer one to each other (thus spectra are more congested) and ii) peaks are expected to be broader as an effect of multiple cage occupation [104]. Only the transition between the ground state and the first excited rotational state has been observed up to date; the associated peak was found to be essentially superposed to that of H_2 molecules confined in small cages and had no detectable splitting [104]. No translational excitations have been experimentally identified so far. Rigorous treatment of the quantum dynamics of multiple guest molecules in one large cage is not possible with the state-of-the-art tools and theoretical predictions only exist for the case of single cage occupation [97, 99].

In the large cage of sII, hydrogen molecules are expected to be arranged at the corners of a tetrahedron at temperatures below $\sim$50 K, as found by a neutron diffraction work [7] and several simulation studies [97, 107, 108, 109]. The tetrahedron simply reproduces the geometry of the cage, with each corner located directly behind the center of one of the four hexagonal water faces, as shown in the top panel of Figure 6.1. Similarly, tetrahedral arrangement in the large cage has been found for other small molecules such as neon [5] and helium [110] for which multiple occupation of the large cage is possible.

Structure C1 has the same rhombohedral space group as ice II ($R\bar{3}$, No 148) but significantly perturbed cell parameters a=12.73 Å and c=5.97 Å at 2.1 GPa [12]. There are 36 water molecules and six hydrogen molecules in the unit cell, implying a theoretical water-to-hydrogen molar ratio of 6 to 1. As can be seen in the bottom panel of Figure 6.1, the hydrogen-bonded proton-ordered water network of structure C1 is characterized by six-membered water rings that are aligned to form hexagonal channels running along the c axis. Similar structures have been observed in He and Ne hydrates [112, 113]. At variance with the water network of ice Ih and structure MH-III, the six-membered rings of structure C1 are separated by four-membered rings in the ab plane. Hydrogen molecules are located along the hexagonal channels exclusively, at approximately midway between two adjacent six-membered rings. Two types of six-membered water rings exist–a puckered ring similar to that found in ice Ih and a much flatter ring alternate along the channels (Figure 6.1). Based on the rotational Raman spectra of ref [12], H_2 molecules in this structure are essentially free to rotate.

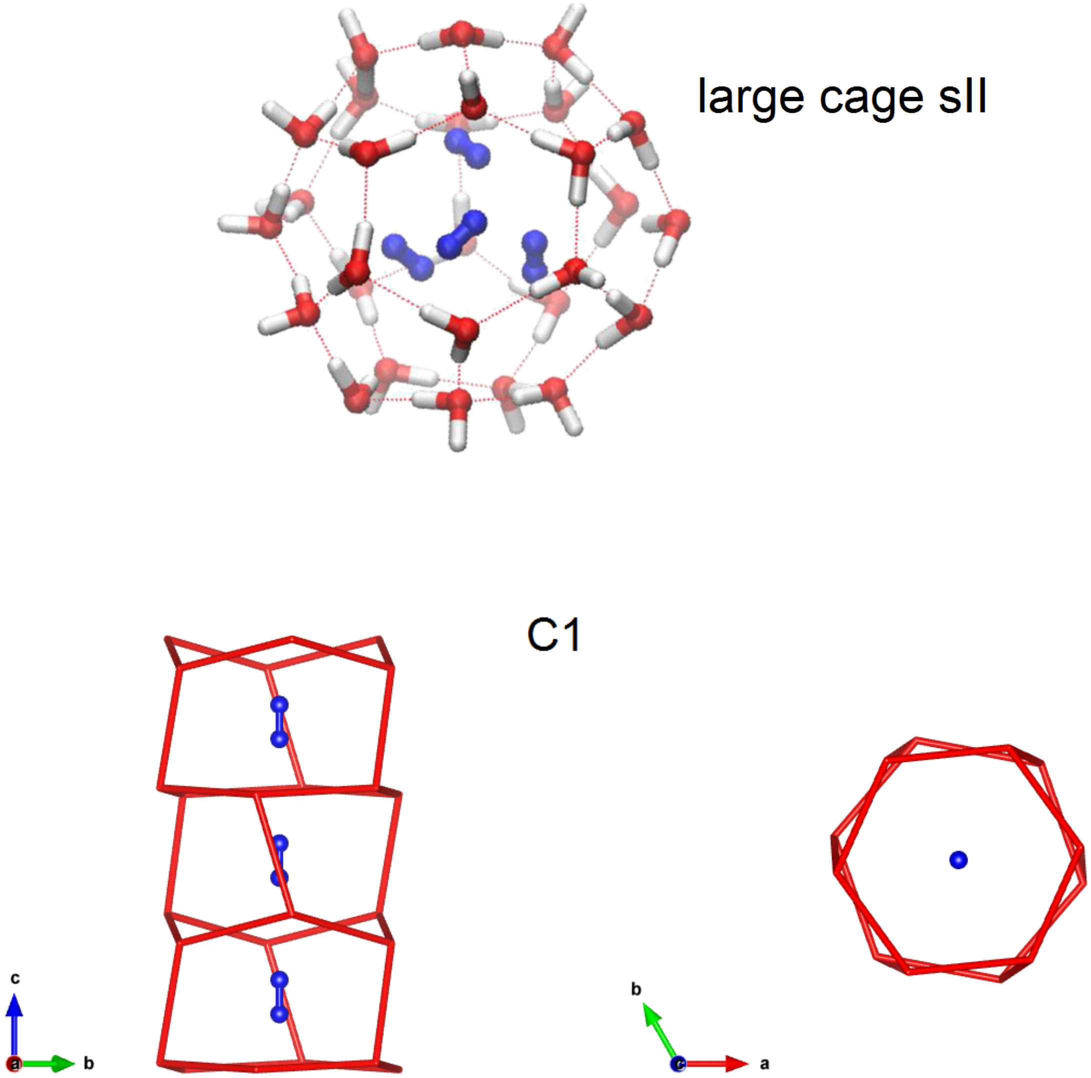

Figure 6.1: Top: Large ($5^{12}6^4$) cage of clathrate structure II with quadruple occupation of H_2 molecules, reproduced from [111]. Oxygen and hydrogen atoms of the water molecules are represented in red and in white, respectively. Hydrogen molecules are in blue. Hydrogen bonds are represented as dashed lines. At low temperature, hydrogen molecules preferentially 'sit' behind one of the four hexagonal faces and are thus arranged at the corners of a tetrahedron. Bottom: Hexagonal channel of hydrogen-filled ice II (structure C1) in two different crystallographic planes. For clarity the oxygen and hydrogen atoms have been omitted. Sticks correspond to hydrogen bonds. In both structure II and structure C1, hydrogen molecules are free to rotate.

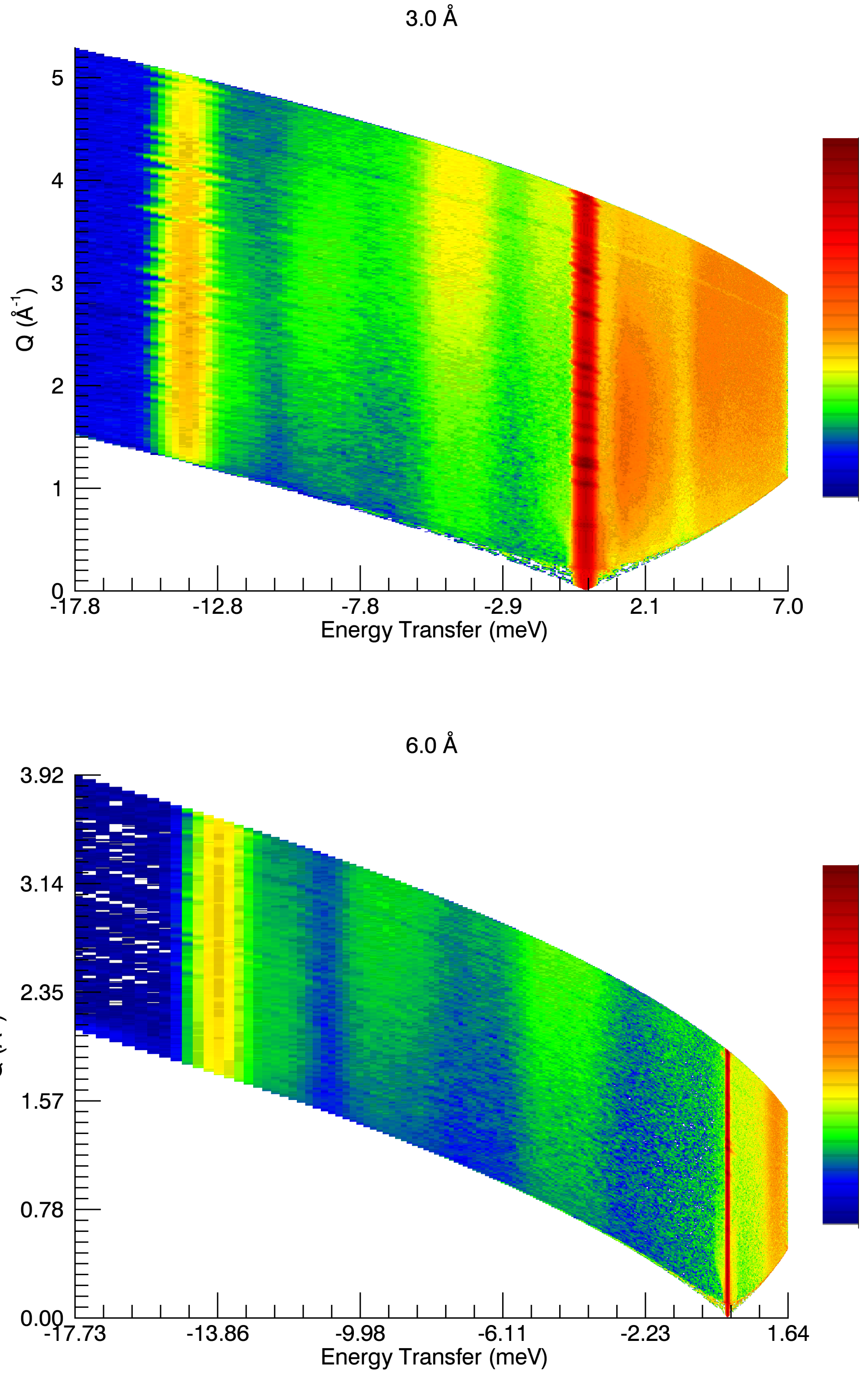

Figure 6.2: Color plots in the $(Q, \hbar\omega)$ space representing IN5 measurements of clathrate sII H_2–D_2O hydrate at ambient pressure and 1.5 K, using neutron wavelengths of 3.0 and 6.0 Å. The color scale is a logarithmic scale in arbitrary units. The region at energy transfer values below -17.8 meV is not plotted.

We performed extensive inelastic neutron scattering measurements of hydrogen hydrate having clathrate sII and structure C1 at low temperature (below 50 K) using the neutron spectrometers IN5 and IN6 at the ILL. Hydrogen hydrate samples were prepared following the procedure described in chapter 2. Some of them were measured at ambient pressure on the neutron diffractometer D20 of the ILL prior to the inelastic neutron scattering experiments. All experiments involving clathrate sII were limited to pressures below 0.5 GPa and were performed on the instrument IN5 using a gas pressure cell. H_2–D_2O hydrogen hydrate having clathrate sII was measured at ambient pressure and at 0.25–0.3 GPa. Simple D_2 and binary He–H_2 hydrates having clathrate structure II were also measured to investigate the effect of substituting H_2 guests with D_2 and the effect of helium inclusion in the structure on the quantum dynamics of the hydrogen molecules. Finally, measurements of H_2–D_2O hydrogen hydrate having structure C1 were taken at 1.4 GPa on the instrument IN6 using a Paris-Edinburgh cell.

Examples of IN5 data of clathrate sII H_2–D_2O hydrate at ambient pressure and 1.5 K taken using two different incident neutron wavelengths of 3.0 and 6.0 Å are reported in the form of color plots in Figure 6.2. Data in Figure 6.2 contain many inelastic features and each of them correspond to a different roto-translational transition of H_2 confined in the small or in the large cage of the structure. Assignment of those features will be reported in the next subsection. Data are restricted to the accessible region of the $(Q, \hbar\omega)$ space that is defined by the incident neutron wavelength and by the placement of the detectors, as mentioned in subsection 4.1.2. Comparing the regions of the $(Q, \hbar\omega)$ space accessible for wavelengths of 3.0 and 6.0 Å, one can see that the first one is considerably larger than the second; this improvement is of course at the expenses of the energy resolution.

All results are reported in the following pages in the form of the preprint version of an article entitled “Quantum dynamics of H_2 and D_2 confined in hydrate structures as a function of pressure and temperature” and authored by Umbertoluca Ranieri, Michael Marek Koza, Werner F. Kuhs, Richard Gaal, Stefan Klotz, Andrzej Falenty, Dirk Wallacher, Jacques Ollivier, Philippe Gillet, and Livia E. Bove. The article is followed by its Supporting Information file. Author contributions are as follows: U.R., W.F.K., A.F., and D. W. prepared the samples. U.R., M.M.K., W.F.K., R.G., S.K., J.O. and L.E.B. performed the experiments. U.R., M.M.K. and L.E.B. analyzed the data. All authors discussed the results. U.R. wrote the manuscript.

6.2.2 Article: “Quantum dynamics of H_2 and D_2 confined in hydrate structures as a function of pressure and temperature”

Quantum dynamics of H_2 and D_2 confined in hydrate structures as a function of pressure and temperature

Umbertoluca Ranieri,[*,†,‡] Michael Marek Koza,[‡] Werner F. Kuhs,[¶] Richard Gaal,[†] Stefan Klotz,[§] Andrzej Falenty,[¶] Dirk Wallacher,[‖] Jacques Ollivier,[‡] Philippe Gillet,[†] and Livia E. Bove[*,§,†]

†EPSL, IPHYS, École polytechnique fédérale de Lausanne (EPFL), Station 3, CH-1015 Lausanne, Switzerland

‡Institut Laue-Langevin, 71 avenue des Martyrs, CS 20156, 38042 Grenoble, Cedex 9, France

¶GZG Abt. Kristallographie, Universität Göttingen, Goldschmidtstrasse 1, 37077 Göttingen, Germany

§Sorbonne Université, CNRS UMR 7590, Institut de minéralogie, de physique des matériaux et de cosmochimie, IMPMC, 75005 Paris, France

‖Department of Sample Environments, Helmholtz-Zentrum Berlin für Materialien und Energie, Germany

Abstract

We present an extensive inelastic neutron scattering study of the low-temperature quantum dynamics of molecular hydrogen trapped within nanocavities of two hydrate structures, namely clathrate structure II and filled ice structure C1. Simple H_2 hydrate having clathrate structure II was investigated at different pressures and temperatures. Simple D_2 and binary He–H_2 hydrates having clathrate structure II and simple H_2 hydrate having structure C1 were investigated at different temperatures. Molecular quantum rotations and translations, as well as combinations of these are identified in the spectra for H_2 and D_2 molecules in the small and large cages of clathrate structure II and in the channels of structure C1, and their energy is provided.

1. Introduction

Hydrogen hydrates are non-stoichiometric inclusion compounds in which hydrogen "guest" molecules are trapped inside crystalline networks formed by hydrogen-bonded "host" water molecules. The presence of guest molecules prevents the water framework to collapse when an external pressure is applied. *Simple* hydrogen hydrates (having hydrogen molecules as the sole guests) form at pressures above ∼0.1 GPa and crystallize into clathrate structure II (sII), whose water network is characterized by two polyhedral cavities, or "cages", of different symmetries and sizes.[1–3] Clathrate sII has a cubic unit cell containing 16 small water cages and 8 large water cages. The small cage (noted 5^{12}) is made of 12 pentagonal faces formed by 20 water molecules; it has the shape of an oblate symmetric top with an average radius of 3.91 Å. The large cage ($5^{12}6^4$) is made of 12 pentagonal faces and 4 hexagonal faces formed by 28 water molecules; it is almost spherical and has an average radius of 4.73 Å.[2] While the small cage of clathrate sII is occupied by a single hydrogen molecule, up to four hydrogen molecules are trapped in the large cage.[3]

At higher pressures simple hydrogen hydrate transforms into so-called *filled ice* structures, for which the water networks resemble those of some known phases of ice.[4] Three high-pressure structures have been recognized so far: structure C0 between 0.4 and 0.7 GPa,[5,6] filled ice structure C1 between 0.7 and ∼2.5 GPa[7] and filled ice structure C2 above ∼2.5 GPa.[7] Structures C1 and C2 present water networks resembling those of ice II and ice Ic, respectively.[4,7] The water network of structure C0 does not possess the cages typical of clathrate structures and is unrelated to any known phase of ice; instead, it shows chiral channels of molecular size where the hydrogen molecules are trapped.[5,6] Hydrogen may also form *binary* (or *double*) hydrates together with molecules such as carbon dioxide[8] or tetrahydrofuran.[9,10] Those binary hydrates may adopt clathrate structure I (sI),[8] clathrate sII[9] or clathrate structure H (sH).[10]

Hydrogen hydrates provide an outstanding opportunity for investigating the effect of nanoscale confinement on both quantum and classical dynamics of hydrogen molecules trapped within simple nanocavities made of one single type of host molecule, namely water. This provides not only fundamental information on the nature of the water–gas interaction in condensed matter but also insights on the possibility to store hydrogen in more complex nanoporous materials.[11,12] The study of rotational, translational and vibrational excitations of molecular hydrogen trapped within nanocavities of different dimensions is a very active field of research; for example, carbon nanotubes,[13,14] metal-organic frameworks,[15] fullerene,[16,17] and organic clathrates[18] have been recently used as confining media. Inelastic neutron scattering (INS) is the experimental technique of choice for such investigations due to the exceptionally large neutron scattering cross section of the proton and to its ability to distinguish H_2 and D_2 through the very different cross sections of the two isotopes. Furthermore, INS has the capability to access transitions involving a change in nuclear spin state, such as transitions converting *ortho* and *para* species. Extensive INS investigations have been performed in the last fifteen years on clathrate hydrates of different gases (including methane,[19,20] argon,[21,22] xenon,[21,22] oxygen,[21,22] nitrogen,[21,22] and krypton[23]) and considerably improved our understanding of the water–gas interaction in general and of the coupling between gas and water dynamics in gas hydrates in particular.

At low temperature, nanoscale confinement leads to quantization of the translational degrees of freedom of the confined molecule and the discrete energy levels depend on the confinement size and on the mass of the molecule. The transition between the ground state and the first excited translational state for H_2 confined in the small cage of clathrate sII has been identified one decade ago at energies of 9–12 meV.[24,25] This was achieved by INS using binary clathrate sII hydrogen-tetrahydrofuran hydrate samples, where hydrogen molecules reside exclusively in the small cages of the structure.[24,25] This result was later supported by simulation studies;[26,27] also, the isotopic effect on the translational energies was investigated during similar experiments on HD[25,28] or D_2.[29] More recently the equivalent mode for H_2 confined in the medium cage of clathrate sH (average cavity radius of 4.04 Å) was identified at 6–8 meV using binary clathrate sH hydrogen-MTBE (methyl *tert*-butyl ether) hydrate samples, where hydrogen molecules reside exclusively in the small and medium cages of the structure.[28,30]

However, equivalent translational excitations for H_2 and D_2 confined in the large cage of clathrate sII have not been characterized yet. Some theoretical predictions exist[31–33] but rigorous fully quantum treatment of the dynamics of two or more hydrogen molecules in one large cage is not possible with the state-of-the-art tools. No information exist in literature about the effect of high pressure on the dynamics of hydrogen confined in clathrate hydrates. Applying pressure (P) is an efficient way to modify the cage size and explore the water-hydrogen interaction potential; for example, increasing P to 0.25 GPa implies a change in lattice parameter close to 1% for clathrate sII.

Similarly, the dynamics of hydrogen confined in the high-pressure structures C0, C1, and C2 remains almost unexplored. The transition between the ground state and the first excited translational state for H_2 confined in structure C0 was recently identified at approximately 3 and 20 meV by INS[34] but no equivalent studies have been reported in literature on structures C1 and C2.

In this work we present low-temperature (T<50 K) INS spectra of simple H_2 and D_2 hydrates having clathrate sII. We observe low-energy modes which can be attributed to translational excitations of H_2 and D_2 molecules confined in the large cages of the structure. These modes were not resolved in prior experiments on hydrogen hydrate reported in the literature.[29,35] We also measured binary He–H_2 hydrate having clathrate sII and simple H_2 hydrate having the high-pressure structure C1. The water network of all samples was deuterated to highlight the modes of the trapped hydrogen molecules. With the present experiments we have investigated the effect of four different changes on the quantum dynamics of confined H_2 molecules: i) the effect of applying pressure on clathrate sII, ii) the effect of helium inclusion in the large cages of clathrate sII, iii) the effect of substituting H_2 guests with D_2 in clathrate sII and iv) the effect of changing the crystalline water topology from clathrate sII to structure C1.

The experiments were performed at the time-of-flight spectrometers IN5 and IN6 at the Institut Laue-Langevin in Grenoble (France). Simple clathrate sII H_2 hydrate was measured at ambient P and 0.25–0.3 GPa, binary sII He–H_2 hydrate was measured at 0.4–0.5 GPa, simple sII D_2 hydrate was measured at ambient P and simple C1 H_2 hydrate was measured at 1.4 GPa.

The paper is organized as follows. In section 2 we outline the theoretical background relevant to this work and in section 3 we describe sample preparation, instrumental details and experimental protocol. The results and their discussion are presented in sections 4 and 5. We conclude our study in section 6.

2. Theoretical background

2.1 Quantum roto-translational energy levels of confined H_2 and D_2. Hydrogen molecules (H_2, HD, or D_2) intrinsically have quantized rotations. When they are trapped inside hydrate cavities, their translations are also quantized because of the confinement. Due to the nanoscale size of the confinement and since the hydrogen molecules are light and have large rotational constants, both the discrete translational and rotational levels are well separated in energy. Rotational states are characterized by the rotational quantum number J=0,1,2,... . Translational states are described by different quantum numbers depending on the nanocavity considered. For hydrogen in the small cage of clathrate sII, it was suggested to use two quantum numbers of the 2D isotropic oscillator plus a Cartesian quantum number for the third dimension.[26,29] For hydrogen in the large cage of sII, the translational energy levels were described using the quantum numbers of the 3D harmonic oscillator.[32] Here, changes in the translational energy levels will be simply labeled Δn=0,1,2,... for hydrogen in both types of cages.

The rotational wavefunctions are symmetric for rotational states with even J and anti-symmetric for rotational states with odd J. In the case of the homonuclear isotopologues H_2 and D_2, the symmetry constraints on the total wavefunctions result in the existence of two different allotropic species: *para* and *ortho*. H_2 molecules with total nuclear spin I=0 are referred to as *para*-H_2 (p-H_2) and can only exist with even rotational states J=0,2,... . H_2 molecules with I=1 are referred to as *ortho*-H_2 (o-H_2) and can only exist with odd rotational states J=1,3,... . On the other hand, p-D_2 refers to the D_2 molecules with I=1 and odd J, and o-D_2 refers to the D_2 molecules with I=0 or 2 and even J. Transitions that interchange *para* and *ortho* species thus necessarily involve changes in rotational state (they can also include simultaneous changes in translational state). Also, the first rotational transition (ΔJ=1), or rotational *fundamental*, necessarily involves o-p conversion, as it corresponds to the purely rotational (Δn=0) transition between the ground state of p-H_2 (J=0) and the ground state of o-H_2 (J=1), or between the ground state of o-D_2 (J=0) and the ground state of p-D_2 (J=1).

The energies of the rotational states of a diatomic molecule are given by $BJ(J+1)$ with

B the rotational constant, and the degeneracies are given by $2J+1$.[36] B=7.37 meV for a free H_2 molecule within the rigid rotor approximation. Hence, the energy difference between the ground state of p-H_2 (J=0) and the ground state of o-H_2 (J=1) is expected to be 14.74 meV; this means that the rotational fundamental is expected at 14.74 meV. In the gas phase the experimental value for the rotational fundamental (14.6 meV) is indeed very close to this value, whereas in solid (phase I) hydrogen the experimental peak associated to the rotational fundamental is broad and centered at about 14.05 meV.[37] In general, line shift of the rotational fundamental peak from the value of 14.6 meV can be used to monitor the degree of perturbation imposed by the molecular environment on the rotational behavior of the hydrogen molecule. As far as the molecule behaves as a free (or almost free) rotor, rotational energy levels are only marginally perturbed upon confinement with respect to those of the gas phase. This is indeed the case in many confining environments,[13,16,17] including clathrate cages.[29,30,38] Upon exchange of H_2 with D_2 the rotational fundamental is expected to scale by a factor of 2, since $B_{D_2}=B_{H_2}/2$.

Conversely, translational energy levels have a strong dependence upon cage size, as already mentioned in the introduction. For example, within the simple model of a particle constrained within a sphere, the translational energy levels scale as $E \propto 1/mr^2$, where m is the mass of the particle and r is the radius of the sphere.[36] For both H_2 and D_2, the translational fundamental (Δn=1) is defined as the purely translational (ΔJ=0) transition between the ground *para* state and the first excited translational *para* state or between the ground *ortho* state and the first excited translational *ortho* state. The translational fundamental is at energies of approximately 22.5 meV for H_2 confined in fullerene C_{60} (cavity radius of 3.5 Å),[16] at 9–12 meV for H_2 confined in the small cage of clathrate sII,[24,25,39] and at 6–8 meV in the medium cage of clathrate sH.[28,30] It is predicted by simulations[32] to be at ~2.05 meV for H_2 singly occupying a large cage of sII. The translational energies are generally expected to scale by a factor comprised between $\sqrt{2}$ (expected for a harmonic oscillator) and 2 (expected for a squared well potential) upon exchange of H_2 with D_2.[29]

For a hydrogen molecule confined in the small cage of a clathrate sII, degeneracy of both the rotational and translational states is lifted by the angular and radial anisotropy of the potential energy surface for the hydrogen molecule in the cage.[24,25,29] For H_2 in the small cage of sII, previous INS studies[24,25,39] reported the triplet associated with the ground state of o-H_2 (J=1) at approximately 13.7, 14.5, and 15.2 meV, indicating an energy splitting of approximately 1.5 meV. Similar values were given by theoretical studies.[26,27] The first excited translational level is also split into a triplet and the three energy sub-levels were reported to be at 8.8, 9.9 meV, and 12.5 meV in ref 25, and at 8.8, 10.0, and 12.8 meV in ref 24 for H_2 in the small cage. The triplet is thus characterized by a large energy splitting of about 4 meV–a result also supported by theoretical investigations.[26,27]

The experimental energy levels as given in ref 25 for the first excited translational and rotational states of H_2 confined in the small cage of clathrate sII are reported in Figure 1a while the energy sub-levels are reported in Figure 1b (Figure 1a reports their weighted averages). In other words, for the purpose of illustration, Figure 1a neglects the removal of degeneracy of the states and Figure 1b takes it into account. Transitions between the quantum roto-translational states of H_2 in the small cage (SC) of clathrate sII are labeled in this paper as follows: "SC1" is the rotational fundamental (J=1→0 or 0→1, Δn=0), "SC2" is the translational fundamental for o-H_2 (J=1→1, Δn=1) and "SC3" is the simultaneous change in rotational and translational state between the ground state of o-H$_2$ and the first excited translational state of p-H$_2$ (J=1→0 or 0→1, Δn=1).

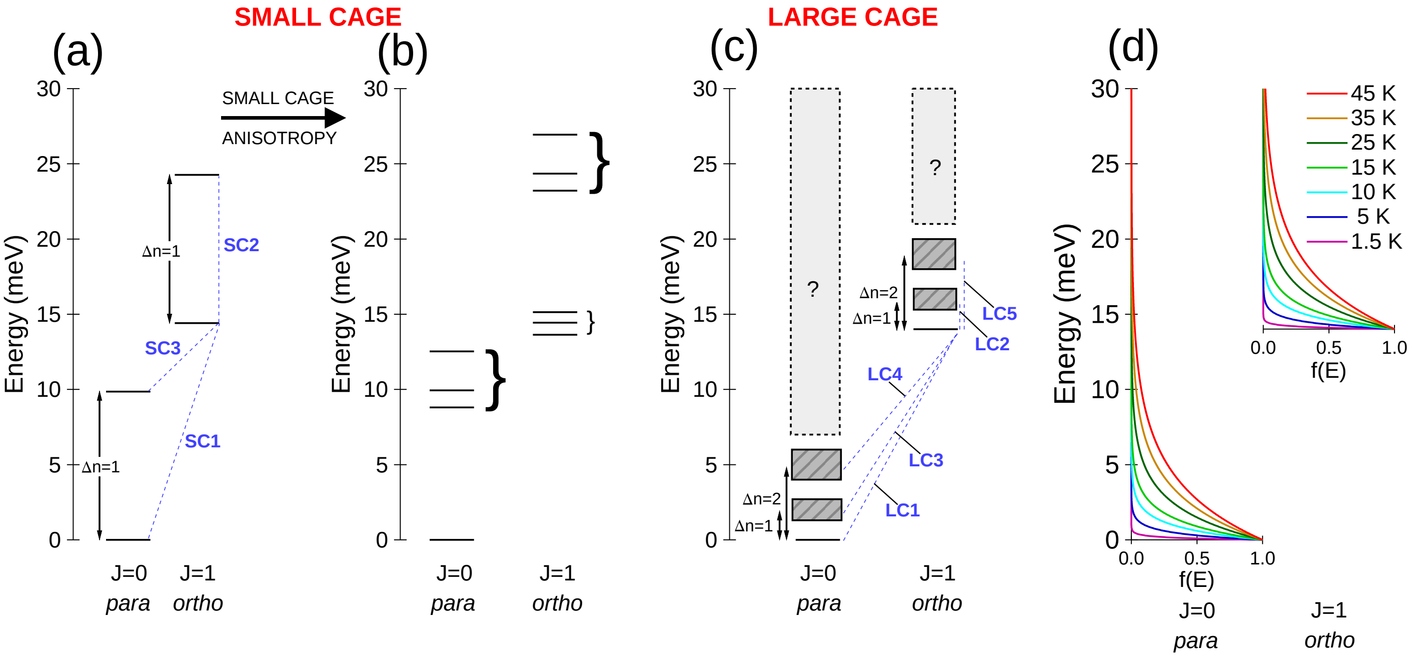

Figure 1: (a) Scheme showing the energy levels of the first excited rotational and translational states of H$_2$ in the small cage of clathrate sII at ambient P. The removal of degeneracy of the states is neglected. (b) Same as panel a, but the removal of degeneracy of the states is considered. The energy levels and sublevels in panels a and b were taken from ref 25. (c) Scheme showing the energy levels of the first excited rotational, and first and second excited translational states of H$_2$ in the large cage of clathrate sII at ambient P. The dashed rectangles represent the energy levels obtained in this work. In panels a and c blue labels identify some transitions we will refer to in the following, with that labeling. (d) Boltzmann factor $f(E)$ as given by eq 1 at different temperatures.

Very little is known about the quantum dynamics of molecular hydrogen confined in the large cage of clathrate sII. By comparing the spectra of simple sII hydrogen hydrate and binary sII hydrogen-tetrahydrofuran hydrate, the contribution from the rotational fundamental of hydrogen in the large cages was calculated to be a broad, unstructured peak centered at about 14 meV.[29] No translational peaks have been experimentally identified in literature. The energy bands for the first and the second excited translational states as obtained in the present work are reported in Figure 1c. Since the large cage of sII is almost spherical, the energy splitting of the first excited translational level of a single hydrogen molecule confined therein is expected to be small. Xu et al.[32] calculated the fully coupled quantum 5D roto-translational energy levels and wavefunctions of a hydrogen molecule *singly* occupying a large cage and, indeed, found very small splittings. The first excited translational level of p-H$_2$ was calculated to be at 2.03–2.06 meV and that of o-D$_2$ at 0.86–0.92 meV. No equivalent information has been reported in literature for o-H$_2$ and p-D$_2$, for which the rotational splitting is also to be considered for the translational fundamental transition.

Transitions of H_2 in the large cage (LC) are labeled in this paper as follows: "LC1"' is the rotational fundamental (J=1→0 or 0→1, Δn=0), "LC2' is the translational fundamental for o-H_2 (J=1→1, Δn=1), "LC3" is the simultaneous change in rotational and translational state between the ground state of o-H_2 and the first excited translational state of p-H_2 (J=1→0 or 0→1, Δn=1), "LC4" is the simultaneous change in rotational and translational state between the ground state of o-H_2 and the second excited translational state of p-H_2 (J=1→0 or 0→1, Δn=2) and "LC5" is the purely translational transition between the ground *ortho* state and the second excited translational *ortho* state (J=1→1, Δn=2).

Finally, the high-pressure structure C1 has the same space group as ice II (R$\overline{3}$) but with significantly perturbed rhombohedral cell parameters.[7] Its water network is characterized by six-membered water rings which are aligned along the c axis to form hexagonal channels in a similar way as in ice II. Hydrogen molecules are located in the channels at approximately midway between two adjacent water rings. Water–hydrogen distances are much shorter than in clathrate hydrates. Based on our unpublished neutron diffraction data on a D_2–D_2O sample, the distance between the equilibrium position of the hydrogen molecule and the closest oxygen atom is only 3.04 Å at 1.4 GPa. In fact, the space accessible in the channels of structure C1 is smaller than that accessible in the voids of all other known hydrate networks, as previously noticed in the literature (see the SI of ref 6). The channel of structure C1 can be seen as a prototypical example of *anisotropic* nanocavity of very reduced dimensions in the same way as fullerene C_{60} can be seen as an example of *isotropic* nanocavity of very reduced dimensions. It has been recognized in the past that hydrogen molecules rotate almost freely in structure C1[7] but no information is available in literature on their translational motion.

2.2 Inelastic neutron scattering cross section. The expression for the differential cross section defining INS spectra is reported in the Appendix. The cross section is linearly proportional to the statistical weight of the initial state of the sample, namely the Boltzmann factor divided by the sum over states (if the state is not degenerated). The Boltzmann factor $f(E)$ is given by:

$$f(E) = \exp\left(-\frac{E}{k_B T}\right), \tag{1}$$

where E is the energy of the state and k_B the Boltzmann constant. For H_2 and D_2 at a given temperature, the quantum levels of each of the two allotropic species are populated according to the Boltzmann distribution, but the two species do *not* equilibrate with each other. At equilibrium and at room temperature, the concentration of o-H_2 in H_2 is 0.75 and the concentration of p-D_2 in D_2 is 0.333. If the two species were able to interconvert with each other, then thermodynamic equilibrium would imply that virtually all hydrogen molecules would be in the lowest energy configuration at low temperature (p-H_2 for H_2 and o-D_2 for D_2). For example at 20 K the concentrations of o-H_2 in H_2 and of p-D_2 in D_2 would be only 0.002 and 0.022, respectively. However, *ortho-para* interconversion can be extremely slow in the absence of a spin catalyst or significant paramagnetic interactions, so o-H_2 and p-D_2 are metastable at low temperature and their concentrations depend on the history of the sample. This is indeed the case for hydrogen confined in clathrate structures, as previously reported in literature.[29,40] It is also the case in structure C1, as shown below in our results.

Figure 1d reports the Boltzmann factor at different temperatures according to eq 1 for p-H$_2$ and o-H$_2$, whose respective ground states are separated by ~14 meV. As can be seen in Figure 1d, at the lowest temperature of our study (1.5 K) only the ground state of p-H$_2$ and the ground state of o-H$_2$ (if o-H$_2$ exists as a metastable configuration in the sample) are macroscopically populated. This will be used in the following in the interpretation of the experimental spectra. In the spectra we measured at 1.5 K on our samples (where o-H$_2$ does exist as a metastable configuration), all observed transitions must involve either the ground state of p-H$_2$ or the ground state of o-H$_2$ as initial state. If the ground state of o-H$_2$ is split into sub-levels more than 0.12 meV apart, then only the lowest-lying sub-level is populated at 1.5 K. The two other sub-levels of the ground state of o-H$_2$ start to be significantly populated at temperatures above 5 K . The first excited translational state of H$_2$ in the *large* cages is significantly populated above 15–25 K and the first excited translational state of H$_2$ in the *small* cages starts to be populated at the highest temperatures of our study (35–45 K).

Finally, since INS from discrete molecular systems is not subjected to selection rules, all transitions are allowed and the expected spectrum consists of all combinations between translational and rotational transitions. However, it is possible to show that contributions to the neutron spectra from purely translational transitions of o-H$_2$ and from transitions that interchange o-H$_2$ and p-H$_2$ scale as the square of the incoherent neutron scattering length b_i, while the contribution from purely translational transitions of p-H$_2$ scales as the square of the coherent neutron scattering length b_c.[16] For the proton[41] b_c^2 is only 2% of b_i^2 and, therefore, the scattering intensity arising from purely translational transitions of p-H$_2$ is negligible and will not be considered in the following. For the deuteron b_c^2 and b_i^2 are comparable[41] and no similar considerations apply. The derivation of this result is reported in the Appendix.

2.3 Diffusion model for hydrogen molecules inside the large cage of clathrate sII. By neutron diffraction, Lokshin et al.[3] have shown that the equilibrium positions of four D$_2$ molecules confined in the large cage of clathrate sII at low T (below 50 K) are located at a distance of approximately 1.80 Å from the center of the cage, arranged at the corners (vertexes) of a regular tetrahedron (thus located at 2.93 Å from each other). Each position is located directly behind the center of one of the four tetrahedrally positioned hexagonal water faces of the cage. Lokshin et al.[3] did not study the dependence on temperature of the equilibrium positions and did not consider the cases of cage occupations smaller than four. Later, several simulations[31,42,43] supported the view provided by neutron diffraction[3] and investigated the effect of changing temperature and cage occupation on the equilibrium positions.

The diffusive (classical) motion performed by hydrogen molecules inside the large cage of sII has been recently investigated by quasielastic neutron scattering.[35] Here we are interested at the quantum equivalent of the diffusive jump motion observed by Russina et al.[35] Upon decreasing temperature, the diffusion mechanism for the confined hydrogen molecules is expected to become quantized and quantized translational excitations for hydrogen in the large cage should appear in the low-temperature spectra as inelastic (Stokes and anti-Stokes) peaks. In practice, upon cooling down, the quasielastic signal in the spectra progressively vanishes and inelastic peaks gradually dominate the signal. The crossover is expected when the De Broglie thermal wavelength λ_{th} of hydrogen becomes roughly comparable to the characteristic confinement size. Considering the van der Waals radius of the oxygen atom, the radius of the accessible volume is about 1.9–2.7 Å in the small cage and 3.3–3.5 Å in the large cage of clathrate sII.[35] The De Broglie thermal wavelength is defined as:

$$\lambda_{th} = \frac{h}{\sqrt{2\pi M k_b T}}, \tag{2}$$

where M is the mass of the molecule. It is comparable to the radius of the accessible volume in the large cage at about 10–15 K for H_2 and 5–10 K for D_2. The values of λ_{th} for H_2 and D_2 below 45 K are plotted in Figure S3 of the SI.

In this work, the inelastic peaks associated with the translational fundamental for o-H_2 in the large cage (J=1→1, Δn=1) will be fitted by Gaussian functions. The dependence of their intensity $I(Q)$ on the modulus Q of the wavevector transfer will be fitted by

$$I(Q) = A \exp\left(-\frac{1}{3}Q^2{<}u^2{>}\right)\left[j_0^2(Q\frac{d_{HH}}{2}) + 2j_2^2(Q\frac{d_{HH}}{2})\right]\left[1 - j_0(Qd)\right] + B, \tag{3}$$

where A is an arbitrary scaling factor including all Q-independent factors, $j_l(x)$ is the l^{th}-order spherical Bessel function of the first kind, and B is a flat background. In the previous expression, $\exp\left(-\frac{1}{3}Q^2{<}u^2{>}\right)$ is the Debye-Waller factor, ${<}u^2{>}$ being the mean square displacement of the proton. Then $\left[j_0^2(Q\frac{d_{HH}}{2}) + 2j_2^2(Q\frac{d_{HH}}{2})\right]$ comes from the rotational form factor for the transition J=1→1 within the rotating harmonic oscillator model, d_{HH} being the bond length of the hydrogen molecule (0.741 Å), as reported for example in refs 29,44. Finally, $[1 - j_0(Qd)]$ is the well-known formula for the jump motion between two sites separated by a distance d (see for example ref 45 and references therein). Eq 3 is valid under the assumption that vibrational, rotational, and translational degrees of freedom are not coupled. The four parameters $A, B, {<}u^2{>}$, and d were left free to vary in our fits.

3. Experimental

3.1 Sample preparation. All samples of this study were initially prepared following the same procedure in the form of clathrate sII hydrogen hydrate (H_2–D_2O or D_2–D_2O). Preparations were performed at the Helmholtz-Centre Berlin (Germany) by exposing ice I_h spheres at 244 K to H_2 or D_2 gas at 0.28 GPa. Ice spheres with typical diameter of several tens of micrometers were formed by spraying D_2O water into liquid N_2 and, in order to limit contamination with H_2O frost, the spraying was performed in a sealed glovebox under inert N_2 atmosphere. We prepared four H_2–D_2O and one D_2–D_2O hydrate samples; in the following, we label them with numbers from 1 to 5 as illustrated in Table 1. Samples were grown in cylindrical aluminum vials of 6 or 8 mm in diameter, ∼1 or 2 cm^3 each, and stored using a liquid N_2 dewar.

We observed by neutron diffraction that samples prepared following this procedure have average hydrogen occupations of typically 0.85–1.0 molecules in the small cage and 1.5–1.8 molecules in the large cage. Samples labeled 1 and 4 of this study have been characterized on the neutron diffractometer D20 at the Institut Laue-Langevin prior to the INS experiments. Their diffraction patterns and Rietveld fits are reported in section 1 of the Supporting Information (SI). We obtained average cage occupations of 1.05 H_2 molecules in the small cage and 1.78 H_2 molecules in the large cage for sample 1, and 0.87 D_2 molecules in the small cage and 1.70 D_2 molecules in the large cage for sample 4.

3.2 Instruments. IN5 and IN6 are direct-geometry time-of-flight spectrometers using cold neutrons at the Institut Laue-Langevin. During the measurements on IN5, the wavelength λ of the incoming neutrons was 3.0, 3.5, 4.8, or 6.0 Å, corresponding to instrumental elastic energy resolutions of respectively 0.35, 0.22, 0.09, or 0.05 meV full width at half maximum. The covered Q range at zero energy transfer ($\hbar\omega$=0) is given by $0.2/\lambda$[Å]–$11.8/\lambda$[Å] (for example 0.04–2.46 Å^{-1} for λ=4.8 Å). During the IN6 experiment, λ was 5.1 Å, corresponding to an elastic energy resolution of 0.08 meV full width at half maximum and a covered Q range at zero energy transfer of 0.3–2.05 Å^{-1}. The instrumental energy resolution is nearly Gaussian on IN5 (down to 1/10 000 of its height) and has a small Lorentzian component on IN6. The data recorded in those investigations are openly available.[46–48]

3.3 Experimental protocol and high-pressure equipment. Experimental conditions of all measurements performed in this study on IN5 and IN6 are summarized in Table 1. The crystal structure of the samples could be checked simultaneously with the INS measurements from the powder diffraction patterns which were obtained directly on IN5 or IN6 by considering the elastic scattering only. The samples contained no detectable unreacted ice I_h. However, sample labeled 4 contained ~10% of stacking-faulty ice I.

Table 1: Experimental conditions of the measurements performed in this study

label	composition	structure	P(GPa)	T(K)	instrument	λ	subsection
1	H_2–D_2O	sII	ambient	1.5	IN5	3.0, 3.5, 4.8, 6.0	4.1
2	H_2–D_2O	sII	ambient	1.5, 5, 15, 25, 35, 45	IN5	4.8	4.1
2	H_2–D_2O	sII	0.25	1.5, 5, 10, 15	IN5	4.8	4.2
2	H_2–D_2O	sII	0.3	25	IN5	4.8	4.2
3	He–H_2–D_2O	sII	0.4	1.8, 5, 10, 15, 25	IN5	4.8	4.3
3	He–H_2–D_2O	sII	0.5	35, 45	IN5	4.8	4.3
4	D_2–D_2O	sII	ambient	1.5	IN5	4.8	4.4
4	D_2–D_2O	sII	ambient	1.5, 5, 10, 15, 25	IN5	6.0	4.4
5	H_2–D_2O	C1	1.4	6, 40	IN6	5.1	4.5

Samples labeled 1 to 4 were measured on IN5. Sample temperature was controlled using a standard "orange" cryostat. Sample labeled 1 (clathrate sII H_2–D_2O) was measured with four different incident neutron wavelengths (3.0, 3.5, 4.8, and 6.0 Å) at ambient P and 1.5 K. Corresponding results are reported in subsection 4.1.

Sample labeled 2 (clathrate sII H_2–D_2O) was first measured at ambient P and different temperatures between 1.5 and 45 K and then measured at 0.25–0.3 GPa and different temperatures between 1.5 and 25 K within the same pressure cell. Results are presented in subsections 4.1 and 4.2, respectively. We used a continuously-loaded cylindrical gas pressure cell of aluminum alloy. The internal diameter of this cell is 6 mm and thereby the sample could be measured in the same cylindrical aluminum vial in which it had been prepared. Helium was used as the pressure transmitting gas because it has no incoherent neutron scattering cross section and its freezing pressure is higher than any other substance. Pressure was measured by a manometer attached to the capillary connecting the cell with the gas compressor. As long as helium is fluid, the manometer reading is strictly the pressure on the sample.

The measurement of sample 2 at 0.25–0.3 GPa was complicated by the fact that helium gas may enter the clathrate structure, even at temperatures as low as 30 K. During many compression runs, we observed the IN5 diffraction pattern of the sample to change as a function of time as helium "contaminated" the sample (on a time scale of typically ten minutes at 30 K). To overcome this obstacle, the aluminum vial containing sample 2 was plugged using a copper plug covered by indium and we exposed the sample to helium gas for a time as short as possible (of the order of a few minutes) and solid helium was used to keep the sample under pressure for the duration of the measurements ($\sim$10 hours). As the target pressure for our experiment was 0.3 GPa and the freezing temperature of helium at this pressure is around 30 K, helium gas pressure was increased to 0.3 GPa at the sample temperature of 30 K. The increase took only a few minutes and was fast enough to avoid contamination of the sample. As soon as pressure reached 0.3 GPa helium solidified; then the sample was cooled down to 1.5 K and measured at different T (1.5, 5, 10, 15, and 25 K). We checked that at all investigated temperatures from 1.5 to 25 K, the IN5 diffraction patterns of the sample can be successfully refined without considering inclusion of helium. Examples of IN5 diffraction patterns of sample 2 at ambient P and at 0.25 GPa are presented in Figure S4 of the SI. Finally, it must be noted that in our experimental setup, i.e. at approximately constant volume, the helium solidification at 0.3 GPa induced a small pressure drop, which can be estimated, based on the known change in molar volume for helium in these conditions,[49] to be approximately 0.05 GPa. So, measurements at 1.5, 5, 10, and 15 K were taken at 0.25 GPa (instead of 0.3 GPa) while at 25 K the pressure was 0.3 GPa because helium was liquid again (see Table 1).

Sample labeled 3 (clathrate sII He–H_2–D_2O) was a helium-contaminated clathrate sII H_2–D_2O at 0.4–0.5 GPa and low T. We compressed a simple H_2 hydrate sample to 0.5 GPa at 45 K, then we let helium contaminate the sample during approximately 20 minutes and, eventually, we decreased the temperature and measured the produced binary hydrogen-helium hydrate at 1.5, 5, 10, 15, 25, 35, and 45 K. Upon cooling down the temperature from 45 K at 0.5 GPa, helium solidified and pressure dropped down by 0.1 GPa to 0.4 GPa. Hence, measurements at 1.5, 5, 10, 15, and 25 K were taken at 0.4 GPa and measurements at 35 and 45 K were taken at 0.5 GPa (see Table 1). Corresponding results are presented in subsection 4.3. As the compression was performed on the instrument, we were able to follow its effect on the diffraction pattern of the sample. We took 2 minutes scans and observed the IN5 diffraction pattern of the sample to substantially change within the first ten minutes following the compression and to remain constant afterward. This is in agreement with the recent observation that helium can migrate remarkably easily into the empty clathrate sII at temperatures as low as 20–30 K.[50] On the other hand, based on our experience with the leaching process of neon,[51] we do not expect that H_2 is able to migrate out of the structure at 45 K. We also noticed that after releasing pressure and increasing temperature to 80–90 K the diffraction pattern of the sample changed back to the starting pattern of H_2 hydrate and that the recovered sample showed low-temperature spectra almost identical to those of the starting sample. This indicates that helium contamination is reversible and that hydrogen occupation in the sample is not affected. In summary, we interpret our observations as follows: at 0.5 GPa and 45 K helium gas entered the clathrate structure on a minute time scale and occupied the large cages exclusively (which were not completely filled in the starting sample) until the maximum (four-fold) cage occupation was achieved. This would imply that about 2.2 helium atoms occupied the large cages in average. The IN5 diffraction pattern of clathrate sII He–H_2 hydrate at 0.4 GPa and 1.5 K (sample 3) is presented in Figure S5 of the SI and compared to the expected patterns of simple He hydrate and binary He–H_2 hydrate with different cage occupations.

Finally, sample labeled 4 (clathrate sII D_2–D_2O) was measured at ambient P and different temperatures between 1.5 and 25 K. Results for D_2–D_2O are presented in subsection 4.4.

On the instrument IN6 we measured H_2–D_2O having structure C1 at 1.4 GPa and low T (sample 5). To reach such a high pressure, we employed the VX5 Paris-Edinburgh press in combination with a loading clamp and recently developed ceramics anvils which are highly transparent to neutrons.[52] Approximately 40 mm^3 of sample was loaded in the clamp module[53] of the press and compressed to 1.4 GPa at liquid nitrogen temperature by applying a load of 140–150 kN on the anvils. Once the sample was under pressure, the assembled clamp was warmed up from liquid nitrogen temperature to room T and inserted in the Paris-Edinburgh press. Afterward, the press was installed on IN6 and T was decreased by cooling down the whole Paris-Edinburgh press in a dedicated cryostat. Simple H_2 hydrate was measured at 1.4 GPa and temperatures of 6 and 40 K (see Table 1). The P uncertainty is about 0.1 GPa. Corresponding results are presented in subsection 4.5. More details on the experimental setup and on the loading procedure were given in ref 54. To allow for a meaningful comparison between spectra recorded on the same instrument, we measured IN6 spectra of clathrate sII H_2–D_2O at ambient P and temperatures of 1.5 and 40 K. This complementary measurement is not reported in Table 1 but the spectra are presented in subsection 4.5.

4. Results

Experimental INS spectra reported in this section represent the measured intensity, which is proportional to the dynamic structure factor $S(2\theta, \hbar\omega)$, as a function of energy transfer $\hbar\omega$. Since the signal from the sample gains intensity with Q, excluding data at low scattering angles increases the signal-to-noise ratio. All IN5 spectra were summed over the scattering angle 2θ range between 40 and 135°; IN6 spectra were summed over the scattering angles between 24 and 115°. None of the peaks and bands observed in the spectra are dispersive with Q. To illustrate this, individual Q cuts of one specific spectrum (clathrate sII H_2 hydrate at ambient P and 1.5 K) are reported in Figure S6 of the SI, as an example. In most plots error bars of the IN5 spectra are omitted for clarity; they are 3–4% of the value at most, except for the D_2 hydrate sample (subsection 4.4) for which they are slightly bigger.

The energy transfer $\hbar\omega$ is defined here as being positive (resp. negative) in case of energy gain for the sample (resp. loss). Then excitations appearing at positive (resp. negative) energies correspond to upward (resp. downward) transitions in the energy schemes of Figures 1a, 1b and 1c. The event for which $\hbar\omega$ is positive (resp. negative) is denoted Stokes (resp. anti-Stokes) scattering. Every measured peak and band in our INS spectra will be assigned in the following to a quantum roto-translational transition of hydrogen in the small cage or in the large cage and referred to as one of the labels defined in subsection 2.1 and reported in Figures 1a and 1c: SC1, SC2, SC3, LC1, LC2, LC3, LC4, and LC5. Also, our assignment of the measured features to those labels is systematically reported (in blue) in the following figures. It has been previously shown that the signal due to lattice vibrations, which is expected to give a weak double-peak band between 5 and 12 meV (and thus between −12 and −5 meV as well), is largely dominated by the overwhelming signal associated with the dynamics of the protons in the hydrogen molecules.[39]

4.1 Clathrate sII H_2 hydrate at ambient pressure. Figure 2 reports the spectra of H_2 hydrate having sII, measured at 1.5 K with four different neutron wavelengths λ between 3.0 and 6.0 Å. Many peaks and bands appear in the spectra over most of the plotted energy transfer range. Their intensity is modulated with Q and therefore their relative intensity may differ between spectra at different neutron wavelengths, as the accessible region in the $(Q,\hbar\omega)$ space depends on λ. For the same reason, the accessible $\hbar\omega$ range on the Stokes side differ between the four spectra of Figure 2.

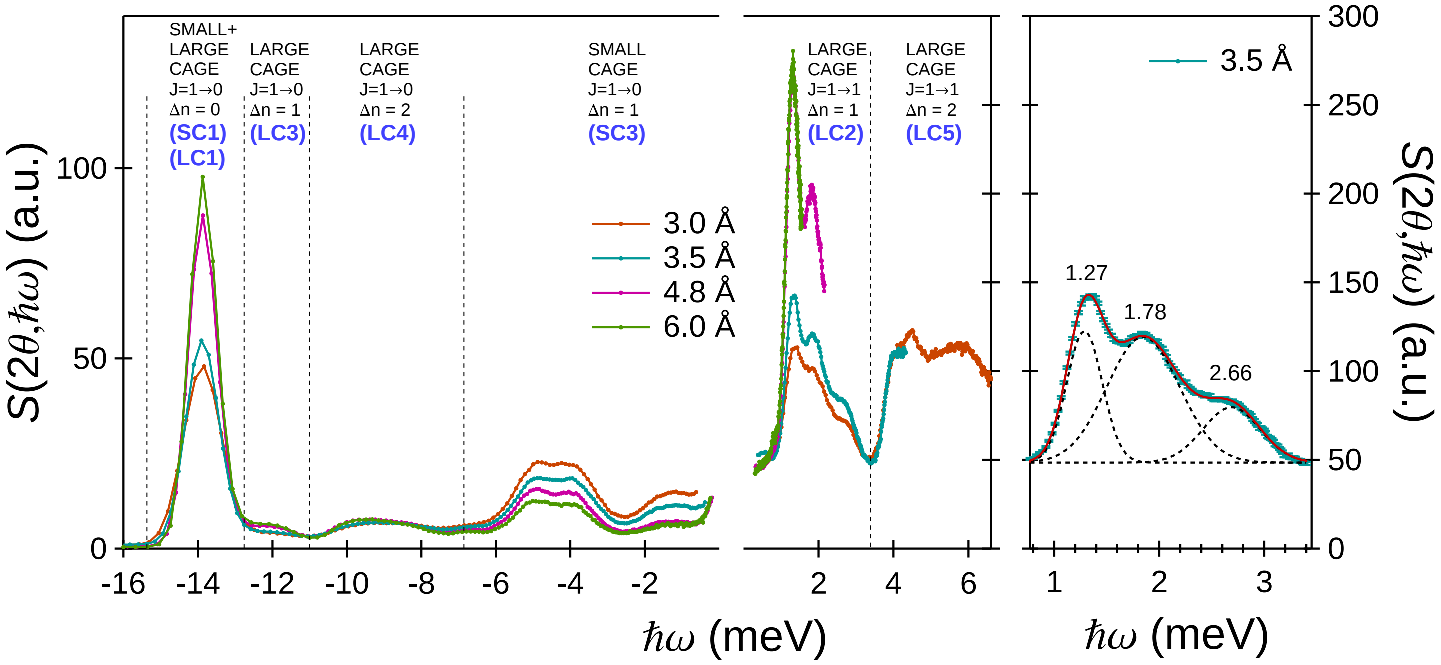

Figure 2: Left: IN5 spectra of clathrate sII H_2 hydrate at ambient P and 1.5 K (sample 1 of Table 1), measured with the indicated incident neutron wavelengths. The elastic line is not plotted; positive and negative $\hbar\omega$ have different y-axis scales. Right: Spectrum at 3.5 Å in the range 0.9–3.2 meV compared to its total best fit and the three individual Gaussian components.

The anti-Stokes side of the spectra contains an intense peak at about −14 meV corresponding to the downward SC1 and LC1 rotational fundamental transitions for H_2 in the small *and* large cages of clathrate sII.[24,25,29,39] The peak is centered at −13.8 meV at ambient P and 1.5 K. Contributions from H_2 in the small and large cages of the structure are superposed. The observation of this peak having o-H_2 as initial state demonstrates that o-H_2 exists as a metastable configuration in our sample, as expected from literature observations.[29,40]

The second more intense signal on the anti-Stokes side in the spectra of Figure 2 is constituted of three peaks located at about −5, −4, and −1 meV. We assign those three excitations to the downward SC3 transition from the ground *ortho* state to the first excited translational *para* state for H_2 in the small cages. A fit of the spectrum collected with λ=3.0 Å using three Gaussian functions show that the peaks are located at −4.94(2), −3.80(2), and −1.19(2) meV. Those values are in excellent agreement with the energy differences between the lowest-lying sub-level of the ground state of o-H_2 (13.7 meV in ref 25) and the three sub-levels of the first excited translational state of p-H_2 (8.8, 9.9, and 12.5 meV in ref 25). A band centered at about −4.5 meV had been previously reported in literature for binary sII hydrogen-tetrahydrofuran clathrate hydrate and interpreted exactly the same way.[24] However, in ref 24 the double-peak structure of the band was not resolved and the peak at −1.19 meV was not accessible.

The Stokes side in the spectra of Figure 2 contains three intense peaks in the range between 1 and 3 meV. We assign those three excitations to the upward LC2 translational fundamental transition for o-H_2 in the large cages. As can be seen in Figure 2, the spectrum measured at 3.5 Å is well fitted by three Gaussian functions and a flat background over the range from 1 to 3 meV. With the principle of detailed balance taken into account, the fit provides peak positions of 1.265(1), 1.780(7), and 2.66(1) meV at ambient P and 1.5 K. Respective peak areas (in a constant-Q spectrum) at ambient P and 1.5 K are 174(1), 218(1), and 54(2) in arbitrary units.

The intensity of the three peaks as a function of Q was estimated by integrating the spectrum measured at 3.0 Å over three strips centered in 1.3, 1.85, and 2.7 meV. The integration ranges were 0.2 meV broad and the Q step was 0.08 Å^{-1}. The results of this integration are reported in Figure 3. The intensity of the three peaks has maxima at about 1.6 Å^{-1} and is well fitted using eq 3 (Figure 3). The fits provide jump length d values of about 2.25 Å with no significant difference between the three inelastic excitations and mean squared displacement $<u^2>$ values ranging between 0.12 and 0.35 Å^2. Specifically, we found d=2.27(6), 2.20(4), and 2.25(3) Å and $<u^2>$=0.35(3), 0.28(2), and 0.12(1) Å^2 for the peaks at 1.3, 1.85, and 2.7 meV, respectively.

The spectrum of Figure 2 collected with a wavelength of 3.0 Å contains an additional signal in the Stokes side, in the range between 4 and 6 meV. The signal consists of a narrow peak at about 4.1 meV and a broad peak centered at about 5.3 meV. We assign both peaks to the upward LC5 purely translational transition from the ground *ortho* state to the second excited translational *ortho* state for H_2 molecules in the large cages.

Finally, spectra of Figure 2 show a weak peak at −12 meV and a large unstructured weak band centered at about −9 meV. We assign the peak at −12 meV to the downward LC3 transition from the ground *ortho* state to the first excited translational *para* state for H_2 in the large cages. Similarly, we assign the band at −9 meV to the downward LC4 transition from the ground *ortho* state to the second excited translational *para* state for H_2 in the large cages. The energies indeed correspond to the energy difference between the ground state of o-H_2 (14 meV from ref 29) and the first excited translational state of p-H_2 (between 1 and 3 meV as found above) and to the energy difference between the same level and the second excited translational state of p-H_2 (between 4 and 6 meV as found above).

Figure 4 reports the temperature dependence of the spectra of H_2 hydrate having sII between 1.5 and 45 K. This measurement as well as those shown in subsections 4.2 and 4.3

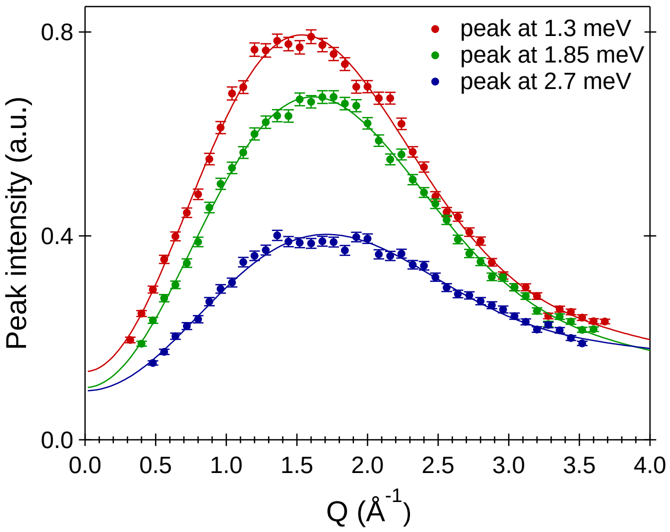

Figure 3: Q dependence of the measured intensity of the peaks at 1.3, 1.85, and 2.7 meV in the spectrum of clathrate sII H_2 hydrate measured with λ=3.0 Å and reported in Figure 2. Best fits using eq 3 are also shown.

was performed using an incident neutron wavelength of 4.8 Å to optimize the neutron flux on the sample. However, in this instrumental configuration the accessible energy transfer range is narrower and therefore on the Stokes side the peak at 2.66 meV and the band between 4 and 6 meV could not be accessed.

As T increases, the rotational fundamental peak (downward SC1 and LC1 transitions) at -13.8 meV develops a shoulder on the left-hand side and loses intensity, so that the total peak area is approximately constant (Figure 4). This can be readily understood as follows: at 1.5 K only the lowest lying sub-level of the ground state of o-H_2 is populated, while the two other levels become progressively populated as temperature is increased (see Figure 1d).

As can be seen in Figure 4, the two low-energy peaks in the range 1–2 meV of the spectra (upward LC2 transition) progressively loose intensity upon increasing T. Between 5 and 25 K, as the first excited translational level of o-H_2 becomes populated, the signal associated with the downward LC2 transition is clearly observed in the range between -3 and -1 meV. This is the anti-Stokes equivalent of the signal appearing between 1 to 3 meV.

On the other hand, with increasing T a quasielastic signal appears in the spectra (Figure 4). This can be understood within the scenario mentioned in subsection 2.3. Upon increasing T, the dynamics of H_2 progressively changes from a quantum to a classical regime in a temperature range around 10–15 K as the De Broglie thermal wavelength becomes comparable to the characteristic confinement size. Correspondingly, the inelastic intensities loose intensity and the quasielastic signal gains intensity.

At 35 and 45 K, the quasielastic broadening is well reproduced by a Lorentzian function whose width is Q independent over the investigated Q range. This is illustrated in Figure S7 of the SI, which reports the individual Q cuts of the spectrum at 45 K and the Q dependence of the width of the Lorentzian fit. The quasielastic signal physically originates from the intra-cage jump motion of H_2 molecules in the large cage of the structure, being

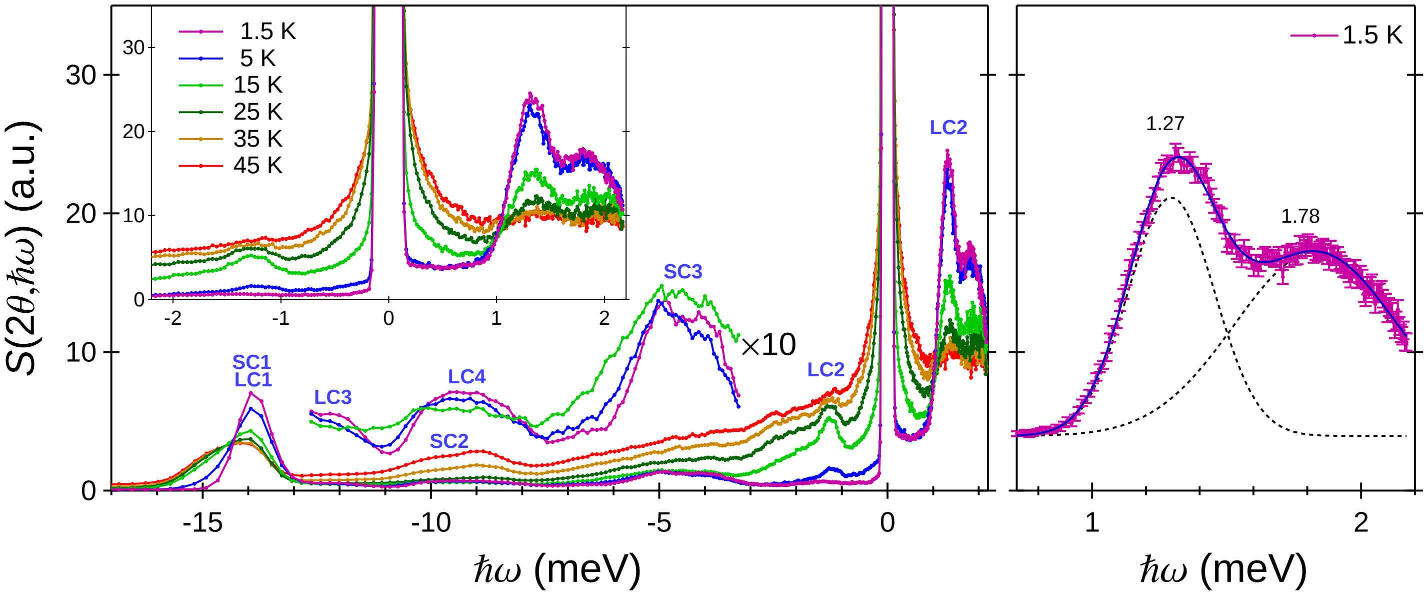

Figure 4: Left: IN5 spectra of clathrate sII H_2 hydrate at ambient P (sample 2 of Table 1), at the indicated temperatures, measured with λ=4.8 Å. In the inset, the same spectra are plotted over a shorter energy transfer range to highlight the low-energy peaks. Right: Stokes low-energy peaks in the spectrum at 1.5 K compared to the total best fit and the two individual Gaussian components.

the classical equivalent of the low-temperature inelastic peaks. Our fits provide average half widths at half maximum of approximately 0.57 and 0.74 meV at 35 and 45 K, respectively, corresponding to characteristic times of approximately 1.2 and 0.9 picoseconds. It must be noticed that the quasielastic contribution from H_2 in the small cages is too slow to contribute over the T range investigated here.[35,55]

Figure 4 also shows that with increasing T from 1.5 to 15 K the peak at -12 meV (downward LC3 transition), the band at -9 meV (downward LC4 transition) and the band at -5 to -4 meV (downward SC3 transition) become less well defined in the spectra. At 15 K they are already almost indistinguishable from the tail of the quasielastic signal, which is comparable to them in intensity. For the band at -9 meV and the band at -5 to -4 meV one can clearly see a shoulder developing on the left-hand side with increasing T, in the same way as the peak at -13.8 meV also develops a similar shoulder on the left-hand side. This results from the fact that the population in the ground state of o-H_2 is progressively shared between the three energy sub-levels as T increases (see Figure 1d).

Finally, spectra at 35 and 45 K in Figure 4 contain an additional signal on the anti-Stokes side, namely a double-peak band at -10 to -9 meV which gains intensity with increasing T. The band can be assigned to the downward SC2 translational fundamental transition for o-H_2 in the small cages. In particular, it corresponds to the transition from the two lowest-lying sub-levels of the first excited translational state of o-H_2 to its ground state. Energies match indeed the literature values of 8.8 and 9.9 meV from ref 25 (see Figure 1b). This band can be observed at 35–45 K on the anti-Stokes side because the energy levels start to be significantly populated at those temperatures (see Figure 1d).

4.2 Clathrate sII H_2 hydrate at 0.25–0.3 GPa. Upon compression to 0.25–0.3 GPa, the spectra change significantly. Figure 5 reports the spectra of H_2 hydrate having sII at 0.25–0.3 GPa and temperatures between 1.5 and 25 K. For comparison the spectrum at ambient pressure and 1.5 K is reported again. As can be seen in Figure 5, the rotational fundamental peak (downward SC1 and LC1 transitions) is unchanged while all other features are shifted in energy as an effect of compression.

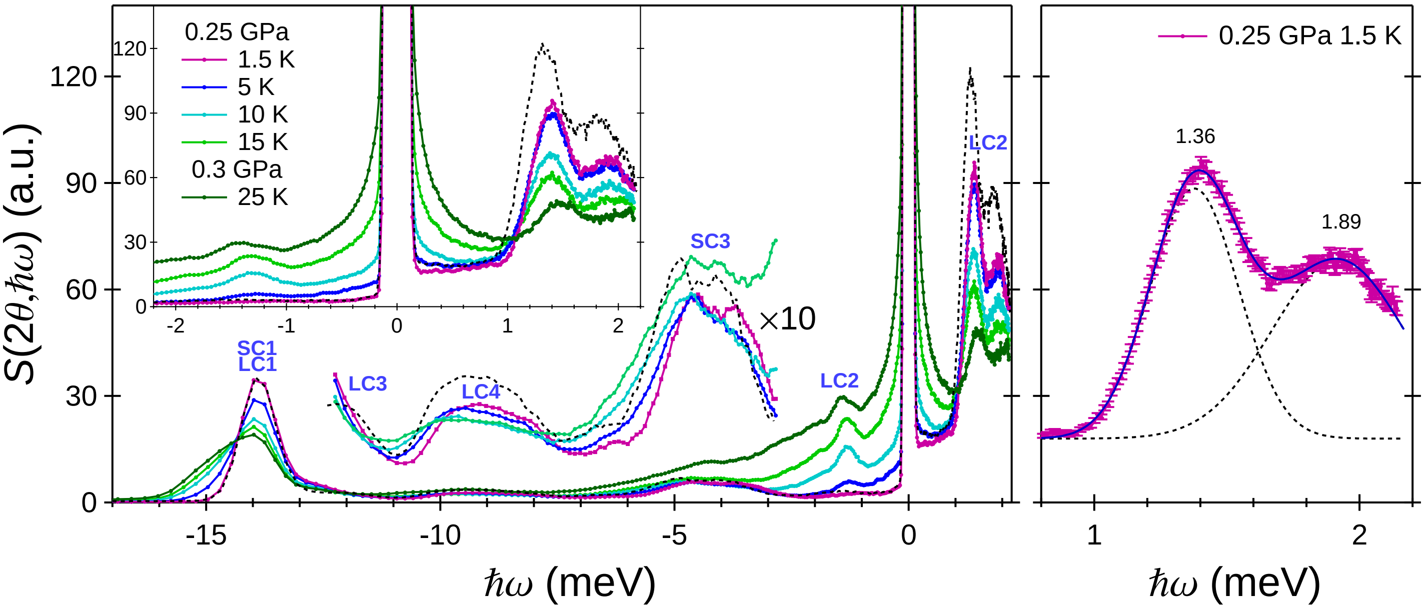

Figure 5: Left: IN5 spectra of clathrate sII H_2 hydrate at 0.25 GPa (sample 2 of Table 1), at the indicated temperatures, measured with λ=4.8 Å. In the inset, spectra are plotted over a shorter energy transfer range to highlight the low-energy modes. The black dashed line is the arbitrarily normalized spectrum of sII H_2 hydrate at ambient P and 1.5 K already presented in Figure 4. Right: Stokes low-energy peaks in the spectrum at 1.5 K compared to the total best fit and the two individual Gaussian components.

The band at −5 to −4 meV (downward SC3 transition) shifts to smaller energies by approximately 0.3 meV (Figure 5). This is the expected effect of applying pressure: the confinement size for H_2 in the small cage decreases and thus the energy of the first excited translational *para* state for H_2 in the small cages increases.

Upon increasing P, the translational fundamental peaks (upward LC2 transition) at 1–2 meV shift to higher energies by approximately 0.1 meV, indicating stronger confinement for H_2 molecules in the large cages. A fit using two Gaussian functions and a flat background shows that the peaks have shifted from 1.27 and 1.78 meV to 1.36 and 1.89 meV when comparing ambient P to 0.25 GPa. As previously mentioned in subsection 3.3, at the highest investigated T of 25 K the pressure was 0.3 GPa; correspondingly, the two peaks are further shifted by the additional pressure. With increasing T a quasielastic signal progressively appears while the inelastic low-energy peaks loose intensity, reproducing the crossover previously commented for the ambient-P spectra of Figure 4.

Finally, in the spectra of sII H_2 hydrate at 0.25 GPa the band at -10 to -9 meV (downward LC4 transition) is shifted to smaller energies by approximately 0.2 meV (Figure 5) compared to the ambient-P spectra, consistently with an increase in the energy of the second excited translational *ortho* state for H_2 in the large cages upon reducing the size of the large cages. The peak at about -12 meV (downward LC3 transition) cannot be distinguished in Figure 5 due to a small contamination of He in the large cages, which translates into a peak at about the same energy as will be shown in the next subsection.

4.3 Clathrate sII He–H_2 hydrate at 0.4–0.5 GPa. Inclusion of helium in the large cages of the structure implies major changes in the spectra. Figure 6 reports the spectra of He–H_2 hydrate having sII at 0.4–0.5 GPa and temperatures between 1.8 and 45 K. For comparison the spectrum at ambient pressure and 1.5 K is reported again. The binary He–H_2 hydrate was obtained as described in subsection 3.3 and, as explained therein, helium massively occupies the large cages of the structure while hydrogen occupation in both cages is unchanged.

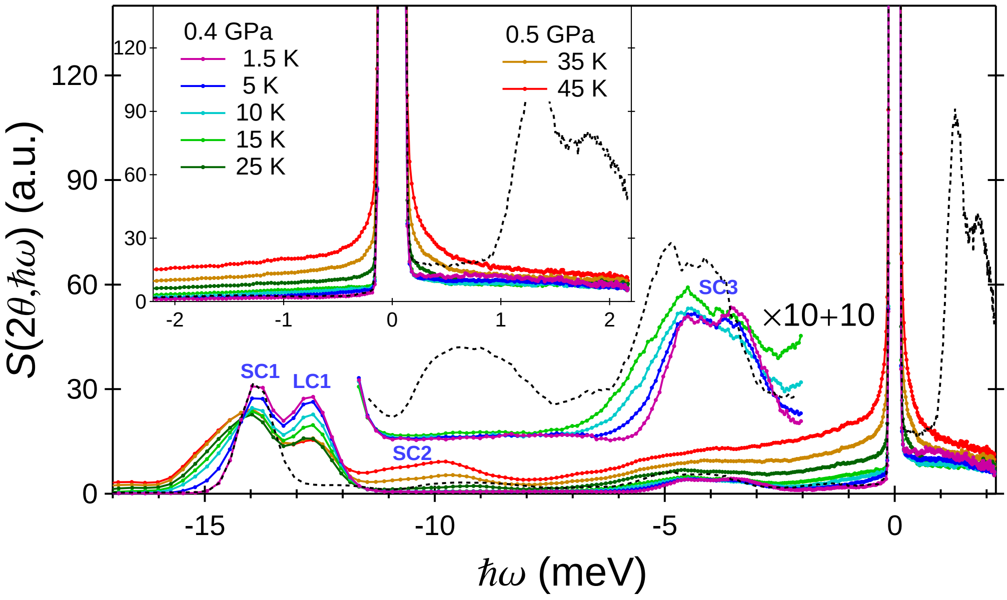

Figure 6: IN5 spectra of binary clathrate sII He–H_2 hydrate at 0.4 GPa (sample 3 of Table 1), at the indicated temperatures, measured with λ=4.8 Å. In the inset, the same spectra are plotted over a shorter energy transfer range to highlight the absence of low-energy modes. The black dashed line is the arbitrarily normalized spectrum of sII H_2 hydrate at ambient P and 1.5 K already presented in Figure 4.

As can be seen in Figure 6, the peak at -13.8 meV slightly shifted to -14.0 meV while a strong new peak appeared at -12.8 meV as an effect of helium inclusion in the large cages. The new peak has a temperature dependence very comparable to that of the peak at -14.0 meV and a comparable Q dependence (see Figure S8 of the SI for the Q dependence of the peaks area). The peak at -14.0 meV is likely to correspond to the rotational fundamental peak (downward SC1 transition) for H_2 in the *small* cages and the new peak at -12.8 meV would correspond to the rotational fundamental peak (downward LC1 transition) for H_2 in the *large* cages filled by helium.

Figure 6 also shows that the band at -5 to -4 meV (downward SC3 transition) is further shifted to smaller energies compared to the spectra of H_2 hydrate at 0.25 GPa reported in Figure 5. This is an effect of further reducing the size of the small cages.

Remarkably, no low-energy peaks (upward LC2 transition) and almost no quasielastic signal are observed in the spectra of He–H_2 hydrate at 0.4–0.5 GPa. This indicates that the translational motion for H_2 in the large cage is hindered upon inclusion of helium in that cage. Consistently, the band associated with the downward LC4 transition is not observed in the spectra either. It is clear from Figure 6 that the intensity of the quasielastic signal is dramatically reduced upon inclusion of helium compared to the spectra of Figure 4 and 5.

Finally, the band centered between -10 to -9 meV in the spectra of H_2 hydrate at ambient P and 35–45 K (downward SC3 transition) is shifted to higher energies by almost 1 meV in the spectra of Figure 6, indicating a massive ($\sim$0.8 meV) upshift of the first excited translational level for H_2 in the small cages.

4.4 Clathrate sII D_2 hydrate at ambient pressure. Figure 7 reports the spectra of D_2 hydrate having sII at ambient P and temperatures between 1.5 and 25 K, measured with an incident neutron wavelength of 6.0 Å. We will restrict our discussion to the effect of substituting H_2 with D_2 on the low-energy modes and therefore spectra of Figure 7 are plotted over a small $\hbar\omega$ range close to the elastic line. Because of the smaller neutron scattering cross section of the deuteron compared to the proton, the spectra of D_2–D_2O are affected by a poorer signal to noise ratio compared to the spectra of H_2–D_2O. Nevertheless, their quality is still satisfactory to determine the energy associated with the different excitations.

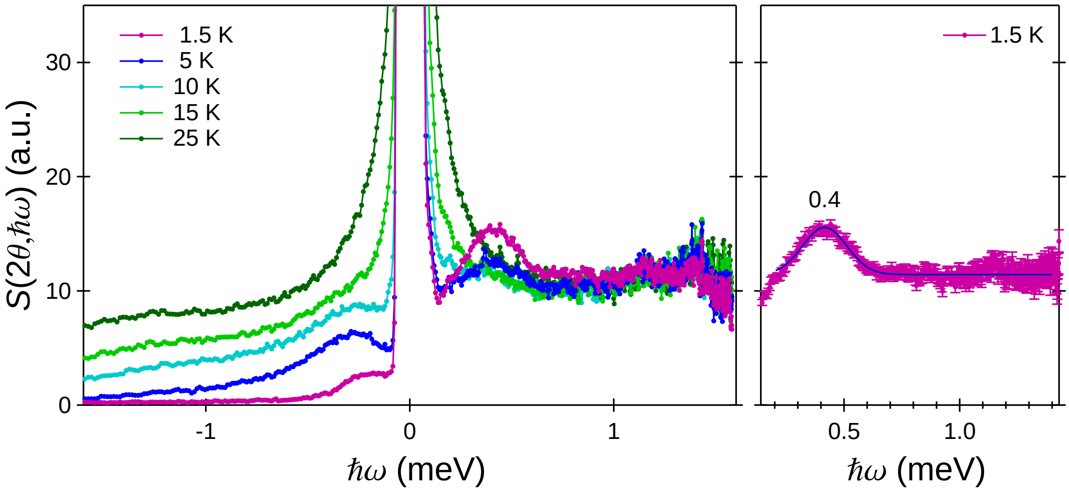

Figure 7: Left: IN5 spectra of clathrate sII D_2 hydrate at ambient P (sample 4 of Table 1), at the indicated temperatures, measured with λ=6.0 Å. Right: Stokes low-energy peak in the spectrum at 1.5 K compared to its best Gaussian fit.

The spectra of D_2 hydrate at 1.5, 5, and 10 K contain a clear peak at 0.4 meV, which has to be assigned to the upward translational fundamental transition of D_2 molecules confined in the large cages of the structure. The peak is well fitted by a Gaussian function and a flat background, as shown in Figure 7 for the spectrum at 1.5 K. Its anti-Stokes equivalent, associated with the downward translational fundamental transition of D_2 confined in the large cages, is clearly observed on the anti-Stokes side of the spectra at 5 and 10 K in Figure 7.

The Q dependence of the intensity of the peak at 0.4 meV was calculated using the spectrum measured at 1.5 K with an incident neutron wavelength of 4.8 Å (not shown in Figure 7) and is reported in Figure S9 of the SI. Similarly to the previously shown case of H_2 hydrate (subsection 4.1), the calculation was done by integrating the spectrum over a 0.15 meV-broad strip centered at 0.4 meV. The intensity of the peak has a maximum at about 1.5 $Å^{-1}$ and can be fitted using eq 3 provided that either the parameter $<u^2>$ or d is fixed. This is because over the small Q range accessible with λ=4.8 Å, the parameters d and $<u^2>$ cannot be adjusted simultaneously. Choosing to fix $<u^2>$ to two thirds its value for H_2 (0.35 $Å^2$) the fit provides a jump length d=2.54(3) Å.

No other peak is observed over the range between 0.6 and 1.6 meV on the Stokes side of the spectra (see Figure 7). We note that the error bars are relatively large over that range and that a small amount of H_2 impurities contained in the cages of our D_2–D_2O sample must also contribute above 1 meV. In addition, the energy level structure of D_2 is expected to be substantially more congested compared to that of H_2 and this may lead to peaks partially superposing each other in the spectra. We also note that the high flat background measured in the range above 0.6 meV of the spectra strongly suggests that indeed other excitations exist but could not be resolved.

Upon increasing T, the peak at 0.4 meV progressively looses intensity and a quasielastic signal appears, indicating that the dynamics of D_2 changes from a quantum to a classical regime. When comparing Figure 7 to Figure 4, it is clear that the crossover occurs at lower temperatures for D_2 compared to H_2. This observation is in agreement with the fact that the De Broglie thermal wavelength of D_2 is smaller than that of H_2 and already comparable to the characteristic confinement size in the large cage at about 5–10 K. Finally, it must be noted that the quasielastic signal observed in the spectra of Figure 7 is presumably partially due to H_2 impurities. As the incoherent neutron scattering cross section of the proton is 40 times larger than that of the deuteron, the scattering arising from 2–3% H_2 impurities in the sample contributes substantially to the signal.

4.5 C1 H_2 hydrate at 1.4 GPa. Figure 8 reports the spectra of H_2 hydrate in the C1 structure at 1.4 GPa, at two different temperatures (6 and 40 K). Data statistics is poorer compared to that of all previously shown spectra due to the limited amount of sample contained in the high-pressure cell (the VX5 Paris-Edinburgh press) and to the small aperture of the cell in the vertical direction. For comparison, Figure 8 also reports the ambient-P spectra of clathrate sII H_2 hydrate at 1.5 and 40 K measured on IN6. This allows us to compare the spectra of the structure C1 and clathrate sII H_2 hydrates measured on the same instrument.

As can be seen on Figure 8, the spectra of structure C1 H_2 hydrate contain only one clear inelastic peak at about -14 meV, corresponding to the downward rotational fundamental transition for H_2 confined in the structure. The peak is centered at -13.8 meV at 6 K and it is significantly narrower than the same peak in the spectra of clathrate sII hydrogen hydrate. This indicates that, similarly to the case of H_2 confined in clathrate sII, the rotational behavior of H_2 confined in structure C1 is only slightly perturbed by the molecular environment,

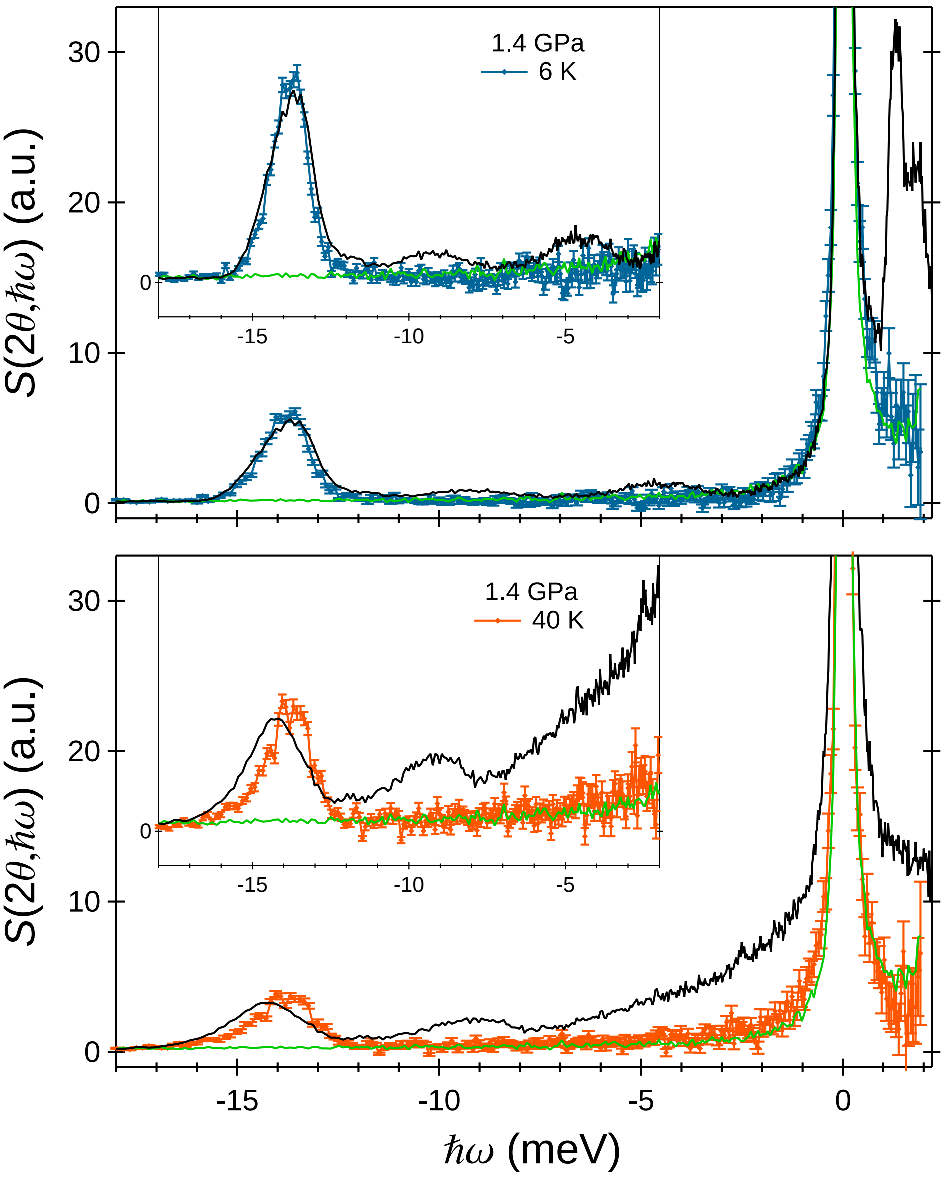

Figure 8: Top: IN6 spectra of structure C1 H_2 hydrate at 1.4 GPa and 6 K (blue, sample 5 of Table 1) and of clathrate sII H_2 hydrate at ambient *P* and 1.5 K (black). Bottom: IN6 spectra of structure C1 H_2 hydrate at 1.4 GPa and 40 K (orange) and of sII H_2 hydrate at ambient *P* and 40 K (black). Spectra were normalized to have the same integrated intensity for the peak at about -14 meV. Instrumental elastic resolution of IN6 as measured by a vanadium scan is reported in light green. In the insets, the same spectra are plotted over a shorter energy transfer range.

despite the extreme confinement.

At 40 K, the same peak at about −14 meV contains a shoulder on the left-hand side (Figure 8). This is also in strong analogy with the observation previously reported for clathrate sII in subsection 4.1 and indicates sizable angular anisotropy of the potential energy surface for the H_2 molecules in structure C1. Nevertheless, at the same T (40 K) the peak of structure C1 is again narrower than that of clathrate sII. It is difficult to compare those effects quantitatively since, for clathrate sII, the peak contains superposed contributions from H_2 in the small and large cages.

No other inelastic peaks or bands are observed in the spectra of structure C1 H_2 hydrate and, interestingly, no quasielastic signal at 40 K either. This is consistent with the fact that the space accessible for the hydrogen molecule in the cavity of structure C1 is significantly smaller compared to the space accessible in the cages of clathrate sII, as mentioned in subsection 2.1.

5. Discussion

5.1 Quantum translational dynamics of H_2 and D_2 confined in the large cage of clathrate sII. The triplet at energies between 1 and 3 meV in the low-temperature spectra of clathrate sII H_2 hydrate can be unambiguously assigned to the translational fundamental transition for o-H_2 in the large cage, that is, to the purely translational transition between the ground and the first excited translational *ortho* states (J=1→1, Δn=1). At ambient P and 1.5 K, the fit provides peak positions of 1.27, 1.78, and 2.66 meV (see subsection 4.1), indicating a significant splitting of about 1.4 meV. The Q dependences of the intensity of the three peaks are very well reproduced using the well-known formula for the jump motion between two sites (eq 3) and provide jump lengths of about 2.25 Å, with no significant difference between the three peaks. Previous literature experimental[3,35] and simulation[31,42,43] studies have found that at temperatures below ∼50 K the hydrogen atoms are arranged in the large cage at the corners of a tetrahedron. It is then very tempting to conclude that the quantized jump motion we observe here takes place between equilibrium sites at the four corners of a tetrahedron and that our experimental jump length of about 2.25 Å is a measure of the edges of the tetrahedron. This value is to be compared with the value of 2.93 Å obtained by Lokshin et al.[3] for D_2 and that of 2.4 Å obtained by Russina et al.[35] for H_2 at the lowest temperature they investigated.

As described in subsection 4.4, only a single peak at about 0.4 meV could be detected in the low energy transfer range of the spectra of clathrate sII D_2 hydrate at low temperature. While there is little doubt that the peak at 0.4 meV can be assigned to the translational fundamental transition for D_2 in the large cage, it is not completely clear at present how this peak is to be compared to the triplet we found for H_2. It is possible that other peaks could not be detected by our experiment for different reasons (because very broad and partially suporposing each other, or masked by the elastic line, or masked by the contribution from H_2 impurities). The Q dependence of the intensity of the peak at 0.4 meV in D_2 hydrate provides a jump length of about 2.55 Å, again using the formula for the jump motion between two sites (eq 3). This suggests that D_2 molecules are at a larger distance from the cage center compared to H_2 molecules at the same temperature and for a comparable average cage occupation. Nevertheless, as mentioned above, the value for D_2 is slightly doubtful since the energy resolution requirement constrains the Q range accessible in the spectra. To our knowledge, no investigation of the effect of substituting H_2 with D_2 on the equilibrium positions of hydrogen within the large cage of sII exists in literature; the experimental studies measured either D_2 (by neutron diffraction)[3] or H_2 (by quasielastic neutron scattering),[35] and all simulation studies considered H_2 exclusively.[31,42,43]

Explaining the existence of a triplet in the spectra of H_2 and a single peak in the spectra of D_2 is not straightforward, also because of the anomalously large shift between the peak positions for H_2 (1.27, 1.78, and 2.66 meV) and the peak position for D_2 (0.4 meV). By analogy with the triplet associated with the translational fundamental transition for H_2 molecules singly occupying the small cage of clathrate sII,[24,25,29] it seems intuitive to interpret our triplet in a similar way–as being due to the translational fundamental transition for H_2 molecules singly occupying the large cage. However, this interpretation is incompatible with the large shift in peak positions between H_2 and D_2. If the peaks at 1.27, 1.78, and 2.66 meV were associated with the motion of a single H_2 molecule, they would have to scale in energy in a rather conventional way upon exchange of H_2 with D_2, for example by a factor close to 2.3 as found in the simulation work by Xu et al.[32] Hence, they cannot be shifted to 0.4 meV for D_2. For comparison, the equivalent mode of hydrogen in the (singly occupied) small cages of sII was experimentally found to scale by a factor of about 1.4 upon exchange of H_2 with HD.[25]

We infer that the triplet in the spectra of H_2 could be related to the existence of a distribution of different hydrogen occupations for the large cages (we recall that the refined average large cage occupation for the H_2 and D_2 hydrate samples are 1.78 and 1.70, respectively). The peak at 1.27 meV would be associated with the translational dynamics of a single H_2 molecule in a singly, doubly, or triply occupied cage, the peak at 1.78 meV would come from the correlated translations of two H_2 molecules in the same doubly occupied cage, and finally the peak at 2.66 meV would come from the correlated translations of three H_2 molecules in the same triply occupied cage. Then the peak at 1.27 meV would be expected to scale in energy by a factor close to 2 upon exchange of H_2 guests with D_2 and should be at around 0.65 meV for D_2. The peaks at 1.78 and 2.66 meV would scale by factors as large as 4 and 6, respectively, and should be at around 0.45 meV for D_2. This hypothesis has to be confirmed by future studies. Within this interpretation, relative peak areas can be used to estimate the fraction of H_2 molecules that are hosted in singly, doubly and triply occupied large cages. This part is developed in section 2 of the SI. We recall that Xu et al.[32] calculated roto-translational energy levels of p-H_2 and o-D_2 hosted in a singly occupied large cage of sII and found that the three almost degenerate energy sub-levels of the first excited translational state of p-H_2 are located at 2.03–2.06 meV. This is in rather modest agreement with our experimental value of 1.27 meV for o-H_2, assuming that our interpretation is correct and that H_2 in singly occupied large cages indeed give rise to the peak at 1.27 meV.

It should be stressed that we obtain essentially the same jump length for the three inelastic peaks of our spectra for H_2. This would indicate that the size of the tetrahedron is not significantly affected by the cage occupation. Conversely, simulation studies[31,42,43] found a strong dependence on the cage occupation number for the radial distance from the H_2 to the cage center. For example, a recent path-integral molecular dynamics simulation work[43] reported average radial distances at 50 K of about 1.3 Å for occupation one, 1.6 Å for occupation two, 1.75 Å for occupation three, and 1.9 Å for occupation four. Those values can be converted into 2.1, 2.6, 2.9, and 3.1 Å for the edges of the circumscribed tetrahedron. However, none of the simulation studies[31,42,43] have explored the temperature regime below 25 K where the tetrahedron size likely becomes smaller *and* less sensitive to the occupation number due to the delocalized nature of the proton.

In subsection 4.1 we also identified the second excited translational state of o-H_2 in the large cage of sII at energies between 4 and 6 meV but could not discriminate between contributions from single and multiple hydrogen occupations. For comparison, Xu et al.[32] predicted the second excited translational state of p-H_2 in a singly occupied large cage as five sub-levels very close to each other between 4.86 at 5.62 meV and a sixth at considerably higher energy (9.0 meV, which is out of the energy range accessible in our spectra). In this case the agreement between experiments and simulations seems to be good.

Finally, in subsection 4.3 we observed that all transitions involving an excited translational state of H_2 in the large cage as initial and/or final state are suppressed in the spectra upon inclusion of He atoms in the large cages. This result can be rationalized very easily as follows: the four tetrahedrally arranged positions within large cages were all occupied by either hydrogen or helium for this sample and no translational motion was possible (no jumps are expected in the configuration with four molecules on the same tetrahedron). In fact, similarly to the case of simple sII H_2 hydrate, it was recently found[50] that in simple sII He hydrate up to four guest atoms occupy the large cages and sit at the corners of tetrahedron. It is then very reasonable to assume that in our binary He–H_2 hydrate both types of guests also occupy tetrahedrally arranged positions and that a total occupation up to four is possible. Because He atoms can easily migrate into the large cages[50] and based on the changes we have seen in the diffraction patterns (see subsection 3.3), we can conclude that virtually all large cages of our binary He–H_2 hydrate sample must have been filled by a mixture of He and H_2 with the maximum four-fold occupation. Future studies might check if the same suppression of the translational motion can be obtained by filling the large cages with any other sufficiently small guest atom or molecule, including hydrogen itself.

5.2 Effect of pressure on the quantum dynamics of H_2 confined in the small and large cages of clathrate sII. As mentioned in subsection 2.1, it is well known that rotational and translational energy levels of molecular hydrogen inside a nanocavity have very different dependences on the size of confinement. Rotational energies typically remain close to the values of the gas phase, whereas translational energies depend considerably on the confinement size. For example, the first excited rotational state (i.e. the ground state of o-H_2) turned out to be essentially superposed at about 14 meV for H_2 molecules confined in the small[24,25] and large[29] cages of clathrate sII and in the medium cage of sH,[30,38] indicating that H_2 exhibits nearly free rotations in all those cages. On the other hand, the energy of the first excited translational state varies between 9–12 meV for H_2 in the small cages of sII[24,25] to 6–8 meV for H_2 in the medium cages of sH,[28,30] to 1–3 meV for H_2 in the large cages of sII as shown in the present study.

Compressing our clathrate sII H_2 hydrate sample from ambient P to 0.25 GPa induced a small but significant change in the cage sizes. Consistently, we have found that the peak associated with the rotational fundamental (J=1→0, Δn=0) is insensitive to the pressure change while peaks associated with purely translational transitions or transitions involving a simultaneous change of rotational and translational state are very sensitive to pressure variation. Assuming a bulk modulus of about 10 GPa in the P-T range investigated here, the pressure step between ambient and 0.25 GPa corresponds to a change in volume of about 2.5% for hydrogen hydrate. If the compression is homothetic (i.e. the structure shrinks isotropically), the size of both cages is reduced by 0.9% between ambient P and 0.25 GPa.

In subsection 4.2 we have seen that upon compression to 0.25 GPa the band at -5 to -4 meV (downward SC3 transition) of sII H_2 hydrate shifted to smaller energies by $\sim$0.3 meV, the peaks at 1.27 and 1.78 meV (upward LC2 transition) shifted to 1.36 and 1.89 meV, and the band at -10 to -9 meV (downward LC4 transition) shifted to smaller energies by $\sim$0.2 meV. We can thus confidently conclude that for H_2 molecules in the small cage the two lowest-lying sub-levels of the first excited translational state shifts to higher energies by $\sim$0.3 meV, and that for H_2 molecules in the large cage the first excited translational state shifts to higher energies by $\sim$0.1 meV and the second excited translational state shifts to higher energies by $\sim$0.2 meV. The ensemble of these results could be taken as a benchmark for future computational works.

We observed an even stronger shift of the translational energies of H_2 in the small cages for the binary He–H_2 hydrate sample at 0.4–0.5 GPa (see subsection 4.3). The band at -5 to -4 meV (downward SC3 transition) is shifted to smaller energies by $\sim$0.5 meV for this sample compared to simple H_2 hydrate at ambient P, and the double-peak band at -10 to -9 meV (downward SC2 transition) is shifted to higher energies by $\sim$0.8 meV. This indicates that for our binary He–H_2 hydrate sample the first excited translational level of H_2 in the small cages is shifted to higher energies by $\sim$0.5 meV at 0.4 GPa and by $\sim$0.8 meV at 0.5 GPa, compared to simple H_2 hydrate at ambient P. Of course, it is reasonable to imagine that for this specific sample, which contained singly occupied small cages and four-fold occupied large cages, the compression is not homothetic and the small cages are reduced in size much more than the large cages upon compression. Finally, we have also seen a remarkable effect of the inclusion of helium on the rotational behavior of H_2. The new peak observed at -12.8 meV in subsection 4.3 must correspond to the rotational fundamental peak for H_2 in the large cages and therefore reveals an appreciable perturbation of the rotational behavior of the H_2 molecules in the configuration where the large cages are massively occupied by He atoms.

5.3 Quantum dynamics of H_2 confined in structure C1. No spectroscopic studies existed in literature on hydrogen hydrate having the high-pressure structure C1 over the low energy transfer range investigated here. By Raman spectroscopy, Vos et al.[7] measured the peaks associated with the purely rotational (Δn=0) transitions J=0→2 and J=1→3 of H_2 confined in structure C1 (those transitions are generally noted $S_0(0)$ and $S_0(1)$ in the Raman literature). They found the two peaks at approximately 44.6 and 73.8 meV, very close to the values for H_2 in the gas phase (44.0 and 72.8 meV respectively), and concluded that H_2 exhibits nearly free rotation in the channels of structure C1.

In subsection 4.5 we reported our measurement of the purely rotational transition J=1→0 (or downward rotational fundamental transition) of H_2 in structure C1, which is not active in Raman spectroscopy. We found that the corresponding peak is at -13.8 meV at 6 K, again close to the value for H_2 in the gas phase (-14.6 meV). The existence of this peak and the metastability of o-H_2 giving rise to it comes as no surprise. Interestingly, the peak is at the same energy as in simple clathrate sII H_2 hydrate but is narrower. At 40 K the same peak is broader as an effect of increasing T but not as broad as that of H_2 in clathrate sII at the same temperature. Hence, the splitting of the ground state of o-H_2 in structure C1 seems to be relatively small, despite the very strong anisotropy of the water channels where H_2 molecules sit, but straightforward comparison with clathrate sII is not possible because for simple H_2 hydrate the contributions from H_2 in the small and large cages are superposed.

We could not detect any translational peak in the spectra of structure C1 hydrogen hydrate at low temperature. By analogy with the dynamics observed for H_2 confined in the channels of structure C0,[34] one would expect to see a very splitted translational fundamental, with a low-energy mode corresponding to the motion along the direction of the water channels and a high-energy mode corresponding to the motion across the channels. For structure C0, the first component was observed at ∼3 meV and the second at ∼20 meV.[34] The high-energy component should be expected at even higher energy in structure C1 compared to structure C0 (because the radius of the channels is smaller, see subsection 2.1), and therefore would have been inaccessible in the present study. However, the low-energy peak component should have been accessible, if intense enough and at energies below 14 meV. Spectroscopic investigations covering an energy transfer range up to 30–40 meV on the Stokes side will be needed to determine the translational energy levels of H_2 in structure C1. They could also establish the splitting of the ground state of o-H_2 from the peak associated with the upward rotational fundamental transition.

6. Conclusion

To summarize, we investigated the quantum dynamics of H_2 and D_2 molecules confined in hydrate structures as a function of pressure and temperature by inelastic neutron scattering measurements at temperatures between 1.5 and 45 K. The considered hydrate structures were the clathrate structure II and the high-pressure filled ice structure C1.

In clathrate sII hydrogen molecules occupy both small (5^{12}) and large ($5^{12}6^4$) cages. By making use of the fact that the quantum roto-translational energy levels of H_2 in the *small* cage are well-known,[24–27,29,39] we were able to distinguish the translational contribution from hydrogen in the *large* cages, for which only the rotational fundamental was known from literature.[29] The main outcome of this work is the identification of the translational fundamental transition for H_2 in the large cage of clathrate sII, appearing in the low-temperature spectra as a triplet located at energies between 1 and 3 meV. Similarly, we identify the purely translational transition from the ground state to the second excited translational state, appearing in the spectra as two broad bands between 4 and 6 meV.

At ambient P and 1.5 K, the three peaks can be well fitted by Gaussian functions centered at 1.27, 1.78, and 2.66 meV. The Q dependences of the intensity of the three excitations are very well reproduced assuming a jump motion between equilibrium sites inside the cages and provide similar jump lengths of about 2.25 Å. Our results support the accepted view[3,31,35,42,43] that hydrogen molecules confined in the large cages of clathrate sII are preferentially arranged at the corners of a tetrahedron and provide an experimental measure of the edges of the tetrahedron. The observed low-temperature quantized jump motion is likely to be allowed by quantum tunneling through a potential barrier.

The temperature and pressure dependences of the spectrum of H_2 in clathrate sII hydrate were also studied and they both confirm that the low-energy peaks we observe are indeed associated with the translational fundamental for H_2 molecules in the large cage. As temperature increases over the range 1.5–25 K, spectra show a progressive change from low-energy inelastic peaks to quasielastic signal, corresponding to the crossover from quantized to diffusive hydrogen motion.

We also measured a binary He–H_2 hydrate sample having clathrate sII. In this sample, which was produced under an excess of helium gas, the amount of H_2 molecules in the two types of cages is basically unchanged whereas He atoms massively entered the large cages. As a consequence, all transitions involving an excited translational state of H_2 in the large cage as initial and/or final state are suppressed in the spectra. The rotational fundamental transition and the transitions involving translations of H_2 in the small cage remain visible.

Finally, we measured a clathrate sII D_2 hydrate sample and identified a peak at 0.4 meV that must be assigned to the translational fundamental transition for D_2 molecules in the large cage. Comparing the energy of this peak to the energies of the splitted translational fundamental for H_2 (1.27, 1.78, and 2.66 meV) points at a strong, unconventional effect of the isotopic exchange which seems incompatible with a single hydrogen motion and suggests the existence of translations involving one, two, or three H_2 molecules at the same time. Further investigation is needed to shed light on this point. We hope that our study will motivate the development of new methodology for the rigorous fully quantum treatment of the dynamics of multiple H_2 molecules confined inside nanocavities.

Appendix

Let us define $\boldsymbol{k_i}$ and $\boldsymbol{k_f}$ the initial and final neutron wavevectors. The energy transfer $\hbar\omega$ is defined as $(\hbar^2/2m)(k_i^2 - k_f^2)$ and the wavevector transfer $\boldsymbol{Q}$ is defined as $\boldsymbol{k_i} - \boldsymbol{k_f}$. The mass of the neutron is noted by m. We also define E_i and E_f the initial and final energies of the sample. Using the first Born approximation, the partial differential cross section which is accessed experimentally is given by[16,56]

$$\frac{\mathrm{d}^2\sigma}{\mathrm{d}\Omega\mathrm{d}E_f} = \frac{k_f}{k_i}\frac{(2\pi)^4 m^2}{\hbar^4}\sum_{i,f} p_i |\langle f|V|i\rangle|^2 \delta(\hbar\omega + E_i - E_f), \tag{4}$$

with $|i\rangle$ and $|f\rangle$ the initial and final states of the system formed by the sample and the neutron, p_i the statistical weight of the initial state of the sample and $|\langle i|V|f\rangle|$ the matrix element of the interaction potential. The interaction potential from a single H_2 (or D_2) molecule is[16]

$$V = \sum_{\alpha} \mathrm{e}^{i\boldsymbol{Q}\cdot\boldsymbol{R_\alpha}} \left[b_c + \frac{b_i}{2}\boldsymbol{s}\cdot\boldsymbol{I_\alpha} \right], \tag{5}$$

where α=1,2 labels the two protons (or deuterons) within the molecule. Each nucleus has a spin $\boldsymbol{I_\alpha}$ and its position vector is $\boldsymbol{R_\alpha}$=$\boldsymbol{R_0} + (-1)^\alpha \boldsymbol{\rho}/2$, with $\boldsymbol{R_0}$ the vector defining the center of mass of the molecule and $\boldsymbol{\rho}$ the vector connecting the two nuclei. Here b_c and b_i are the coherent and incoherent neutron scattering lengths of the proton (or deuteron). The neutron spin is noted by $\boldsymbol{s}$. Performing the sum over α, eq 5 becomes[16]

$$V = \mathrm{e}^{i\boldsymbol{Q}\cdot\boldsymbol{R_0}} \left[2b_c \cos(\frac{1}{2}\boldsymbol{Q}\cdot\boldsymbol{\rho}) + \frac{b_i}{2}\cos(\frac{1}{2}\boldsymbol{Q}\cdot\boldsymbol{\rho})\boldsymbol{s}\cdot(\boldsymbol{I_1}+\boldsymbol{I_2}) + i\frac{b_i}{2}\sin(\frac{1}{2}\boldsymbol{Q}\cdot\boldsymbol{\rho})\boldsymbol{s}\cdot(\boldsymbol{I_1}-\boldsymbol{I_2}) \right]. \tag{6}$$

For the case of H_2 it is worth commenting eq 6 in some details. The first term of eq 6 scales as b_c. The second term scales as b_i and drives purely translational transitions of o-H_2 only. The third term also scales as b_i and drives transitions that interchange o-H_2 and p-H_2 (these can be purely rotational transitions or a combination of translation and rotation). As b_c^2 is only 2% of b_i^2, eq 6 implies that contribution from the purely translational transitions of p-H_2 to the neutron spectra, which are driven only by the first term, is negligible compared to those from the purely translational transitions of o-H_2 and from the transitions that interchange o-H_2 and p-H_2.

Acknowledgement

This work was supported by the Swiss National Science Foundation under grant number 200021-149847 and by the French state funds managed by ANR within the Blanc International programme PACS under reference ANR-13-IS04-0006-01. We acknowledge the Institut Laue-Langevin for provision of beam time, and Claude Payre and James Maurice for technical assistance during the high-pressure experiments. Our thanks also go to Thomas C. Hansen for help during the measurements on D20 and useful discussions. We thank Robert Pick for a critical reading of the manuscript.

Supporting Information Available

Structural details of samples 1 and 4, tentative estimation of the distribution of the hydrogen occupation numbers of sample 1, and supporting Figures S1 to S9 as described in the text. This material is available free of charge via the Internet at `http://pubs.acs.org/`.

References

(1) Mao, W. L.; Mao, H.-k.; Goncharov, A. F.; Struzhkin, V. V.; Guo, Q.; Hu, J.; Shu, J.; Hemley, R. J.; Somayazulu, M.; Zhao, Y. Hydrogen Clusters in Clathrate Hydrate. *Science* **2002**, *297*, 2247.

(2) Sloan, E. D.; Koh, C. A. *Clathrate Hydrates of Natural Gases*, 3rd ed.; CRC Press: Boca Raton, 2008.

(3) Lokshin, K. A.; Zhao, Y.; He, D.; Mao, W. L.; Mao, H.-k.; Hemley, R. J.; Lobanov, M. V.; Greenblatt, M. Structure and Dynamics of Hydrogen Molecules in the Novel Clathrate Hydrate by High Pressure Neutron Diffraction. *Phys. Rev. Lett.* **2004**, *93*, 125503.

(4) Loveday, J. S.; Nelmes, R. J. High-Pressure Gas Hydrates. *Phys. Chem. Chem. Phys.* **2008**, *10*, 913–1068.

(5) Efimchenko, V. S.; Kuzovnikov, M. A.; Fedotov, V. K.; Sakharov, M. K.; Simonov, S. V.; Tkacz, M. New Phase in the Water–Hydrogen System. *J. Alloys Compd.* **2011**, *509S*, S860–S863.

(6) Amos, D. M.; Donnelly, M.-E.; Teeratchanan, P.; Bull, C. L.; Falenty, A.; Kuhs, W. F.; Hermann, A.; Loveday, J. S. A Chiral Gas–Hydrate Structure Common to the Carbon Dioxide–Water and Hydrogen–Water Systems. *J. Phys. Chem. Lett.* **2017**, *8*, 4295–4299.

(7) Vos, W. L.; Finger, L. W.; Hemley, R. J.; Mao, H.-k. Novel H_2-H_2O Clathrates at High Pressures. *Phys. Rev. Lett.* **1993**, *71*, 3150.

(8) Kim, D.-Y.; Lee, H. Spectroscopic Identification of the Mixed Hydrogen and Carbon Dioxide Clathrate Hydrate. *J. Am. Chem. Soc.* **2005**, *127*, 9996–9997.

(9) Florusse, L. J.; Peters, C. J.; Schoonman, J.; Hester, K. C.; Koh, C. A.; Dec, S. F.; Marsh, K. N.; Sloan, E. D. Stable Low-Pressure Hydrogen Clusters Stored in a Binary Clathrate Hydrate. *Science* **2004**, *306*, 469.

(10) Strobel, T. A.; Koh, C. A.; Sloan, E. D. Water Cavities of sH Clathrate Hydrate Stabilized by Molecular Hydrogen. *J. Phys. Chem. B Lett.* **2008**, *112*, 1885–1887.

(11) Struzhkin, V. V.; Militzer, B.; Mao, W. L.; Mao, H.-k.; Hemley, R. J. Hydrogen Storage in Molecular Clathrates. *Chem. Rev.* **2007**, *107*, 4133–4151.

(12) Kumar, K. V.; Preuss, K.; Titirici, M.-M.; Rodríguez-Reinoso, F. Nanoporous Materials for the Onboard Storage of Natural Gas. *Chem. Rev.* **2017**, *117*, 1796–1825.

(13) Narehood, D. G.; Kostov, M. K.; Eklund, P. C.; Cole, M. W.; Sokol, P. E. Deep Inelastic Neutron Scattering of H_2 in Single-Walled Carbon Nanotubes. *Phys. Rev. B* **2002**, *65*, 233401.

(14) Mondelo-Martell, M.; Huarte-Larrañaga, F. 5D Quantum Dynamics of the H_2@SWNT System: Quantitative Study of the Rotational-Translational Coupling. *J. Chem. Phys.* **2015**, *142*, 084304.

(15) FitzGerald, S. A.; Hopkins, J.; Burkholder, B.; Friedman, M.; Rowsell, J. L. C. Quantum Dynamics of Adsorbed Normal- and Para-H_2, HD, and D_2 in the Microporous Framework MOF-74 Analyzed using Infrared Spectroscopy. *Phys. Rev. B* **2010**, *81*, 104305.

(16) Horsewill, A. J.; Panesar, K. S.; Rols, S.; Ollivier, J.; Johnson, M. R.; Carravetta, M.; Mamone, S.; Levitt, M. H.; Murata, Y.; Komatsu, K. et al. Inelastic Neutron Scattering Investigations of the Quantum Molecular Dynamics of a H_2 Molecule Entrapped inside a Fullerene Cage. *Phys. Rev. B* **2012**, *85*, 205440.

(17) Xu, M.; Jiménez-Ruiz, M.; Johnson, M. R.; Rols, S.; Ye, S.; Carravetta, M.; Denning, M. S.; Lei, X.; Bačić, Z.; Horsewill, A. J. Confirming a Predicted Selection Rule in Inelastic Neutron Scattering Spectroscopy: The Quantum Translator-Rotator H_2 Entrapped Inside C_{60}. *Phys. Rev. Lett.* **2014**, *113*, 123001.

(18) Strobel, T. A.; Ramirez-Cuesta, A. J.; Daemen, L. L.; Bhadram, V. S.; Jenkins, T. A.; Brown, C. M.; Cheng, Y. Quantum Dynamics of H_2 Trapped within Organic Clathrate Cages. *Phys. Rev. Lett.* **2018**, *120*, 120402.

(19) Gutt, C.; Press, W.; Hüller, A.; Tse, J. S.; Casalta, H. The Isotope Effect and Orientational Potentials of Methane Molecules in Gas Hydrates. *J. Chem. Phys.* **2001**, *114*, 4160.

(20) Matanović, I.; Xu, M.; Moskowitz, J. W.; Eckert, J.; Bačić, Z. Methane Molecule Confined in the Small and Large Cages of Structure I Clathrate Hydrate: Quantum Six-Dimensional Calculations of the Coupled Translation-Rotation Eigenstates. *J. Chem. Phys.* **2009**, *131*, 224308.

(21) Chazallon, B.; Itoh, H.; Koza, M.; Kuhs, W. F.; Schober, H. Anharmonicity and Guest–Host Coupling in Clathrate Hydrates. *Phys. Chem. Chem. Phys.* **2002**, *4*, 4809–4816.

(22) Schober, H.; Itoh, H.; Klapproth, A.; Chihaia, V.; Kuhs, W. F. Guest-Host Coupling and Anharmonicity in Clathrate Hydrates. *Eur. Phys. J. E* **2003**, *12*, 41–49.

(23) Tse, J. S.; Klug, D. D.; Zhao, J. Y.; Sturhahn, W.; Alp, E. E.; Baumert, J.; Gutt, C.; Johnson, M. R.; Press, W. Anharmonic Motions of Kr in the Clathrate Hydrate. *Nature Mater.* **2005**, *4*, 917–921.

(24) Tait, K. T.; Trouw, F.; Zhao, Y.; Brown, C. M.; Downs, R. T. Inelastic Neutron Scattering Study of Hydrogen in d_8-THF/D_2O Ice Clathrate. *J. Chem. Phys.* **2007**, *127*, 134505.

(25) Ulivi, L.; Celli, M.; Giannasi, A.; Ramirez-Cuesta, A. J.; Bull, D. J.; Zoppi, M. Quantum Rattling of Molecular Hydrogen in Clathrate Hydrate Nanocavities. *Phys. Rev. B* **2007**, *76*, 161401(R).

(26) Xu, M.; Sebastianelli, F.; Bačić, Z. Quantum Dynamics of H_2, D_2, and HD in the Small Dodecahedral Cage of Clathrate Hydrate: Evaluating H_2-Water Nanocage Interaction Potentials by Comparison of Theory with Inelastic Neutron Scattering Experiments. *J. Chem. Phys.* **2008**, *128*, 244715.

(27) Xu, M.; Ulivi, L.; Celli, M.; Colognesi, D.; Bačić, Z. Quantum Calculation of Inelastic Neutron Scattering Spectra of a Hydrogen Molecule inside a Nanoscale Cavity based on Rigorous Treatment of the Coupled Translation-Rotation Dynamics. *Phys. Rev. B* **2011**, *83*, 241403(R).

(28) Colognesi, D.; Powers, A.; Celli, M.; Xu, M.; Bačić, Z.; Ulivi, L. The HD Molecule in Small and Medium Cages of Clathrate Hydrates: Quantum Dynamics Studied by Neutron Scattering Measurements and Computation. *J. Chem. Phys.* **2014**, *141*, 134501.

(29) Colognesi, D.; Celli, M.; Ulivi, L.; Xu, M.; Bačić, Z. Neutron Scattering Measurements and Computation of the Quantum Dynamics of Hydrogen Molecules trapped in the Small and Large Cages of Clathrate Hydrates. *J. Phys. Chem. A* **2013**, *117*, 7314–7326.

(30) Celli, M.; Powers, A.; Colognesi, D.; Xu, M.; Bačić, Z.; Ulivi, L. Experimental Inelastic Neutron Scattering Spectrum of Hydrogen Hexagonal Clathrate-Hydrate Compared with Rigorous Quantum Simulations. *J. Chem. Phys.* **2013**, *139*, 164507.

(31) Sebastianelli, F.; Xu, M.; Bačić, Z. Quantum Dynamics of Small H_2 and D_2 Clusters in the Large Cage of Structure II Clathrate Hydrate: Energetics, Occupancy, and Vibrationally Averaged Cluster Structures. *J. Chem. Phys.* **2008**, *129*, 244706.

(32) Xu, M.; Sebastianelli, F.; Bačić, Z. Coupled Translation–Rotation Zigenstates of H_2, HD, and D_2 in the Large Cage of Structure II Clathrate Hydrate: Comparison with the Small Cage and Rotational Raman Spectroscopy. *J. Phys. Chem. A* **2009**, *113*, 7601–7609.

(33) Felker, P. M. Fully Quantal Calculation of H_2 Translation-Rotation States in the (p-H_2)$_2$@$5^{12}6^4$ Clathrate Hydrate Inclusion Compound. *J. Chem. Phys.* **2014**, *141*, 184305.

(34) del Rosso, L.; Celli, M.; Colognesi, D.; Rudić, S.; English, N. J.; Burnham, C. J.; Ulivi, L. Dynamics of Hydrogen Guests in Ice XVII Nanopores. *Phys. Rev. Mater.* **2017**, *1*, 065602.

(35) Russina, M.; Kemner, E.; Mezei, F. Intra-Cage Dynamics of Molecular Hydrogen Confined in Cages of Two Different Dimensions of Clathrate Hydrates. *Sci. Rep.* **2016**, *6*, 27417.

(36) Atkins, P. W. *Molecular Quantum Mechanics*, 2nd ed.; Oxford University Press: Oxford, 1983.

(37) Bickermann, A.; Spitzer, H.; Stiller, H.; Scherm, R. The Rotational State $J = 1$ in Orientationally Disordered and Ordered Solid Hydrogen. *Z. Phys. B* **1978**, *31*, 339–343.

(38) Valdés, Á.; Kroes, G.-J. Theoretical Investigation of Two H_2 Molecules Inside the Cages of the Structure H Clathrate Hydrate. *J. Phys. Chem. C* **2012**, *116*, 21664–21672.

(39) Ulivi, L.; Celli, M.; Giannasi, A.; Ramirez-Cuesta, A. J.; Zoppi, M. Inelastic Neutron Scattering from Hydrogen Clathrate Hydrates. *J. Phys.: Condens. Matter* **2008**, *20*, 104242.

(40) Senadheera, L.; Conradi, M. S. Hydrogen Nuclear Spin Relaxation in Hydrogen–Ice Clathrate. *J. Phys. Chem. A* **2008**, *112*, 8303–8309.

(41) Sears, V. F. Neutron Scattering Lengths and Cross Sections. *Neutron News* **1992**, *3*, 29–37.

(42) Witt, A.; Sebastianelli, F.; Tuckerman, M. E.; Bačić, Z. Path Integral Molecular Dynamics Study of Small H_2 Clusters in the Large Cage of Structure II Clathrate Hydrate: Temperature Dependence of Quantum Spatial Distributions. *J. Phys. Chem. C* **2010**, *114*, 20775–20782.

(43) Burnham, C. J.; Futera, Z.; English, N. J. Quantum and Classical Inter-Cage Hopping of Hydrogen Molecules in Clathrate Hydrate: Temperature and Cage-Occupation Effects. *Phys. Chem. Chem. Phys.* **2017**, *19*, 717–728.

(44) Zoppi, M. Neutron scattering of homonuclear diatomic liquids. *Physica B* **1993**, *183*, 235–246.

(45) Bove, L. E.; Klotz, S.; Paciaroni, A.; Sacchetti, F. Anomalous Proton Dynamics in Ice at Low Temperatures. *Phys. Rev. Lett.* **2009**, *103*, 165901.

(46) Bove, L.; Alabarse, F.; Frick, B.; Gaal, R.; Giura, P.; Iizuka, R.; Klotz, S.; Komatsu, K.; Koza, M. M.; Kuhs, W. F. et al. New Frontiers for QENS under High Pressure: Probing Hydrogen Diffusion under Extreme Conditions. **2013**, Institut Laue–Langevin (ILL) doi:10.5291/ILL–DATA.LTP–6–6.

(47) Ranieri, U.; Bove, L. E.; Gaal, R.; Klotz, S.; Koza, M. M.; Kuhs, W. F. Microscopic Diffusion of Hydrogen Molecules in Ice Clathrate under High Pressure. **2016**, Institut Laue–Langevin (ILL) doi:10.5291/ILL–DATA.6–07–5.

(48) Ranieri, U.; Bove, L. E.; Gaal, R.; Klotz, S.; Koza, M. M.; Kuhs, W. F. Microscopic Diffusion of Hydrogen Molecules in Ice Clathrate under High Pressure. **2018**, Institut Laue–Langevin (ILL) doi:10.5291/ILL–DATA.6–07–29.

(49) Mills, L. R.; Liebenberg, H. D.; Bronson, J. C. Equation of State and Melting Properties of ^{4}He from Measurements to 20 kbar. *Phys. Rev. B* **1980**, *21*, 5137–5148.

(50) Kuhs, W. F.; Hansen, T. C.; Falenty, A. Filling Ices with Helium and the Formation of Helium Clathrate Hydrate. *J. Phys. Chem. Lett.* **2018**, *9*, 3194–3198.

(51) Falenty, A.; Hansen, T. C.; Kuhs, W. F. Formation and Properties of Ice XVI Obtained by Emptying a Type sII Clathrate Hydrate. *Nature* **2014**, *516*, 231–233.

(52) Komatsu, K.; Klotz, S.; Shinozaki, A.; Iizuka, R.; Bove, L. E.; Kagi, H. Performance of Ceramic Anvils for High Pressure Neutron Scattering. *High Press. Res.* **2014**, *34*, 494–499.

(53) Klotz, S.; Philippe, J.; Bull, C. L.; Loveday, J. S.; Nelmes, R. J. A 3 kbar Hydrogen-Compatible Gas Loader for Paris-Edinburgh Presses. *High Press. Res.* **2013**, *33*, 214–220.

(54) Ranieri, U.; Koza, M. M.; Kuhs, W. F.; Klotz, S.; Falenty, A.; Gillet, P.; Bove, L. E. Fast Methane Diffusion at the Interface of Two Clathrate Structures. *Nature Comm.* **2017**, *8*, 1076.

(55) Pefoute, E.; Kemner, E.; Soetens, J. C.; Russina, M.; Desmedt, A. Diffusive Motions of Molecular Hydrogen Confined in THF Clathrate Hydrate. *J. Phys. Chem. C* **2012**, *116*, 16823–16829.

(56) Schober, H. An Introduction to the Theory of Nuclear Neutron Scattering in Condensed Matter. *J. Neutron Res.* **2014**, *17*, 109–357.

Supporting information for: Quantum dynamics of H_2 and D_2 confined in hydrate structures as a function of pressure and temperature

Umbertoluca Ranieri,[*,†,‡] Michael Marek Koza,[‡] Werner F. Kuhs,[¶] Richard Gaal,[†] Stefan Klotz,[§] Andrzej Falenty,[¶] Dirk Wallacher,[‖] Jacques Ollivier,[‡] Philippe Gillet,[†] and Livia E. Bove[*,§,†]

†*EPSL, IPHYS, École polytechnique fédérale de Lausanne (EPFL), Station 3, CH-1015 Lausanne, Switzerland*

‡*Institut Laue-Langevin, 71 avenue des Martyrs, CS 20156, 38042 Grenoble, Cedex 9, France*

¶*GZG Abt. Kristallographie, Universität Göttingen, Goldschmidtstrasse 1, 37077 Göttingen, Germany*

§*Sorbonne Université, CNRS UMR 7590, Institut de minéralogie, de physique des matériaux et de cosmochimie, IMPMC, 75005 Paris, France*

‖*Department of Sample Environments, Helmholtz-Zentrum Berlin für Materialien und Energie, Germany*

1. Structural details

Samples labeled 1 and 4 in the main text were measured at ambient pressure by neutron diffraction on the diffractometer D20 at the Institut Laue-Langevin. Sample 1 (clathrate sII H_2 hydrate) was measured at 100 K using a neutron wavelength λ=1.5460 Å and sample 4 (clathrate sII D_2 hydrate) was measured at 110 K using λ=2.4183 Å. A Rietveld refinement of the diffraction patterns was performed using FullProf. Measured patterns and Rietveld refinement results are reported in Figures S1 and S2. Observed and calculated diffraction intensities are in good agreement. Structural parameters are reported in Tables S1 and S2.

During the refinements, occupations of the D atoms forming the water molecules were lowered by 2% to simulate the effect of having some H_2O water contamination in the samples. In order to limit correlations between the parameters, all isotropic displacement factors B_{iso} were kept fixed to reasonable values. Coordinates of the hydrogen or deuterium atoms forming the guest molecules were also fixed. For the small cage we used the fractional coordinates 0, 0, 0.02165 so that the $H \cdots H$ (or $D \cdots D$) distance (0.741 Å) was respected and the center of mass of the guest molecule was at the cage center. For the large cage we used the coordinates 0.401, 0.4316, 0.4316; in this split model H or D atoms are located at the vertices of a small triangle and there are four tetrahedrally arranged triangles per large cage. The edge of the triangle was set to correspond to the $H \cdots H$ (and $D \cdots D$) distance and the edge of the tetrahedron was set to correspond to the approximate value obtained in the main text for the jump length d in our model for the motion of H_2 (2.25 Å). For sample 4 (D_2 hydrate) we included in the refinement a 2% H_2 impurities in the cages.

Lattice constants resulting from the Rietveld refinements are 17.1294(5) and 17.1112(5) Å for samples 1 and 4, respectively. Resulting average cage occupations were 1.05(2) H_2 molecules in the small cage and 1.78(6) H_2 molecules in the large cage for sample 1, and 0.868(6) D_2 molecules in the small cage and 1.70(2) D_2 molecules in the large cage for sample 4.

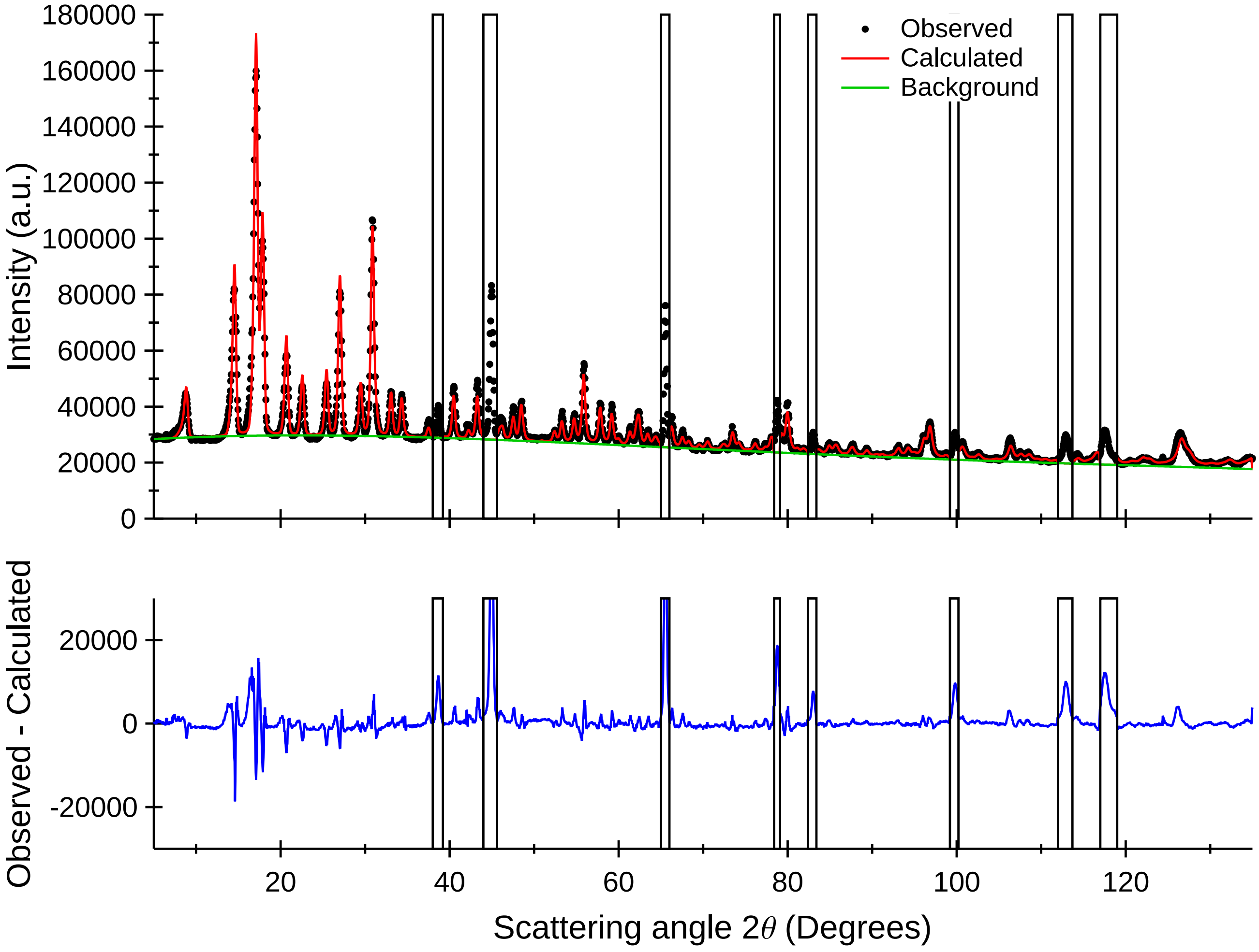

Figure S1: Rietveld refinement results for the D20 diffraction pattern of sample 1 (clathrate sII H_2 hydrate), measured at 100 K using λ=1.5460 Å. Rectangles mark the angular regions excluded in the refinement because affected by the aluminium sample can.

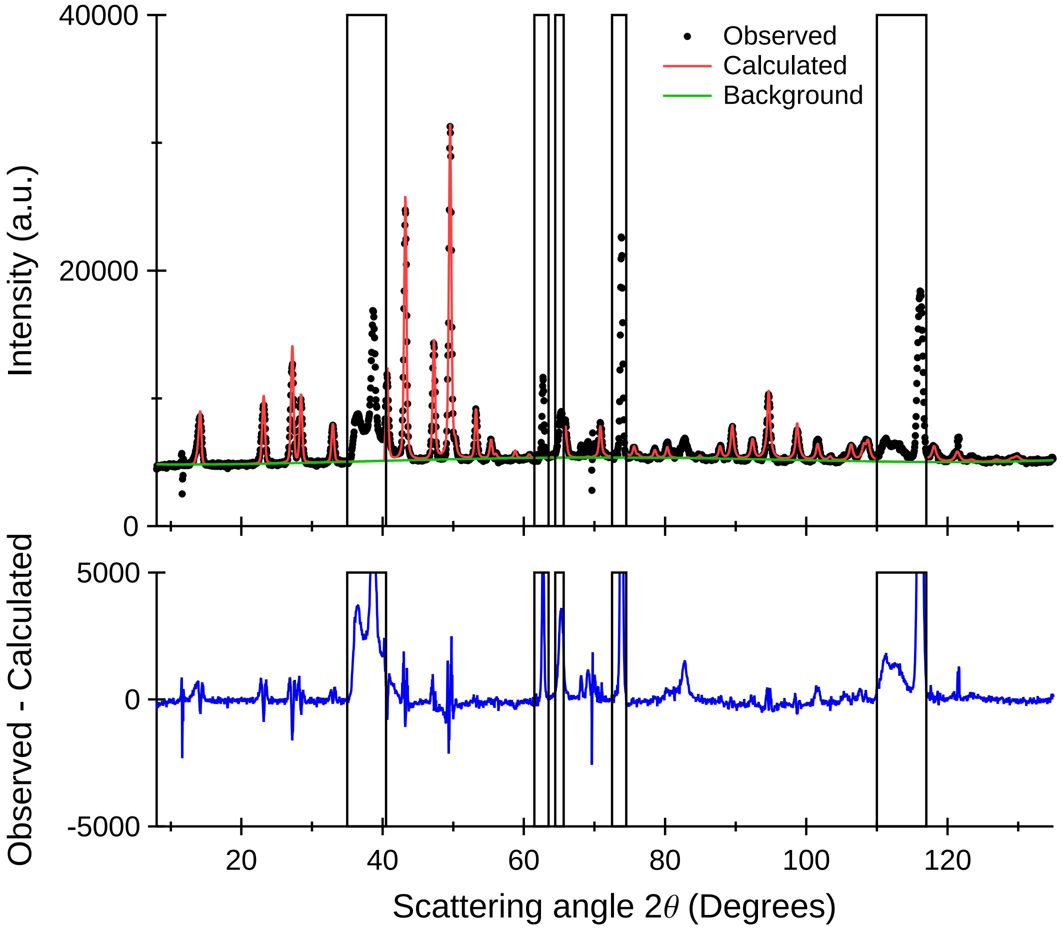

Figure S2: Rietveld refinement results for the D20 diffraction pattern of sample 4 (clathrate sII D_2 hydrate), measured at 110 K using λ=2.4183 Å. Rectangles mark the angular regions excluded in the refinement because affected by the aluminium sample can or by stacking-faulty ice I.

Table S1: Structural parameters for sample 1 (clathrate sII H_2 hydrate). $B_{iso}=8\pi^2<u_{iso}{}^2>$ in Å^2, with $<u_{iso}{}^2>$ the averaged atomic mean square displacement. Occupancy (Occ.) is the occupancy of the crystallographic site multiplied by the site multiplicity and divided by the general multiplicity. The non-zero digits of the estimated standard deviation as resulting from the Rietveld refinement are given in parentheses.

Atom	x	y	z	B_{iso}	Occ.
O1	0.875	0.875	0.875	1.2	0.0417
O2	0.78209(37)	0.78209(37)	0.78209(37)	1.2	0.1667
O3	0.81735(24)	0.81735(24)	0.62859(37)	1.2	0.5
D1	0.84019(47)	0.84019(47)	0.84019(47)	1	0.0817
D2	0.81872(53)	0.81872(53)	0.81872(53)	1	0.0817
D3	0.79514(47)	0.79514(47)	0.72617(55)	1	0.245
D4	0.80446(54)	0.80446(54)	0.68490(63)	1	0.245
D5	0.89137(35)	0.89137(35)	0.63008(73)	1	0.245
D6	0.73222(44)	0.85275(42)	0.58704(47)	1	0.49
H1	0	0	0.02165	20	0.176(3)
H2	0.401	0.4316	0.4316	75	0.148(5)

Table S2: Structural parameters for sample 4 (clathrate sII D_2 hydrate). $B_{iso}=8\pi^2<u_{iso}{}^2>$ in Å^2, with $<u_{iso}{}^2>$ the averaged atomic mean square displacement. Occupancy (Occ.) is the occupancy of the crystallographic site multiplied by the site multiplicity and divided by the general multiplicity. The non-zero digits of the estimated standard deviation as resulting from the Rietveld refinement are given in parentheses.

Atom	x	y	z	B_{iso}	Occ.
O1	0.875	0.875	0.875	1.2	0.0417
O2	0.78338(63)	0.78338(63)	0.78338(63)	1.2	0.1667
O3	0.81474(38)	0.81474(38)	0.62857(51)	1.2	0.5
D1	0.84625(57)	0.84625(57)	0.84625(57)	1	0.0817
D2	0.81569(79)	0.81569(79)	0.81569(79)	1	0.0817
D3	0.79173(75)	0.79173(75)	0.72862(73)	1	0.245
D4	0.80618(89)	0.80618(89)	0.68480(83)	1	0.245
D5	0.89437(45)	0.89437(45)	0.62483(88)	1	0.245
D6	0.73038(84)	0.85619(76)	0.59223(88)	1	0.49
D7	0	0	0.02165	13	0.145(1)
D8	0.401	0.4316	0.4316	50	0.141(2)
H1	0	0	0.02165	20	0.003
H2	0.401	0.4316	0.4316	75	0.003

2. Estimating the distribution of the hydrogen occupations in the large cages of sample 1 from the relative peak areas

If the interpretation given in subsection 5.1 of the main text is correct and the triplet at 1.27, 1.78, and 2.66 meV in the spectra of H_2 is related to the existence of translations involving one, two, or three H_2 molecules at the same time, then it should be possible to estimate the fraction of H_2 molecules that are hosted in singly, doubly and triply occupied large cages from the relative peak areas. This requires that one knows the participation ratios of doubly and triply occupied cages to the peak at 1.27 meV. This information is given by the simple model of a particle performing diffusive jump motion between the four equivalent sites located at the corners of a tetrahedron, under the assumption that this classical diffusion model can be transposed to the present quantum case. The scattering law, which was calculated by Jobic et al.,[S1] is composed of a delta function and one or two Lorentzians whose widths are Q independent and proportional to $1/\tau$, with τ the residence time at the sites. The Lorentzians depend on the number of occupied sites. For a powder sample, Jobic et al. obtained[S1]

i) for a single molecule per tetrahedron

$$S(Q,\omega) = \frac{1}{4}[1+3j_0(Qd)]\delta(\omega) + \frac{3}{4}[1-j_0(Qd)]L\left(\frac{4}{\tau},\omega\right), \tag{1}$$

ii) for two molecules per tetrahedron

$$S(Q,\omega) = \frac{1}{4}[1+3j_0(Qd)]\delta(\omega) + \frac{1}{2}[1-j_0(Qd)]L\left(\frac{2}{\tau},\omega\right) + \frac{1}{4}[1-j_0(Qd)]L\left(\frac{4}{\tau},\omega\right), \tag{2}$$

iii) for three molecules per tetrahedron

$$S(Q,\omega) = \frac{1}{4}[1+3j_0(Qd)]\delta(\omega) + \frac{2}{3}[1-j_0(Qd)]L\left(\frac{1}{\tau},\omega\right) + \frac{1}{12}[1-j_0(Qd)]L\left(\frac{4}{\tau},\omega\right), \tag{3}$$

where d is the jump length and $L(\Gamma,x) = \frac{1}{\pi}\frac{\Gamma}{\Gamma^2+x^2}$ is a Lorentzian centered at $x=0$. No motion is allowed in the case of four molecules per tetrahedron. We assume that the three

Lorentzians of different widths in the classical regime correspond to the three inelastic peaks at different energies in the quantum regime.

The fraction of H_2 molecules hosted in singly, doubly, and triply occupied large cages are respectively noted x_1, x_2, and x_3. From the peak areas reported in subsection 4.1 of the main text (174, 218, and 54 in arbitrary units) and the intensities of the Lorentzians of eqs 1, 2, and 3, we obtain x_1=13%, x_2=73%, and x_3=14%. This corresponds to an average occupation for the large cages of about 1.85, in very good agreement with the value of 1.78(6) obtained from the Rietveld refinement of the diffraction pattern. We would like to underline that in the model of ref S1 H_2 in doubly occupied large cages contribute to the first peak (at 1.27 meV) exactly half as much as they contribute to the second peak (see eq 2) but H_2 in triply occupied large cages only contribute a little to the first peak (eq 3). Then, as occupation number equal two is predominant in our sample, the first peak is to a large extent due to single H_2 motion in doubly occupied large cages.

3. Other Supporting Figures

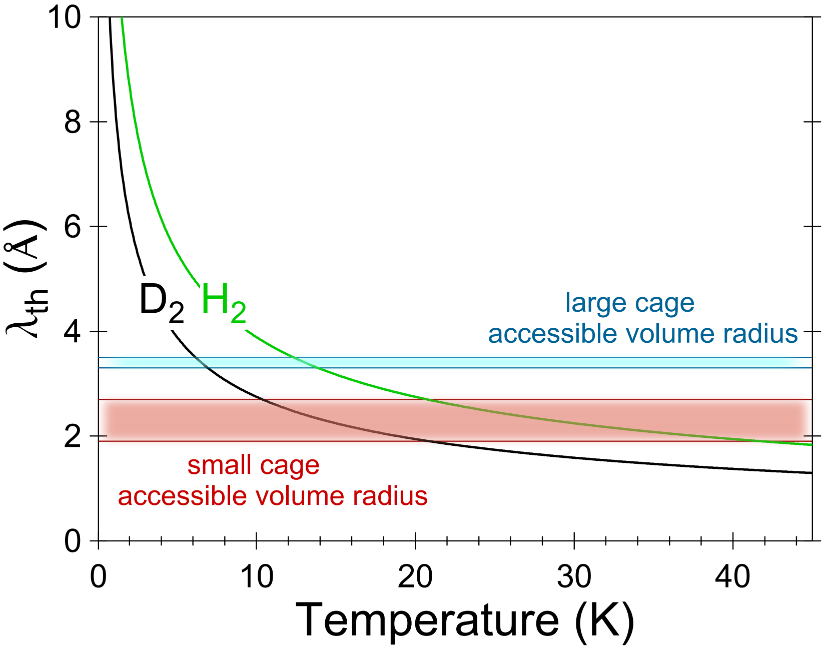

Figure S3: Temperature dependence of the De Broglie thermal wavelength λ_{th} for H_2 and D_2 (eq 2 of the main text). Transparent fields represent the accessible volume radius in the small and in the large cage of clathrate sII.

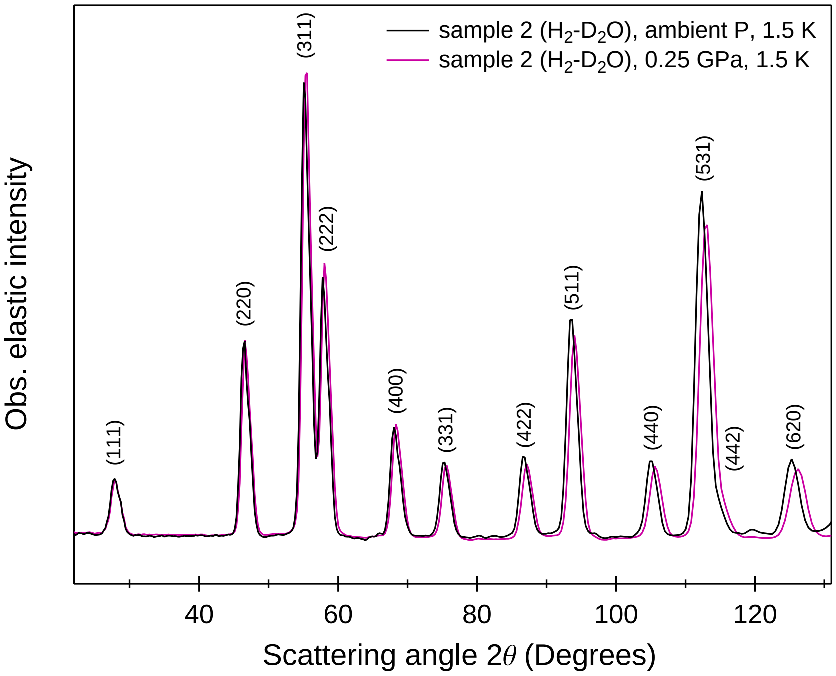

Figure S4: IN5 (λ=4.8 Å) powder diffraction patterns of sample 2 (clathrate sII H_2 hydrate) before and after compression to 0.25 GPa. The black line was arbitrarily shifted and scaled for clarity. Bragg reflections are indexed in the space group of clathrate structure II (Fd$\bar{3}$m).

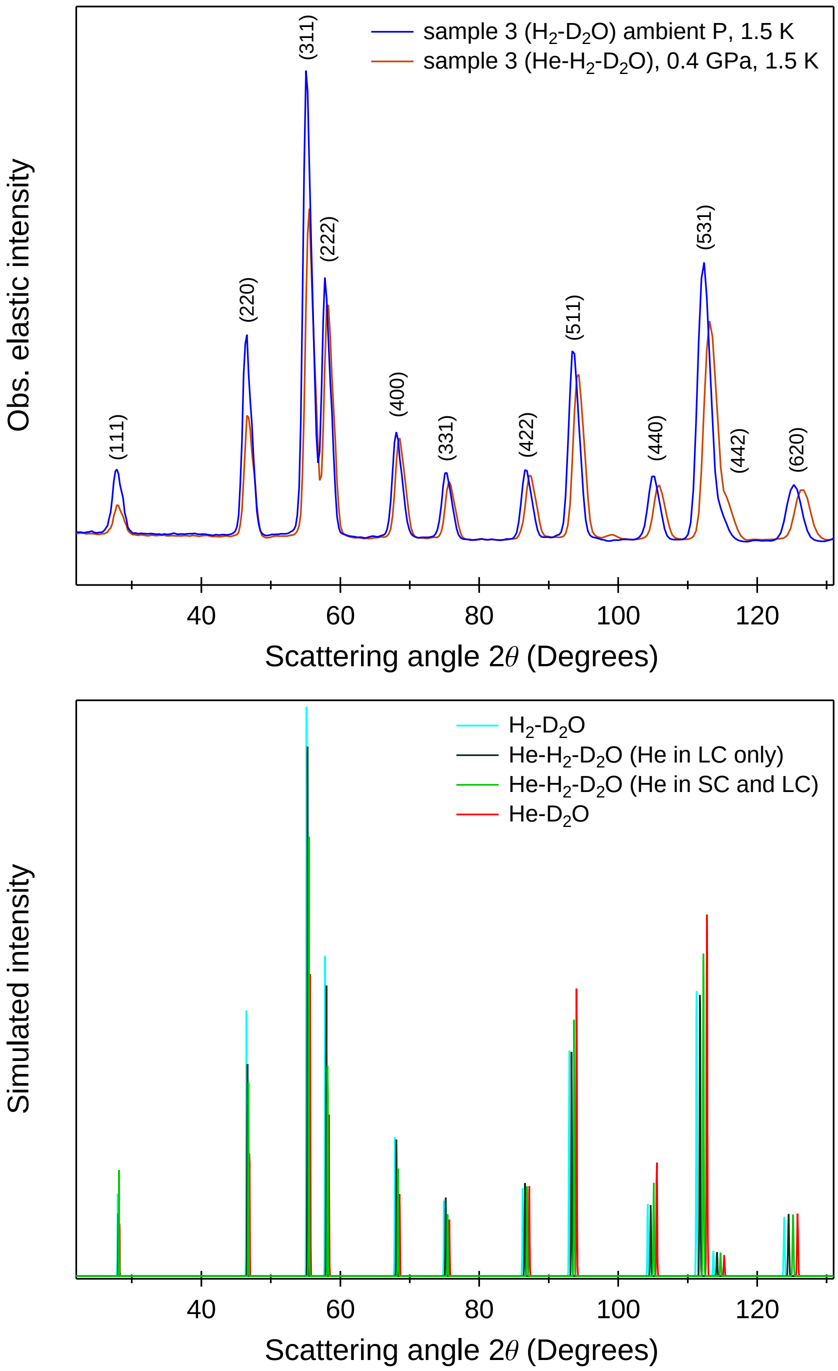

Figure S5: Top: IN5 (λ=4.8 Å) powder diffraction pattern of sample 3 (clathrate sII He–H_2 hydrate) compared to that of the same sample after pressure release and thermal treatment at 80–90 K (clathrate sII H_2 hydrate). Bottom: Simulated Bragg intensities for 1) clathrate sII H_2 hydrate with 1 H_2 per small cage (SC) and 1.75 H_2 per large cage (LC), 2) He–H_2 hydrate with 2.25 He per LC, 1 H_2 per SC, and 1.75 H_2 per LC, 3) He–H_2 hydrate with 0.5 He per SC, 2.25 He per LC, 0.5 H_2 per SC, and 1.75 H_2 per LC, and 4) He hydrate with 1 He per SC and 4 He per LC. Peak positions are shifted for better visibility. The structural parameters of section 1 were used for the simulations. He atoms were placed in 0, 0, 0 and 0.425, 0.425, 0.425 and had Biso of 20 and 60 for SC and LC, respectively.

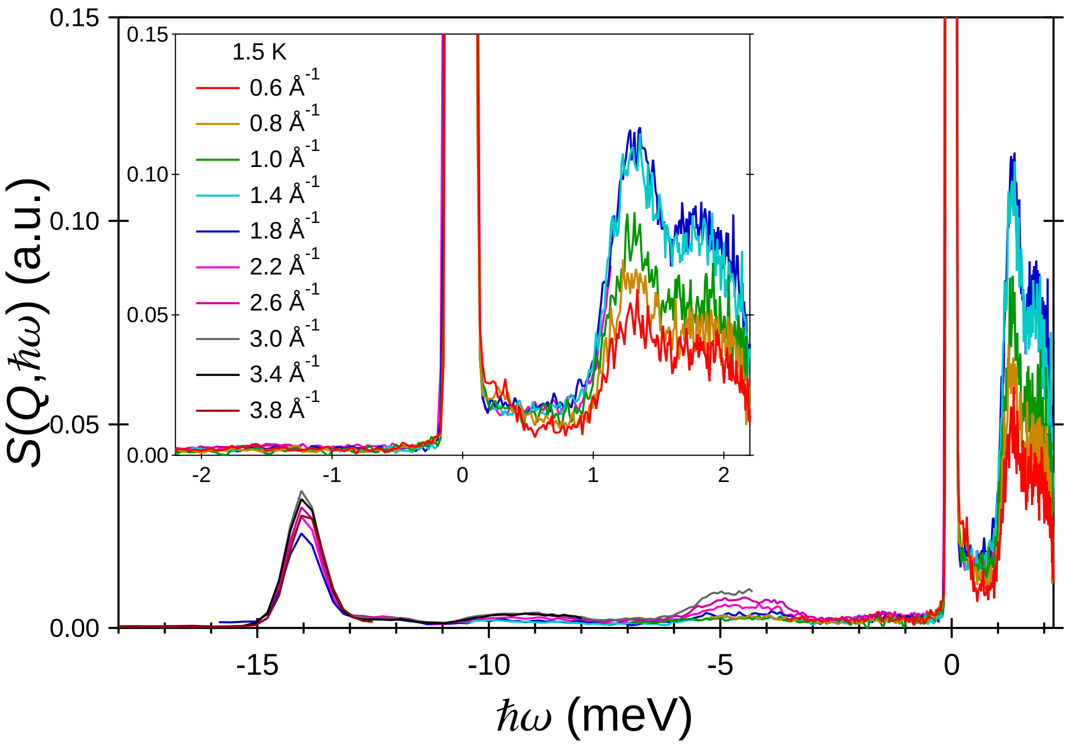

Figure S6: Individual Q cuts (with 0.2 Å^{-1} thickness) of the IN5 spectrum of clathrate sII H_2 hydrate at ambient pressure and 1.5 K reported in Figure 4 of the main text (sample 2). Some Q cuts are omitted for clarity. In the inset, the same plot is zoomed over a shorter energy transfer range.

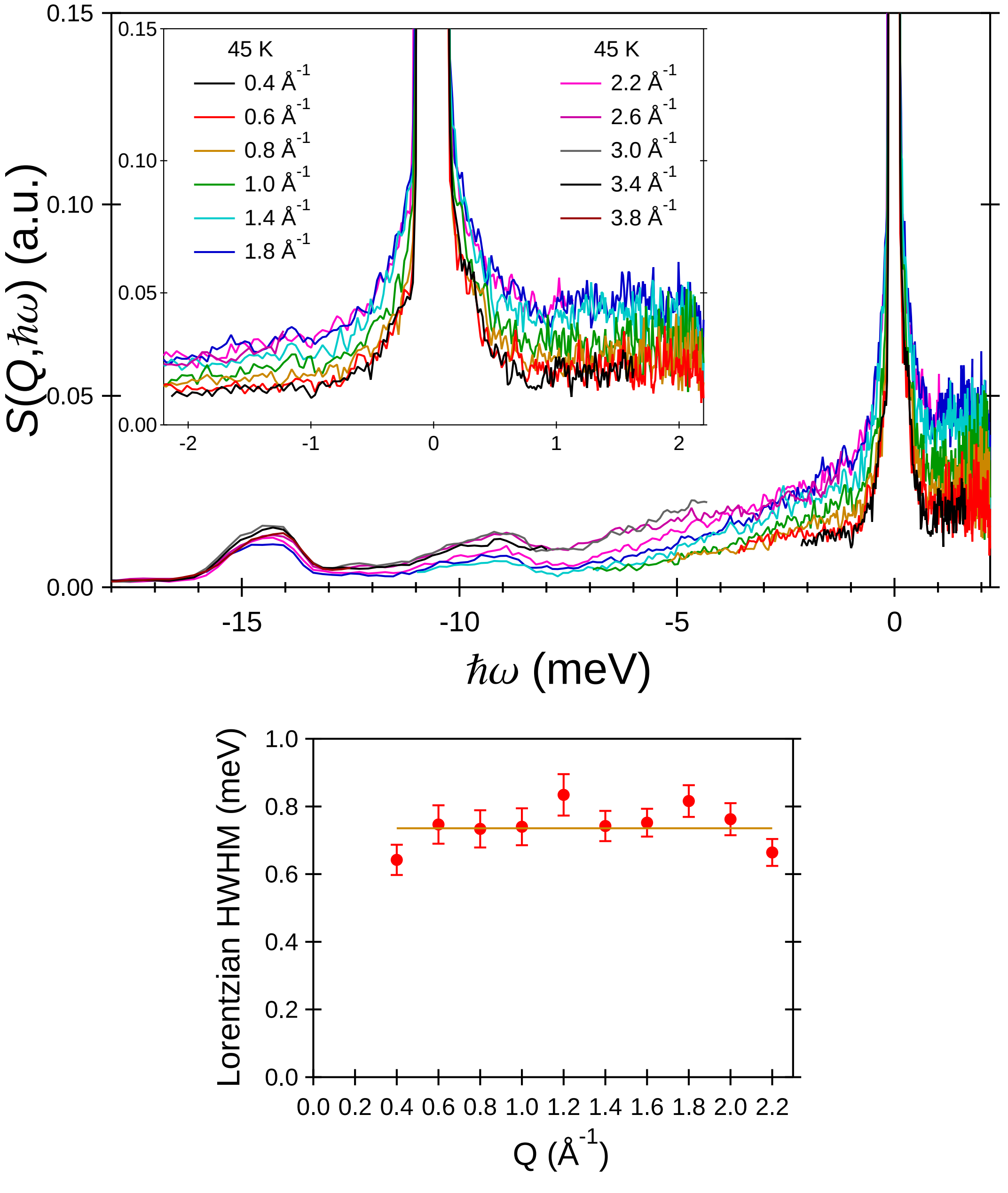

Figure S7: Top: Individual Q cuts (with 0.2 Å^{-1} thickness) of the IN5 spectrum of clathrate sII H_2 hydrate at ambient pressure and 45 K reported in Figure 4 of the main text (sample 2). Some Q cuts are omitted for clarity. In the inset, the same plot is zoomed over a shorter energy transfer range to highlight the quasielastic signal. Bottom: Half-width half-maximum of the Lorentzian best fit of the quasielastic signal as a function of Q.

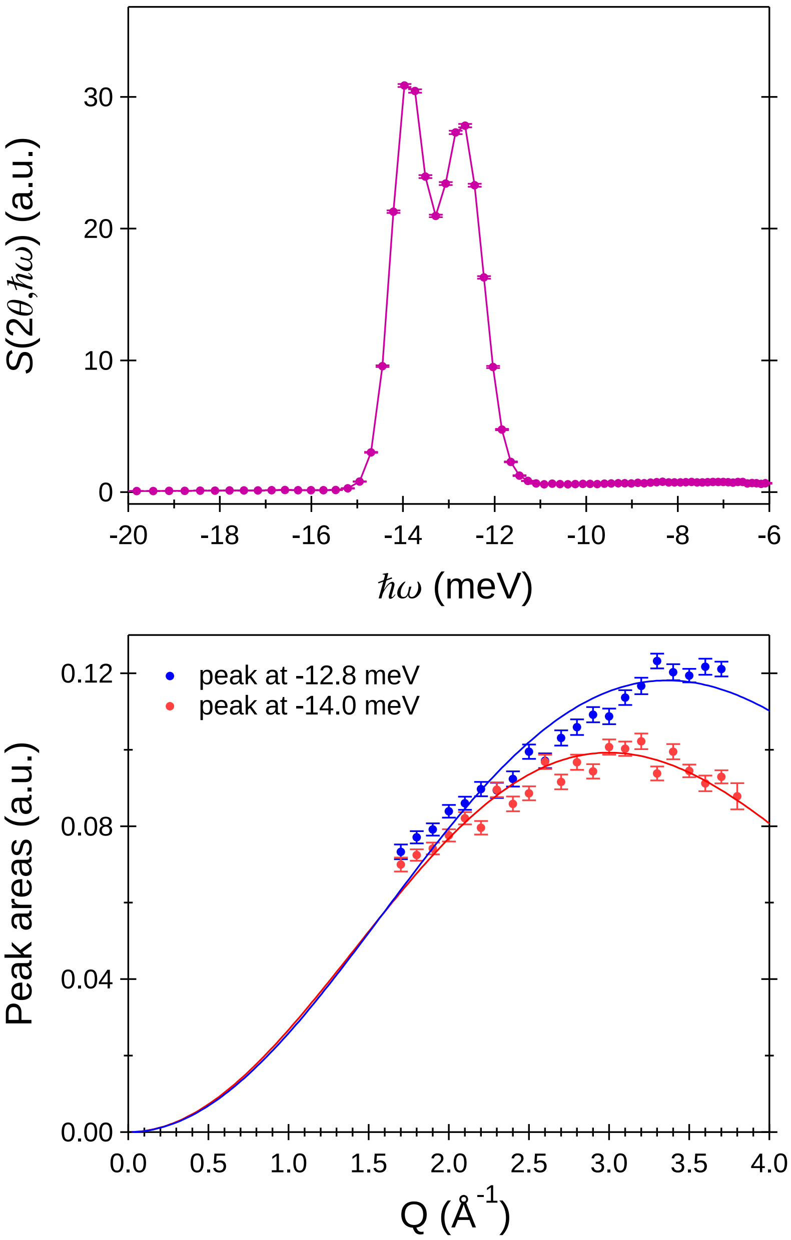

Figure S8: Top: IN5 spectrum of clathrate sII He–H_2 hydrate at 0.4 GPa and 1.8 K summed over all scattering angles between 40 and 135° (already reported in Figure 6 of the main text), plotted over the energy transfer range of interest. Two peaks at -12.8 and -14.0 meV are clearly distinguishable. Individual Q cuts (with 0.1 Å^{-1} thickness) were then fit to two Gaussians and a linear background to extract the Q dependence of the peak areas. Bottom: Peak areas as a function of wavevector transfer Q. The peak area variation with Q is fit here to the expected functional form for an ideal quantum rotating H_2 molecule, whose expression is $A\,\exp(-Q^2{<}u^2{>}/3)\;j_1^2(Qd_{HH}/2)$, where j_1 is the first-order spherical Bessel function of the first kind. The amplitude A and the mean square displacement ${<}u^2{>}$ are adjustable parameters and d_{HH} is fixed to 0.741 Å. The resulting ${<}u^2{>}$ is 0.179(4) Å^2 for the peak at -12.8 meV and 0.248(4) Å^2 for the peak at -14.0 meV.

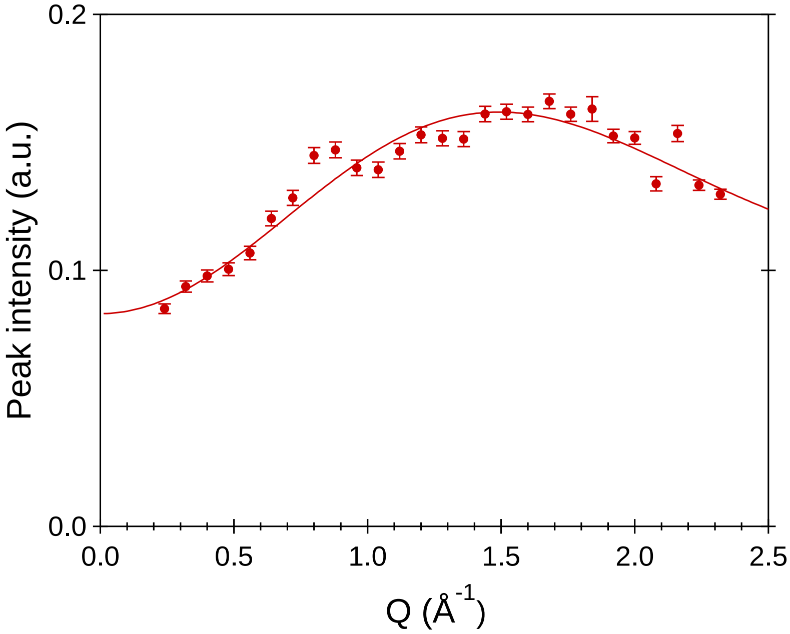

Figure S9: Q dependence of the measured intensity at 0.4 meV in the spectrum of clathrate sII D_2 hydrate at ambient pressure and 1.5 K, measured at λ=4.8 Å. The best fit using eq 3 of the main text is also shown. The parameter $<u^2>$ was fixed to two thirds its value for H_2 (0.35 Å^2) while A, B, and d were adjustable parameters. The resulting d is 2.54(3) Å.

References

(S1) Jobic, H.; Bée, M.; Méthivier, A.; Combet, J. Influence of the Cation Composition on the Dynamics of Xylenes in X-type Zeolites. *Microporous Mesoporous Mater.* **2001**, *42*, 135–155.

6.2.3 Next future steps

We have reported the first experimental observation of translational excitations for H_2 in the large cage of clathrate sII. Our results indicate that the translational fundamental transition would correspond to a quantized jump motion between equilibrium sites arranged at the corners of a tetrahedron. Consistently, this motion turned out to be suppressed when, after compression with helium gas, helium atoms massively enter the large cages and the maximum four-fold cage occupation is achieved. It is likely that a similar suppression of the translational motion can be obtained by compressing with any other gas small enough to enter the structure, including hydrogen itself. Performing such an experiment with another gas could be a way to verify our interpretation.

The translational fundamental transition appears in our low-temperature spectra as a triplet located at energies between 1 and 3 meV and we infer that the three peaks are related to the existence of a distribution of occupation numbers for the large cages. This assignment should be checked in future studies by systematically producing and measuring samples with different average large cage occupations in order to see how the peak areas depend on the average occupation.

We have also reported the first observation of the purely rotational transition $J{=}1{\rightarrow}0$ for H_2 in the nanometric channels of structure C1. We could not detect any translational peak; experiments covering a wider energy transfer range will be needed to complement our study. Possible future studies also include low-temperature inelastic neutron scattering studies of the other known high-pressure filled ice structure of hydrogen hydrate, namely structure C2, which is formed at pressures above $\sim$2.5 GPa [12].

Finally, the work presented here could be certainly extended in the future to the hydrates of other hydrogenated guest molecules. For example, experiments [114] and simulations [115] have studied the quantum dynamics of methane in the cages of clathrate sI at ambient pressure but no investigations exist at high pressure.

7 Conclusion

This dissertation was concerned with the study of the guest dynamics in methane hydrates and hydrogen hydrates under high pressure, over a wide range up to 150 GPa. Three different types of dynamics were studied: i) classical translational dynamics at structure interfaces, ii) vibrational and orientational dynamics, and iii) quantum rotational and translational dynamics. The main results are briefly summarized in the following.

- In section 5.2 we presented a published experimental investigation of the classical translational dynamics of methane molecules in a CH_4–D_2O methane hydrate sample showing coexistence of clathrate sI and sII. Persistent coexistence of the two structures was achieved by applying a pressure of 0.8 GPa using a Paris-Edinburgh press; their relative amount in the sample remained approximately constant throughout the duration of the experiment (~21 h). Methane diffusion was probed by quasielastic neutron scattering at different temperatures between 212 and 282 K.

  The quasielastic signal of the sample was analyzed using both a Lorentzian function (corresponding to a three-dimensional diffusion) and a two-dimensional diffusion model. The fits obtained within the two models are indistinguishable in our spectra within the instrumental energy resolution and provide comparable results: the Q dependence of the width of the Lorentzian function and of the analogous of the width in the two-dimensional diffusion model corresponds to a translational random jump diffusion. The resulting translational diffusion coefficient is very high (of the order of 10^{-4} cm^2 s^{-1}), and has a weak temperature dependence. From the integrated areas of the quasielastic and elastic lines we estimate that about one third of the methane molecules in the sample are mobile.

  The observed remarkably fast methane diffusion can be ascribed to a hyper-diffusion phenomenon associated with a peculiar layered structure of the interface or, alternatively, to methane nanobubbles formation at grain boundaries. Insights from molecular dynamics simulations are needed to shed light on this point. No other similar investigations of the interface diffusion of guest molecules in clathrate hydrates exist in literature. Our work possibly opens a new field concerning unknown interface phenomena and has various potential implications, for example regarding the replacement kinetics in the processes of gas exchange between CH_4 and CO_2 in case of sI–sII conversion. This process has recently attracted broad attention for its potential technological application in the context of energy recovery from natural gas clathrate hydrate sediments.

- In section 5.3 we presented a published study of the vibrational and orientational dynamics of methane molecules embedded in the high-pressure filled ice structure of methane hydrate (MH-III) between 2 and 45 GPa by experiments and simulations (subsections 5.3.1 to 5.3.3) as well as unpublished data of methane hydrate up to 150 GPa (subsection 5.3.4).

  We used Raman spectroscopy in diamond anvil cell on CH_4–D_2O methane hydrate samples to follow the pressure dependence of several vibrational modes, namely the CH stretching, the CH_4 rocking, the OD stretching, and the lattice mode. By comparison with ab-initio molecular dynamics simulations of MH-III including nuclear quantum effects, we found gradual orientational ordering of the guest molecules with increasing pressure and eventually complete locking-in at about 20 GPa. The locking-in of methane reorientations at 20 GPa goes along with a change in the slope of the pressure dependence of several vibrational modes at about the same pressure in the Raman spectra. It is followed by progressive significant angular distortion of the methane molecules.

  It must be emphasized that orientational ordering of the methane molecules in MH-III is in striking contrast with the almost free rotations observed in clathrate sI methane hydrate at ambient pressure by many techniques (inelastic neutron scattering [114], NMR [116, 117], molecular dynamics simulation [118], and neutron diffraction [119]). This is primarily an effect of free volume reduction with increasing pressure in MH-III.

  Moreover, our simulations indicate strong mode coupling between the rocking mode of methane and the stretching modes of water at 30–40 GPa, when their frequencies approach in the experimental spectra. In summary, our results indicate that, upon compression to 45 GPa, MH-III evolves towards a mixed molecular crystal where the very distinction between guests and hosts is no more meaningful. No hints of hydrogen bonding between water and methane were found. At 45 GPa MH-III is probably a stoichiometric compound; however, this is to be verified by future studies.

  In our Raman spectra up to 150 GPa, we observed no signal from free methane, indicating that no decomposition occurred up to the highest investigated pressure. Previous experimental studies of methane hydrate had checked methane hydrate stability only up to 86 GPa [13, 74, 75]. Above 40–50 GPa, MH-III is expected to transform into another high-pressure hydrate structure [13, 74, 75, 76]. The new high-pressure structure remains to be identified. Above 100 GPa, we observed appearance of a mode similar to the T_{2g} mode observed in the excess D_2O ice and possibly indicating symmetrization of the hydrogen bonds in the high-pressure hydrate structure.

The study of gas hydrates having high-pressure filled ice structures is a relatively new field. Filled ice structures have been observed for eight different gas hydrates in the literature (methane, hydrogen, argon, nitrogen, krypton, carbon dioxide, neon, and helium hydrate) and among them only methane and hydrogen hydrates have been investigated above 10 GPa [9, 11]. It is likely that future studies will find that other gas hydrates are also stable in the extremely high pressure regime. This knowledge could be relevant to the modeling of the interiors of large icy bodies in the Universe where water and simple gas molecules are expected to coexist.

- In section 6.2 we investigated the quantum roto-translational dynamics of hydrogen molecules confined in hydrate structures by inelastic neutron scattering experiments at temperatures below 50 K. Simple H_2 and D_2, and binary He–H_2 hydrate samples having clathrate sII were studied at ambient pressure and pressures up 0.5 GPa in a gas pressure cell. Simple H_2 hydrate having the high-pressure structure C1, in which hydrogen molecules sit in narrow hexagonal channels, was studied at 1.4 GPa in a Paris-Edinburgh press. The water network of all samples was deuterated.

  In simple clathrate sII hydrogen hydrate, H_2 molecules occupy both the small and the large cages of the structure. Molecules in the two types of environment may contribute very differently to the spectra. We identified the transitions from the ground state to the first and to the second excited translational states of H_2 in the large cage of clathrate sII, appearing in the spectra as low-energy inelastic peaks. The first excited translational state turned out to be at energies of 1–3 meV and the second excited translational state at 4–6 meV. Those energy values are much lower than those previously reported in the literature for H_2 in the small cage of clathrate sII [95, 103], primarily because the radius of the accessible volume in the large cage is about 1.5 times larger than that in the small cage.

  For the transition from the ground state to the first excited translational state for H_2 in the large cages, the Q dependence of the signal intensity corresponds to a quantized jump motion with a jump length of about 2.25 Å. It is very likely that this motion takes place between four tetrahedrally arranged equilibrium positions inside the cage and that is allowed by quantum tunneling. The signal is clearly split into three peaks and the existence of a triplet seems to be related to the distribution of different hydrogen occupation numbers in the large cages. As temperature increases over the range 1.5–25 K and the De Broglie wavelength of H_2 becomes shorter than the confinement size, the inelastic peaks progressively vanish and a quasielastic signal appears. This is a nice evidence of crossover between quantum and classical dynamics.

Upon compression to 0.25 GPa, we observed a shift in energy for all peaks associated with transitions involving a change in the translational state of the H_2 molecules in the small or in the large cage of sII, as an effect of changing the confinement size and thus shifting the energy of the levels. The only peak associated with a purely rotational transition was insensitive to pressure variation. Remarkably, upon compression to 0.4–0.5 GPa and inclusion of helium in the large cages, peaks related to a change in the translational state of H_2 molecules in the small cage were again shifted in energy but peaks related to a change in the translational state of H_2 molecules in the large cages were suppressed.

Finally, we investigated the effect of substituting H_2 molecules with D_2 and observed a strong, unconventional change in the peaks position, which suggests a correlated dynamics of the hydrogen molecules in the large cages and certainly calls for further investigation to be confirmed.

In the inelastic neutron scattering spectra of structure C1, only one inelastic peak was detected and assigned to the purely rotational transition $J{=}1{\rightarrow}0$ (i.e. the transition from the ground state of *ortho*-H_2 to the ground state of *para*-H_2). Presumably, translational modes were only weakly intense or out of the energy transfer range accessible in our experiment.

Hydrogen hydrates provide an exceptional opportunity for investigating the quantum dynamics of hydrogen molecules in nanocavities of different symmetries and sizes. Four different structures of simple hydrogen hydrate are known to form in the GPa pressure range [6, 11, 12], including three non-clathrate structures. By applying pressure, one can efficiently change the cage size and also induce transformation into a different structure. However, except for the recent study of ref [120], all literature works focused on clathrate structures at ambient pressure. Here we have proven the potential of high-pressure, low-temperature experiments of hydrogen hydrates, both in the pressure range up to 0.5 GPa using a gas pressure cell and in the GPa range using a Paris-Edinburgh press.

Bibliography

[1] E. D. Sloan and C. A. Koh. *Clathrate Hydrates of Natural Gases.* CRC Press, Boca Raton, 3rd edition, 2008.

[2] A. H. Nguyen and V. Molinero. Cross-nucleation between clathrate hydrate polymorphs: Assessing the role of stability, growth rate, and structure matching. *J. Chem. Phys.*, 140:084506, 2014.

[3] V. V. Struzhkin, B. Militzer, W. L. Mao, H.-k. Mao, and R. J. Hemley. Hydrogen storage in molecular clathrates. *Chem. Rev.*, 107:4133–4151, 2007.

[4] M. E. Casco, J. Silvestre-Albero, A. J. Ramírez-Cuesta, F. Rey, J. L. Jordá, A. Bansode, A. Urakawa, I. Peral, M. Martínez-Escandel, K. Kaneko, and F. Rodríguez-Reinoso. Methane hydrate formation in confined nanospace can surpass nature. *Nature Comm.*, 6:6432, 2015.

[5] A. Falenty, T. C. Hansen, and W. F. Kuhs. Formation and properties of ice XVI obtained by emptying a type sII clathrate hydrate. *Nature*, 516:231–233, 2014.

[6] W. L. Mao, H.-k. Mao, A. F. Goncharov, V. V. Struzhkin, Q. Guo, J. Hu, J. Shu, R. J. Hemley, M. Somayazulu, and Y. Zhao. Hydrogen clusters in clathrate hydrate. *Science*, 297:2247, 2002.

[7] K. A. Lokshin, Y. Zhao, D. He, W. L. Mao, H.-k. Mao, R. J. Hemley, M. V. Lobanov, and M. Greenblatt. Structure and dynamics of hydrogen molecules in the novel clathrate hydrate by high pressure neutron diffraction. *Phys. Rev. Lett.*, 93:125503, 2004.

[8] H. Hirai, T. Tanaka, T. Kawamura, Y. Yamamoto, and T. Yagi. Structural changes in gas hydrates and existence of a filled ice structure of methane hydrate above 40 GPa. *J. Phys. Chem. Solids*, 65:1555–1559, 2004.

[9] J. S. Loveday and R. J. Nelmes. High-pressure gas hydrates. *Phys. Chem. Chem. Phys.*, 10:913–1068, 2008.

[10] V. S. Efimchenko, M. A. Kuzovnikov, V. K. Fedotov, M. K. Sakharov, S. V. Simonov, and M. Tkacz. New phase in the water–hydrogen system. *J. Alloys Compd.*, 509S:S860–S863, 2011.

[11] D. M. Amos, M.-E. Donnelly, P. Teeratchanan, C. L. Bull, A. Falenty, W. F. Kuhs, A. Hermann, and J. S. Loveday. A chiral gas–hydrate structure common to the carbon dioxide–water and hydrogen–water systems. *J. Phys. Chem. Lett.*, 8:4295–4299, 2017.

[12] W. L. Vos, L. W. Finger, R. J. Hemley, and H.-k. Mao. Novel H_2-H_2O clathrates at high pressures. *Phys. Rev. Lett.*, 71:3150, 1993.

[13] S.-i. Machida, H. Hirai, T. Kawamura, Y. Yamamoto, and T. Yagi. A new high-pressure structure of methane hydrate surviving to 86 GPa and its implications for the interiors of giant icy planets. *Phys. Earth Planet. Inter.*, 155:170–176, 2006.

[14] S.-i. Machida, H. Hirai, T. Kawamura, Y. Yamamoto, and T. Yagi. Isotopic effect and amorphization of deuterated hydrogen hydrate under high pressure. *Phys. Rev. B*, 83:144101, 2011.

[15] M. Choukroun, S. W. Kieffer, X. Lu, and G. Tobie. Clathrate hydrates: implications for exchange processes in the outer solar system. In M. S. Gudipati and J. Castillo-Rogez, editors, *The Science of Solar System Ices*. Springer, New York, 2013.

[16] L. A. Stern, S. H. Kirby, and W. B. Durham. Peculiarities of methane clathrate hydrate formation and solid-state deformation, including possible superheating of water ice. *Science*, 273:1843–1848, 1996.

[17] L. A. Stern, S. H. Kirby, W. B. Durham, S. Circone, and W. F. Waite. Laboratory synthesis of pure methane hydrate suitable for measurement of physical properties and decomposition behavior. In M. D. Max, editor, *Natural Gas Hydrate in Oceanic and Permafrost Environments*. Springer, Dordrecht, 2000.

[18] W. F. Kuhs, R. Dorwarth, D. Londono, and J. L. Finney. In-situ study on composition and structure of ar-clathrate. In N. Maeno and T. Hondoh, editors, *Physics and Chemistry of Ice*. Hokkaido University Press, Sapporo, 2002.

[19] K. A. Lokshin and Y. Zhao. Fast synthesis method and phase diagram of hydrogen clathrate hydrate. *Appl. Phys. Lett.*, 88:131909, 2006.

[20] W. F. Kuhs, D. K. Staykova, and A. N. Salamatin. Formation of methane hydrate from polydisperse ice powders. *J. Phys. Chem. B*, 110:13283–13295, 2006.

[21] T. C. Hansen, A. Falenty, and W. F. Kuhs. Lattice constants and expansivities of gas hydrates from 10 K up to the stability limit. *J. Chem. Phys.*, 144:054301, 2016.

[22] M. Chaouachi, S. H. Neher, A. Falenty, and W. F. Kuhs. Time resolved coarsening of clathrate crystals: The case of gas hydrates. *Cryst. Growth Des.*, 17:2458–2472, 2017.

[23] J. Peters, M. Trapp, D. Hughes, S. Rowe, B. Demé, J.-L. Laborier, C. Payre, J.-P. Gonzales, S. Baudoin, N. Belkhier, and E. Lelièvre-Berna. High hydrostatic pressure equipment for neutron scattering studies of samples in solutions. *High Press. Res.*, 32:97–102, 2011.

[24] S. Klotz. *Techniques in High Pressure Neutron Scattering.* CRC press, Boca Raton, 2012.

[25] K. Komatsu, S. Klotz, A. Shinozaki, R. Iizuka, L. E. Bove, and H. Kagi. Performance of ceramic anvils for high pressure neutron scattering. *High Press. Res.*, 34:494–499, 2014.

[26] Y. A. Dyadin, E. G. Larionov, A. Y. Manakov, F. V. Zhurko, E. Y. Aladko, T. V. Mikina, and V. Y. Komarov. Clathrate hydrates of hydrogen and neon. *Mendeleev Commun.*, 9:209–210, 1999.

[27] S. Klotz, J. Philippe, C. L. Bull, J. S. Loveday, and R. J. Nelmes. A 3 kbar hydrogen-compatible gas loader for Paris-Edinburgh presses. *High Press. Res.*, 33:214–220, 2013.

[28] A. Jarayaman. Diamond anvil cell and high-pressure physical investigations. *Rev. Mod. Phys.*, 55:65–108, 1983.

[29] G. L. Squires. *Introduction to the Theory of Thermal Neutron Scattering.* Cambridge University Press, Cambridge, 2012.

[30] H. Schober. An introduction to the theory of nuclear neutron scattering in condensed matter. *J. Neutron Res.*, 17:109–357, 2014.

[31] V. F. Sears. Neutron scattering lengths and cross sections. *Neutron News*, 3:29–37, 1992.

[32] H. Jobic and D. N. Theodorou. Quasi-elastic neutron scattering and molecular dynamics simulation as complementary techniques for studying diffusion in zeolites. *Microporous Mesoporous Mater.*, 102:21–50, 2007.

[33] M. Bée. *Quasielastic Neutron Scattering.* Adam Hilger, Bristol, 1988.

[34] J. Ollivier and J.-M. Zanotti. Diffusion inélastique de neutrons par temps de vol. *Collection SFN*, 10:379–423, 2010.

[35] J. R. D. Copley and T. J Udovic. Neutron time-of-flight spectroscopy. *J. Res. Natl. Inst. Stand. Technol.*, 98:71, 1993.

[36] J. R. Ferraro, K. Nakamoto, and C. W. Brown. *Introductory Raman Spectroscopy.* Elsevier, San Diego, 2nd edition, 2003.

[37] J. Zhu, S. Du, X. Yu, J. Zhang, H. Xu, S. C. Vogel, T. C. Germann, J. S. Francisco, F. Izumi, K. Momma, Y. Kawamura, C. Jin, and Y. Zhao. Encapsulation kinetics and dynamics of carbon monoxide in clathrate hydrate. *Nature Comm.*, 5:4128, 2014.

[38] C. Petuya, F. Damay, D. Talaga, and A. Desmedt. Guest partitioning in carbon monoxide hydrate by Raman spectroscopy. *J. Phys. Chem. C*, 121:13798–13802, 2017.

[39] C. Petuya, F. Damay, B. Chazallon, J.-L. Bruneel, and A. Desmedt. Guest partitioning and metastability of the nitrogen gas hydrate. *J. Phys. Chem. C*, 122:566–573, 2018.

[40] D. K. Staykova, W. F. Kuhs, A. N. Salamatin, and T. Hansen. Formation of porous gas hydrates from ice powders: Diffraction experiments and multistage model. *J. Phys. Chem. B*, 107:10299–10311, 2003.

[41] J. M. Schicks and J. A. Ripmeester. The coexistence of two different methane hydrate phases under moderate pressure and temperature conditions: Kinetic versus thermodynamic products. *Angew. Chem. Int. Ed.*, 43:3310–3313, 2004.

[42] J. M. Schicks and M. Luzi-Helbing. Kinetic and thermodynamic aspects of clathrate hydrate nucleation and growth. *J. Chem. Eng. Data*, 60:269–277, 2015.

[43] M. R. Walsh, C. A. Koh, E. D. Sloan, A. K. Sum, and D. T. Wu. Microsecond simulations of spontaneous methane hydrate nucleation and growth. *Science*, 326:1095–1098, 2009.

[44] M. Lauricella, S. Meloni, S. Liang, N. J English, P. G. Kusalik, and G. Ciccotti. Clathrate structure-type recognition: Application to hydrate nucleation and crystallisation. *J. Chem. Phys.*, 142:244503, 2015.

[45] D. R. Hafemannz and S. L. Miller. The clathrate hydrates of cyclopropane. *J. Phys. Chem.*, 73:1392–1397, 1969.

[46] S. Subramanian, R. A. Kini, S. F. Dec, and E. D. Sloan. Structural transition studies in methane + ethane hydrates using Raman and NMR. *Proc. Gas hydrates, Challenges for the Future, Annals of the New York Academy of Sciences*, 912:873–886, 2000.

[47] A. J. Rondinone, B. C. Chakoumakos, C. J. Rawn, and Y. Ishii. Neutron diffraction study of structure I and structure II trimethylene oxide clathrate deuterate. *J. Phys. Chem. B*, 107:6046–6050, 2003.

[48] J. A. Ripmeester and C. I. Ratcliffe. ^{129}Xe NMR studies of clathrate hydrates: New guests for structure II and structure H. *J. Phys. Chem.*, 94:8773–8776, 1990.

[49] E. M. Hendriks, B. Edmonds, R. A. S. Moorwood, and S. Szczepanski. Hydrate structure stability in simple and mixed hydrates. *Fluid Phase Equilib.*, 117:193–200, 1996.

[50] T. Pietrass, H. C. Gaede, A. Bifone, A. Pines, and J. A. Ripmeester. Monitoring xenon clathrate hydrate formation on ice surfaces with optically enhanced ^{129}Xe NMR. *J. Am. Chem. Soc.*, 117:7520–7525, 1995.

[51] I. L. Moudrakovski, A. A. Sanchez, C. I. Ratcliffe, and J. A. Ripmeester. Nucleation and growth of hydrates on ice surfaces: New insights from ^{129}Xe NMR experiments with hyperpolarized xenon. *J. Phys. Chem. B*, 105:12338–12347, 2001.

[52] M. Choukroun, Y. Morizet, and O. Grasset. Raman study of methane clathrate hydrates under pressure: New evidence for the metastability of structure II. *J. Raman Spectrosc.*, 38:440–451, 2007.

[53] I.-M. Chou, A. Sharma, R. C. Burruss, J. Shu, H.-k. Mao, R. J. Hemley, A. F. Goncharov, L. A. Stern, and S. H. Kirby. Transformations in methane hydrates. *Proc. Natl. Acad. Sci. USA*, 97:13484–13487, 2000.

[54] J. Shu, X. Chen, I.-M. Chou, W. Yang, J. Hu, R. J. Hemley, and H.-k. Mao. Structural stability of methane hydrate at high pressures. *Geosci. Front.*, 2:93–100, 2011.

[55] B. Peters, N. E. R. Zimmermann, G. T. Beckham, J. W. Tester, and B. L. Trout. Path sampling calculation of methane diffusivity in natural gas hydrates from a water-vacancy assisted mechanism. *J. Am. Chem. Soc.*, 130:17342–17350, 2008.

[56] H. Lo, M.-T. Lee, and S.-T. Lin. Water vacancy driven diffusion in clathrate hydrates: Molecular dynamics simulation study. *J. Phys. Chem. C*, 121:8280–8289, 2017.

[57] K. R. Harris and N. J. Trappeniers. The density dependence of the self-diffusion coefficient of liquid methane. *Physica*, 104A:262–280, 1980.

[58] Z. M. Jendi, P. Servio, and A. D. Rey. Molecular mobility in carbon dioxide hydrates. *Mol. Syst. Des. Eng.*, 2:500–506, 2017.

[59] J. Baumert, C. Gutt, V. Shpakov, J. S. Tse, M. Krisch, M. Müller, H. Requardt, D. D. Klug, S. Janssen, and W. Press. Lattice dynamics of methane and xenon hydrate: Observation of symmetry-avoided crossing by experiment and theory. *Phys. Rev. B*, 68:174301, 2003.

[60] L. E. Bove, S. Klotz, Th. Strässle, M. Koza, J. Teixeira, and A.M. Saitta. Translational and rotational diffusion in water in the Gigapascal range. *Phys. Rev. Lett.*, 111:185901, 2013.

[61] S. Klotz, Th. Strässle, and L. E. Bove. Quasi-elastic neutron scattering in the multi-GPa range and its application to liquid water. *Appl. Phys. Lett.*, 103:193504, 2013.

[62] U. Ranieri, P. Giura, F. A. Gorelli, M. Santoro, S. Klotz, P. Gillet, L. Paolasini, M. M. Koza, and L. E. Bove. Dynamical crossover in hot dense water: The hydrogen bond role. *J. Phys. Chem. B*, 120:9051–9059, 2016.

[63] Y. A. Dyadin, E. Y. Aladko, and E. G. Larionov. Decomposition of methane hydrates up to 15 kbar. *Mendeleev Comm.*, 7:34–35, 1997.

[64] Á. Vidal-Vidal, M. Pérez-Rodríguez, and M. M. Piñeiro. Direct transition mechanism for molecular diffusion in gas hydrates. *RSC Adv.*, 6:1966–1972, 2016.

[65] C. Liu, Z. Zhang, and G.-J. Guo. Effect of guests on the adsorption interaction between a hydrate cage and guests. *RSC Adv.*, 6:106443–106452, 2016.

[66] C. J. Burnham and N. J. English. Free-energy calculations of the intercage hopping barriers of hydrogen molecules in clathrate hydrates. *J. Phys. Chem. C*, 120:16561–16567, 2016.

[67] J. R. Cendagorta, A. Powers, T. J. H. Hele, O. Marsalek, Z. Bačić, and M. E. Tuckerman. Competing quantum effects in the free energy profiles and diffusion rates of hydrogen and deuterium molecules through clathrate hydrates. *Phys. Chem. Chem. Phys.*, 18:32169–32177, 2016.

[68] S. Liang, D. Liang, N. Wu, L. Yi, and G. Hu. Molecular mechanisms of gas diffusion in CO_2 hydrates. *J. Phys. Chem. C*, 120:16298–16304, 2016.

[69] M. H. Waage, T. T. Trinh, and T. S. van Erp. Diffusion of gas mixtures in the sI hydrate structure. *J. Chem. Phys.*, 148:214701, 2018.

[70] D. P. Luis, I. E. Romero-Ramirez, A. González-Calderón, and J. López-Lemus. The coexistence temperature of hydrogen clathrates: A molecular dynamics study. *J. Chem. Phys.*, 148:114503, 2018.

[71] L. C. Jacobson and V. Molinero. A methane–water model for coarse-grained simulations of solutions and clathrate hydrates. *J. Phys. Chem. B*, 114:7302–7311, 2010.

[72] J. S. Loveday, R. J. Nelmes, M. Guthrie, S. A. Belmonte, D. R. Allan, D. D. Klug, J. S. Tse, and Y. P. Handa. Stable methane hydrate above 2 GPa and the source of Titan's atmospheric methane. *Nature*, 410:661–663, 2001.

[73] J. S. Loveday, R. J. Nelmes, M. Guthrie, D. D. Klug, and J. S. Tse. Transition from cage clathrate to filled ice: the structure of methane hydrate III. *Phys. Rev. Lett.*, 87:215501, 2001.

[74] H. Hirai, S.-i. Machida, T. Kawamura, Y. Yamamoto, and T. Yagi. Stabilizing of methane hydrate and transition to a new high-pressure structure at 40 GPa. *Am. Mineral.*, 91:826–830, 2006.

[75] S.-i. Machida, H. Hirai, T. Kawamura, Y. Yamamoto, and T. Yagi. Raman spectra of methane hydrate up to 86 GPa. *Phys. Chem. Miner.*, 34:31–35, 2007.

[76] T. Tanaka, H. Hirai, T. Matsuoka, Y. Ohishi, T. Yagi, M. Ohtake, Y Yamamoto, S. Nakano, and T. Irifune. Phase changes of filled ice Ih methane hydrate under low temperature and high pressure. *J. Chem. Phys.*, 139:104701, 2013.

[77] H. Kadobayashi, H. Hirai, H. Ohfuji, M. Ohtake, and Y. Yamamoto. In situ Raman and X-ray diffraction studies on the high pressure and temperature stability of methane hydrate up to 55 GPa. *J. Chem. Phys.*, 148:164503, 2018.

[78] D. D. Klug, J. S. Tse, Z. Liu, and R. J. Hemley. Hydrogen-bond dynamics and Fermi resonance in high-pressure methane filled ice. *J. Chem. Phys.*, 125:154509, 2006.

[79] A. K. Sum, R. C. Burruss, and E. D. Sloan. Measurement of clathrate hydrates via Raman spectroscopy. *J. Phys. Chem. B*, 101:7371–7377, 1997.

[80] H. Hirai, Y. Uchihara, H. Fujihisa, M. Sakashita, E. Katoh, K. Aoki, K. Nagashima, Y. Yamamoto, and T. Yagi. High-pressure structures of methane hydrate observed up to 8 GPa at room temperature. *J. Chem. Phys.*, 115:7066, 2001.

[81] H. Dammak, Y. Chalopin, M. Laroche, M. Hayoun, and J.-J. Greffet. Quantum thermal bath for molecular dynamics simulation. *Phys. Rev. Lett.*, 103:190601, 2009.

[82] M. Ceriotti, D. E. Manolopoulos, and M. Parrinello. Accelerating the convergence of path integral dynamics with a generalized Langevin equation. *J. Chem. Phys.*, 134:084104, 2011.

[83] M. Guthrie, R. Boehler, C. A. Tulk, J. J . Molaison, A. M. dos Santos, K. Li, and R. J. Hemley. Neutron diffraction observations of interstitial protons in dense ice. *Proc. Natl. Acad. Sci. USA*, 110:10552–10556, 2013.

[84] T. Meier, S. Petitgirard, S. Khandarkhaeva, and L. Dubrovinsky. Observation of nuclear quantum effects and hydrogen bond symmetrisation in high pressure ice. *Nature Comm.*, 9:2766, 2018.

[85] H. Hirai, Y. Uchihara, Y. Nishimura, T. Kawamura, Y. Yamamoto, and T. Yagi. Structural changes of argon hydrate under high pressure. *J. Phys. Chem. B*, 106:11089–11092, 2002.

[86] S. Sasaki, S. Hori, T. Kume, and H. Shimizu. Microscopic observation and in situ Raman scattering studies on high-pressure phase transformations of a synthetic nitrogen hydrate. *J. Chem. Phys.*, 118:7892, 2003.

[87] S. Sasaki, S. Hori, T. Kume, and H. Shimizu. Microscopic observation and in-situ Raman scattering studies on high-pressure phase transformations of Kr hydrate. *J. Phys. Chem. B*, 110:9838–9842, 2006.

[88] H. Hirai, S. Kagawa, T. Tanaka, T. Matsuoka, T. Yagi, Y. Ohishi, S. Nakano, Y. Yamamoto, and T. Irifune. Structural changes of filled ice Ic hydrogen hydrate under low temperatures and high pressures from 5 to 50 GPa. *J. Chem. Phys.*, 137:074505, 2012.

[89] T. Iitaka and T. Ebisuzaki. Methane hydrate under high pressure. *Phys. Rev. B*, 68:172105, 2003.

[90] C.-S. Zha, J. S. Tse, and W. A. Bassett. New Raman measurements for H_2O ice VII in the range of 300 cm^{-1} to 4000 cm^{-1} at pressures up to 120 GPa. *J. Chem. Phys.*, 145:124315, 2016.

[91] Y. Akahama and H. Kawamura. Pressure calibration of diamond anvil Raman gauge to 310 GPa. *J. Appl. Phys.*, 100:043516, 2006.

[92] L. Sun, Z. Zhao, A. L. Ruoff, C.-S. Zha, and G. Stupian. Raman studies on solid CH_4 at room temperature to 208 GPa. *J. Phys.: Condens. Matter*, 19:425206, 2007.

[93] P. W. Atkins. *Molecular Quantum Mechanics.* Oxford University Press, Oxford, 2nd edition, 1983.

[94] K. Fukutani and T. Sugimoto. Physisorption and ortho–para conversion of molecular hydrogen on solid surfaces. *Prog. Surf. Sci.*, 88:279–348, 2013.

[95] L. Ulivi, M. Celli, A. Giannasi, A. J. Ramirez-Cuesta, D. J. Bull, and M. Zoppi. Quantum rattling of molecular hydrogen in clathrate hydrate nanocavities. *Phys. Rev. B*, 76:161401(R), 2007.

[96] F. Sebastianelli, M. Xu, Y. S. Elmatad, J. W. Moskowitz, and Z. Bačić. Hydrogen molecules in the small dodecahedral cage of a clathrate hydrate: Quantum translation–rotation dynamics of the confined molecules. *J. Phys. Chem. C*, 111:2497–2504, 2007.

[97] F. Sebastianelli, M. Xu, and Z. Bačić. Quantum dynamics of small H_2 and D_2 clusters in the large cage of structure II clathrate hydrate: Energetics, occupancy, and vibrationally averaged cluster structures. *J. Chem. Phys.*, 129:244706, 2008.

[98] M. Xu, F. Sebastianelli, and Z. Bačić. Quantum dynamics of H_2, D_2, and HD in the small dodecahedral cage of clathrate hydrate: Evaluating H_2–water nanocage interaction potentials by comparison of theory with inelastic neutron scattering experiments. *J. Chem. Phys.*, 128:244715, 2008.

[99] M. Xu, F. Sebastianelli, and Z. Bačić. Coupled translation–rotation eigenstates of H_2, HD, and D_2 in the large cage of structure II clathrate hydrate: Comparison with the small cage and rotational Raman spectroscopy. *J. Phys. Chem. A*, 113:7601–7609, 2009.

[100] M. Xu, L. Ulivi, M. Celli, D. Colognesi, and Z. Bačić. Quantum calculation of inelastic neutron scattering spectra of a hydrogen molecule inside a nanoscale cavity based on rigorous treatment of the coupled translation-rotation dynamics. *Phys. Rev. B*, 83:241403(R), 2011.

[101] M. Xu, L. Ulivi, M. Celli, D. Colognesi, and Z. Bačić. Rigorous quantum treatment of inelastic neutron scattering spectra of a heteronuclear diatomic molecule in a nanocavity: HD in the small cage of structure II clathrate hydrate. *Chem. Phys. Lett.*, 563:1–8, 2013.

[102] A. Powers, O. Marsalek, M. Xu, L. Ulivi, D. Colognesi, M.E . Tuckerman, and Z. Bačić. Impact of the condensed-phase environment on the translation–rotation eigenstates and spectra of a hydrogen molecule in clathrate hydrates. *J. Phys. Chem. Lett.*, 7:308–313, 2016.

[103] K. T. Tait, F. Trouw, Y. Zhao, C. M. Brown, and R. T. Downs. Inelastic neutron scattering study of hydrogen in d_8-THF/D_2O ice clathrate. *J. Chem. Phys.*, 127:134505, 2007.

[104] D. Colognesi, M. Celli, L. Ulivi, M. Xu, and Z. Bačić. Neutron scattering measurements and computation of the quantum dynamics of hydrogen molecules trapped in the small and large cages of clathrate hydrates. *J. Phys. Chem. A*, 117:7314–7326, 2013.

[105] D. Colognesi, A. Powers, M. Celli, M. Xu, Z. Bačić, and L. Ulivi. The HD molecule in small and medium cages of clathrate hydrates : Quantum dynamics studied by neutron scattering measurements and computation. *J. Chem. Phys.*, 141:134501, 2014.

[106] J. D. Bernal and R. H. Fowler. A Theory of Water and Ionic Solution, with Particular Reference to Hydrogen and Hydroxyl Ions. *J. Chem. Phys.*, 1:515, 1933.

[107] A. Witt, F. Sebastianelli, M. E. Tuckerman, and Z. Bačić. Path integral molecular dynamics study of small H_2 clusters in the large cage of structure II clathrate hydrate: Temperature dependence of quantum spatial distributions. *J. Phys. Chem. C*, 114:20775–20782, 2010.

[108] P. M. Felker. Fully quantal calculation of H_2 translation-rotation states in the (p-H_2)$_2$@$5^{12}6^4$ clathrate hydrate inclusion compound. *J. Chem. Phys.*, 141:184305, 2014.

[109] C. J. Burnham, Z. Futera, and N. J. English. Quantum and classical intercage hopping of hydrogen molecules in clathrate hydrate: Temperature and cage-occupation effects. *Phys. Chem. Chem. Phys.*, 19:717–728, 2017.

[110] W. F. Kuhs, T. C. Hansen, and A. Falenty. Filling ices with helium and the formation of helium clathrate hydrate. *J. Phys. Chem. Lett.*, 9:3194–3198, 2018.

[111] C. J. Burnham, Z. Futera, and N. J. English. Study of hydrogen-molecule guests in type II clathrate hydrates using a force-matched potential model parameterised from ab initio molecular dynamics. *J. Chem. Phys.*, 148:102323, 2018.

[112] C. Lobban, J. L. Finney, and W. F. Kuhs. The p–T dependency of the ice II crystal structure and the effect of helium inclusion. *J. Chem. Phys.*, 117:3928, 2002.

[113] X. Yu, J. Zhu, S. Du, H. Xu, S. C. Vogel, J. Han, T. C. Germann, J. Zhang, C. Jin, J. S. Francisco, and Y. Zhao. Crystal structure and encapsulation dynamics of ice II-structured neon hydrate. *Proc. Natl. Acad. Sci. USA*, 111:10456–10461, 2014.

[114] C. Gutt, W. Press, A. Hüller, J. S. Tse, and H. Casalta. The isotope effect and orientational potentials of methane molecules in gas hydrates. *J. Chem. Phys.*, 114:4160, 2001.

[115] I. Matanović, M. Xu, J. W. Moskowitz, J. Eckert, and Z. Bačić. Methane molecule confined in the small and large cages of structure I clathrate hydrate: Quantum six-dimensional calculations of the coupled translation-rotation eigenstates. *J. Chem. Phys.*, 131:224308, 2009.

[116] D. W. Davidson, S. K. Garg, S. R. Gough, R. E. Hawkins, and J. A. Ripmeester. Characterization of natural gas hydrates by nuclear magnetic resonance and dielectric relaxation. *Can. J. Chem.*, 55:3641–3650, 1977.

[117] S. K. Garg, S. R. Gough, and D. W. Davidson. A wideline NMR study of reorientation of some sphericaltop molecules enclathrated in water. *J. Chem. Phys.*, 63:1646, 1975.

[118] J. S. Tse, M. L. Klein, and I. R. McDonald. Computer simulation studies of the structure I clathrate hydrates of methane, tetrafluoromethane, cyclopropane, and ethylene oxide. *J. Chem. Phys.*, 81:6146, 1984.

[119] C. Gutt, B. Asmussen, W. Press, M. R. Johnson, Y. P. Handa, and J. S. Tse. The structure of deuterated methane–hydrate. *J. Chem. Phys.*, 113:4713, 2000.

[120] L. del Rosso, M. Celli, D. Colognesi, S. Rudić, N. J. English, C. J Burnham, and L. Ulivi. Dynamics of hydrogen guests in ice XVII nanopores. *Phys. Rev. Mater.*, 1:065602, 2017.

Umbertoluca RANIERI

Email umbertoluca.ranieri@gmail.com
Phone +33 750529276
Date of Birth 20/2/1991

EDUCATION

PhD in physics
2018

Ecole Polytechnique Fédérale de Lausanne (EPFL) (Switzerland)
Joint PhD programme between the EPFL and the ILL research centre in France.
Thesis title: “Guest dynamics in methane hydrates and hydrogen hydrates under high pressure”. Supervisors: L. E. Bove, Ph. Gillet, & M. M. Koza.

MSc in physics
6/2014

Université Pierre et Marie Curie (France)
Joint master programme between Université Pierre et Marie Curie (now Sorbonne Université) and Universiteit Antwerpen.
Thesis title: “Dynamical anomalies in high-pressure liquid water investigated by inelastic x-ray scattering”. Supervisors: L. E. Bove & P. Giura.

MSc in physics
6/2014

Universiteit Antwerpen (Belgium)

BSc in physics
6/2012

Université Pierre et Marie Curie (France)

High school diploma
7/2009

Liceo Scientifico A. Scacchi di Bari (Italy)

RESEARCH EXPERIENCE

PhD Researcher
8/2016–8/2018

Institut Laue-Langevin (ILL) (France)
- Gas clathrate hydrate samples preparation, spectroscopy and diffraction measurements, data analysis using specialized softwares

PhD Researcher
9/2014–7/2016

EPFL (Switzerland)
- Gas clathrate hydrate samples preparation, spectroscopy and diffraction measurements, data analysis using specialized softwares

Research Trainee
2014 (6 months)

Université Pierre et Marie Curie (France)
- Inelastic x-ray scattering measurements on hot dense water, data analysis using IgorPro

Research Trainee
2013 (2 months)

Universiteit Antwerpen (Belgium)
- Electron microscopy on shape-memory alloys, data analysis using Matlab

Research Trainee
2012 (4 weeks)

Ecole Normale Supérieure de Paris (France)
- Ultrafast spectroscopy measurements on carbon nanotubes

Teaching experience

Teaching assistant	**EPFL** & **Université de Lausanne** (Switzerland)
Spring 2016	“Physique générale I” (Université de Lausanne)
Fall 2015	“Physique générale I” (EPFL)
Spring 2015	“Physique générale I” (Université de Lausanne)

Teaching assistant	**Université Pierre et Marie Curie** (France)
8/2013	Mathematics and physics for 1st year students (“stage de pré-rentrée”)
8/2012	Mathematics and physics for 1st year students (“stage de pré-rentrée”)

Articles in peer-reviewed journals

- S. Schaack, U. Ranieri, P. Depondt, R. Gaal, W. F. Kuhs, A. Falenty, P. Gillet, F. Finocchi, and L. E. Bove, “Orientational ordering, locking-in, and distortion of CH_4 molecules in methane hydrate III under high pressure.” *J. Phys. Chem. C*, 122, 11159–11166 (2018).
- U. Ranieri, M. M. Koza, W. F. Kuhs, S. Klotz, A. Falenty, P. Gillet, and L. E. Bove, “Fast methane diffusion at the interface of two clathrate structures.” *Nature Communications*, 8, 1076 (2017).

  Featured on Phys.org and on the webpage of the Institute of Physics of the CNRS (in French).
- U. Ranieri, P. Giura, F. A. Gorelli, M. Santoro, S. Klotz, P. Gillet, L. Paolasini, M. M. Koza, and L. E. Bove, “Dynamical crossover in hot dense water: the hydrogen bond role.” *J. Phys. Chem. B*, 120, 9051–9059 (2016).

To be submitted

- U. Ranieri, M. M. Koza, W. F. Kuhs, R. Gaal, S. Klotz, A. Falenty, D. Wallacher, J. Ollivier, P. Gillet, and L. E. Bove, “Quantum dynamics of H_2 and D_2 confined in hydrate structures as a function of pressure and temperature.”

In preparation

- U. Ranieri et al., “High-pressure Raman study of methane hydrate up to 150 GPa.”

Conference papers, published abstracts and other publications

- U. Ranieri, M. M. Koza, W. F. Kuhs, S. Klotz, A. Falenty, P. Gillet, and L. E. Bove, “Fast diffusion of methane at the interface of clathrate structures I and II.” *ILL Annual Report 2017*, Scientific Highlights, 58–59.
- U. Ranieri, M. M. Koza, W. F. Kuhs, S. Klotz, A. Falenty, D. Wallacher, P. Gillet, and L. E. Bove, “Guest dynamics in high-pressure clathrate hydrates.” in *Proc. Ninth International Conference on Gas Hydrates*, Denver, Colorado, USA, 6/2017.
- U. Ranieri, L. E. Bove, S. Klotz, T. C. Hansen, A. Falenty, D. Wallacher, M. M. Koza, P. Gillet, and W. F. Kuhs, “Structural changes in hydrogen hydrate in the GPa pressure range.” in *Proc. Ninth International Conference on Gas Hydrates*, Denver, Colorado, USA, 6/2017.
- U. Ranieri, L. E. Bove, S. Klotz, T. C. Hansen, M. M. Koza, P. Gillet, D. Wallacher, A. Falenty, W. F. Kuhs, “Neutron diffraction on methane and hydrogen hydrates under high pressure.” *Acta Cryst.*, 2016, A72, s415.

ORAL PRESENTATIONS

- "Methane dynamics in ice clathrates and hydrates under high pressure." *WATER-X Workshop: Exotic Properties of Water under Extreme Conditions*, La Maddalena, Italy, 6/2018.
- "Guest dynamics in high-pressure clathrate hydrates." *Ninth International Conference on Gas Hydrates*, Denver, Colorado, USA, 6/2017.
- "Hydrogen-bond symmetrization in methane and hydrogen hydrates in the Mbar range," *15èmes Journées de la Matière Condensée, Microsymposium: Nuclear Quantum Effects*, Bordeaux, France, 8/2016.
- "Dynamical anomalies in hot dense water: the hydrogen bond role," *WATER-X Workshop: Exotic Properties of Water under Extreme Conditions*, Nice, France, 7/2016.
- "Guest dynamics in methane and hydrogen hydrates under high pressure," *1st Workshop on Sustainable Energies and Neutron Scattering*, Bordeaux, France, 5–6/2016.
- "Dynamical anomalies in hot dense water," *XIV International Workshop on Complex Systems*, Fai della Paganella, Italy, 3/2015.

POSTER PRESENTATIONS

- "Structural changes in hydrogen hydrate in the GPa pressure range." *Ninth International Conference on Gas Hydrates*, Denver, Colorado, USA, 6/2017.
- "Neutron diffraction on hydrogen hydrate under high pressure,"*Rencontres des Jeunes Physiciens, 2nd Edition*, Grenoble, France, 3/2017.
- "Dynamical anomalies in hot dense water," *25th International Association for the Advancement of High Pressure Science and Technology & 53rd European High Pressure Research Group Meeting*, Madrid, Spain, 8–9/2015.
- "Water dynamics in the GPa range," *52nd European High Pressure Research Group Meeting*, Lyon, France, 9/2014.
- "Dynamical anomalies in water under extreme pressures," *25th Conference of the Condensed Matter Division & 14èmes Journées de la Matière Condensée, Microsymposium: Water and Aqueous Solutions*, Paris, France, 8/2014.

COURSES ATTENDED

- "Gravitational Astronomy," doctoral course at Université de Grenoble, France, 5–6/2018 (12 hrs).
- "Neutron Fields Forever" seminars, ILL, Grenoble, France, 1–6/2018 (38 hrs).
- "Neutron Fields Forever" seminars, ILL, Grenoble, France, 1–6/2017 (32 hrs).
- "Water and solutions with a focus on x-ray techniques," doctoral course at EPFL, Lausanne, Switzerland, 6/2016 (12 hrs).
- "Scientific writing (ENG-613b)," doctoral course at EPFL, Lausanne, Switzerland, 1–3/2016 (20 hrs).
- "Conference and seminar skills: presenting research in English - Level B2," doctoral course at EPFL, Lausanne, Switzerland, 1/2016 (12 hrs).
- "Academic writing for doctoral students - Level C1," doctoral course at EPFL, Lausanne, Switzerland, 9–12/2015 (19 hrs).

- 8th School on neutron diffraction data - Treatment using the FULLPROF Suite, ILL, Grenoble, France, 12/2015 (5 days).
- XIII school on neutron scattering Francesco Paolo Ricci "Instruments and devices for neutron scattering experiments," Foundation and centre for scientific culture Ettore Majorana, Erice, Italy, 7–8/2015 (8 days).
- Hercules Specialized Course "Dynamical properties investigated by neutrons and synchrotron X-rays," ILL & ESRF, Grenoble, France, 9/2014 (5 days).
- Pre-EHPRG Meeting school, European High Pressure Research Group, Lyon, France, 9/2014 (12 hrs).
- MDANSE (Molecular Dynamics to Analyse Neutron Scattering Experiments) school, ILL, Grenoble, France, 5/2014 (2 days).

TECHNICAL SKILLS

Scientific techniques and equipments including: Quasielastic and inelastic neutron scattering, neutron and x-ray diffraction, inelastic x-ray scattering, Raman spectroscopy, diamond anvil cell and Paris-Edinburgh press apparatus.

Computer skills including: Extensive experience in IgorPro and LAMP (Large Array Manipulation Program) for data fitting and in FullProf for Rietveld refinements. Experience in Matlab for linear algebra and image analysis.

SCHOLARSHIPS

Labex-Matisse scholarship for 2013–2014.

International mobility financial support for 2012–2013 from the French Ministry of Higher Education and Research.